NASA Conference Publication 2142

Selected NASA Research in Composite Materials and Structures

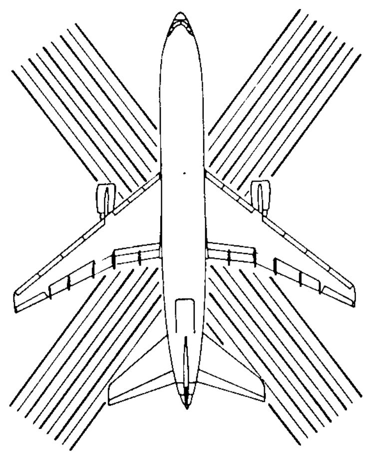

Contributions from Langley Research Center to the Second Industry Review of the NASA Aircraft Energy Efficiency (ACEE) Composite Programs held in Seattle, Washington August 11-13, 1980

NASA

Add 431389- 431394

NASA Conference Publication 2142

Selected NASA Research in Composite Materials and Structures

Contributions from Langley Research Center to the Second Industry Review of the NASA Aircraft Energy Efficiency (ACEE) Composite Programs held in Seattle, Washington August 11-13, 1980

NASA
National Aeronautics and Space Administration

Scientific and Technical Information Branch

1980

FOREWORD

The NASA Aircraft Energy Efficiency (ACEE) Composite Primary Aircraft Structures program has made significant progress in the development of technology for advanced composites in commercial aircraft. Under NASA sponsorship, commercial airframe manufacturers are 3 years into programs to demonstrate technology readiness and cost effectiveness of advanced composites for secondary and medium primary components. Timely dissemination of technical information acquired in these programs is achieved through distribution of quarterly and final written reports and through periodic special oral reviews.

The second special oral review of ACEE Composites Programs was held August 11-13, 1980, at the Olympic Hotel in Seattle, Washington. The conference included comprehensive reviews of six major composite component development programs by ACEE composites contractors: Boeing Commercial Airplane Company, Douglas Aircraft Company, and Lockheed-California Company. In addition, a special session included selected papers on NASA sponsored research in composite material and structures. These latter presentations are collected in this NASA Conference Publication.

Individual authors prepared their narrative and figures in a form that could be directly reproduced in this volume. The material is in facing page format and is essentially the same material used in the oral presentations at the review. The assistance of the Scientific and Technical Information Programs Division of the Langley Research Center in publishing these proceedings is gratefully acknowledged.

Herman L. Bohon
Conference Chairman
Langley Research Center

CONTENTS

FAILURE PREDICTION TECHNIQUES FOR COMPRESSION LOADED COMPOSITE LAMINATES WITH HOLES

Martin M. Mikulas, Jr.

INTRODUCTION

Experimental studies have shown that holes, cracks, delaminations, and impact damage can cause a severe reduction in the load carrying capability of advanced composite materials. The failure loads and associated failure modes that occur due to tension have received considerable attention as documented in references 1 to 5. The failure modes that have been observed in compression (refs. 6 to 9) are quite unlike the local yielding that occurs in isotropic metals. The composite material is composed of high strength, high stiffness, brittle filaments embedded in matrix of low strength and stiffness. The two main compression failure modes are (1) delaminations due to a strength failure of the matrix and (2) microbuckling of the fibers due to low stiffness of the matrix. These failure modes result in composite materials being highly notch sensitive in compression which is quite unlike experiences with metals.

For composites to be used to their full capability, it is necessary that failure prediction techniques be developed for anticipated flaws or damage. Recent studies reported in references 8, 10, and 11 have applied the stress fracture criteria of reference 2 to compression failure of plates with holes. These studies deal with narrow specimens ($\leq$ 13 cm) and small holes ($\leq$ 4 cm). For the range of parameters studied in these references, it was shown that the stress fracture criteria of reference 2 could provide a good failure prediction capability.

In the present paper, attention is focused on the degree of notch sensitivity of composites in compression and whether their failures can be predicted over a wide range of plate and hole sizes. The notch sensitivity of composites is investigated by comparing actual failure loads of laminates with circular holes, with the extreme failure limits that would be expected from an ideal notch insensitive material and from an ideal notch sensitive material. The predictability question is addressed by applying the point stress failure criterion to a wide range of plate widths and hole sizes and comparing with available experimental data. The severity of impact is explored by comparing strength reductions resulting from impact with those resulting from comparable size circular holes. Finally, a comparison is made of the differences to be expected from the effects of cracks and circular holes on failure strength.

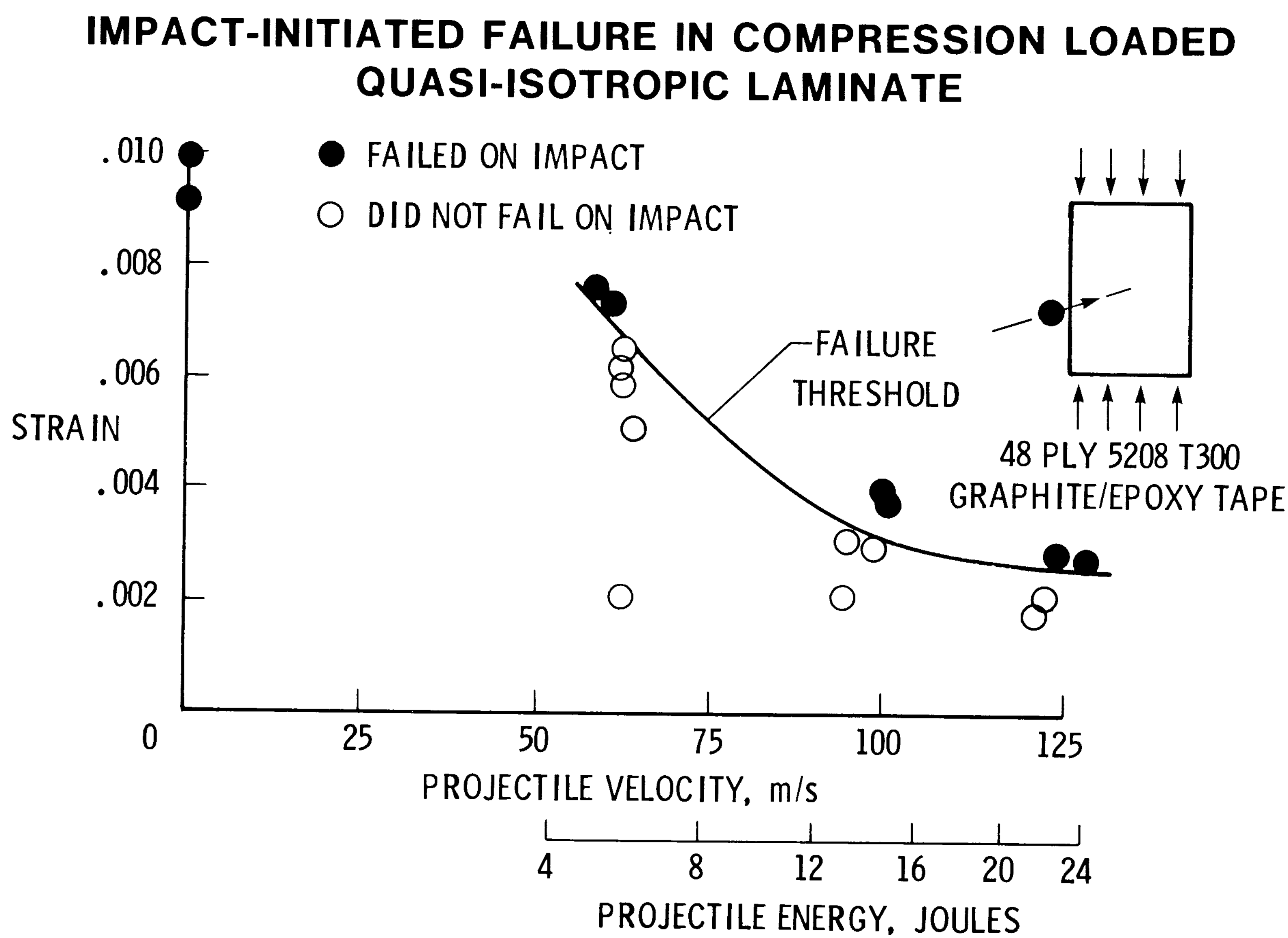
IMPACT-INITIATED FAILURE IN COMPRESSION LOADED QUASI-ISOTROPIC LAMINATE
FAILED ON IMPACT
DID NOT FAIL ON IMPACT
STRAIN
.010
.008
.006
.004
.002
0
25
50
75
100
125
PROJECTILE VELOCITY, m/s
4
8
12
16
20
24
PROJECTILE ENERGY, JOULES
FAILURE THRESHOLD
48 PLY 5208 T300
GRAPHITE/EPOXY TAPE

Figure 1.

IMPACT-INITIATED FAILURE IN COMPRESSION LOADED QUASI-ISOTROPIC LAMINATE

(Figure 1)

The sensitivity of graphite/epoxy laminates to low velocity impact was investigated in references 12 and 13. This was accomplished by impacting 13 cm by 25 cm laminates with a 1.3 cm diameter aluminum sphere while under compressive load. Results for a quasi-isotropic laminate are shown in Figure 1. The panels were subjected to an axial compressive strain as shown by the symbols. The solid symbols represent panels which failed on impact while the open symbols represent panels which did not fail on impact. The line represents a threshold where failure occurs. The failures at zero velocity are control specimens with no impact. These failures are due to buckling of the panel and do not represent the undamaged strength of the material. As will be discussed later, the failure strain of this laminate in compression would be at least .012 to .016. The data points for increasing impact velocity indicate that a significant reduction results from these relatively low velocity impacts. The predominant failure mode as discussed in reference 14 is a delamination. In the next figure, the effects of circular holes on the strength of the same laminate are shown.

EFFECT OF HOLES ON COMPRESSION STRENGTH OF A QUASI-ISOTROPIC LAMINATE

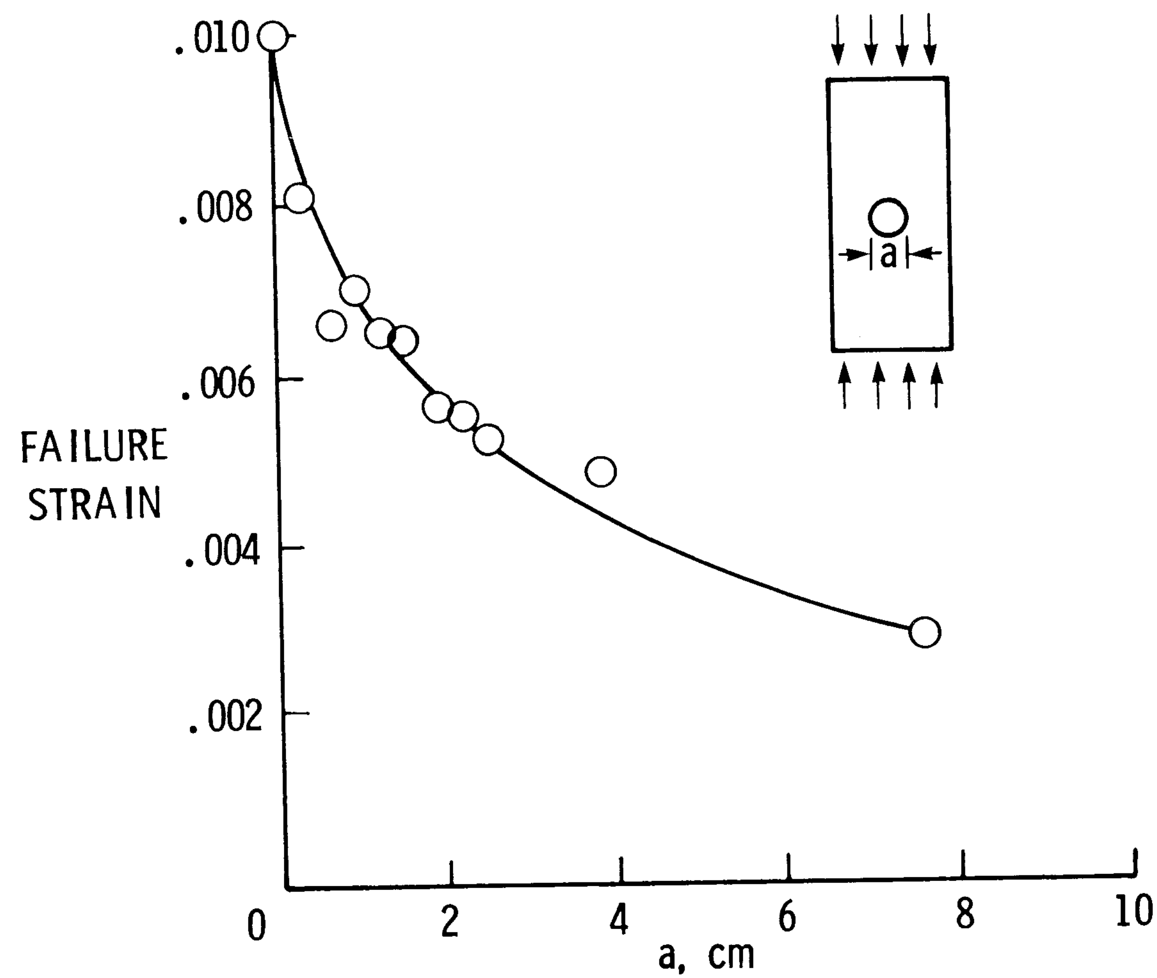

Figure 2.

EFFECT OF HOLES ON COMPRESSION STRENGTH OF A QUASI-ISOTROPIC LAMINATE

(Figure 2)

The sensitivity of compression loaded graphite/epoxy laminates to circular holes was investigated in references 8, 9 and 15. Results for a 13 cm by 25 cm quasi-isotropic laminate are shown in Figure 2. The curve shown is merely a line drawn through the data points. There is a significant reduction in the load carrying capability of the laminate with increasing hole size. This reduction is similar to that which occurs for impact discussed in the previous figure. To obtain insight into whether such reductions in load should be expected, idealized limiting failure cases are considered on the next figure.

IDEALIZED LIMIT CASES FOR FAILURE

NOTCH INSENSITIVE | NOTCH SENSITIVE

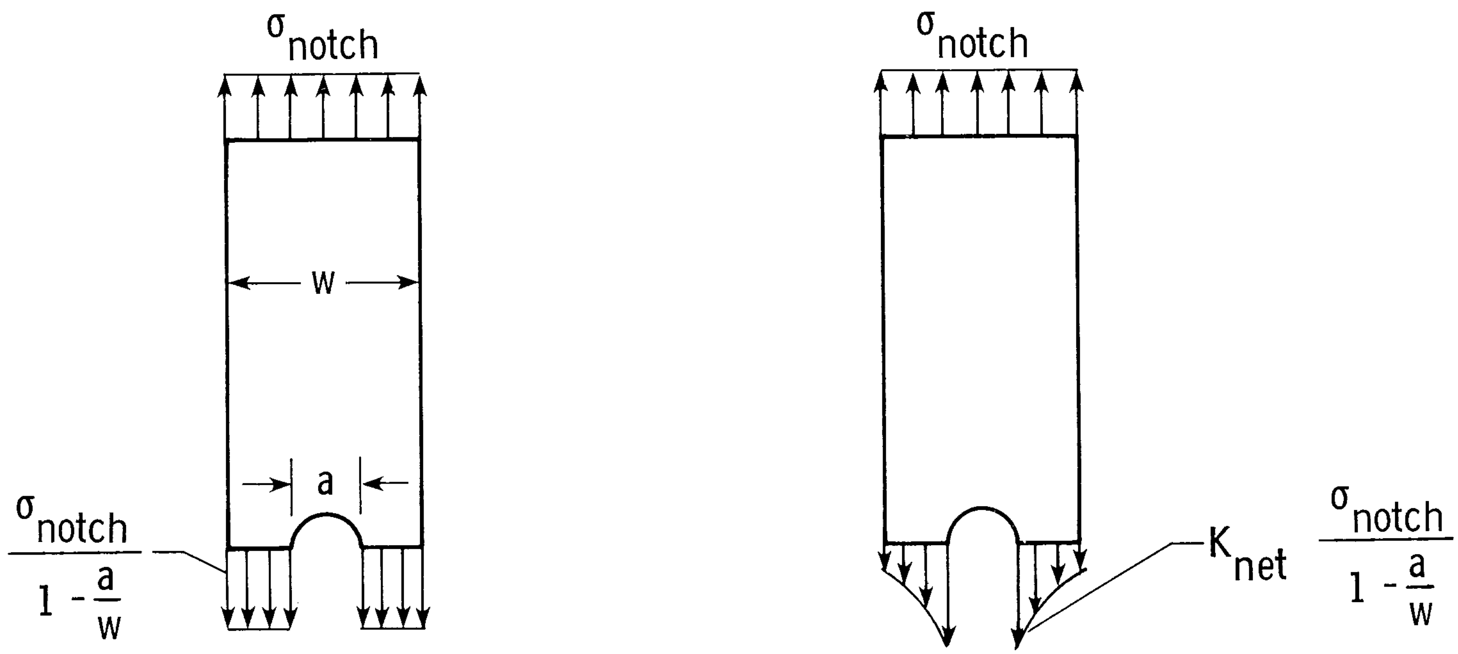

FAILURE OCCURS WHEN AVERAGE NET SECTION STRESS REACHES UNNOTCHED STRESS σ_0 SO THAT

$$\sigma_{notch} = \sigma_0\left(1 - \frac{a}{W}\right)$$

FAILURE OCCURS WHEN PEAK STRESS AT HOLE REACHES UNNOTCHED STRESS σ_0 SO THAT

$$\sigma_{notch} = \sigma_0 \frac{\left(1 - \frac{a}{W}\right)}{K_{net}}$$

Figure 3.

IDEALIZED LIMIT CASES FOR FAILURE

(Figure 3)

The two extreme limiting failure cases that a material could experience are shown in Figure 3. The first limiting case is where the material would be totally insensitive to notches and experience a net area reduction in strength as material was removed. The equation governing such failure is presented under the left-hand sketch. The second limiting case is where the material would be totally sensitive to a notch and experience failure when the maximum stress at the edge of the hole reached the ultimate unnotched strength of the material. The equation governing such a failure is presented under the right-hand sketch where K_{net} is the net section stress concentration factor as presented in reference 16. These equations are plotted on the next figure.

LIMITING VALUES FOR FAILURE

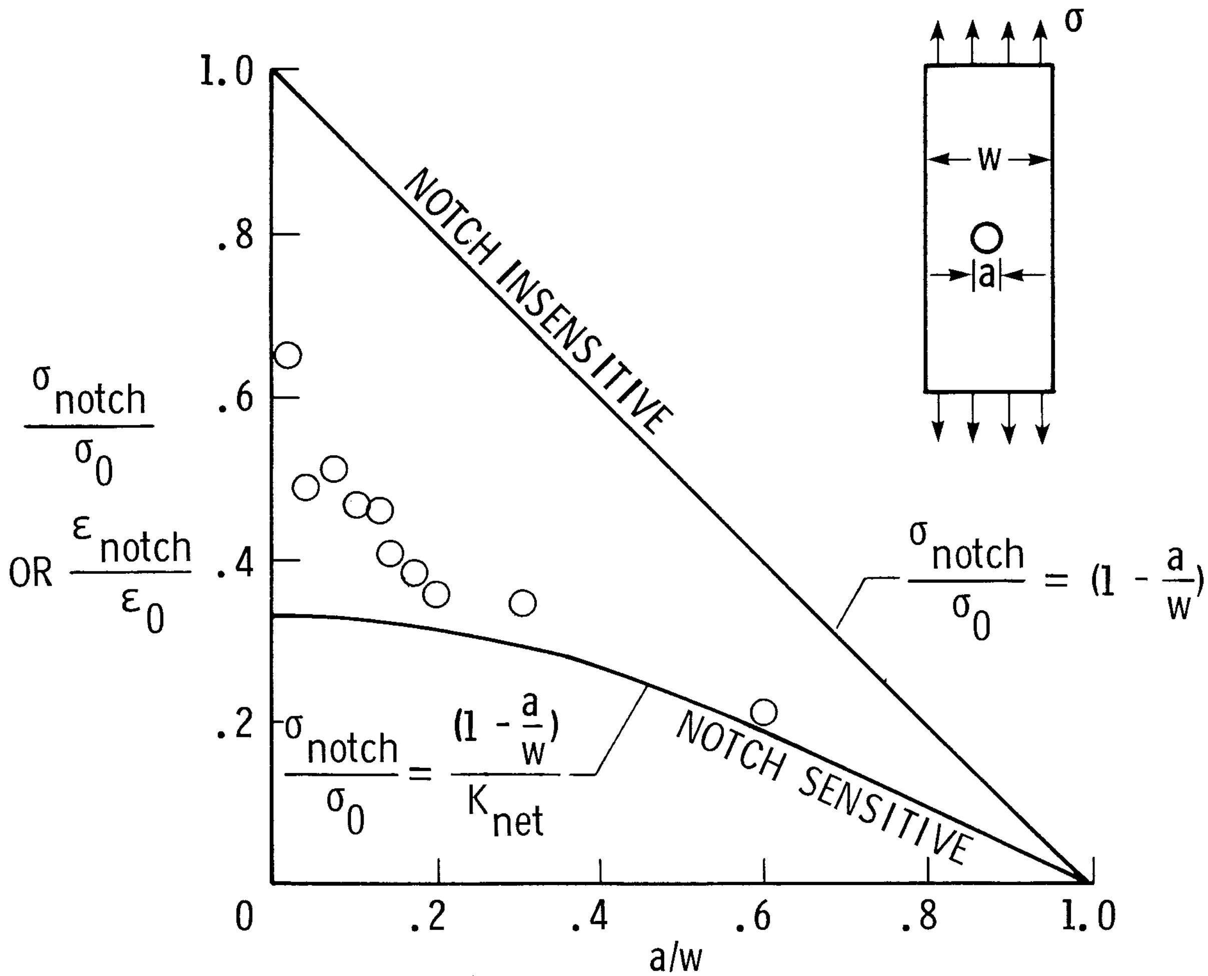

Figure 4.

LIMITING VALUES FOR FAILURE

(Figure 4)

The reductions in laminate strength as predicted by the equations developed on the previous figure are shown on Figure 4. Since only unidirectional loads are considered, this reduction is also directly related to the applied strain required to fail the panel as shown on the ordinate. The data points shown on the figure are the same as those of Figure 2 but normalized with respect to an unnotched failure strain ϵ_o of .014.

Unfortunately, it is quite difficult to obtain the ultimate strength of a high strength composite material in compression (see references 17 and 18). As discussed in Figure 1, the buckling failure strain for the unnotched 13 cm by 25 cm laminate being studied was .01. In reference 19, failure strains as high as .016 were reported for a quasi-isotropic graphite/epoxy laminate. For this paper, an unnotched failure strain of .014 is taken for comparison purposes. Further work is needed to obtain a better understanding of the unnotched compressive strength of composite laminates.

It can be seen in Figure 4 that the experimental data points are bounded by the notch sensitive and notch insensitive values. The fact that the data points are above the notch sensitive curve indicates that the material is not ideally brittle and some load redistribution does occur around the hole. In the subsequent figures, this load redistribution is discussed and a technique is presented for predicting the strength reductions.

LOCAL STRESS RELIEF MECHANISMS

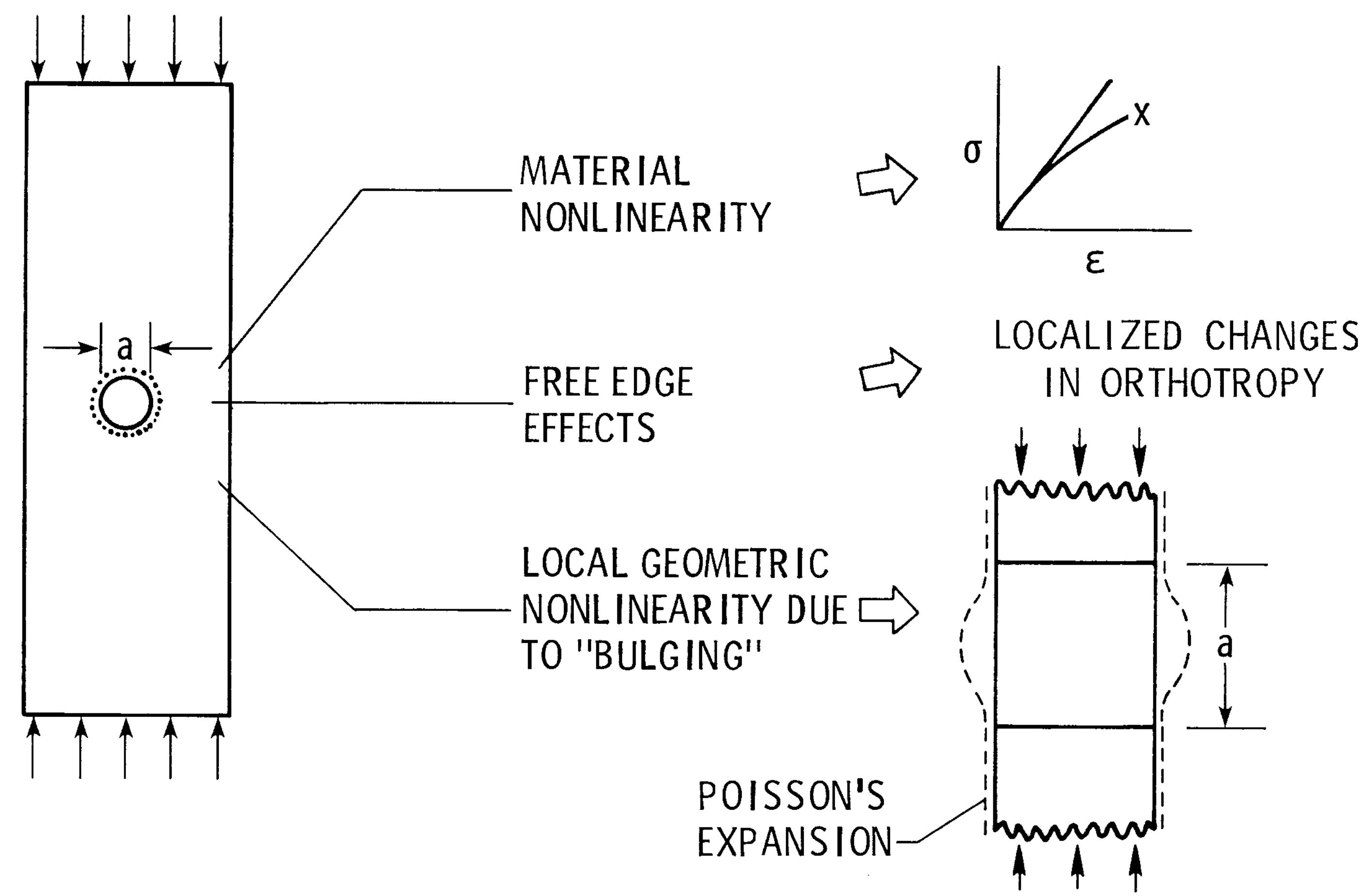

Figure 5.

LOCAL STRESS RELIEF MECHANISMS

(Figure 5)

Mechanisms for relieving stress concentrations around holes in a composite material are depicted on Figure 5. The first mechanism is nonlinear load shortening behavior of the material itself. The second is related to the high interlaminar stresses that occur at a free edge. These high stresses can result in nonlinear matrix behavior or even a local delamination. These effects will result in changing the local orthotropy of the laminate and thus the load distribution. The third mechanism is associated with the Poisson's expansion of the laminate. Since the stresses are much higher around the hole than elsewhere in the laminate, the Poisson's expansion is greater around the hole. This differential expansion, or bulging, as shown in Figure 5 couples with the high compressive stress to cause a geometric nonlinearity. Effects such as these cause the failure loads of a panel with a circular hole to be higher than the notch sensitive curve as shown in Figure 4.

At present, it is beyond the state of the art to quantify the effects of the mechanisms just discussed. In reference 2, stress fracture criteria are developed where the influence of the above mentioned effects can be accounted for in failure studies without knowing exactly what is happening in the vicinity of the hole. The two failure criteria developed in reference 2 are the point stress failure criterion and the average stress failure criterion. The point stress failure criterion was used in this study and is discussed on the next figure.

POINT STRESS FAILURE CRITERION

"FAILURE OCCURS WHEN THE STRESS AT A DISTANCE d_0 AWAY FROM THE EDGE OF THE HOLE REACHES ULTIMATE"

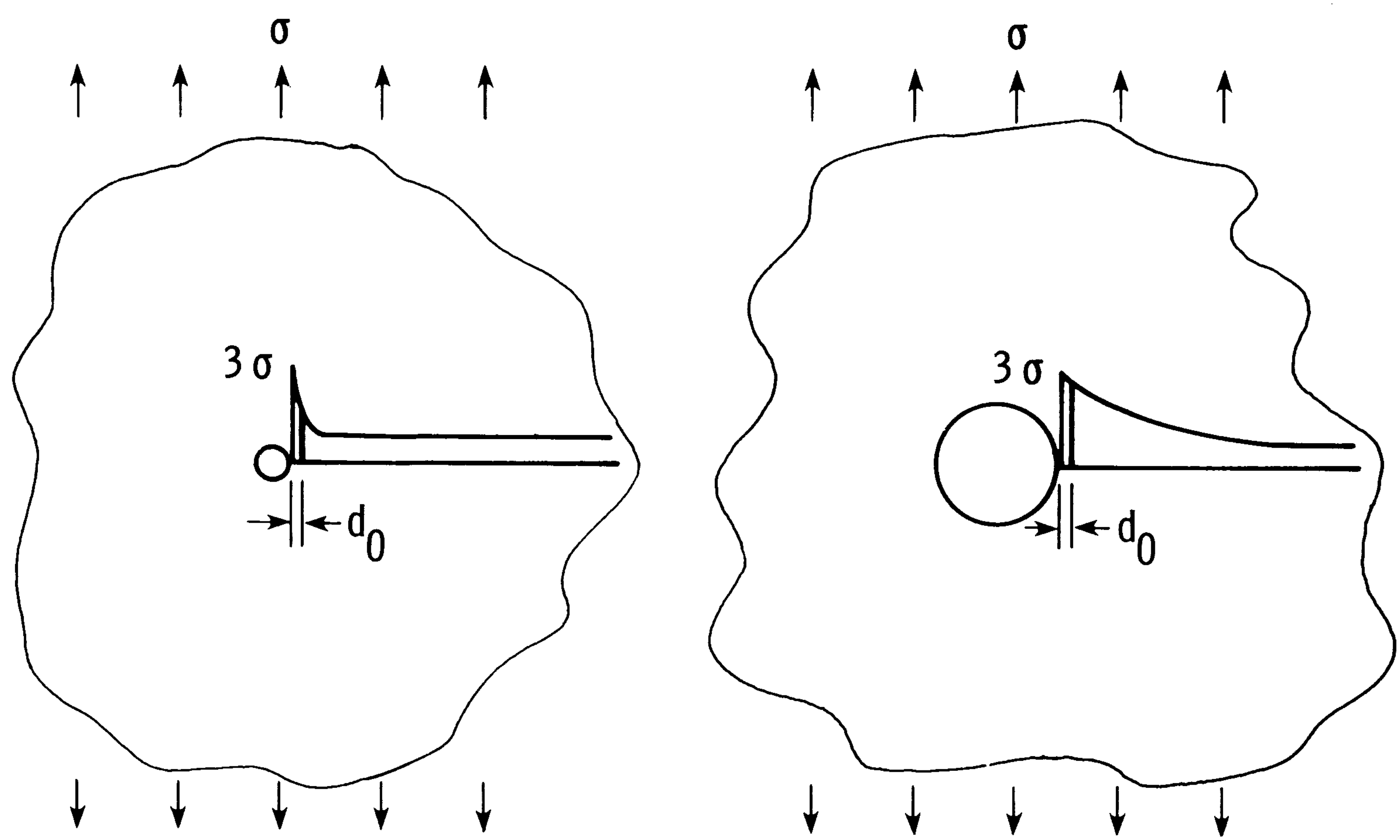

Figure 6.

POINT STRESS FAILURE CRITERION

(Figure 6)

The point stress failure criterion assumes that failure occurs when the stress at a distance d_0 away from the edge of the hole reaches ultimate. The distance d_0 then, in effect, becomes a material property. As can be seen in Figure 6, the peak stress at the edge of a hole is independent of hole size. However, the stress distribution is a function of hole size. Thus, for a fixed value of d_0, a large hole will have a larger predicted strength reduction than a small hole. These reductions are studied in general for a finite width laminate on the next two figures.

STRESS DISTRIBUTION AROUND A HOLE IN A FINITE WIDTH PLATE

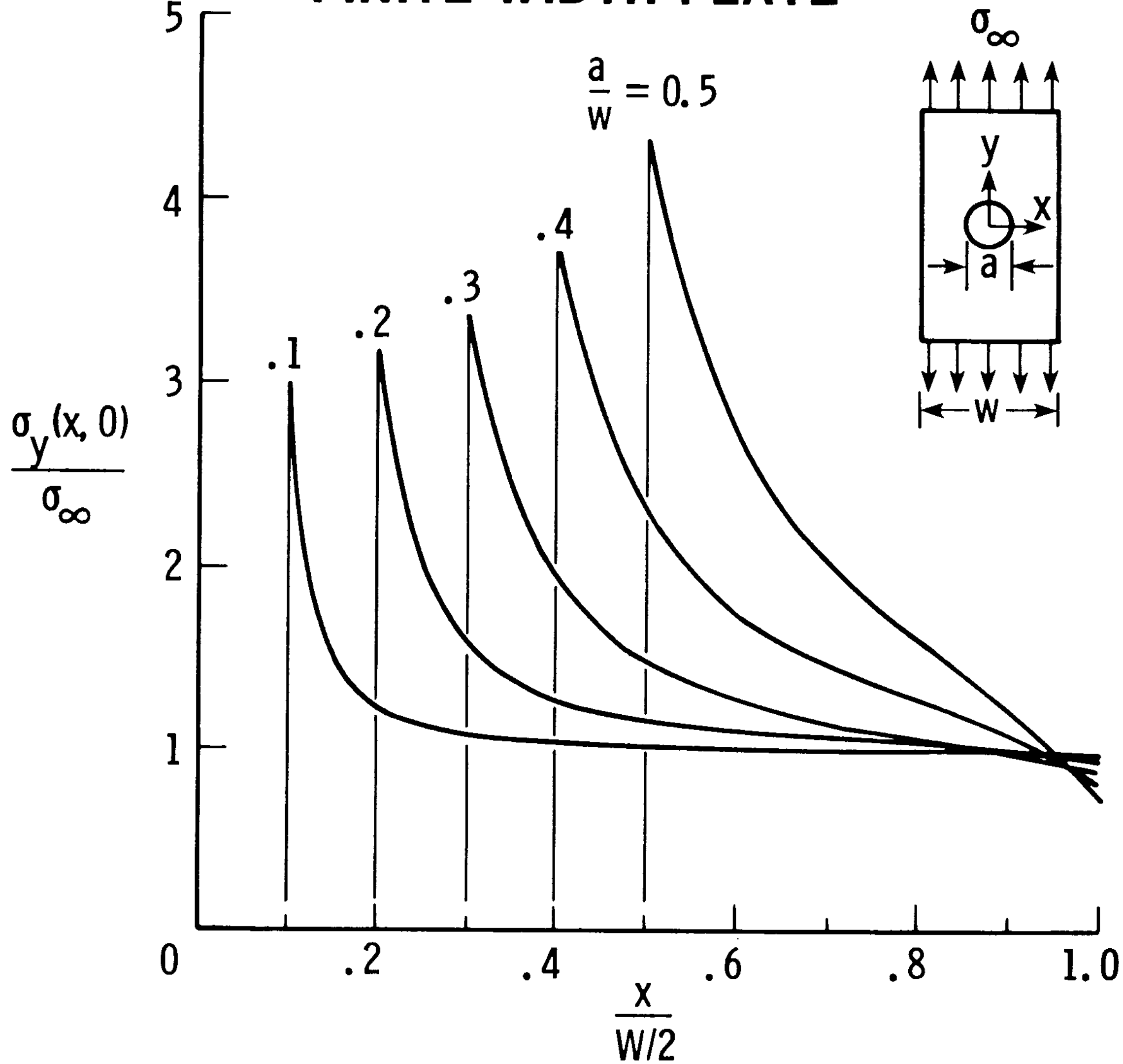

Figure 7.

STRESS DISTRIBUTION AROUND A HOLE IN A FINITE WIDTH PLATE

(Figure 7)

To apply the point stress failure criterion, it is necessary to have the distributions of stress around the holes. The stress distributions around a circular hole in isotropic finite width plates are developed in reference 20 and shown on Figure 7. These stress distributions and some results from the analysis of reference 21 were used to develop the strength reduction results shown on the next figure.

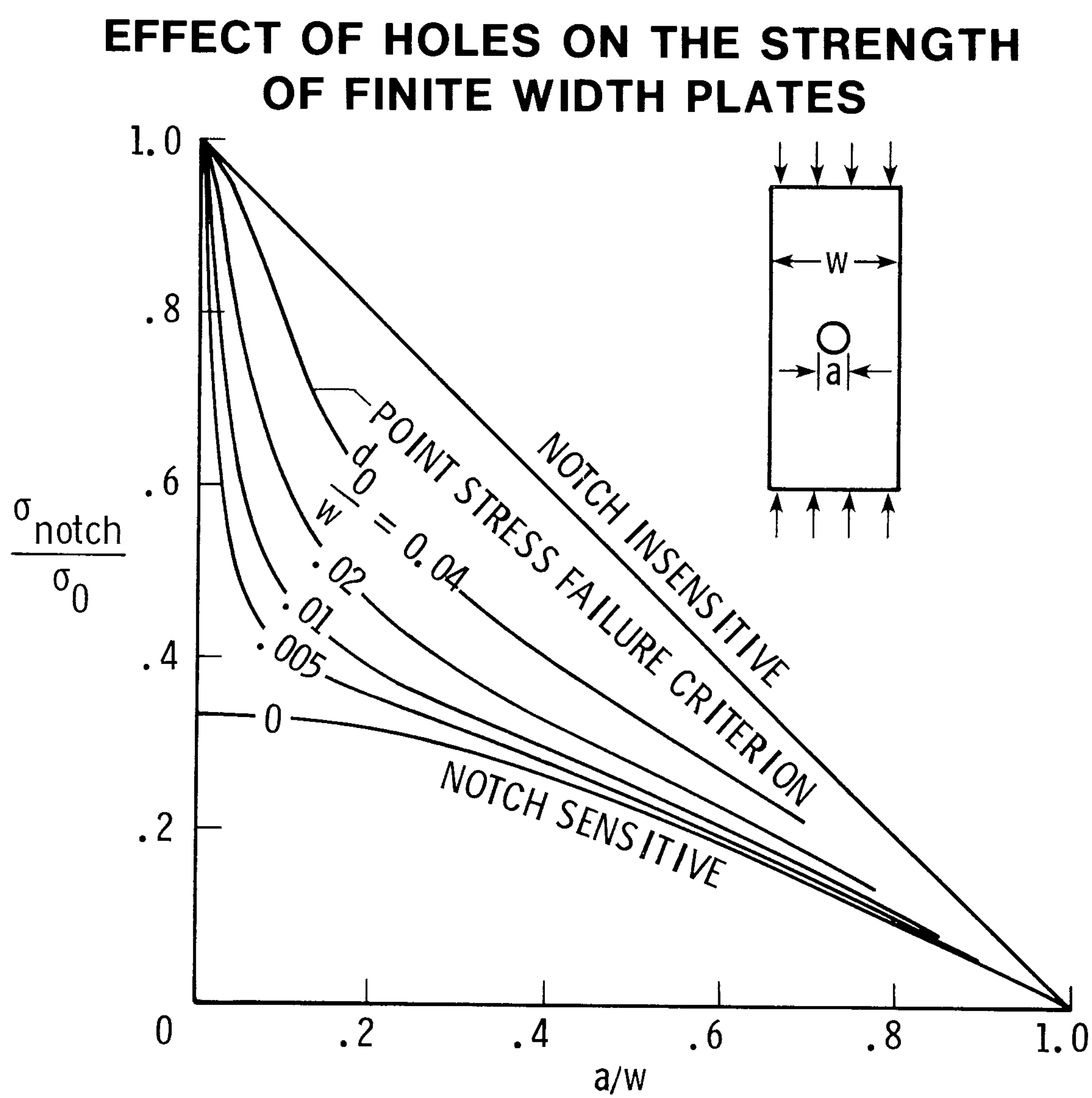
EFFECT OF HOLES ON THE STRENGTH
OF FINITE WIDTH PLATES
1.0
.8
.6
.4
.2
0
$\frac{\sigma_{notch}}{\sigma_0}$
.2
.4
.6
.8
1.0
a/w
w
a
NOTCH INSENSITIVE
POINT STRESS FAILURE CRITERION
$\frac{d_0}{w}$ = 0.04
.02
.01
.005
0
NOTCH SENSITIVE

Figure 8.

EFFECT OF HOLES ON THE STRENGTH OF FINITE WIDTH PLATES

(Figure 8)

The effect circular holes have on the strength of a finite width plate as given by the point stress failure criterion is presented on Figure 8. The point stress failure criterion is defined by two parameters. The first is the unnotched strength of the laminate σ_0 and the second is the characteristic length d_0. For a given width laminate, d_0 is determined by obtaining a best fit to the curves shown on Figure 8. Due to insufficient stress distribution information in references 20 and 21 for large hole sizes, the predicted failure curves were terminated for high values of $\frac{a}{W}$. It is expected, however, that the curves would intersect the notch insensitive upper limit curve at some value of $\frac{a}{W}$ less than 1. This failure prediction approach is applied to a specific example in the next figure.

COMPRESSIVE FAILURE OF A QUASI-ISOTROPIC LAMINATE WITH CIRCULAR HOLES

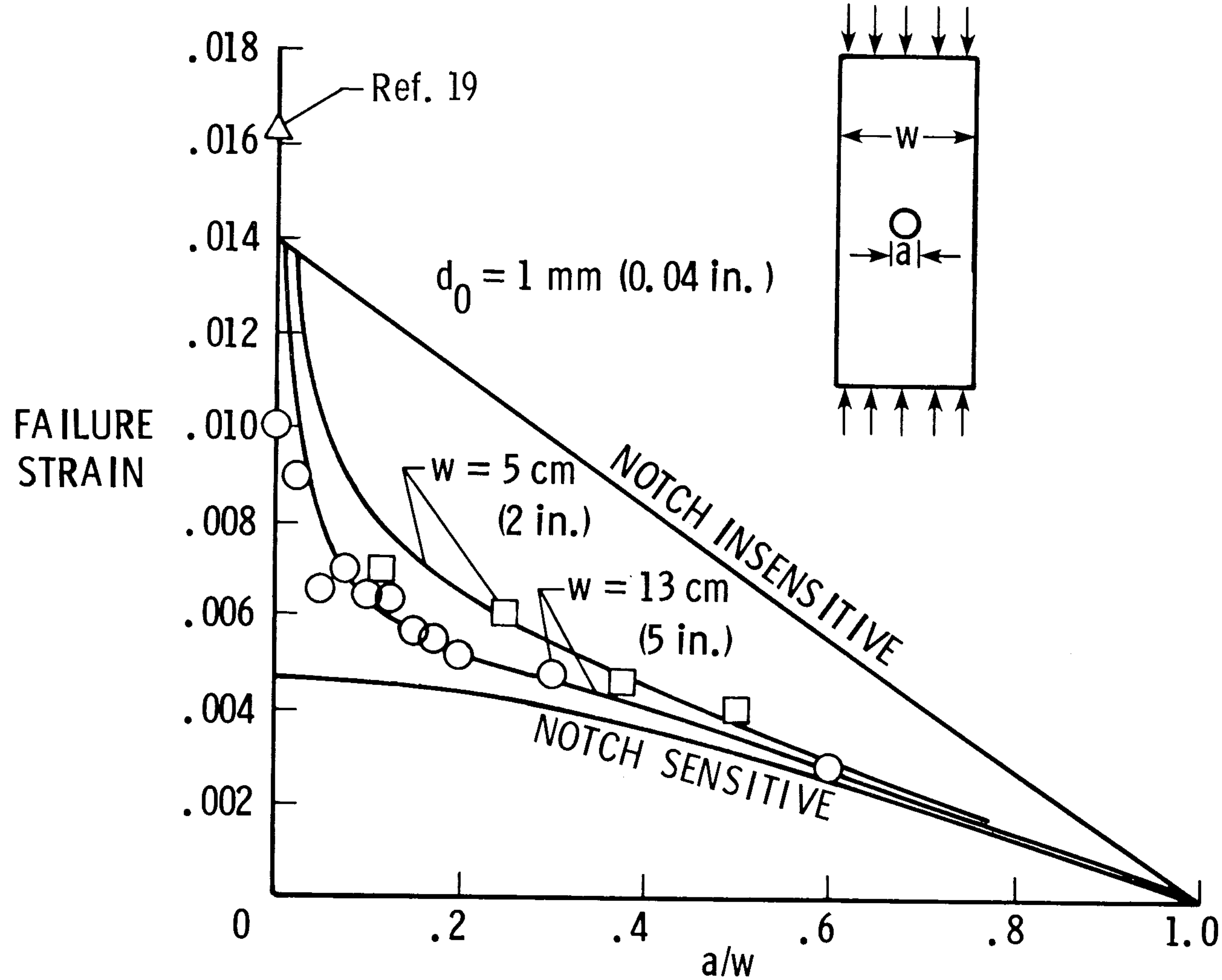

Figure 9.

COMPRESSIVE FAILURE OF A QUASI-ISOTROPIC LAMINATE WITH CIRCULAR HOLES

(Figure 9)

The effect of circular holes on the compression strength of a 48 ply quasi-isotropic laminate is shown on Figure 9. The 13 cm wide laminate data is taken from reference 15 with the exception of the data point at $\frac{a}{w} = .6$ which was produced for this report. The 5 cm wide laminate data was also produced for this report. As was discussed previously, the failure strain .01 for no hole is a result of laminate buckling and does not represent the material strength. An ultimate strain of .014 was used for the laminate as discussed on Figure 4. A good fit to the data was obtained with the point stress failure criterion by choosing a value of the characteristic length d_0 as 1 mm (.04 in.). As can be seen in the figure, this failure criterion characterizes the behavior of both width panels. The trend of wider panels being more notch sensitive and narrow panels being less notch sensitive is quite apparent. The effect is explained on the next figure where the size of the hole is held constant.

COMPRESSIVE FAILURE OF A QUASI-ISOTROPIC LAMINATE WITH CIRCULAR HOLES

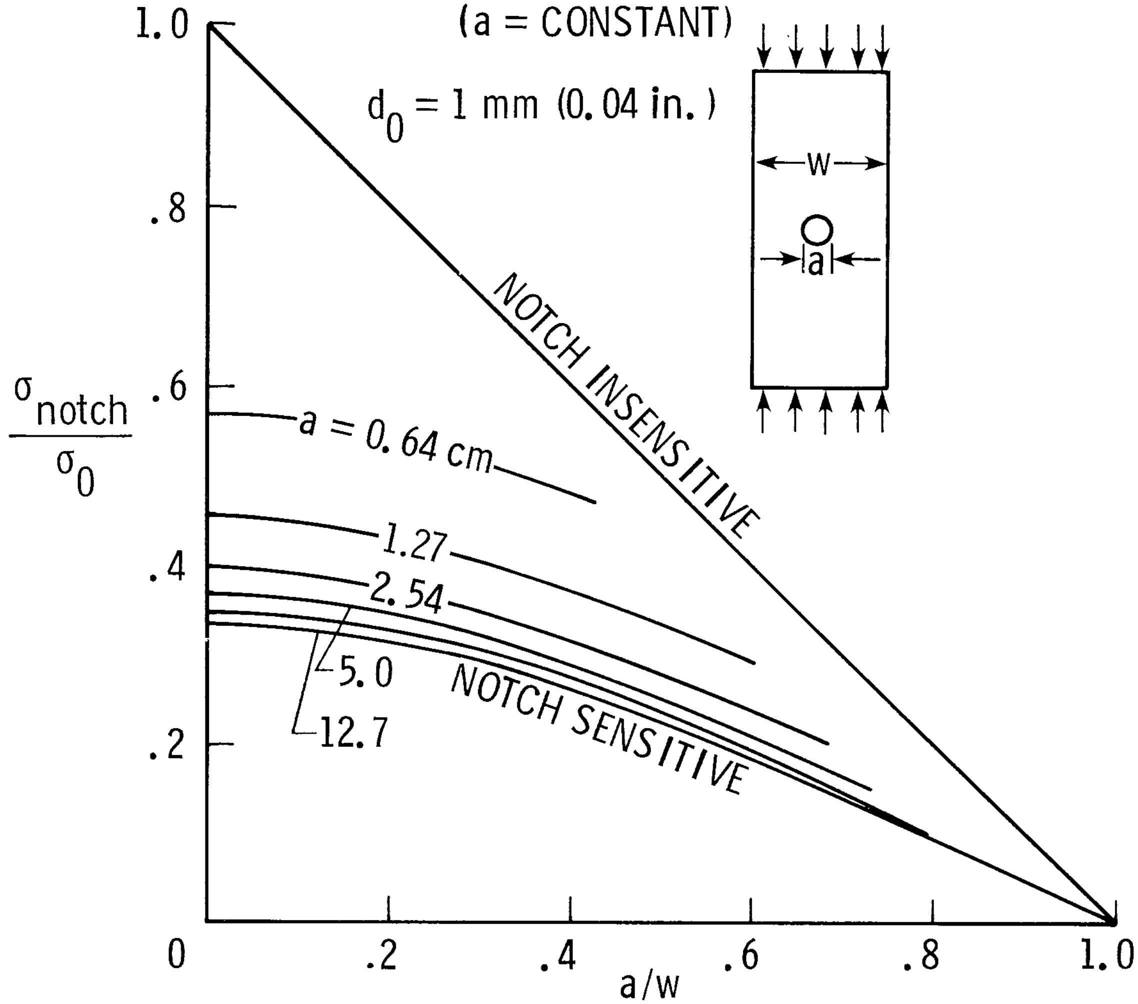

Figure 10.

COMPRESSIVE FAILURE OF A QUASI-ISOTROPIC LAMINATE WITH CIRCULAR HOLES

(Figure 10)

A cross plot of the strength reduction curves of the previous figure for constant hole size is shown normalized on Figure 10. These curves show that for small holes ($a = .64$ cm) the laminate appears quite notch insensitive while for larger holes ($a \sim 5$ cm) the laminate is approaching an almost completely notch sensitive behavior. The failure modes associated with these two cases are quite different. In the notch insensitive case, a considerable amount of load redistribution is taking place and it is likely that failure occurs due to a strength failure in the matrix. In the notch sensitive case, very little load redistribution takes place and is likely that the failure is an ultimate strength failure of the laminate controlled by the stiffness of the matrix. Because of the difference in failure modes for the different size holes, it is important when test programs are being established that the appropriate failure conditions be characterized. In the next figure, the impact sensitivity of a quasi-isotropic laminate is investigated.

EFFECT OF IMPACT DAMAGE ON THE COMPRESSIVE STRENGTH OF A QUASI-ISOTROPIC LAMINATE

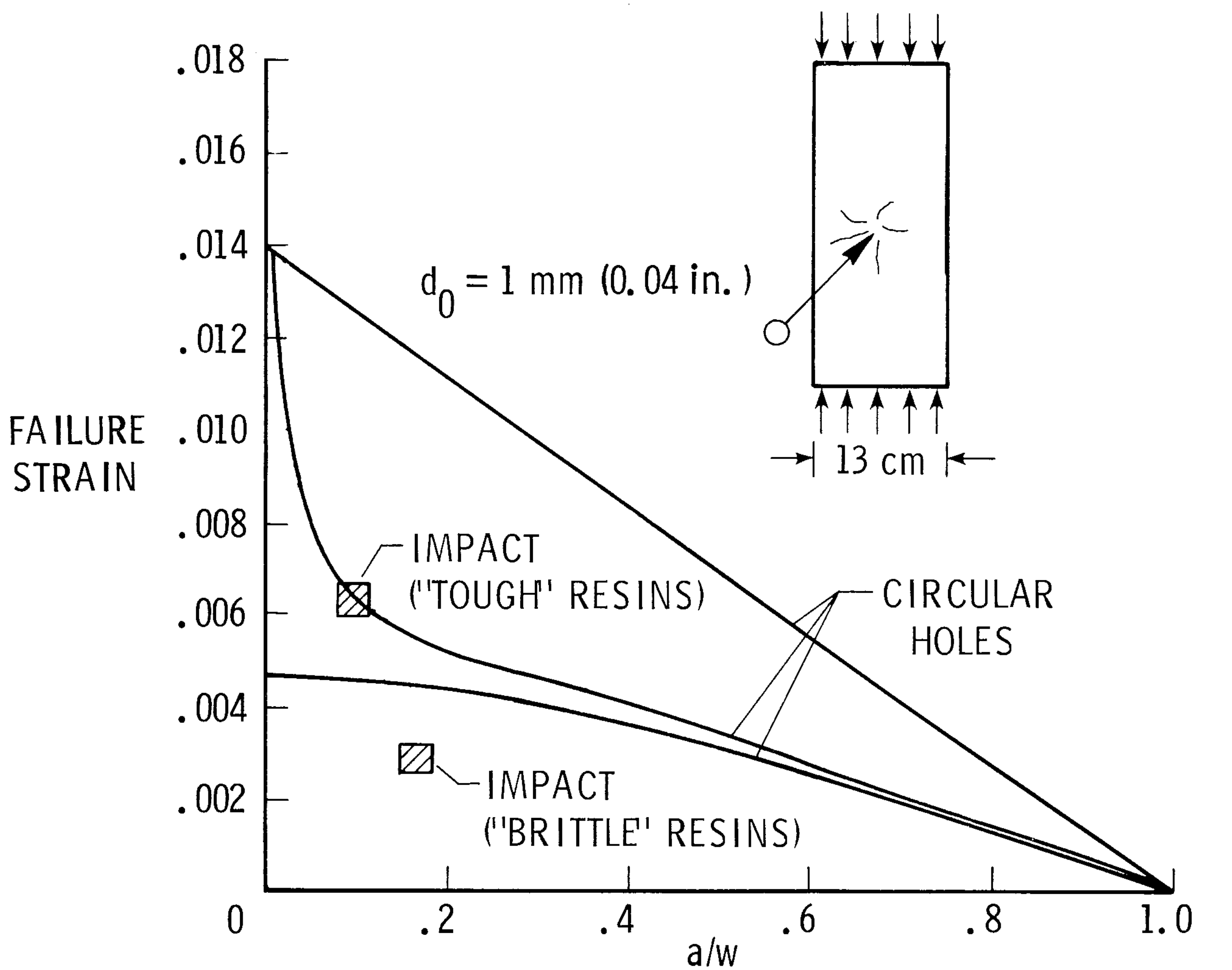

Figure 11.

EFFECT OF IMPACT DAMAGE ON THE COMPRESSIVE STRENGTH OF A QUASI-ISOTROPIC LAMINATE

(Figure 11)

The sensitivity to impact of the quasi-isotropic laminate being studied is indicated by the cross-hatched squares on Figure 11. The lower square is from Figure 1 (reference 13) while the upper square is from reference 22 for a "tough" resin system. The extent of damage was obtained by observing C-scans of the impacted areas for the laminates of references 13 and 22. The observed size of the damage area was used as a flaw size to make the comparison with hole data as shown on Figure 10. The lower data from reference 13 are for a brittle resin. As can be seen, the effect of impact damage on a composite using this resin system is more severe than the effect of an equivalent size hole. In fact, the impact results are even lower than the notch sensitive curve. This is due to the fact that the impact causes severe delamination which is readily propagated by compression through the brittle resin.

A significant improvement in the resistance of composites to impact was reported in reference 22 where alternate resin systems were explored and is indicated by the upper data in this figure. This alternate resin system was shown to possess a highly nonlinear stress-strain curve in reference 22 and is thus labeled "tough." The tough resin eliminates delamination as a failure mode and moves the failure up to a level where resin stiffness, or microbuckling, again limits strength. The use of such tougher resins in high performance applications is currently receiving considerable attention. In the next figure, the effect of circular holes on the tensile strength of a quasi-isotropic graphite/epoxy laminate is investigated.

TENSILE FAILURE OF A QUASI-ISOTROPIC LAMINATE WITH CIRCULAR HOLES

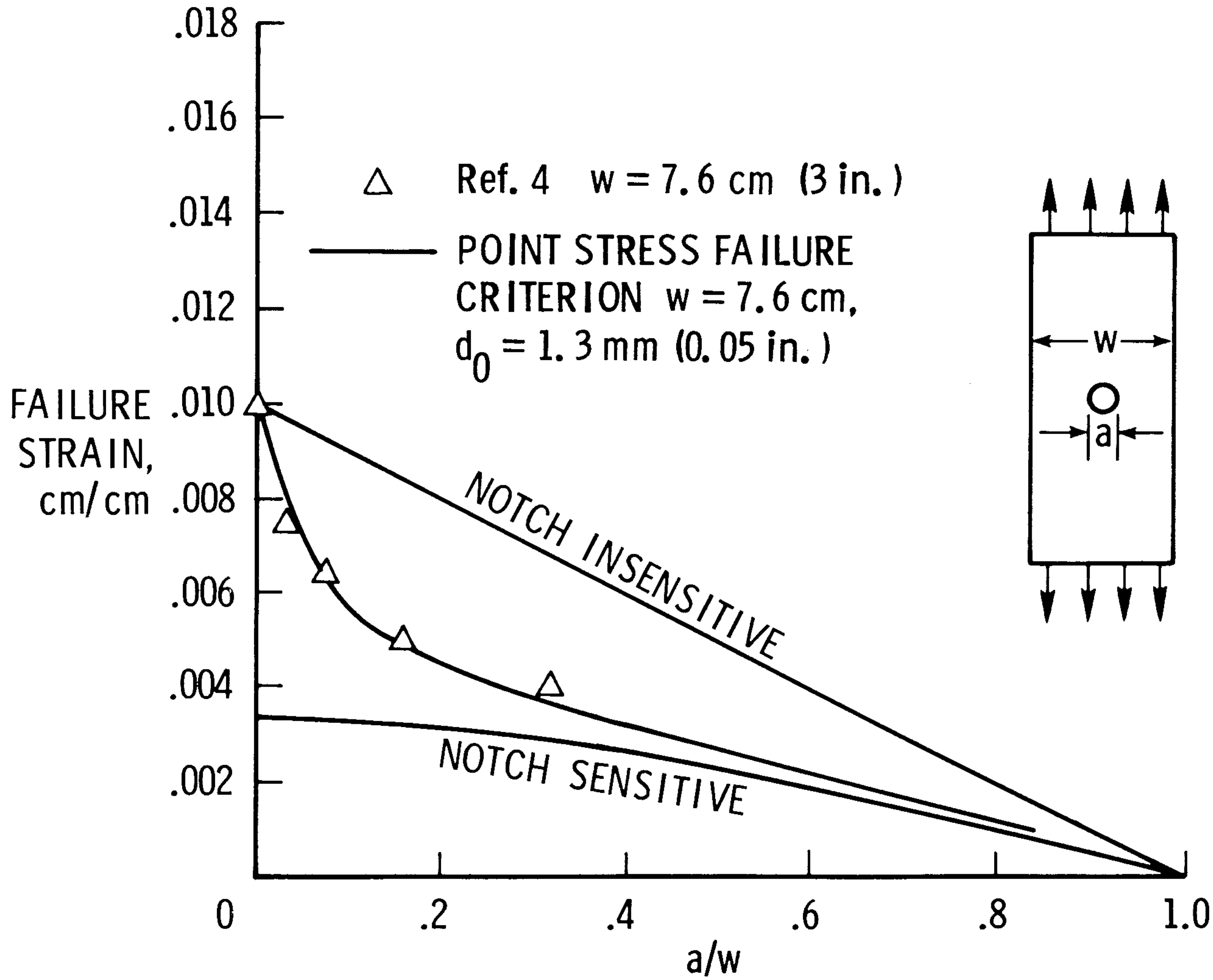

Figure 12.

TENSILE FAILURE OF A QUASI-ISOTROPIC LAMINATE WITH CIRCULAR HOLES

(Figure 12)

The effect of circular holes on the tensile strength of a quasi-isotropic graphite/epoxy laminate is shown on Figure 12. The experimental data are from reference 4 for a 7.6 cm wide laminate. A value of the characteristic length d_0 equal to 1.3 mm for the point stress failure criteria is seen to provide a good fit to the data. It should be noted that in reference 4 only normalized failure results were presented. As can be seen on Figure 12, an ultimate tensile failure strain for the laminate of .01 was chosen for this study. As with the compression case, plotting the results as a function of $\frac{a}{w}$ and including finite width effects provides an excellent perspective of the failure characteristics of the laminate. The next two figures discuss the difference between holes and cracks as related to strength reductions of composites.

STRESS DISTRIBUTIONS AT THE EDGE OF HOLES AND CRACKS

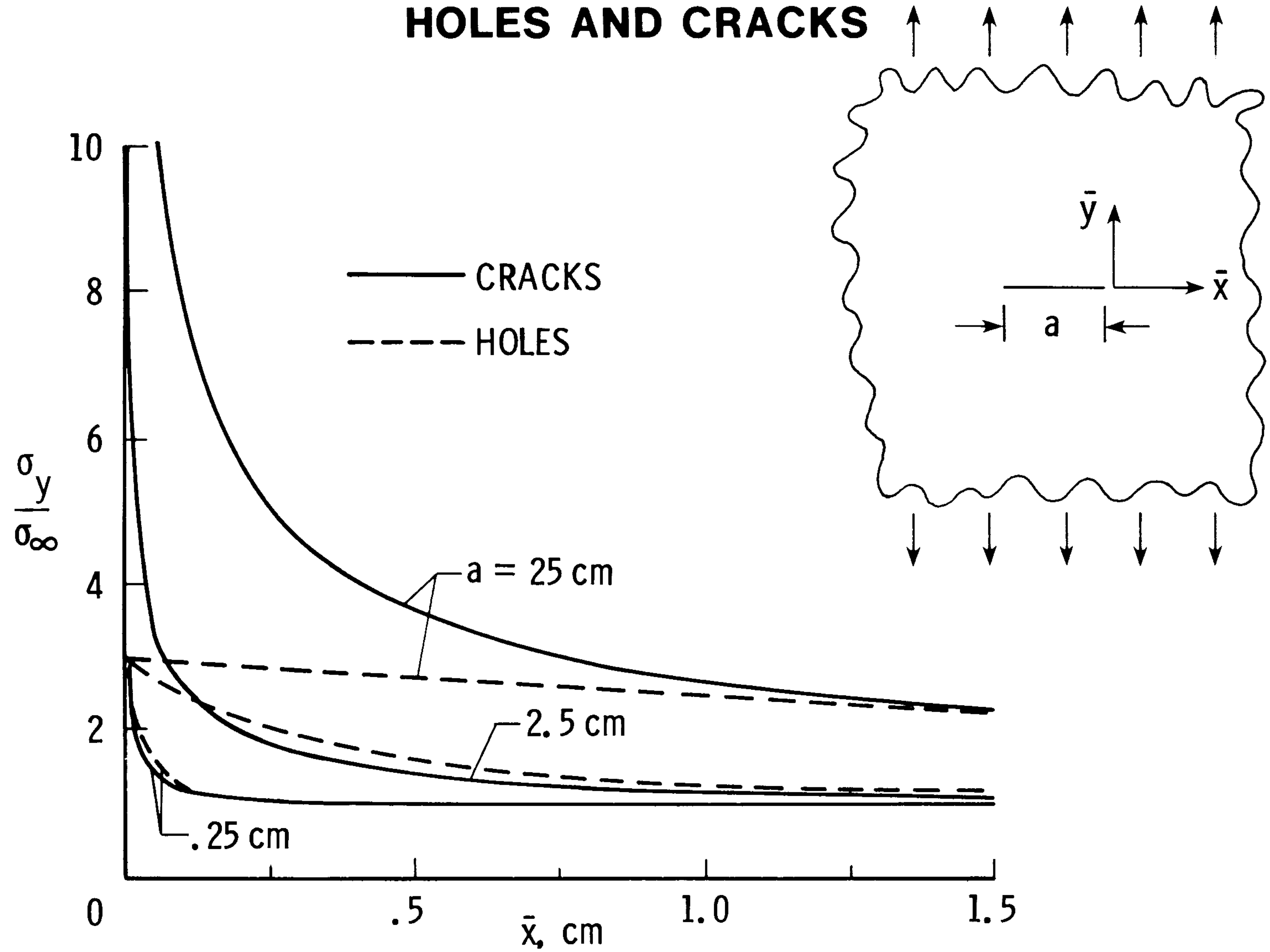

Figure 13.

STRESS DISTRIBUTIONS AT THE EDGE OF HOLES AND CRACKS

(Figure 13)

A comparison between the normal stress distributions σ_y at the edge of a hole and at the edge of a crack in an infinite plate are shown on Figure 13. The exact expression for the y stress along the x axis for a circular hole in an isotropic plate is given by

$$\frac{\sigma_y}{\sigma_\infty} = 1 + \frac{1}{2}\left(\frac{a}{2x}\right)^2 + \frac{3}{2}\left(\frac{a}{2x}\right)^4$$

while the exact expression for the y stress along the x axis for a crack in the anisotropic plate is given by

$$\frac{\sigma_y}{\sigma_\infty} = \frac{x}{\sqrt{x^2 - \left(\frac{a}{2}\right)^2}}$$

where $x = x + \frac{a}{2}$

For all size holes, the maximum edge stress is limited to three times the far field stress while for a crack the stress is infinite. For a small hole (.25 cm), it can be seen that the stress distribution for the circular hole and crack are quite similar for the scale being plotted. For larger holes, however, the singular stress field around a crack begins to overwhelm the stress distribution around a circular hole. The next figure shows the implications of these stress distributions on the strength of composites using the point stress failure criterion.

EFFECT OF HOLE SHAPE ON NOTCH STRENGTH

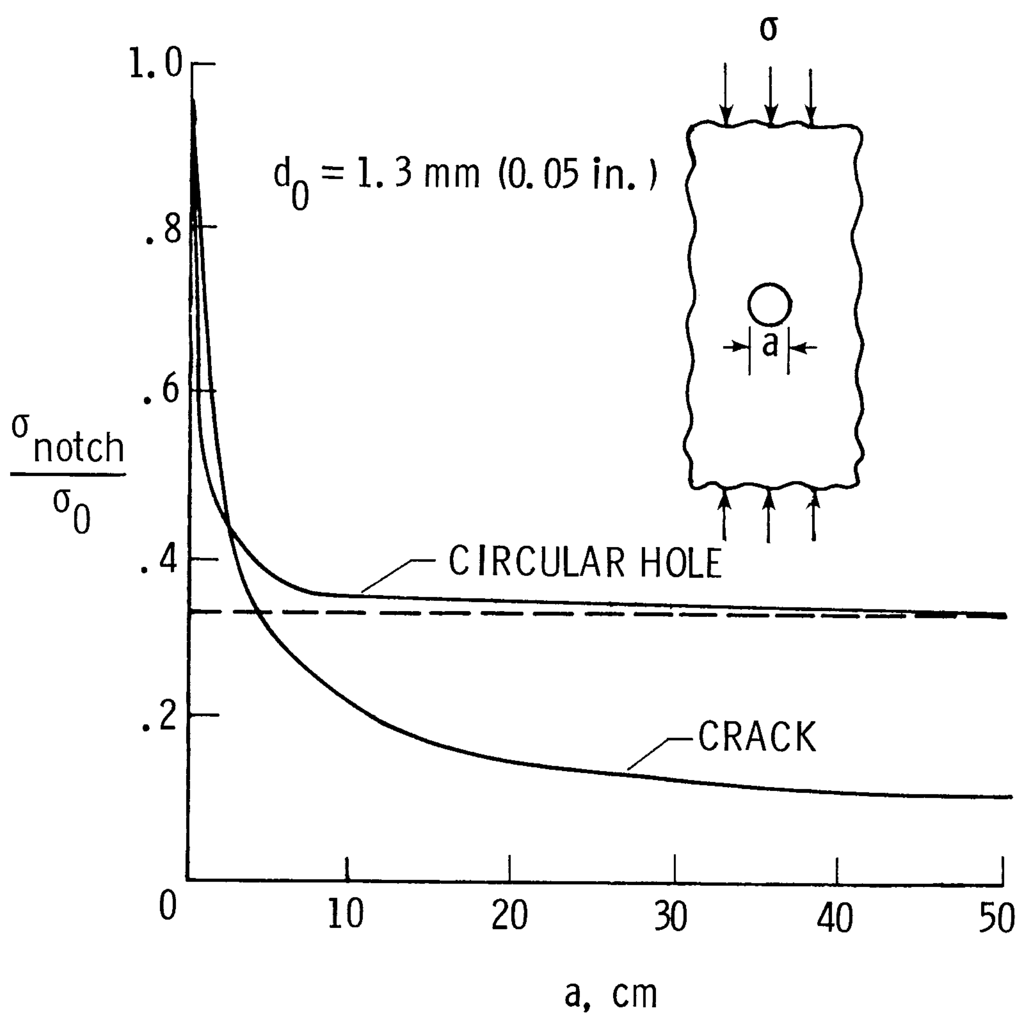

Figure 14.

EFFECT OF HOLE SHAPE ON NOTCH STRENGTH

(Figure 14)

The differences between the effects of a circular hole and a crack on the strength of a laminate are shown on Figure 14. These results are obtained using the point stress failure criterion with a characteristic length d_0 of 1.3 mm. The stress distributions are taken from Figure 13 for an infinite plate. These results show that for small hole sizes, the shape of the hole in a composite laminate is not a significant factor in the reduction in strength. However, for larger holes ($a > 3$ cm) a crack will provide a much larger strength reduction than circular holes. In reference 12, it is reported that failures propagate in compression much like cracks propagate in tension. However, the effect of the shape of the hole on the strength of a composite laminate in compression has yet to be established experimentally.

CONCLUDING REMARKS

A study has been conducted to investigate the notch sensitivity and impact resistance of graphite/epoxy material in compression. Comparisons with idealized limiting failure cases show that the degree of notch sensitivity is dependent upon hole size. Graphite/epoxy laminates with a hole greater than 5 cm were found to behave essentially ideally brittle in compression. That is, failure can be predicted using a classical stress concentration factor. For smaller holes, the point stress failure criterion including finite width effects was shown to provide reasonable failure prediction capability for compression behavior. This failure criterion, together with the idealized limiting failure cases, provides an excellent perspective on the notched performance to be expected from a material system.

The effect of impact damage on the compressive strength of graphite/epoxy was found to be dependent upon the resin system used. For brittle resins, impact resulted in strength reductions that are greater than that found for circular holes with a diameter equal to the size of the impact damaged area. This greater strength reduction for impact is due to the fact that a delamination failure mode is initiated. For tough resins, impact resulted in strength reductions equivalent to that found for circular holes. The tough resin system was able to suppress propagation of the delamination mode such that strength is limited by resin stiffness or microbuckling.

The further development of a general validated failure prediction technique for compression loaded composite laminates will require a considerable amount of additional experimental and analytical research. A major impediment towards this development is the establishment of the necessary experimental data base for a wide range of laminate parameters. It is recommended that the ancillary test programs of future composite component development programs be conducted so as to contribute to the establishment of this data base.

REFERENCES

1. Waddoups, M. E.; Eisenmann, J. R.; and Kaminski, B. E.: "Macroscopic Fracture Mechanics of Advanced Composite Materials," Journal of Composite Materials, Vol. 5, 1971, pp. 446-454.

2. Whitney, J. M.; and Nuismer, R. J.: "Stress Fracture Criteria for Laminated Composites Containing Stress Concentrations," Journal of Composite Materials, Vol. 8, July 1974, pp. 253.

3. Nuismer, R. J.; and Whitney, J. M.: "Uniaxial Failure of Composite Laminates Containing Stress Concentrations," Fracture Mechanics of Composites, ASTM STP 593, American Society for Testing and Materials, 1975, pp. 117-142.

4. Walter, R. W.; Johnson, R. W.; June, R. R.; and McCarty, J. E.: "Designing for Integrity in Long-Life Composite Aircraft Structures," Fatigue of Filamentary Composite Materials, ASTM STP 636, K. L. Reifsnider and K. N. Lauraitis, Eds., American Society for Testing and Materials, 1977, pp. 228-247.

5. Garbo, S. P.; and Ogonowski, J. M.: "Strength Predictions of Composite Laminates with Unloaded Fastener Holes," MCAIR 79-010, Presented at the AIAA/20th Structures, Structural Dynamics and Materials Conference held in St. Louis, Missouri on April 4-6, 1979.

6. Greszczuk, L. B.: "Consideration of Failure Modes in the Design of Composite Structures," MDAC Paper WD 2440, Presented to NATO Advisory Group for Aerospace Research and Development, Munich, Germany, October 1974.

7. Suarez, J. A.; Whiteside, J. B.; and Hadcock, R. N.: "The Influence of Local Failure Modes on the Compressive Strength of Boron/Epoxy Composites," Composite Materials: Testing and Design (Second Conference), ASTM STP 497, American Society for Testing and Materials, 1972, pp. 237-256.

8. Starnes, J. H., Jr.; Rhodes, M. D.; and Williams, J. G.: "Effect of Impact Damage and Holes on the Compressive Strength of a Graphite/Epoxy Laminate," Nondestructive Evaluation and Flaw Criticality for Composite Materials, ASTM STP 696, R. B. Pipes, Ed., American Society for Testing and Materials, 1979, pp. 145-171.

9. Starnes, J. H., Jr.: "Compression Strength of Graphite-Epoxy Structural Components with Cutouts," Proceedings of the Fifth Annual Mechanics of Composites Review, Technical Report AFWAL-TR-80-4020, January 1980, pp. 125-133.

10. Nuismer, R. J.; and Labor, J. D.: "Applications of the Average Stress Failure Criterion: Part II - Compression," Journal of Composite Materials, Vol. 13, January 1979, pp. 49.

11. Garbo, S. P.: "Compression Strength of Laminates with Unloaded Fastener Holes," MCAIR 80-005, Presented at the 21st Structures, Structural Dynamics and Materials Conference held in Seattle, Washington on May 12-14, 1980.

12. Rhodes, M. D.: "Impact Tests on Fibrous Composite Sandwich Structures," NASA Technical Memorandum 78719, October 1978.

13. Rhodes, M. D.; Williams, J. G.; and Starnes, J. H., Jr.: "Low-Velocity Impact Damage in Graphite-Fiber Reinforced Epoxy Laminates," Presented at the 34th Annual Conference Reinforced Plastics/Composite Institute, The Society of the Plastics Industry, Inc. in New Orleans, Louisiana, January 29 - February 2, 1979.

14. Knauss, W. G.; Babcock, C. D.; and Chai, H.: "Visualization of Impact Damage of Composite Plates by Means of the Moire Technique," NASA Contractor Report 159261, NASA Grant NSG-1483, California Institute of Technology, April 1980.

15. Knauss, J. F.; Starnes, J. H., Jr.; and Henneke, E. G., II: "The Compressive Failure of Graphite/Epoxy Plates with Circular Holes," VPI-E-78-5, Interim Report Number 11, NASA-VPI&SU Composites Program, NASA Grant NGR 47-004-129, February 1978. (Available as NASA CR-157115.)

16. Peterson, R. E.: Stress Concentration Factors, John Wiley & Sons, Inc., c.1974.

17. Hadcock, R. N.; and Whiteside, J. B.: "Special Problems Associated with Boron-Epoxy Mechanical Test Specimens." Composite Materials: Testing and Design, ASTM STP 460, American Society for Testing and Materials, 1969, pp. 27-36.

18. Foye, R. L.: "Compression Strength of Unidirectional Composites," AIAA 3rd Aerospace Sciences Meeting, AIAA Paper No. 66-143, January 24-26, 1966.

19. Vaughn, R. L.: "Flight Service Evaluation of an Advanced Composite Empennage Component on Commercial Transport Aircraft," NASA Contractor Report 159286, April 15, 1976.

20. Howland, R. C. J.: "On the Stresses in the Neighbourhood of a Circular Hole in a Strip Under Tension," Philos. Trans. R. Soc. London, ser. A, vol. 229, Jan. 6, 1930, pp. 49-86.

21. Hong, C. S.; and Crews, J. H., Jr.: "Stress-Concentration Factors for Finite Orthotropic Laminates with a Circular Hole and Uniaxial Loading," NASA Technical Paper 1469, May 1979.

22. Williams, J. G.; Anderson, M. S.; Rhodes, M. D.; Starnes, J. H., Jr.; and Stroud, W. J.: "Recent Developments in the Design, Testing and Impact-Damage Tolerance of Stiffened Composite Panels," NASA Technical Memorandum 80077, April 1979.

BUCKLING AND POSTBUCKLING RESEARCH ON FLAT AND CURVED COMPOSITE PANELS

James H. Starnes, Jr.

INTRODUCTION

An ongoing research activity at NASA Langley Research Center is the development of verified design technology for generic advanced-composite structural components loaded in compression. State-of-the-art reviews were presented in 1975 (ref. 1) and 1978 (ref. 2) that summarize the results of Langley research done on buckling-resistant stiffened flat composite compression panels. Current research interests at Langley include both flat and curved composite compression panels that are designed either to be buckling resistant or to have postbuckling strength depending on the expected application of the panels. The present paper briefly summarizes some buckling-resistant research results, some current research activities on panels with postbuckling strength, and some studies of efficient nonlinear analysis methods that support the postbuckling design research.

APPROACH FOR GENERIC RESEARCH ON ADVANCED-COMPOSITE COMPRESSION PANELS

- GIVEN: STRUCTURAL CONFIGURATION, LOADS AND MATERIALS
- DEVELOP: VERIFIED DESIGN TECHNOLOGY FOR EFFICIENT ADVANCED-COMPOSITE STRUCTURAL COMPONENTS
- APPROACH:
  - STRUCTURAL SIZING PROCEDURES
  - ANALYTICAL PROCEDURES
    SIMPLE AND SOPHISTICATED
  - LABORATORY TESTS

Figure 1.

APPROACH FOR GENERIC RESEARCH ON ADVANCED-COMPOSITE COMPRESSION PANELS

(Figure 1)

The objective of Langley's generic research on composite compression panels is to develop verified design technology for efficient advanced-composite structural components. Once the generic structural configuration, material system, and load range of interest are selected for a given application (e.g., wing or fuselage panels), a research approach is followed that includes the use of structural sizing procedures, structural analysis procedures, and laboratory testing of structural specimens. Structural sizing procedures are used to determine a minimum-mass structural design that satisfies all constraints imposed on the structure for the applied loads and known failure modes. The constraints limit the response of the structure (e.g., prevent buckling) and satisfy a number of criteria (e.g., reduce strains below prescribed allowable values). Analytical procedures are used to predict structural response and to evaluate constraint functions during the sizing process. Since many analyses are required during the sizing process, the analytical procedures used by the sizing procedure are usually simple enough to minimize analytical costs but accurate enough to predict the structural behavior. After a sizing procedure has generated a design, more sophisticated or detailed analyses are performed to assure the accuracy of the structural response predictions. Designs generated by a minimum-mass sizing procedure are verified by testing a structural specimen based on the design in the laboratory. Agreement between test and analysis provides confidence that the response of a panel of a given configuration and applied loading is well enough understood to generate design data over a broader range of parameters that affect the panel response. Disagreement between test and analysis provides the opportunity to identify new failure modes and response characteristics requiring new research efforts.

BUCKLING RESISTANT STRUCTURES

- FLAT
- CURVED

Figure 2.

BUCKLING RESISTANT STRUCTURES

(Figure 2)

Most of Langley's buckling-resistant research on compression-loaded composite structural components has focused on stiffened flat panels suitable for aircraft wing applications. An effort involving the design and testing of a lightly-loaded buckling-resistant stiffened composite cylinder was recently completed that is suitable for a space application.

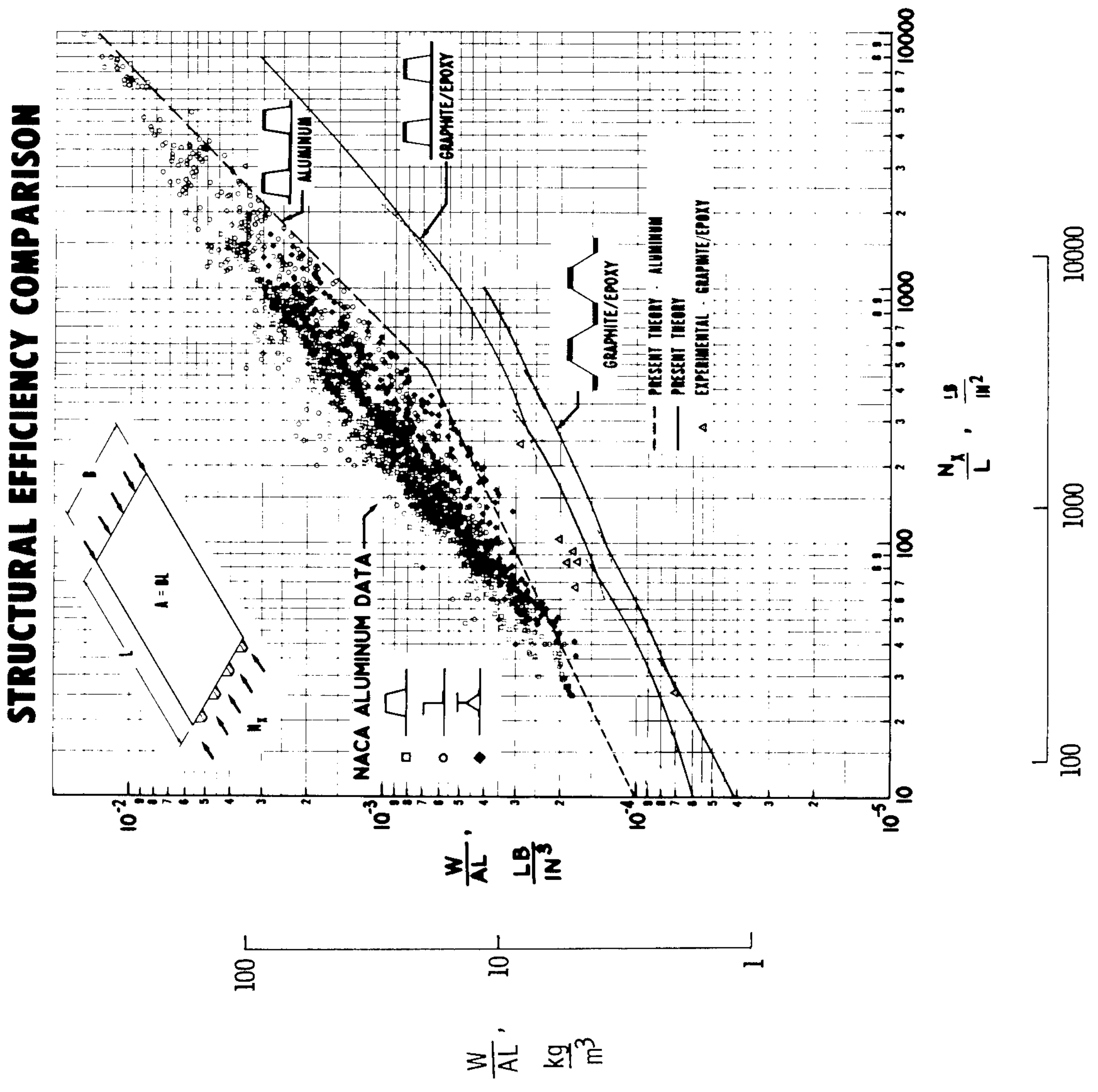

STRUCTURAL EFFICIENCY COMPARISON
A = BL
N_x
NACA ALUMINUM DATA
ALUMINUM
GRAPHITE/EPOXY
GRAPHITE/EPOXY
PRESENT THEORY - ALUMINUM
PRESENT THEORY
EXPERIMENTAL - GRAPHITE/EPOXY
$\frac{W}{AL}$, $\frac{LB}{IN^3}$
$\frac{N_x}{L}$, $\frac{LB}{IN^2}$
$\frac{W}{AL}$, $\frac{kg}{m^3}$
$\frac{N_x}{L}$, $\frac{kN}{m^2}$

Figure 3.

STRUCTURAL EFFICIENCY COMPARISON

(Figure 3)

The advantage of using a sizing procedure with analytical procedures and laboratory testing for buckling-resistant stiffened panels is suggested by comparison between earlier NACA aluminum results and subsequent NASA graphite-epoxy results. A large amount of test data was needed to establish structural-efficiency trends for aluminum panels. Only a small number of carefully selected tests were needed to verify the structural-efficiency relations generated by a sizing procedure for graphite-epoxy hat-stiffened panels.

STIFFENED PANEL DESIGN CODE – PASCO

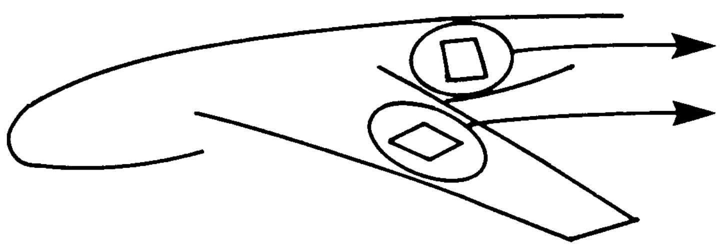

STRUCTURAL PANEL

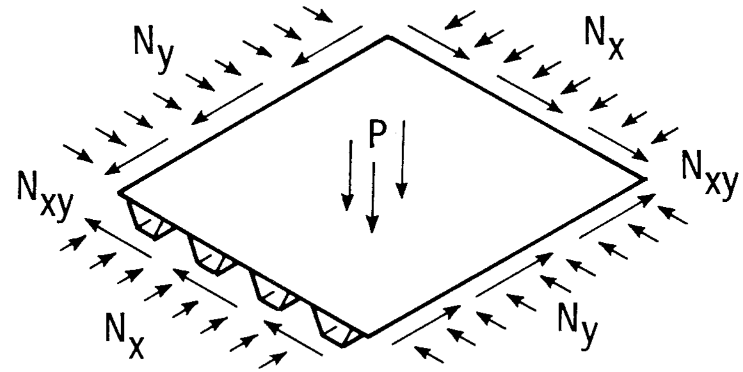

LOADING

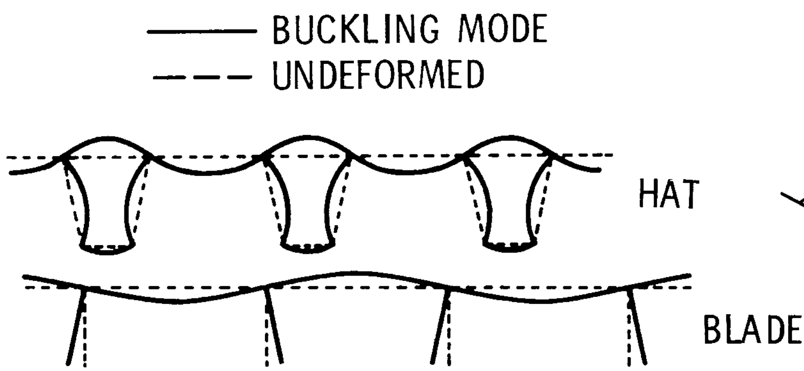

COMPLEX BUCKLING MODES OF
ARBITRARY PANEL CONFIGURATIONS

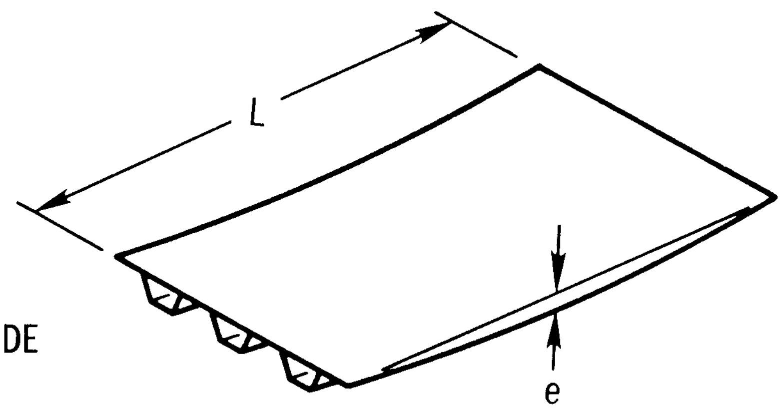

BOW-TYPE IMPERFECTION

Figure 4.

LANGLEY STIFFENED PANEL DESIGN CODE - PASCO

(Figure 4)

A buckling-resistant sizing procedure for composite stiffened panels is the PASCO design code (ref. 3). PASCO can size flat panels that are subjected to combined loads (including thermal loads) and have bow-type geometric initial imperfections. Complex buckling modes are determined by a rapid, accurate analysis procedure suitable for arbitrary panel configurations.

MAIN ELEMENTS OF SIZING CODE

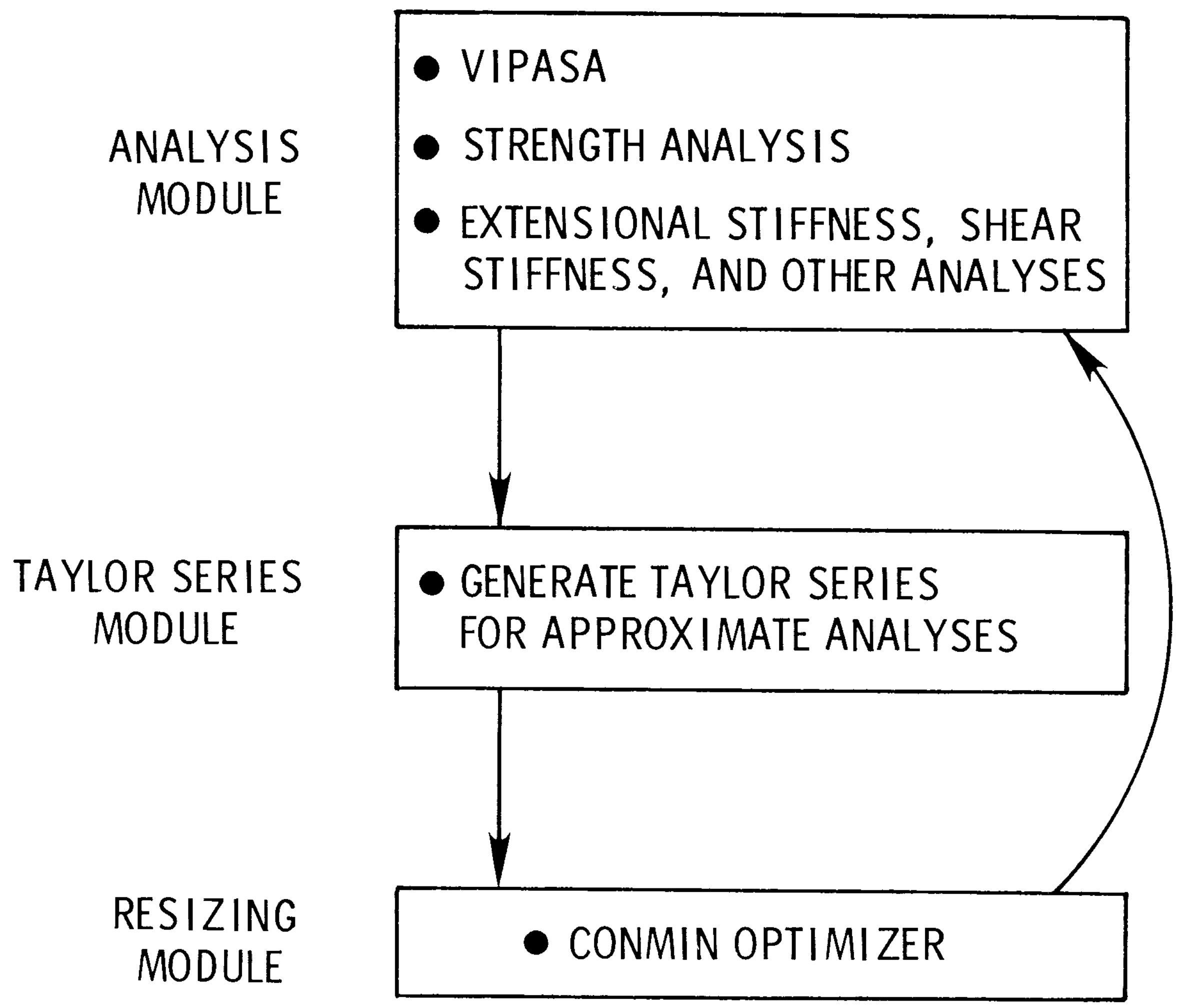

Figure 5.

MAIN ELEMENTS OF SIZING CODE

(Figure 5)

The analysis module in PASCO uses VIPASA (ref. 4) to compute accurately the buckling loads and modes of a panel and simpler analyses for strength and stiffness calculations. Approximations to constraint functions needed by the optimizer are obtained from a Taylor series expansion to reduce computer costs. Minimum-mass designs are determined in PASCO using the CONMIN optimizer (ref. 5).

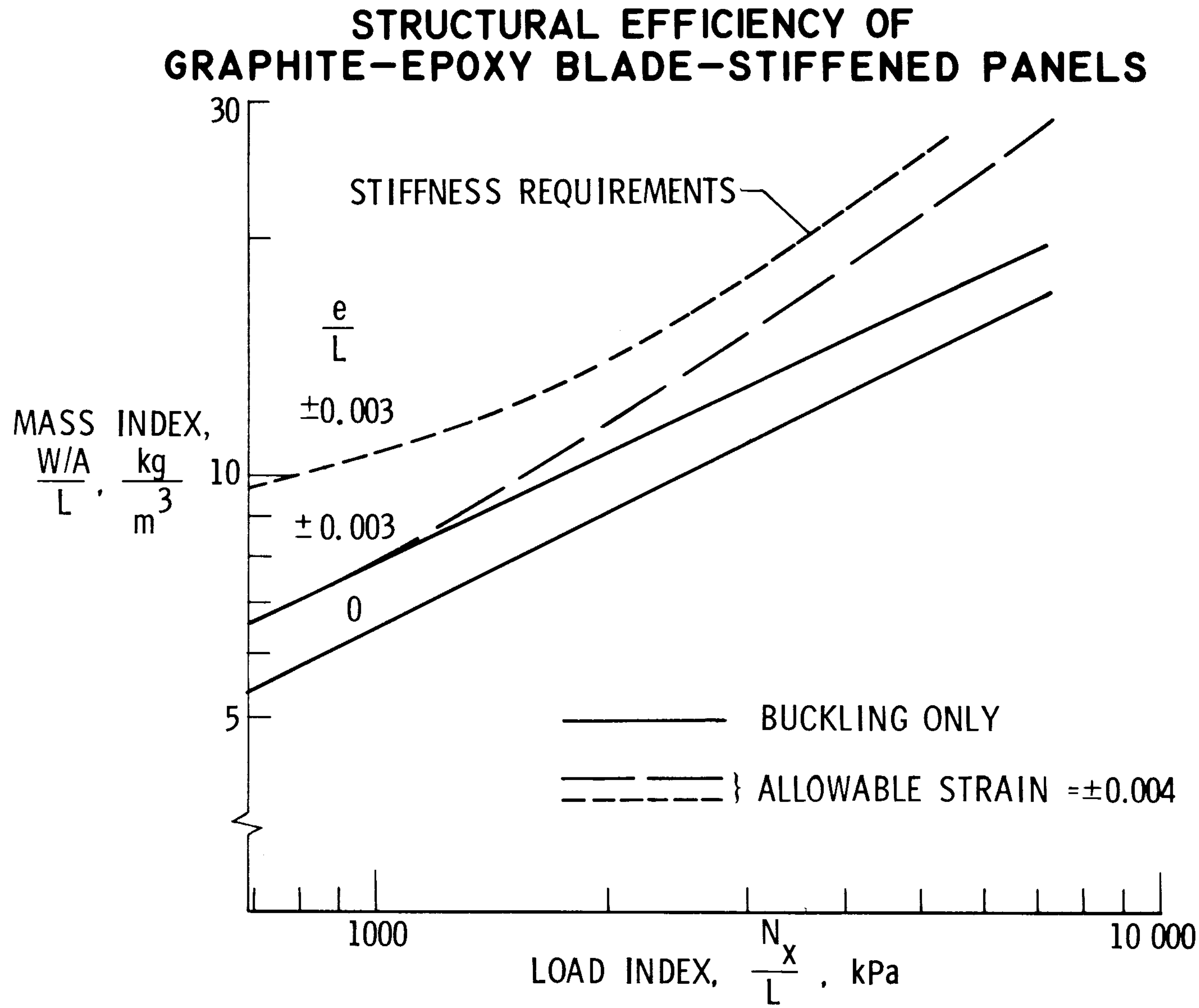
STRUCTURAL EFFICIENCY OF
GRAPHITE–EPOXY BLADE–STIFFENED PANELS
STIFFNESS REQUIREMENTS
e/L
±0.003
±0.003
0
MASS INDEX, W/A / L, kg / m3
30
10
5
BUCKLING ONLY
ALLOWABLE STRAIN =±0.004
1000
10 000
LOAD INDEX, Nx / L, kPa

Figure 6.

STRUCTURAL EFFICIENCY OF GRAPHITE-EPOXY BLADE-STIFFENED PANELS

(Figure 6)

An example of PASCO generated results are the structural efficiency curves for graphite-epoxy blade-stiffened compression panels shown in Figure 6. The mass index (W/AL) for minimum-mass panel designs is shown in Figure 6 as a function of the load index (N_x/L) for buckling, maximum strain and stiffness constraints and for two imperfection amplitudes. In Figure 6, W is the panel mass, L is the panel length, A is the panel planform area (length times width), N_x is the applied compressive load (stress resultant), and e is the imperfection amplitude.

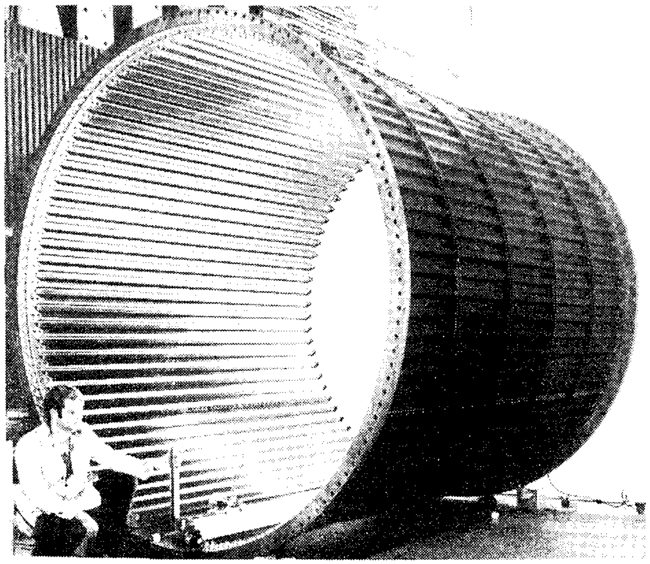

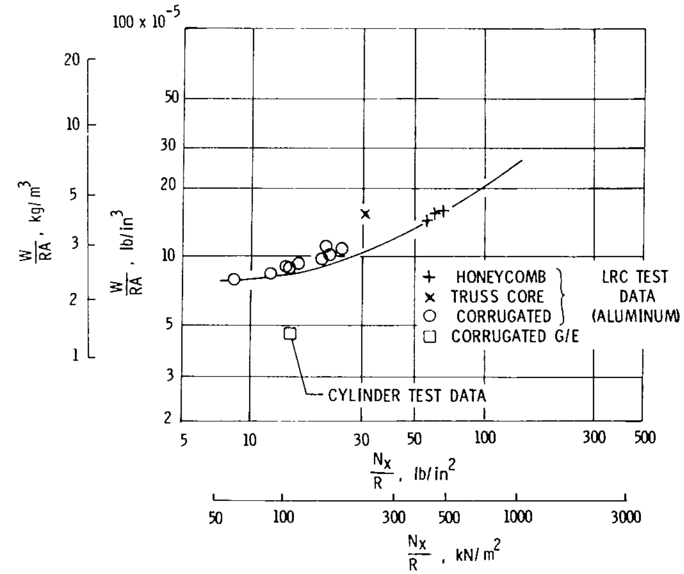

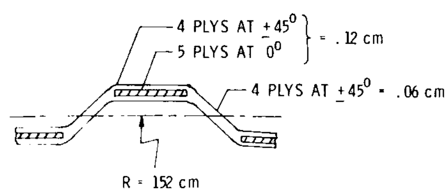

WALL DESIGN

Figure 7.

LOW-MASS GRAPHITE-EPOXY INTERSTAGE STRUCTURE

(Figure 7)

The design and testing of a lightly loaded buckling-resistant open-corrugated graphite-epoxy ring-stiffened cylinder has recently been completed at Langley. The cylinder is 304 cm in diameter and 304 cm long and was designed to carry 0.16 MN/m compression load without buckling. The wall of the cylinder varies between 4 and 9 plies of 0.014-cm-thick graphite-epoxy unidirectional tape. Comparing this composite cylinder design with minimum-mass aluminum designs required to carry the same loading shows a significant mass advantage for the composite design. The buckling test of the composite cylinder indicates that this design will satisfactorily carry the desired load without buckling. Some design and fabrication details of the composite cylinder are given in reference 6.

POSTBUCKLING RESEARCH

- FLAT
- CURVED

Figure 8.

POSTBUCKLING RESEARCH

(Figure 8)

A Langley research program on composite compression panels with postbuckling strength has recently been established to support the application of advanced-composite materials to commercial transport aircraft. Most of the test and analysis results to date are for flat panels, however, curved panel tests have been initiated.

DESIGN OF STIFFENED COMPOSITE PANELS WITH BUCKLED SKIN

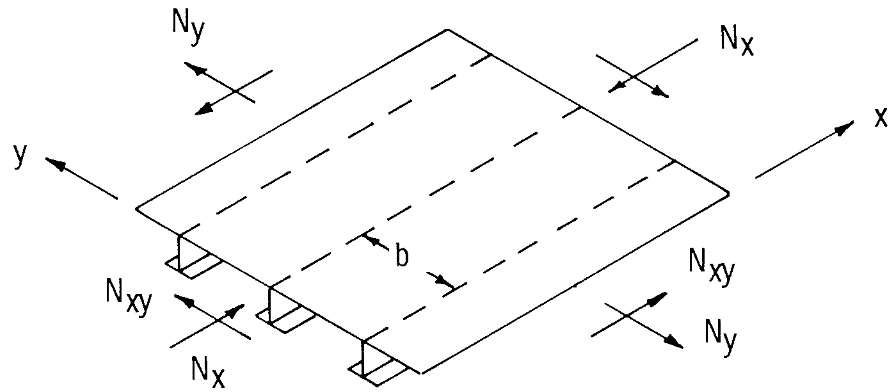

- DESIGN PROBLEM: FIND MINIMUM-MASS DESIGN FOR GENERAL SET OF COMBINED LOADS AND PRESCRIBED STIFFENER SPACING
- CURRENT APPROACH: STIFFENED COMPOSITE PANEL SIZING PROCEDURE DEVELOPED BY J. N. DICKSON, LOCKHEED-GEORGIA COMPANY
- ASSUMPTIONS:
  - SYMMETRIC SKIN LAMINATE
  - LONG PANEL
  - SIMPLE-SUPPORT BOUNDARY CONDITIONS AT SKIN-STIFFENER INTERFACE (v = CONSTANT)
  - FAILURE OCCURS WHEN STIFFENERS BUCKLE, MATERIAL STRENGTH ALLOWABLE IS EXCEEDED, OR PANEL BUCKLES AS A WIDE COLUMN (WITH REDUCED STIFFNESSES)
- APPLIED LOADS CARRIED BY SKIN AND STIFFENERS: $N_{x_{TOTAL}} = N_{x_{SKIN}} + N_{x_{STIFFENER}}$
- SKIN HAS NONLINEAR LOAD-STRAIN RESPONSE AND REDUCED STIFFNESSES IN POSTBUCKLING RANGE

Figure 9.

DESIGN OF STIFFENED COMPOSITE PANELS WITH BUCKLED SKIN

(Figure 9)

A preliminary design of a stiffened composite fuselage panel (ref. 7) shows the advantages of allowing low-strain composite structural components to operate in the postbuckling range. The sizing procedure used in reference 7 was developed by J. N. Dickson of the Lockheed-Georgia Company and finds a minimum-mass design such that panel compression failure is controlled by stiffener buckling and maximum strain limitations. Mr. Dickson's sizing procedure assumes symmetric skin laminates, long panel lengths, and simple-support boundary conditions at the skin-stiffener interfaces. The optimizer used in this sizing procedure is based on reference 5. Applied loads are carried by both the skin and the stiffeners, and the skin has a nonlinear load-strain response and reduced stiffnesses in the postbuckling range.

ASSUMED SKIN-BUCKLING MODE

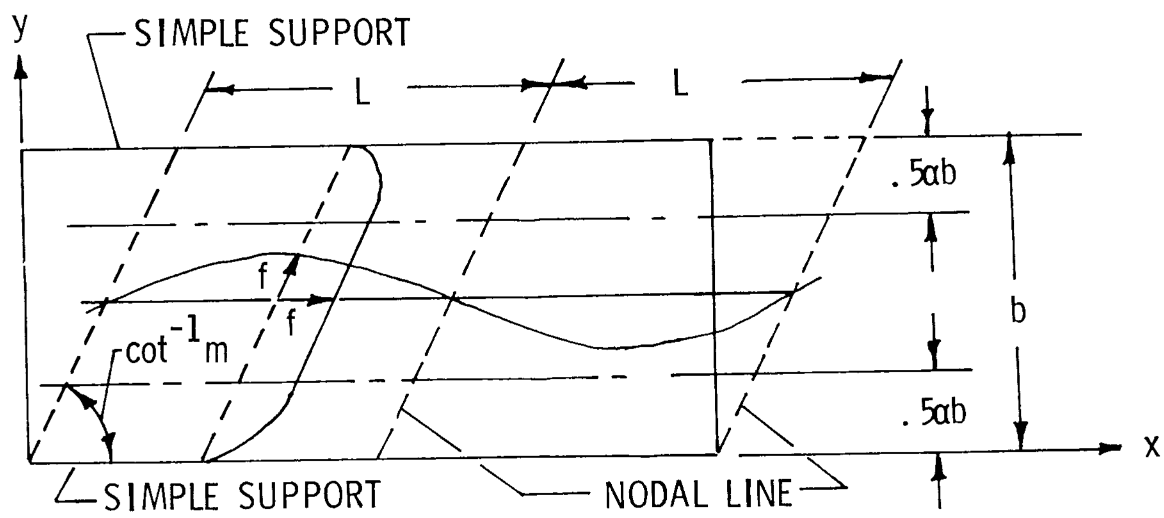

- MODE BASED ON KOITER SHEAR FIELD THEORY EXTENDED TO ORTHOTROPIC LAMINATES

$$w(x, y) = f \sin \frac{\pi}{L}(x - my) \sin \frac{\pi y}{\alpha b}$$

- RAYLEIGH-RITZ PROCEDURE USED TO FIND f, L, m and α
- MODE VALID IN ADVANCED POSTBUCKLING RANGE

Figure 10.

ASSUMED SKIN-BUCKLING MODE

(Figure 10)

The postbuckling skin deformation mode is based on Koiter's shear field theory (ref. 8) as extend to orthotropic laminates by Mr. Dickson. The mode shape depends on four parameters that are determined by the Rayleigh-Ritz procedure. The definition of the deformation mode is valid well into the postbuckling range of the skin response.

BUCKLING OF STIFFENERS

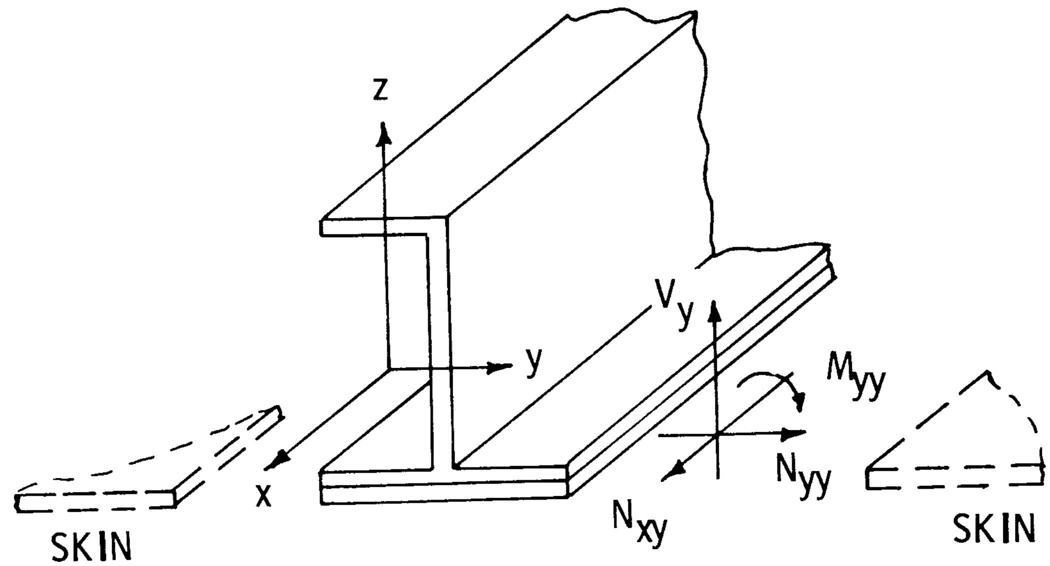

- SKIN FORCES TREATED AS EXTERNAL LOADS ON STRINGER
- TORSIONAL/FLEXURAL STIFFENER DEFORMATION INCLUDED IN STIFFENER BUCKLING ANALYSIS
- LOCAL BUCKLING OF STIFFENER ELEMENTS BASED ON SIMPLE-SUPPORT BOUNDARY CONDITIONS

Figure 11.

BUCKLING OF STIFFENERS

(Figure 11)

Stiffener buckling is determined in Mr. Dickson's sizing procedure based on a column buckling analysis. Skin forces are treated as external loads on the stiffener, and torsional-flexural stiffener deformation modes are included in the stiffener buckling analysis. Local buckling of stiffener elements are based on simple-support boundary conditions.

EFFECT OF PANEL SKIN BUCKLING ON STRUCTURAL EFFICIENCY

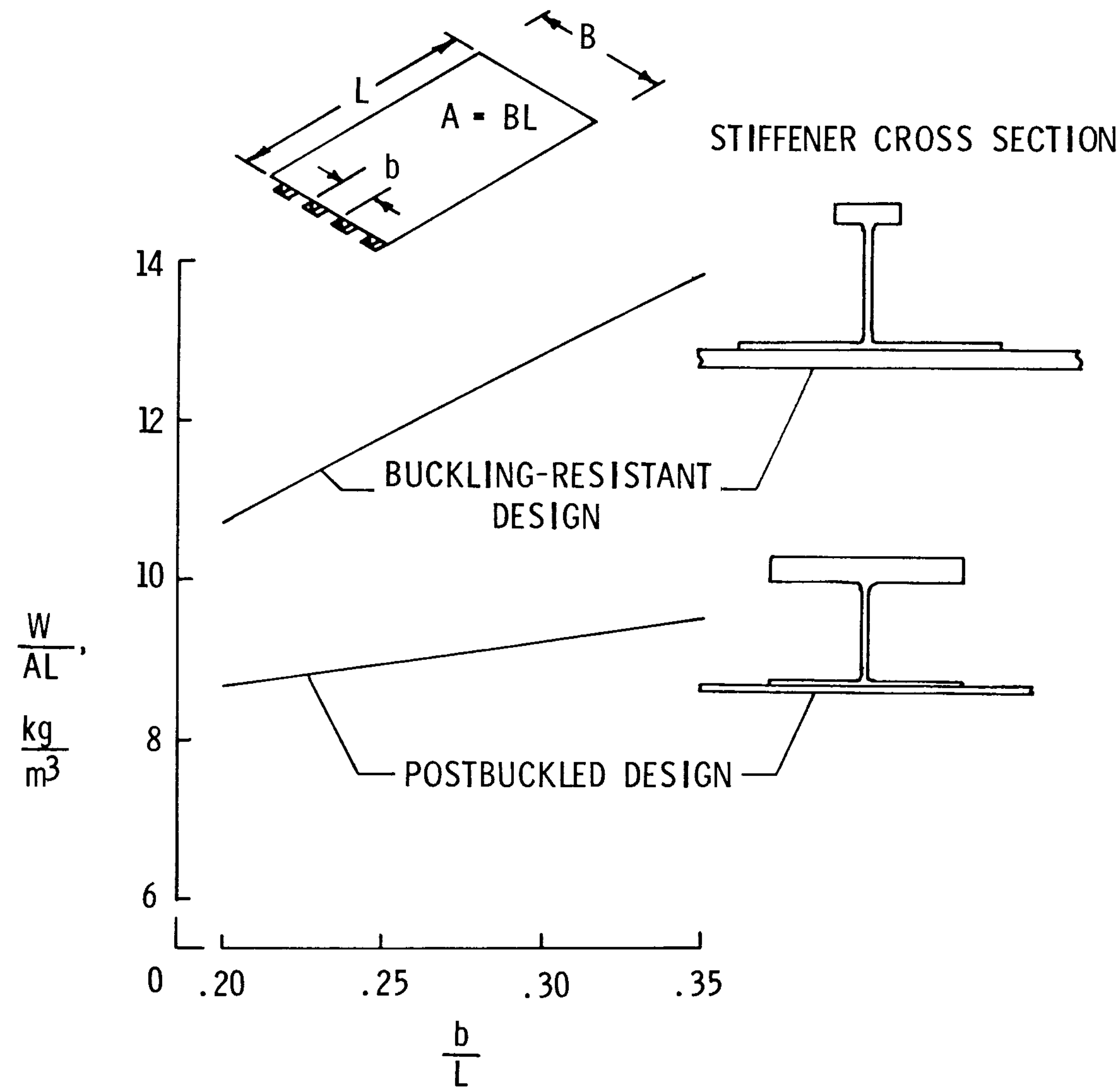

Figure 12.

EFFECT OF PANEL SKIN BUCKLING ON STRUCTURAL EFFICIENCY

(Figure 12)

A comparison (ref. 7) of buckling-resistant panel designs and panel designs with postbuckling strength for I-stiffened graphite-epoxy compression panels shows the advantages of using a postbuckling design concept for low-strain applications. The panels designed to have postbuckling strength have lower masses for the stiffener spacings studied than the buckling-resistant panel designs. These relatively wide stiffener spacings are being studied because of their manufacturing cost-reduction potential. The panel skin of the buckled-skin design is thinner than the skin of the buckling-resistant design because it is limited by maximum strain rather than skin buckling. The stiffener of the buckled-skin design is heavier than the stiffener of the buckling-resistant design because it must carry greater and greater loads as the skin goes farther and farther into the postbuckling range.

- T300-5208
- 24-PLY ORTHOTROPIC LAMINATE
  $(\pm 45/0_2/\pm 45/0_2/\pm 45/0/90)_S$

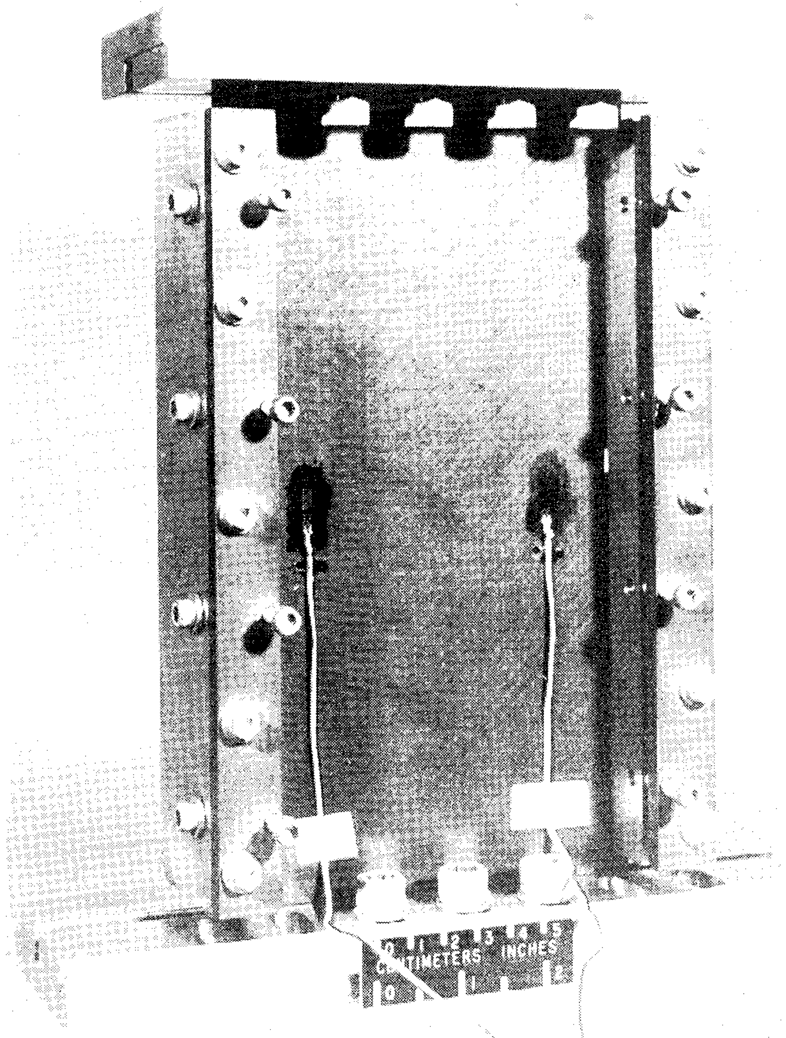

Figure 13.

TEST SPECIMENS AND FIXTURE

(Figure 13)

A number of unstiffened 24-ply graphite-epoxy flat plates have been tested in compression at Langley to determine their postbuckling response. These orthotropic specimens were made of T300-5208 graphite-epoxy unidirectional tape with a $(\pm 45/0_2/\pm 45/0_2/\pm 45/0/90)_s$ stacking sequence. The specimens were flat-end tested with clamped supports on the loaded ends and knife-edge supports on the sides.

POSTBUCKLING OF UNSTIFFENED 24-PLY GRAPHITE-EPOXY FLAT PLATE

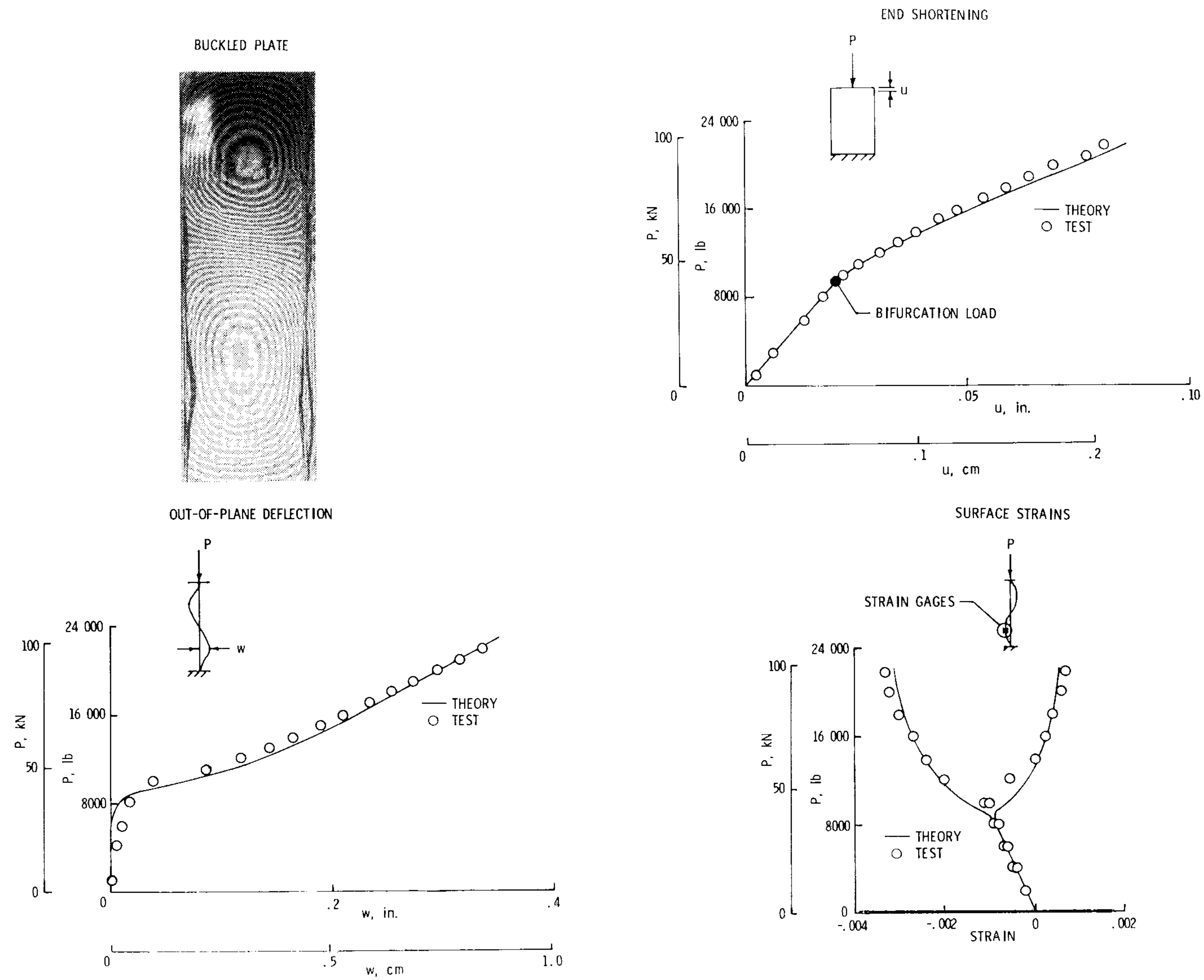

Figure 14.

POSTBUCKLING OF UNSTIFFENED 24-PLY GRAPHITE-EPOXY FLAT PLATE

(Figure 14)

Some test results of a 17.8-cm-wide by 50.8-cm-long 24-ply orthotropic specimen are shown in Figure 14 and compared with the results of a nonlinear analysis of the panel obtained from the STAGS computer code (ref. 9). The photograph shows the moire-fringe pattern corresponding to the out-of-plane deformation of the plate buckled into two longitudinal half waves and one lateral half wave. The three graphs compare test and analysis results of end shortening, out-of-plane deflection and surface strain-gage data as functions of applied load P.

POSTBUCKLING RESPONSE OF UNSTIFFENED 24-PLY FLAT ORTHOTROPIC GRAPHITE-EPOXY PANELS

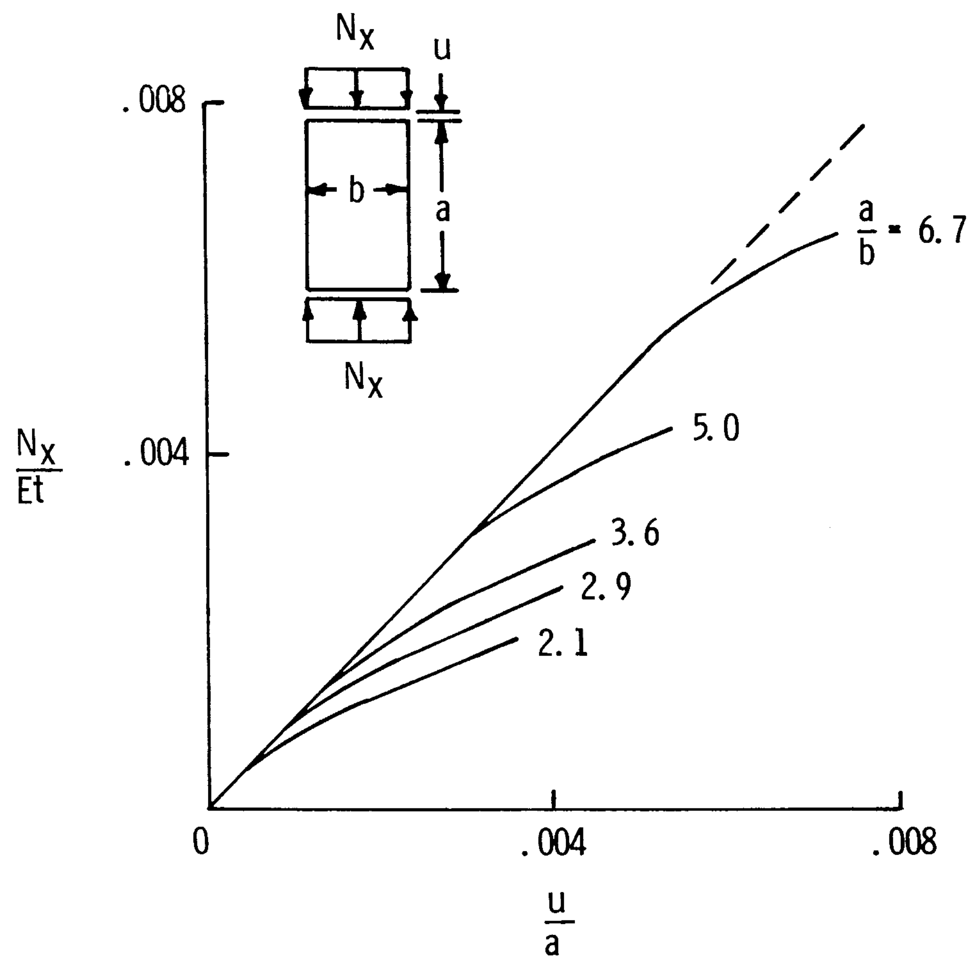

Figure 15.

POSTBUCKLING RESPONSE OF UNSTIFFENED 24-PLY FLAT ORTHOTROPIC GRAPHITE-EPOXY PANELS

(Figure 15)

A summary of test results for 24-ply orthotropic graphite-epoxy panels of various aspect ratios is shown on Figure 15. The applied strain ($P/Etb = N_x/Et$ where P is the applied load, E is the laminate longitudinal modulus, b is the panel width and t is the panel thickness) of each panel is shown as a function of the corresponding measured longitudinal strain (u/a where u is the panel end shortening and a is the panel length). Each panel has some postbuckling strength. The panels with higher initial buckling strains cannot be loaded as far into the postbuckling range before failing as can panels with lower initial buckling strains.

24–PLY UNSTIFFENED LAMINATE RESPONSE

QUASI-ISOTROPIC LAMINATE

1.27-cm-DIAMETER HOLE

97kN APPLIED LOAD

(35 % ABOVE BUCKLING LOAD)

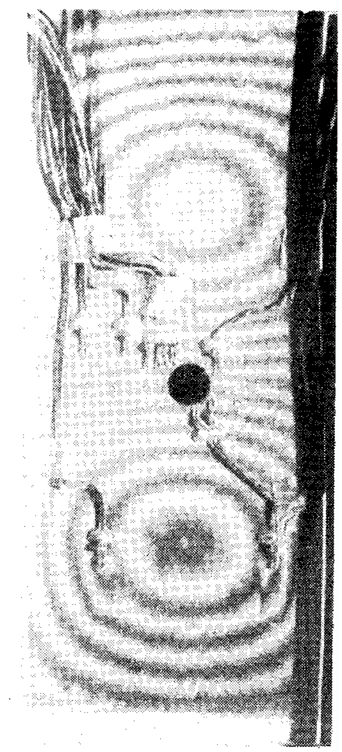

Figure 16.

24-PLY UNSTIFFENED LAMINATE RESPONSE

(Figure 16)

A 12.7-cm-wide by 25.4-cm-long 24-ply quasi-isotropic plate was tested to failure to determine the effect of a 1.27-cm-diameter hole on the postbuckling strength of the plate. This specimen failed at a load 35 percent above the initial buckling load. Comparing the results of this specimen with the results of a similar specimen without a hole indicates that there is no noticeable effect of the hole on the postbuckling strength of the specimen.

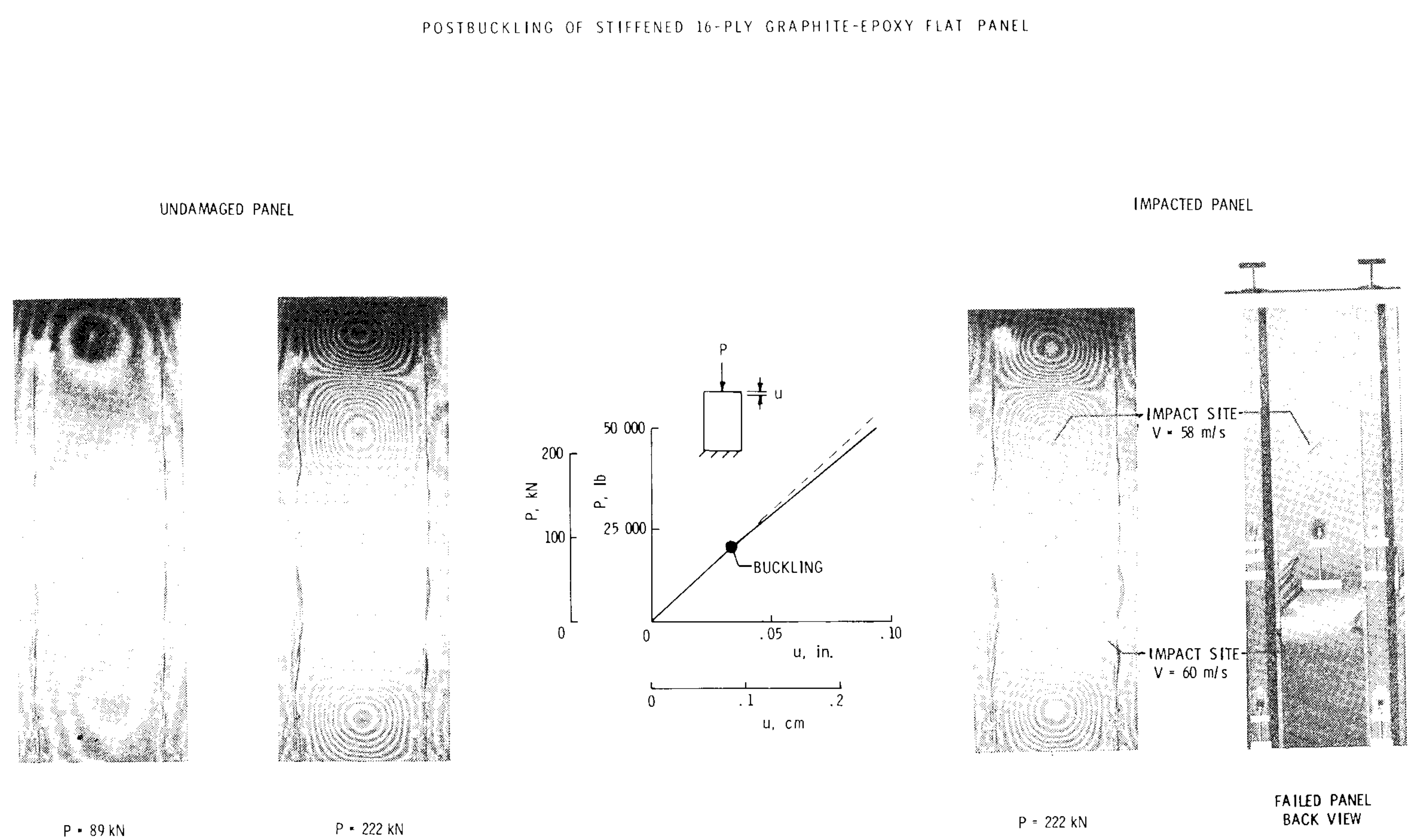
POSTBUCKLING OF STIFFENED 16-PLY GRAPHITE-EPOXY FLAT PANEL
UNDAMAGED PANEL
IMPACTED PANEL
P
u
P, kN
200
100
0
P, lb
50 000
25 000
0
BUCKLING
.05
.10
u, in.
0
.1
.2
u, cm
IMPACT SITE
V = 58 m/s
IMPACT SITE
V = 60 m/s
P = 89 kN
P = 222 kN
P = 222 kN
FAILED PANEL
BACK VIEW

Figure 17.

POSTBUCKLING OF A STIFFENED 16-PLY GRAPHITE-EPOXY PANEL

(Figure 17)

A 16-ply T-stiffened graphite-epoxy flat panel designed to have postbuckling strength was tested with and without impact damage. The panel was 25.4 cm wide and 71.1 cm long and had two longitudinal stiffeners 17.8 cm apart. The skin of the panel was laid up to form a $(\pm 45/0_2/\mp 45/90_2)_s$ laminate. The undamaged panel buckled initially at a load P of 89 kN (longitudinal strain of 0.0011) and was then loaded to 228 kN (strain of 0.0029). Photographs of moire-fringe patterns representing out-of-plane deformations show that the panel buckles into five longitudinal half-waves. A plot of the end shortening U of the panel as a function of the applied load P shows that the stiffness of the panel decreases only slightly after the skin buckles. The stiffeners for this design are heavy enough to maintain most of the panel stiffness after the skin buckles. The panel was unloaded and impacted at two locations with 1.27-cm-diameter aluminum spheres. The skin was impacted at a speed of 56 m/s at a point midway between stiffeners where the moiré-fringe pattern of the undamaged test indicated maximum out-of-plane deflection. A slight amount of back-surface matrix cracking was caused by this impact event. The panel was also impacted at a speed of 60 m/s on the skin at the attachment flange of one of the stiffeners. The second impact event caused some local matrix cracking of the stiffener attachment flange at the impact site. The impact-damaged panel failed at a load of 225 kN when the damage at the stiffener attachment flange propagated across the panel. This damage to the skin-stiffener interface region caused the panel to fail at 74 percent of its predicted failure load of 303 kN.

POSTBUCKLING OF UNSTIFFENED 16-PLY GRAPHITE-EPOXY CURVED PANEL

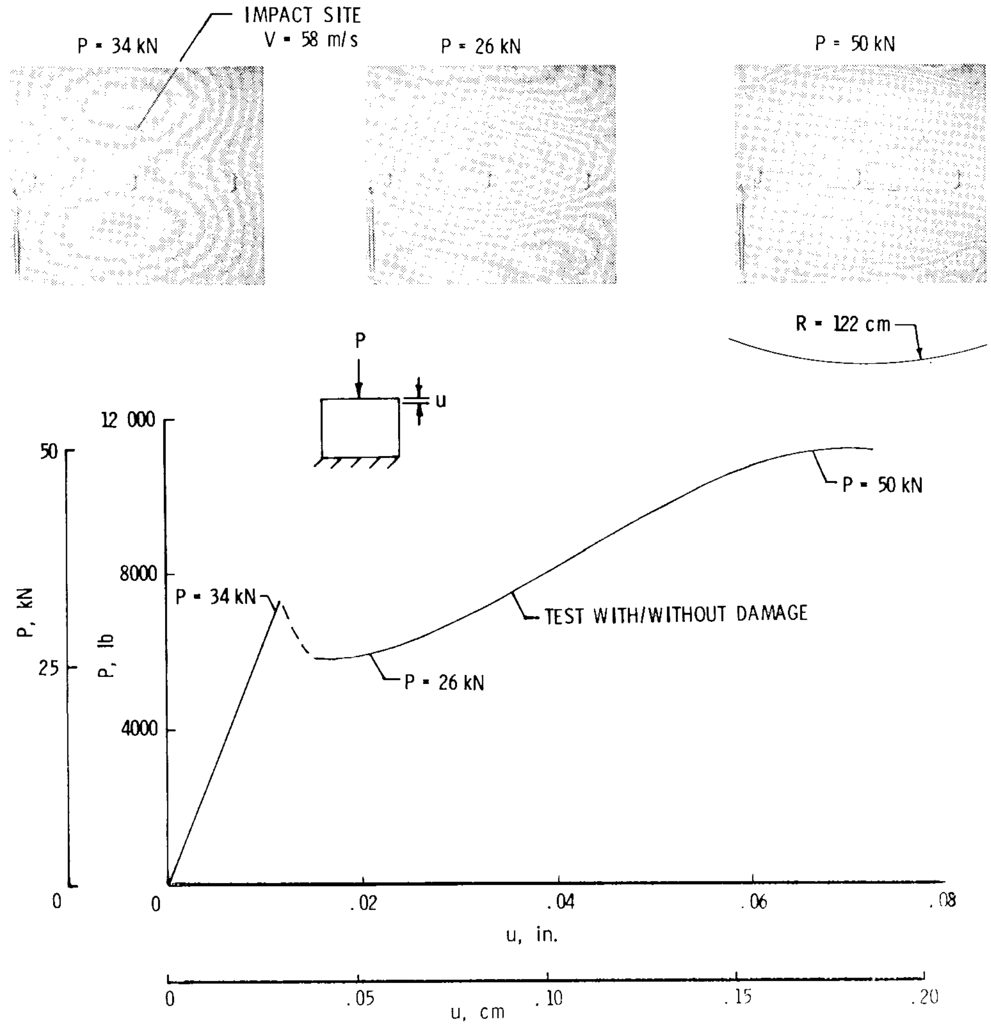

Figure 18.

POSTBUCKLING OF UNSTIFFENED 16-PLY GRAPHITE-EPOXY CURVED PANEL

(Figure 18)

A 16-ply unstiffened graphite-epoxy curved panel was tested with and without impact damage. The panel had a radius of 122 cm, a circumferential arc length of 30.5 cm, and a length of 25.4 cm. The panel was laid up to form a $(\pm 45/\pm 45/90_2/0_2)_s$ laminate. The undamaged panel buckled initially at a load of 35 kN (longitudinal strain of 0.0012) by snapping into a stable postbuckling state at a reduced load of 25 kN. The undamaged panel was further loaded to 27 kN in the postbuckled state and then unloaded. The unloaded panel was impacted near the panel center by a 1.27-cm-diameter aluminum sphere with a speed of 58 m/s. A slight amount of back-surface matrix cracking was caused by the impact event. The damaged panel again buckled at a load of 35 kN by snapping into a stable postbuckled state at a reduced load of 25 kN and then failed at a load of 51 kN when loading was resumed. The end shortening u of the impact-damaged panel is shown in Figure 18 as a function of applied load P. Photographs of moire-fringe patterns representing out-of-plane deflections are shown in the figure just before (34 kN) and after (26 kN) initial buckling and just before (50 kN) panel failure. Failure of the panel occurred at a side support without any apparent influence of the impact damage.

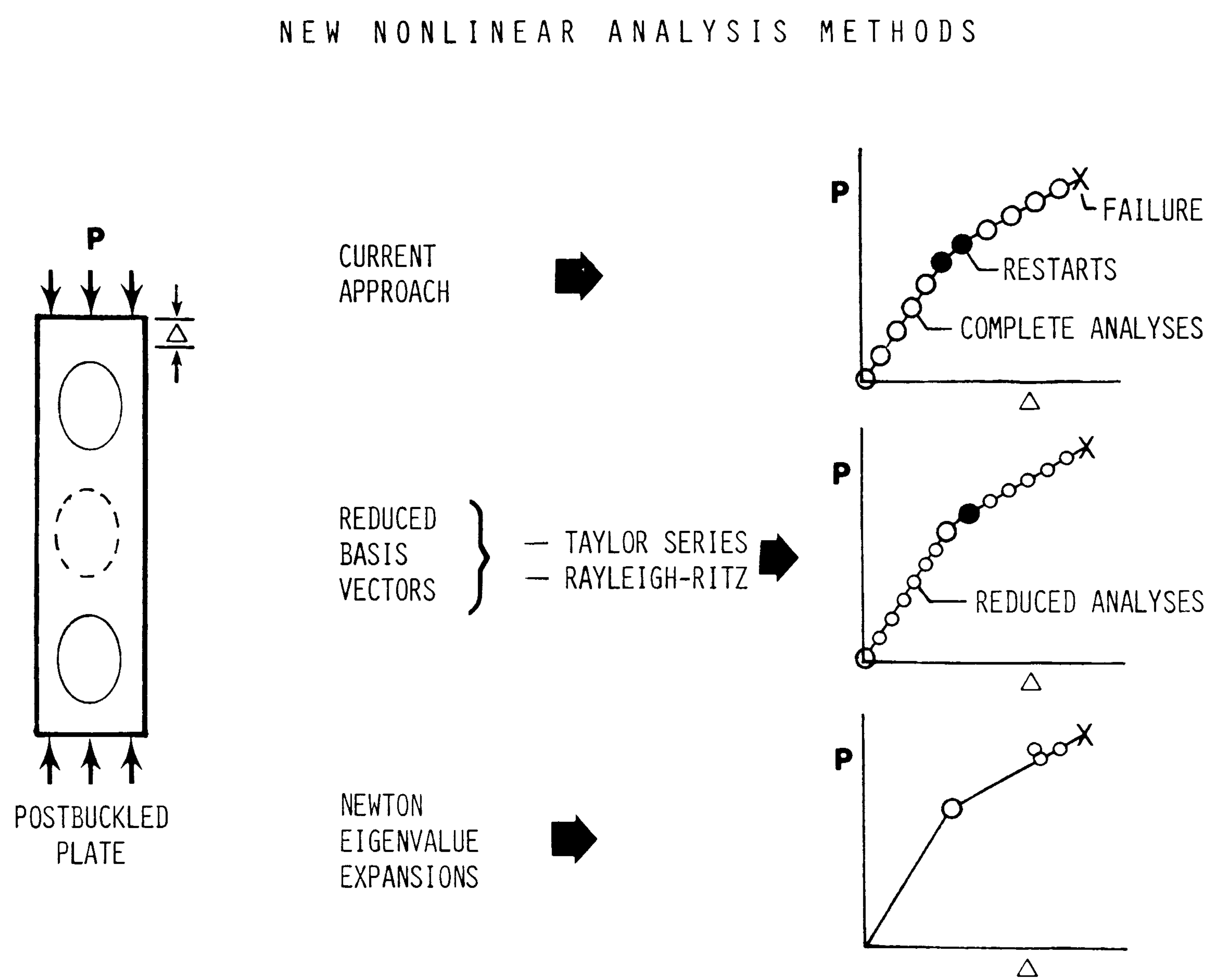
NEW NONLINEAR ANALYSIS METHODS
P
Δ
POSTBUCKLED
PLATE
CURRENT
APPROACH
REDUCED
BASIS
VECTORS
— TAYLOR SERIES
— RAYLEIGH-RITZ
NEWTON
EIGENVALUE
EXPANSIONS
P
FAILURE
RESTARTS
COMPLETE ANALYSES
Δ
P
REDUCED ANALYSES
Δ
P
Δ

Figure 19.

NEW NONLINEAR ANALYSIS METHODS

(Figure 19)

Studies of efficient nonlinear analysis methods indicate that significant computer-cost reductions are possible for postbuckling analyses when compared to current nonlinear analysis methods. For example, the postbuckling response of a rectangular plate loaded in compression can be represented by calculating the end shortening Δ of the plate for increasing values of the applied load P. One current approach (ref. 9) for calculating the load-shortening response of a compression-loaded rectangular plate requires many complete analyses as the load is increased and a number of computer runs restarted from previous applied load values to calculate the postbuckling response of the plate to failure. One alternative approach to calculating the postbuckling response of the plate is to reduce the size of the analysis problem by using a smaller set of generalized coordinates or "reduced basis vectors" to model the response of the plate for limited ranges of the applied load. A single complete analysis is required to generate the reduced basis vectors that are sufficient to represent the response of the plate until the character of the deformation changes enough to introduce computational errors. Once the character of the deformation changes (e.g., at buckling) another complete analysis is performed to update the definition of the reduced basis vectors. Many reduced analyses can be performed at the cost of a single complete analysis. An example of computing reduced basis vectors using a Rayleigh-Ritz approximation is given in Reference 10 and another example using a Taylor series expansion is given in Reference 11. Another alternative approach to calculating the postbuckling response of the plate is based on a procedure described in Reference 12. This approach assumes that the deflected shape of the buckled plate is a multiple of one of the buckling modes and determines the load that keeps the plate in equilibrium for a given amplitude of the buckling mode. This approach requires an eigenvalue solution to find the buckling modes of the plate and a simple iterative procedure to find points on the postbuckling response curve.

POSTBUCKLING OF A PEAR-SHAPED CYLINDER USING TAYLOR SERIES REDUCED BASIS VECTORS

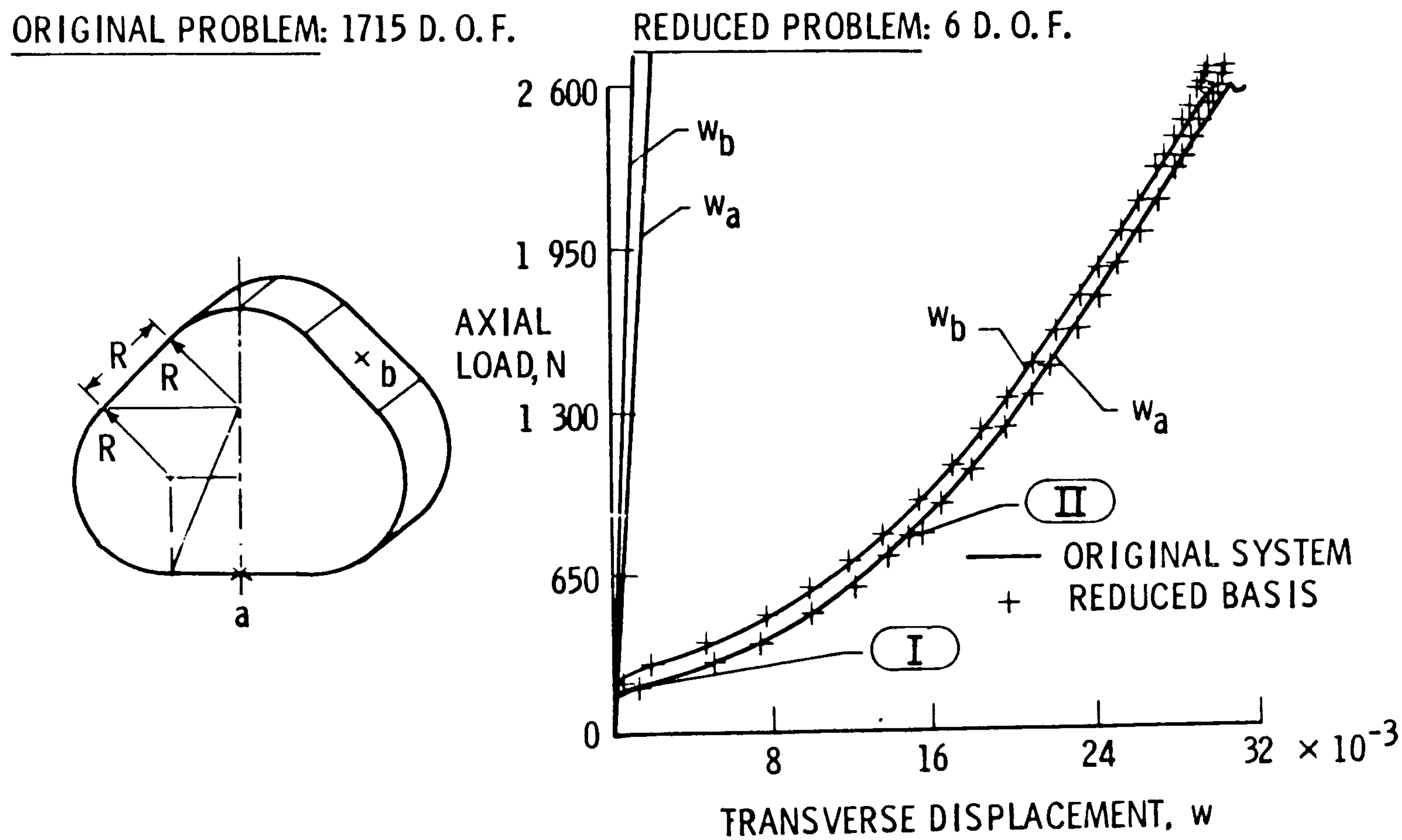

Figure 20.

POSTBUCKLING OF A PEAR-SHAPED CYLINDER USING TAYLOR SERIES REDUCED BASIS VECTORS

(Figure 20)

An example of some results obtained by one of the new nonlinear analysis methods mentioned in Figure 19 is shown in Figure 20. The Taylor-series reduced-basis-vector method described in Reference 11 was used to determine the postbuckling response of a compression-loaded pear-shaped cylinder. Linear and nonlinear solutions for the normal displacements w of two points on the flat surfaces of the pear-shaped cylinder are shown in Figure 20 to emphasize the nonlinear character of the problem. The postbuckling solution of the problem using the conventional STAGS computer code (ref. 9) requires many complete analyses of a 1715-degree-of-freedom problem, while the reduced-basis-vector approach requires only two complete analyses of the 1715-degree-of-freedom problem and a number of reduced analyses of a 6-degree-of-freedom problem. The reduction in the number of degrees of freedom required to predict accurately the postbuckling response of the pear-shaped cylinder significantly reduces the computer cost for solving this nonlinear problem.

CONCLUDING REMARKS

- THE SIZING-ANALYSIS-TEST APPROACH FOR GENERIC ADVANCED-COMPOSITE BUCKLING-RESISTANT COMPRESSION PANELS HAS BEEN SUCCESSFUL.
- TESTS SHOW ADVANCED-COMPOSITE FLAT AND CURVED COMPRESSION PANELS CAN BE LOADED WELL INTO THE POSTBUCKLING RANGE.
- A PRELIMINARY SIZING CODE HAS BEEN DEMONSTRATED FOR GENERIC ADVANCED-COMPOSITE COMPRESSION PANELS WITH POSTBUCKLING STRENGTH.
- LOW-SPEED IMPACT DAMAGE IN STIFFENER-SKIN INTERFACE AREAS OF ADVANCED-COMPOSITE STIFFENED PANELS WITH POSTBUCKLING STRENGTH CAN INITIATE PANEL FAILURE.
- LIMITED TEST DATA SUGGEST THAT ADVANCED-COMPOSITE COMPRESSION PANELS WITH POSTBUCKLING STRENGTH ARE NOT SENSITIVE TO LOW-SPEED IMPACT DAMAGE IN THE BUCKLED SKIN REGION OF THE PANELS.
- HIGHLY-EFFICIENT NONLINEAR ANALYSIS METHODS ARE BEING DEVELOPED FOR IMPROVED POSTBUCKLING DESIGN TECHNIQUES.

REFERENCES

1. Mikulas, M. M., Jr.; Bush, H. G.; and Rhodes, M. D.: Current Langley Research Center Studies on Buckling and Low-Velocity Impact of Composite Panels. Third Conference on Fibrous Composites in Flight Vehicle Design, Part II, NASA TM X-3377, 1976, pp. 633-663.

2. Williams, J. G.; Anderson, M. S.; Rhodes, M. D.; Starnes, J. H., Jr.; and Stroud, W. J.: Recent Developments in the Design, Testing and Impact-Damage Tolerance of Stiffened Composite Panels. NASA TM-80077, 1979.

3. Anderson, M. S.; and Stroud, W. J.: General Panel Sizing Computer Code and Its Application to Composite Structural Panels. AIAA Journal, Vol. 17, no. 8, Aug. 1979. pp. 892-897.

4. Wittrick, W. H.; and Williams, R. W.: Buckling and Vibration of Anisotropic or Isotropic Plate Assemblies Under Combined Loadings. International Journal of Mechanical Sciences, Vol. 16, April 1974, pp. 209-239.

5. Vanderplaats, G. N.; and Moses, F.: Structural Optimization by Methods of Feasible Directions. Computers and Structures, Vol. 3, July 1973, pp. 739-755.

6. Johnson, R., Jr.: Design and Fabrication of a Ring-Stiffened Graphite-Epoxy Corrugated Cylindrical Shell. NASA CR-3206, 1978.

7. Dickson, J. N.; and Biggers, S. B.: Design and Analysis of a Stiffened Composite Fuselage Panel. NASA CR-159302, 1980.

8. Koiter, W. T.: Het Schuifplooiveld by Grote Overschrydingen van de Knikspanning. National Luchvaart Laboratorium Report S295, Amsterdam, Holland, November 1946 (in Dutch).

9. Almroth, B. O.; and Brogan, F. A.: The STAGS Computer Code. NASA CR-2950, 1978.

10. Almroth, B. O.; Stern, P.; and Brogan, F. A.: Automatic Choice of Global Shape Functions in Structural Analysis. AIAA Journal, Vol. 16, May 1978, pp. 525-528.

11. Noor, A. K.; and Peters, J. M.: Reduced Basis Technique for Nonlinear Analysis of Structures. AIAA Journal, Vol. 18, April 1980, pp. 455-462.

12. Thurston, G. A.: Continuation of Newton's Method Through Bifurcation Points. Trans. ASME, Ser. E: Journal of Applied Mechanics, Vol. 36, September 1965, pp. 425-430.

DEVELOPMENT OF A LAMINATE FATIGUE ANALYSIS

G. L. Roderick, T. K. O'Brien,* and J. D. Whitcomb

INTRODUCTION

The fatigue life, residual strength, and stiffness of a notched composite laminate depend on damage growth in and between plies. The damage growth depends on layup (fiber orientation and stacking sequence). Hence, a comprehensive fatigue analysis should link damage growth to layup. Such an analysis is being developed on three premises. First, a few basic failure modes dominate fatigue damage growth in all laminate layups. Second, fatigue tests of simple specimens can be used to relate these failure modes to stresses in and between plies. Third, these stresses can be calculated for notched laminates that contain fatigue damage.

The fatigue analysis will predict damage growth as a function of applied load cycles. In addition, it will relate damage growth to fatigue life, residual strength, and stiffness. Its development is discussed in the following figures.

*Structures Laboratory, AVRADCOM Research and Technology Laboratories.

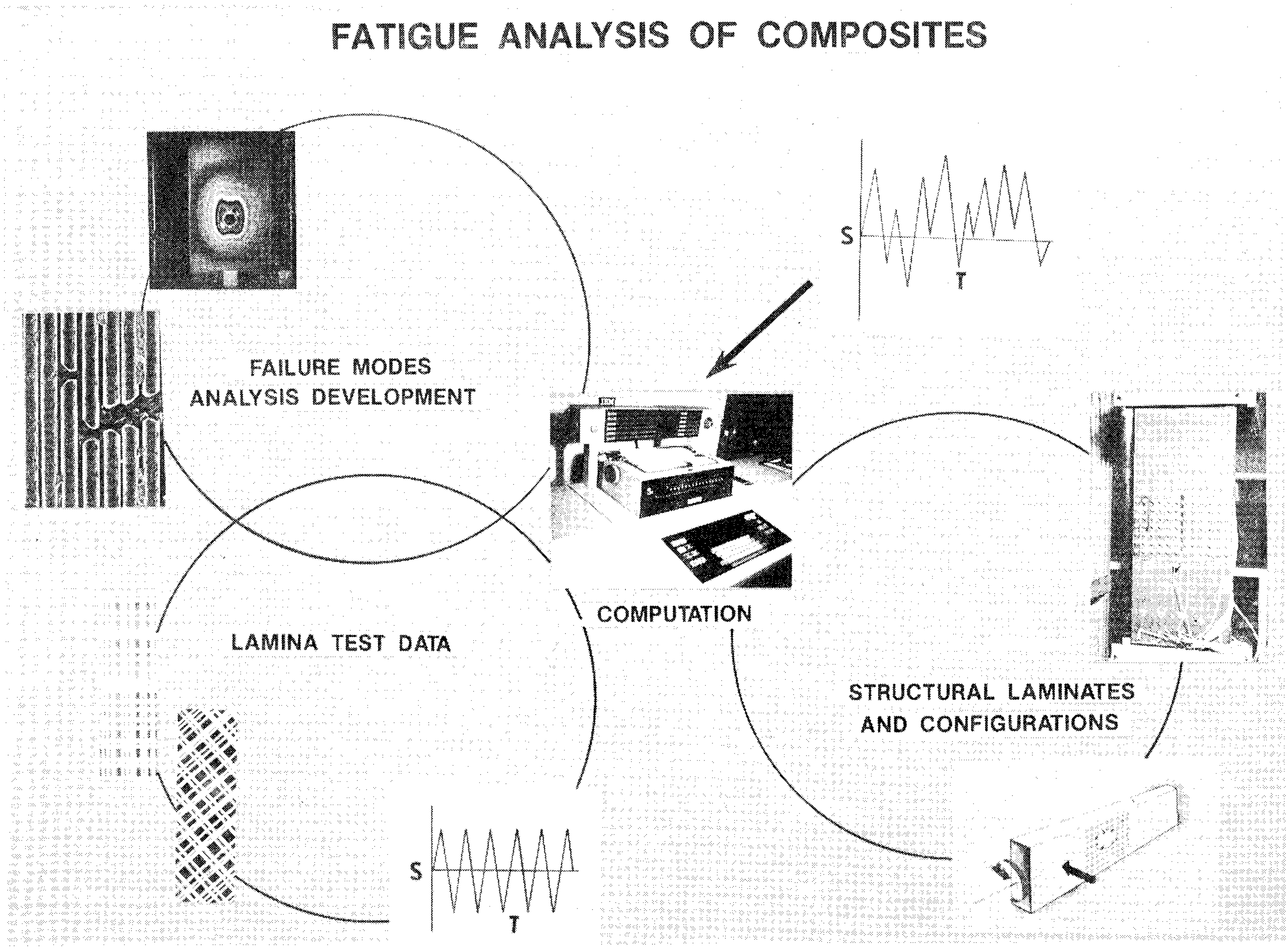
FATIGUE ANALYSIS OF COMPOSITES
FAILURE MODES
ANALYSIS DEVELOPMENT
LAMINA TEST DATA
COMPUTATION
STRUCTURAL LAMINATES
AND CONFIGURATIONS
S
T
S
T

Figure 1.

FATIGUE ANALYSIS OF COMPOSITES

(Figure 1)

The fatigue analysis is being developed by coordinating research in three areas. In the first area, fatigue damage growth in test coupons is studied with methods such as thermography, X-ray radiography, and scanning-electron microscopy. From these studies basic failure modes in composite laminates are identified. In addition, a stress analysis for observed fatigue damage is developed. In the second area, constant-amplitude fatigue tests relate fatigue damage growth to cyclic stresses in and between plies. Inplane damage is related to stresses in plies with tests of ±45 and $90_5/0/90_5$ laminates; interlaminar damage is related to stresses between plies with tests of $[\pm 30/\pm 30/90/\overline{90}]_s$ laminates. A computational model combines research results from these two areas to form a fatigue analysis for simple, notched coupons. The computations are sequential. First, stresses in and between laminate plies are calculated. Next, these stresses are used to predict damage growth for a number of applied load cycles. Then, updated stresses in the damaged laminate are calculated. The process of predicting additional damage growth is repeated until failure occurs. In the third area, complex structural laminates are tested under realistic loads. These tests will be used to evaluate the fatigue analysis. Also, they will identify areas where research efforts should be concentrated. Research in the first two areas is discussed in the following figures.

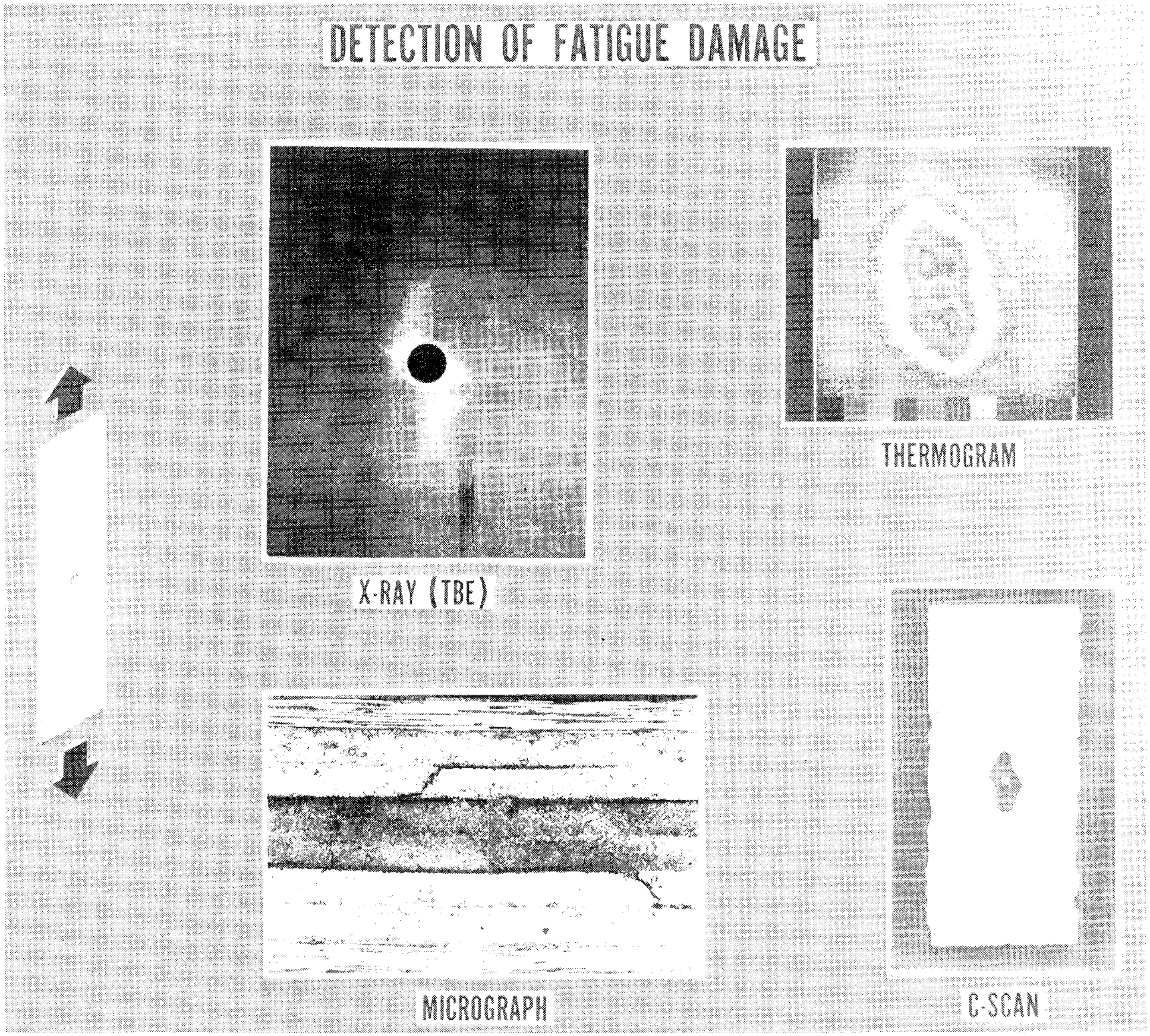
DETECTION OF FATIGUE DAMAGE
X-RAY (TBE)
THERMOGRAM
MICROGRAPH
C-SCAN

Figure 2.

DETECTION OF FATIGUE DAMAGE

(Figure 2)

A variety of nondestructive and destructive methods was used to study fatigue damage. X-rays enhanced with an opaque penetrant revealed the distribution of ply cracks and delaminations in the plan view. Ultrasonic C-scans revealed delaminations; an advantage of C-scans is that no penetrant is required. Thermograms show temperature profiles caused by heat generation in damage zones; with thermography, the progression of damage can be tracked without interrupting a test. Light micrographs of polished sections show the distribution of damage through the thickness. By exploiting the advantages of each of these methods, a complete picture of the fatigue damage process can be obtained.

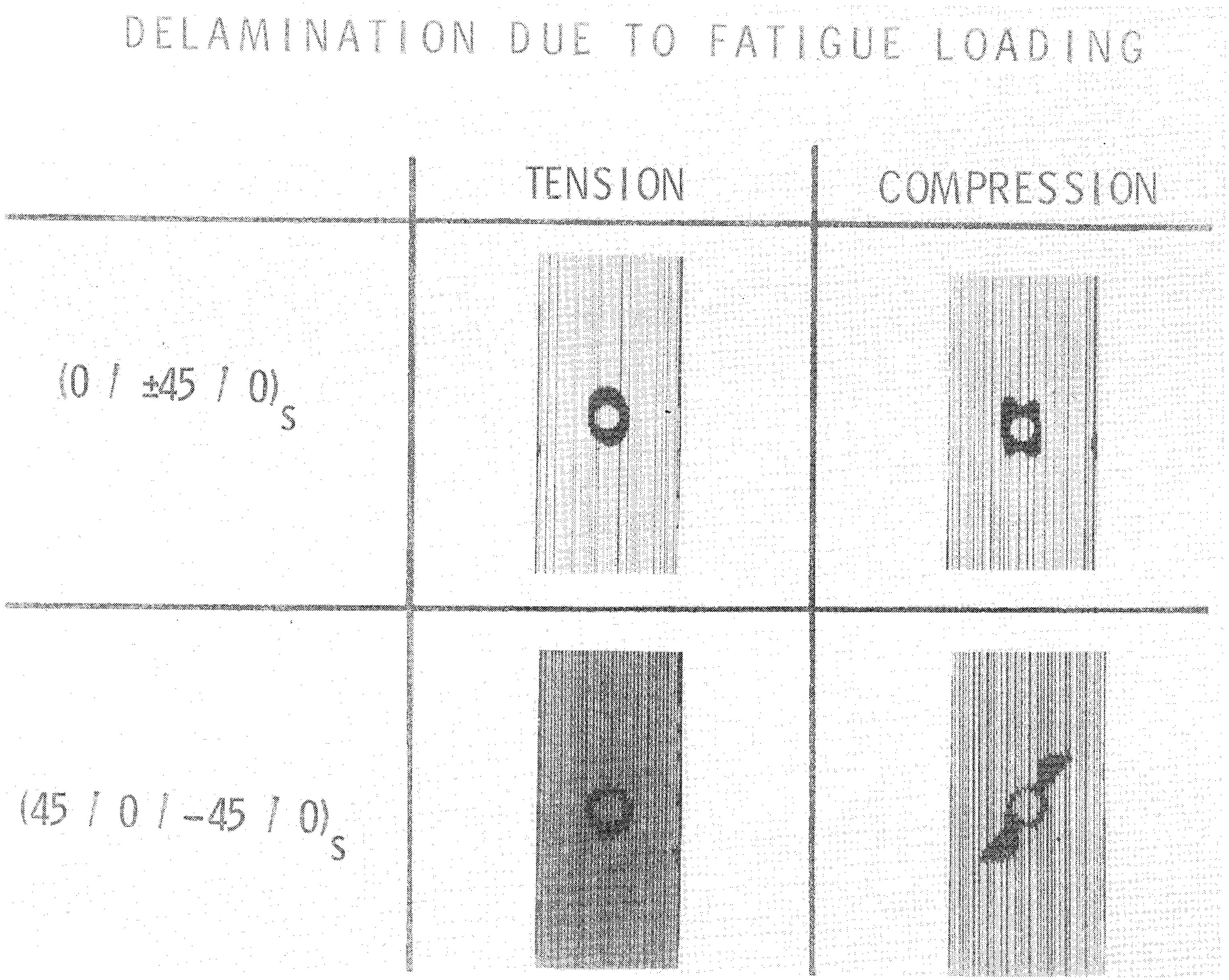
DELAMINATION DUE TO FATIGUE LOADING
TENSION
COMPRESSION
(0 / ±45 / 0)S
(45 / 0 / -45 / 0)S

Figure 3.

DELAMINATION DUE TO FATIGUE LOADING

(Figure 3)

The delamination behavior of graphite/epoxy laminates was studied for tension and compression loading. The figure illustrates examples of this behavior for laminates with two different stacking sequences. Although the outlines of the delamination were different, the $[0/\pm 45/0]_s$ laminates delaminated primarily above and below the hole under either tension or compression loads. In contrast, the $[45/0/-45/0]_s$ laminates delaminated very little under tension loads but significantly under compression loads. Also, under compression loads the location of the delamination was at 45° to the load axis rather than above or below the hole. Further variety in delamination behavior was observed for other fiber orientations, laminate thicknesses, and material systems. The fatigue analysis must be able to predict this diverse behavior.

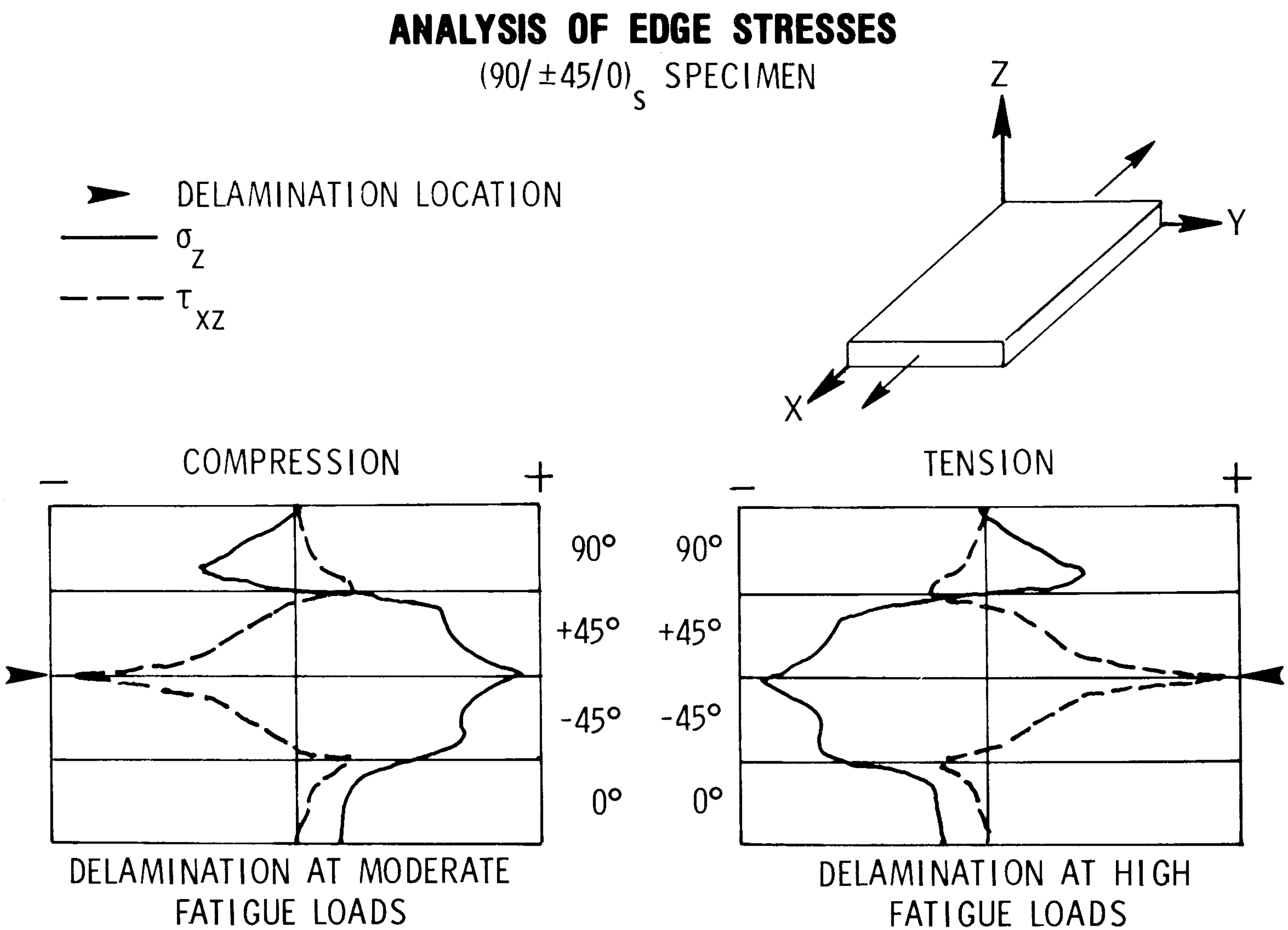
ANALYSIS OF EDGE STRESSES
$(90/\pm45/0)_s$ SPECIMEN
DELAMINATION LOCATION
σ_z
τ_{xz}
Z
Y
X
COMPRESSION
TENSION
−
+
−
+
90°
+45°
-45°
0°
90°
+45°
-45°
0°
DELAMINATION AT MODERATE FATIGUE LOADS
DELAMINATION AT HIGH FATIGUE LOADS

Figure 4.

ANALYSIS OF EDGE STRESSES

(Figure 4)

The relationship between calculated interlaminar stresses and observed delaminations was studied for unnotched graphite/epoxy laminates. The figure shows results for $[90/\pm45/0]_s$ laminates. Delaminations occurred at the +45°/-45° interface for both tension and compression loads. Note that larger loads were required for delamination in tension than in compression. Examination of the calculated stresses reveals that the shear components at the +45°/-45° interface are identical for tension and compression (because the sign of the shear stress is irrelevant). However, the peel stress σ_z is tensile at the critical interface only for compression applied loads. Apparently, delamination can be caused by high shear stresses, but a tensile normal stress greatly encourages delamination growth.

CALCULATED STRESSES VERSUS DELAMINATION

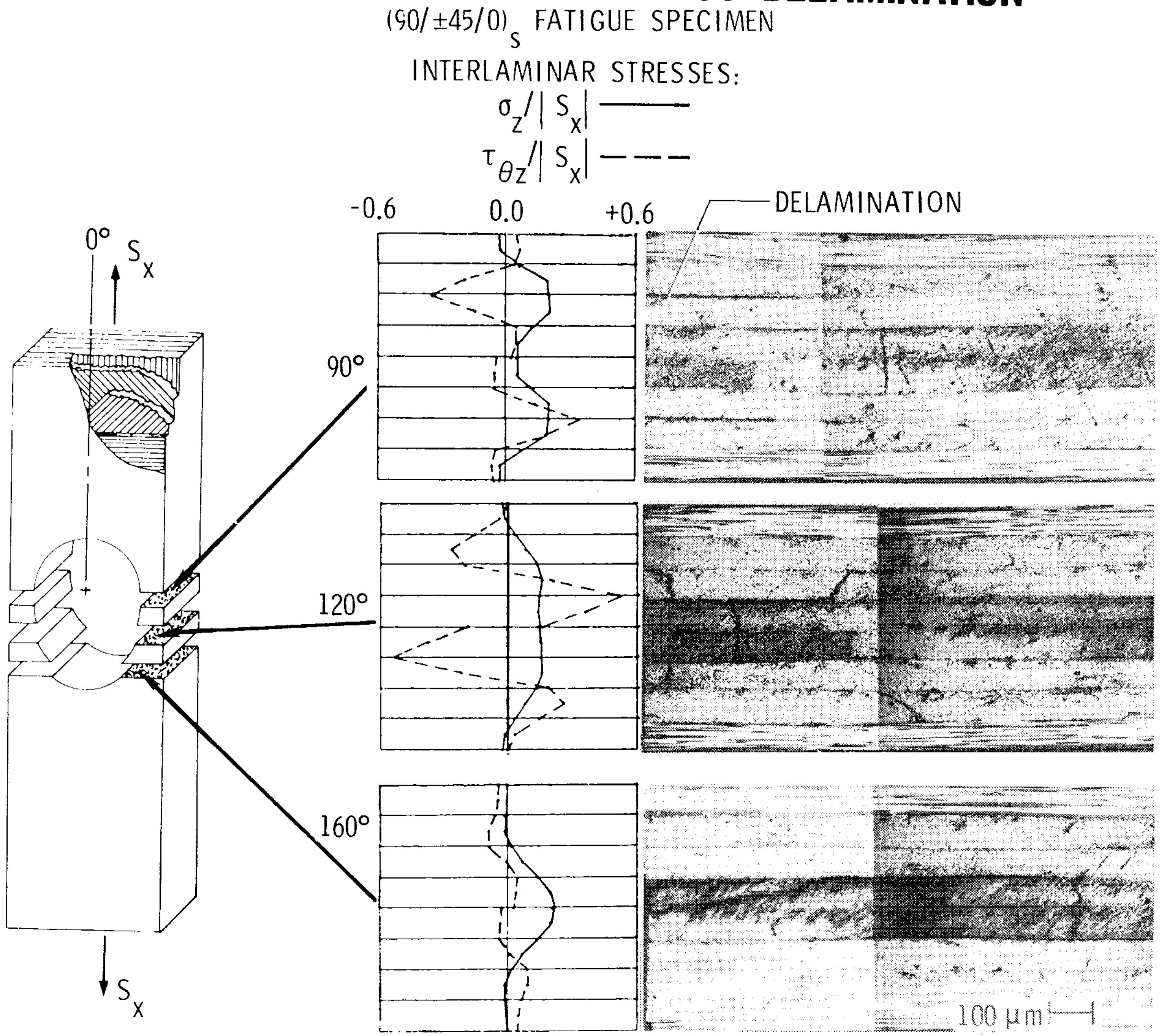

Figure 5.

CALCULATED STRESSES VERSUS DELAMINATION

(Figure 5)

Calculated stresses were compared with delamination locations for notched graphite/epoxy laminates. The figure shows results for a $[90/\pm45/0]_s$ laminate subjected to compression fatigue loads. The shaded surfaces on the specimen schematic are the surfaces shown by the photomicrographs. The stress distributions are through-thickness stress distributions along the intersection of the shaded surfaces and the hole boundary. Delamination location depended on the angular position around the hole. However, in all three cases, the delamination locations corresponded to surfaces where the interlaminar stresses peaked. Hence, even for a complex configuration, delamination locations appear to be predictable on the basis of calculated stresses.

METHOD TO STUDY DELAMINATION IN COMPOSITE LAMINATES

GRAPHITE/EPOXY

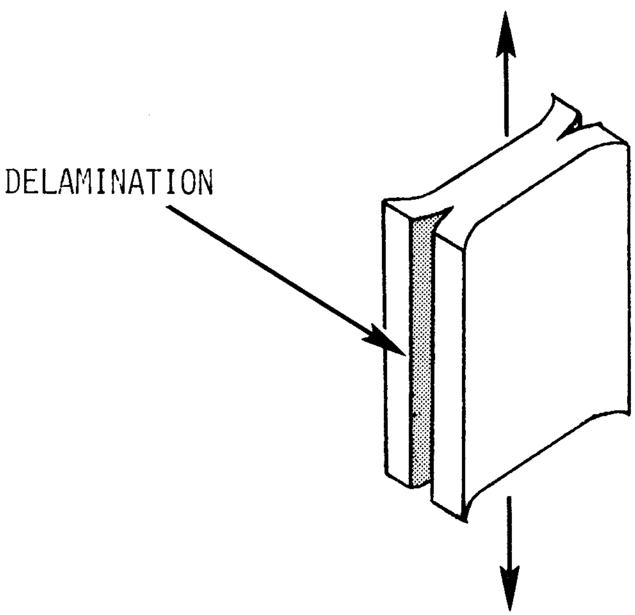

DELAMINATION SPECIMEN
$(\pm 30/\pm 30/90/\overline{90})_S$

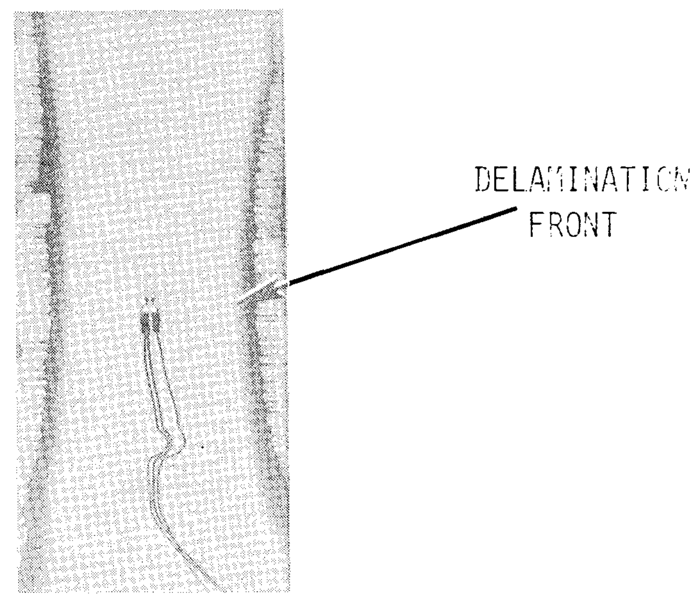

DYE-PENETRANT - ENHANCED RADIOGRAPH OF DELAMINATION

Figure 6.

METHOD TO STUDY DELAMINATION IN COMPOSITE LAMINATES

(Figure 6)

To study the onset and growth of delaminations, unnotched $[\pm 30/\pm 30/90/\overline{90}]_s$ graphite/epoxy laminates, designed to delaminate under tension loads, were tested. Both quasi-static tension tests and constant-strain-amplitude, tension-tension fatigue tests were conducted. During the tests, diiodobutane (DIB), a dye-penetrant opaque to X-rays, was applied to the delaminated edge. Then, the specimen was X-rayed. The typical dye-penetrant-enhanced X-ray clearly showed the extent of delamination. The X-rays were used to determine the onset of delamination under quasi-static tension tests. Also, sequential X-rays taken during fatigue tests were used to determine delamination growth rates.

STRAIN-ENERGY-RELEASE RATE DETERMINED

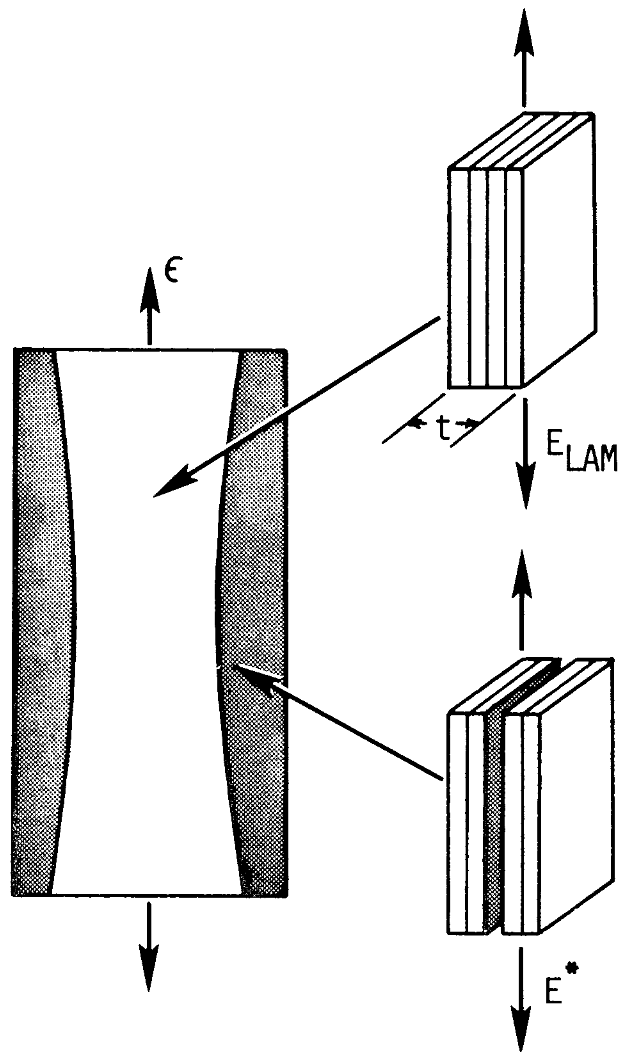

$\mathcal{G}$ = STRAIN ENERGY RELEASED PER UNIT OF NEW SURFACE AREA CREATED

$$\boxed{\mathcal{G} = \epsilon^2 t\left(E^* - E_{LAM}\right)}$$

Figure 7.

STRAIN-ENERGY-RELEASE RATE DETERMINED

(Figure 7)

A simple expression for the strain energy released as delaminations grow was derived. This simple expression for the strain-energy-release rate $\mathcal{G}$ has several advantages. First, $\mathcal{G}$ is independent of delamination size. It depends only on the applied strain ε, the specimen thickness t, the stiffness of the undamaged laminate E_{LAM}, and the stiffness of the laminate when it was completely delaminated E^*. Second, E_{LAM} and E^* can be calculated from simple laminated plate theory. Third, because E^* depends on the location of the delaminated interface, E^* and, hence, $\mathcal{G}$ are sensitive to the location of damage through the laminate thickness. The simple equation was used to develop criteria to predict the onset and growth of delaminations in realistic, unnotched laminates. These criteria are discussed in succeeding figures.

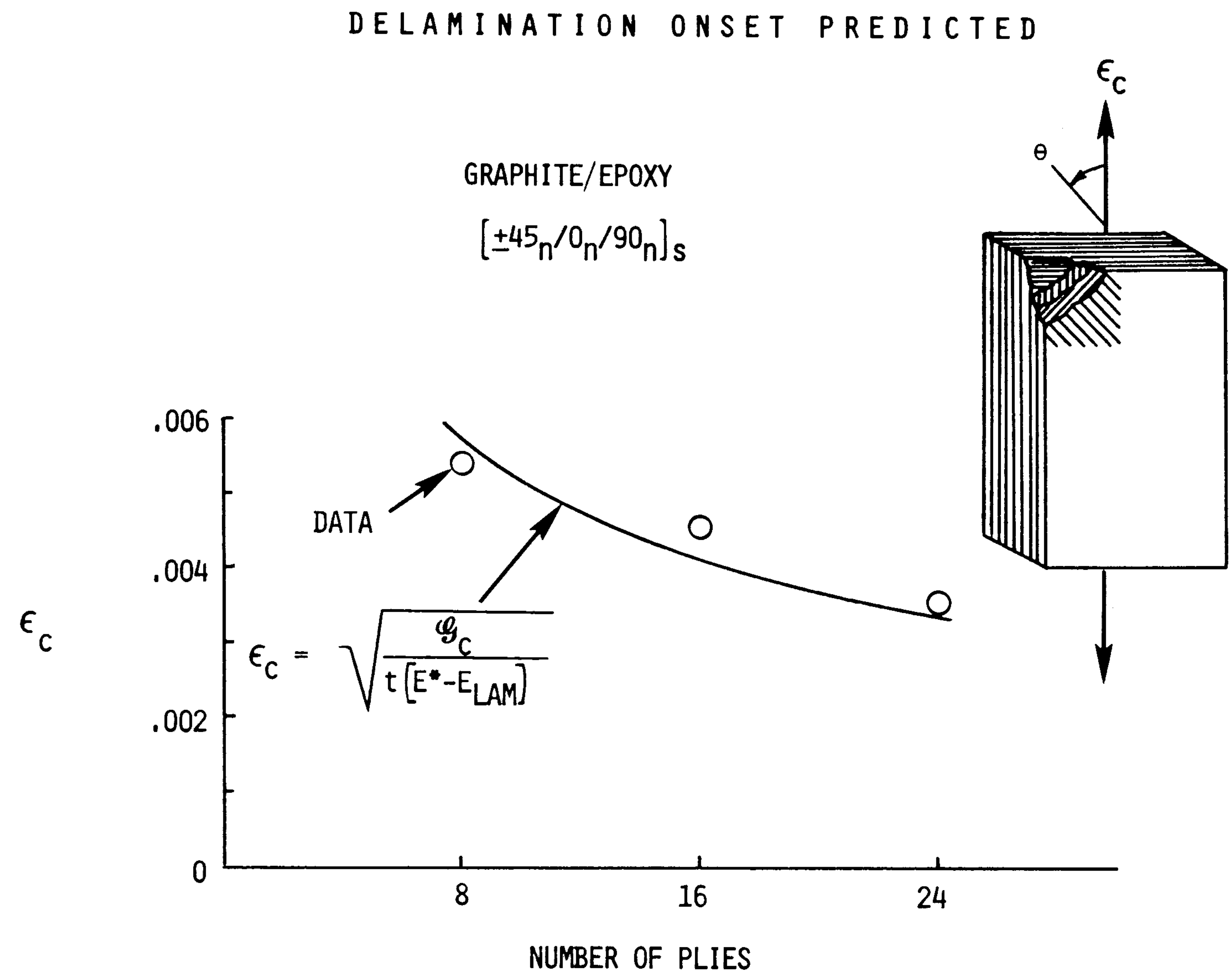
DELAMINATION ONSET PREDICTED
GRAPHITE/EPOXY
$[\pm 45_n/0_n/90_n]_s$
ϵ_c
θ
.006
.004
.002
0
DATA
$\epsilon_c = \sqrt{\dfrac{\mathcal{G}_c}{t[E^* - E_{LAM}]}}$
8
16
24
NUMBER OF PLIES

Figure 8.

DELAMINATION ONSET PREDICTED

(Figure 8)

To predict the onset of delaminations in realistic unnotched laminates, quasi-static tension tests were conducted on the $[\pm 30/\pm 30/90/\overline{90}]_s$ laminates. The applied strain recorded at the onset of delamination ε_c was used to calculate a critical strain-energy-release rate $\mathcal{G}_c$. Then, $\mathcal{G}_c$ was used to predict the onset of delamination in more complex laminates. The figure shows data and predictions for three $[\pm 45_n/0_n/90_n]_s$ laminates, all having the same layup but with different ply thicknesses. For example, $n = 1$ is an 8-ply laminate, $n = 2$ is a 16-ply laminate, and $n = 3$ is a 24-ply laminate. The predictions agreed well with experimental data, indicating that $\mathcal{G}_c$ was a material property. Furthermore, the trend of lower ε_c for thicker laminates was correctly predicted.

FATIGUE OF COMPOSITES
DELAMINATION GROWTH LAW

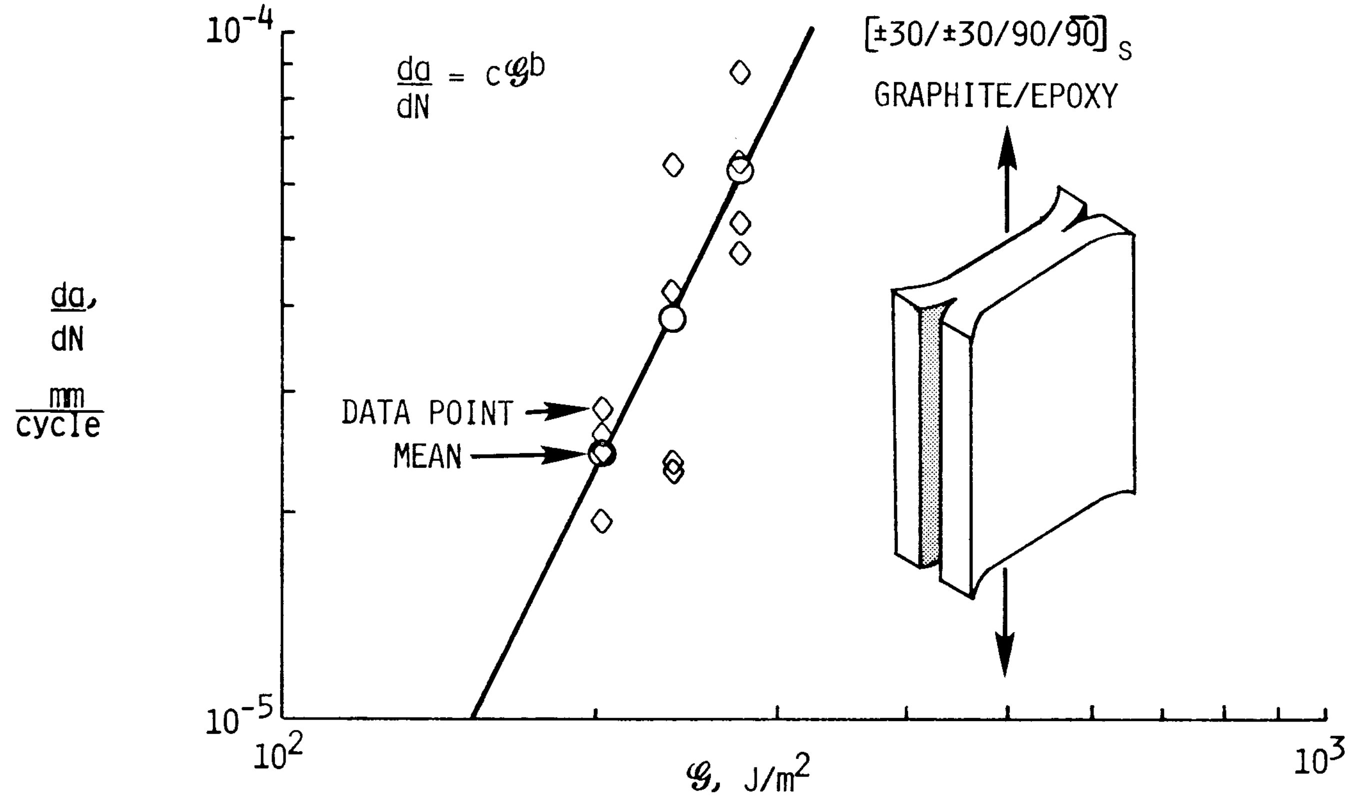

Figure 9.

FATIGUE OF COMPOSITES DELAMINATION GROWTH LAW

(Figure 9)

To predict delamination growth in realistic laminates, a delamination growth law was developed. To this end, four tension-tension fatigue tests of $[\pm30/\pm30/90/\overline{90}]_s$ laminates were run at each of three different constant cyclic strain levels. During the tests, delaminations were tracked with dye-penetrant-enhanced X-radiography. Sequential radiographs showed that once the delamination had initiated along the entire specimen edge, it grew at a constant rate. For each test, the constant delamination growth rate was determined. The diamond symbols are the constant growth rates plotted against the strain-energy-release rate $\mathcal{G}$ calculated from the maximum cyclic strain. The circular symbols represent the mean of the growth rates for tests conducted at the same maximum cyclic strain. The solid line on the figure shows a least-squares fit with a power law of the form $da/dN = c\mathcal{G}^b$. The c and b are empirical constants determined from the fit. As evident from the figure, the fit was quite good. The developed power law will be used in fatigue analysis to predict delamination growth in realistic laminates.

PREDICTION OF DELAMINATION GROWTH DUE TO LOCAL INSTABILTY

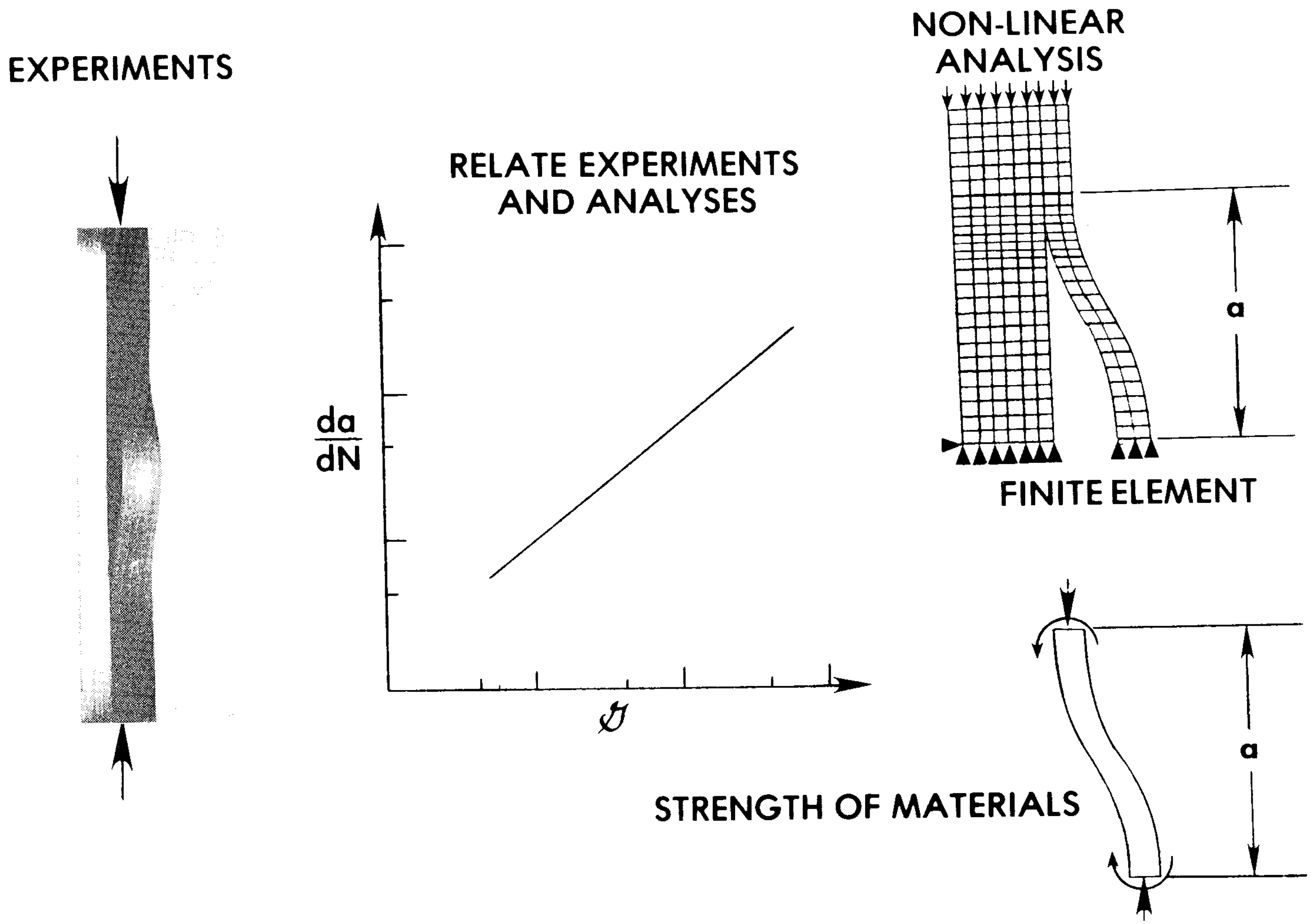

Figure 10.

PREDICTION OF DELAMINATION GROWTH DUE TO LOCAL INSTABILITY

(Figure 10)

Under compressive loads, local instability may cause delamination growth. To predict this behavior, experimental and analytical studies are under way. Simple specimens like that shown have been tested. Under compressive fatigue loads, initial delaminations in these specimens grow. To analyze the delamination growth, a geometrically nonlinear finite-element stress analysis was developed. However, the analysis is expensive. Accordingly, a "strength of materials" analysis has also been developed based on insight gained from the finite-element analysis. The ultimate goal of the work is to predict delamination growth when local instability occurs.

WEIBULL FIT OF SHEAR MODULUS CHANGE

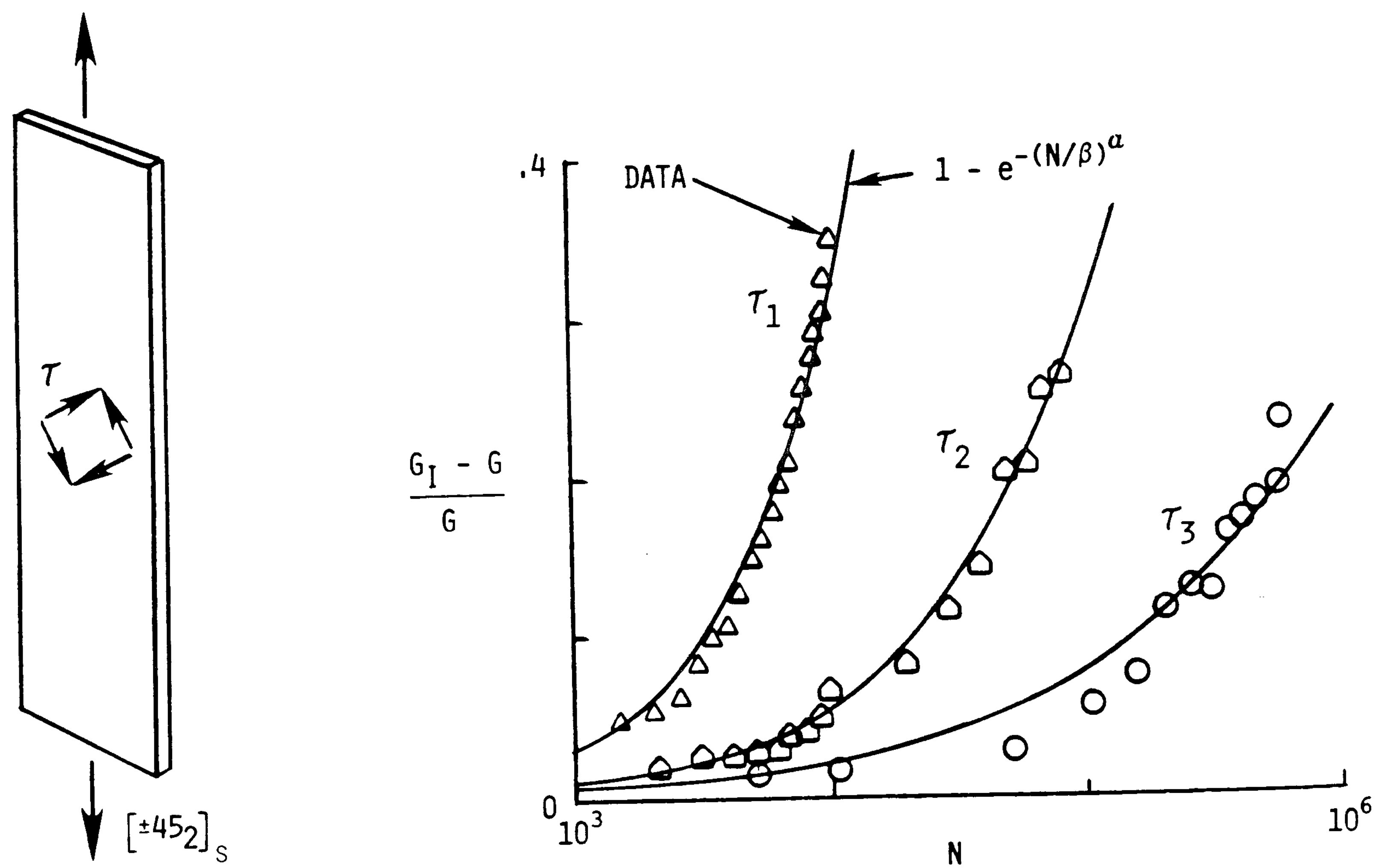

Figure 11.

WEIBULL FIT OF SHEAR MODULUS CHANGE

(Figure 11)

The change in inplane shear modulus was related to cyclic stress levels with a two-parameter Weibull function. The shear modulus change was determined from constant-amplitude fatigue tests of simple, unnotched fatigue tests of $[\pm 45_2]_s$ laminates. In the figure, the change in shear modulus, which is normalized by the initial shear modulus, is plotted against the number of applied load cycles. The symbols in the figure represent the normalized shear modulus change calculated from deflections of ±45 laminates. The lines in the figure are curve fits of the data with two-parameter Weibull probability density functions. The Weibull parameters α and β are different for each curve. As shown in the figure, the curve fits are quite good. The results show that Weibull functions can be used to represent inplane shear modulus change in terms of inplane cyclic stresses. This relationship will be used in the fatigue analysis to predict inplane damage growth.

SHEAR MODULUS PREDICTION FOR STRAIN-CONTROLLED FATIGUE TEST OF $[\pm 45_2]_S$ LAMINATES

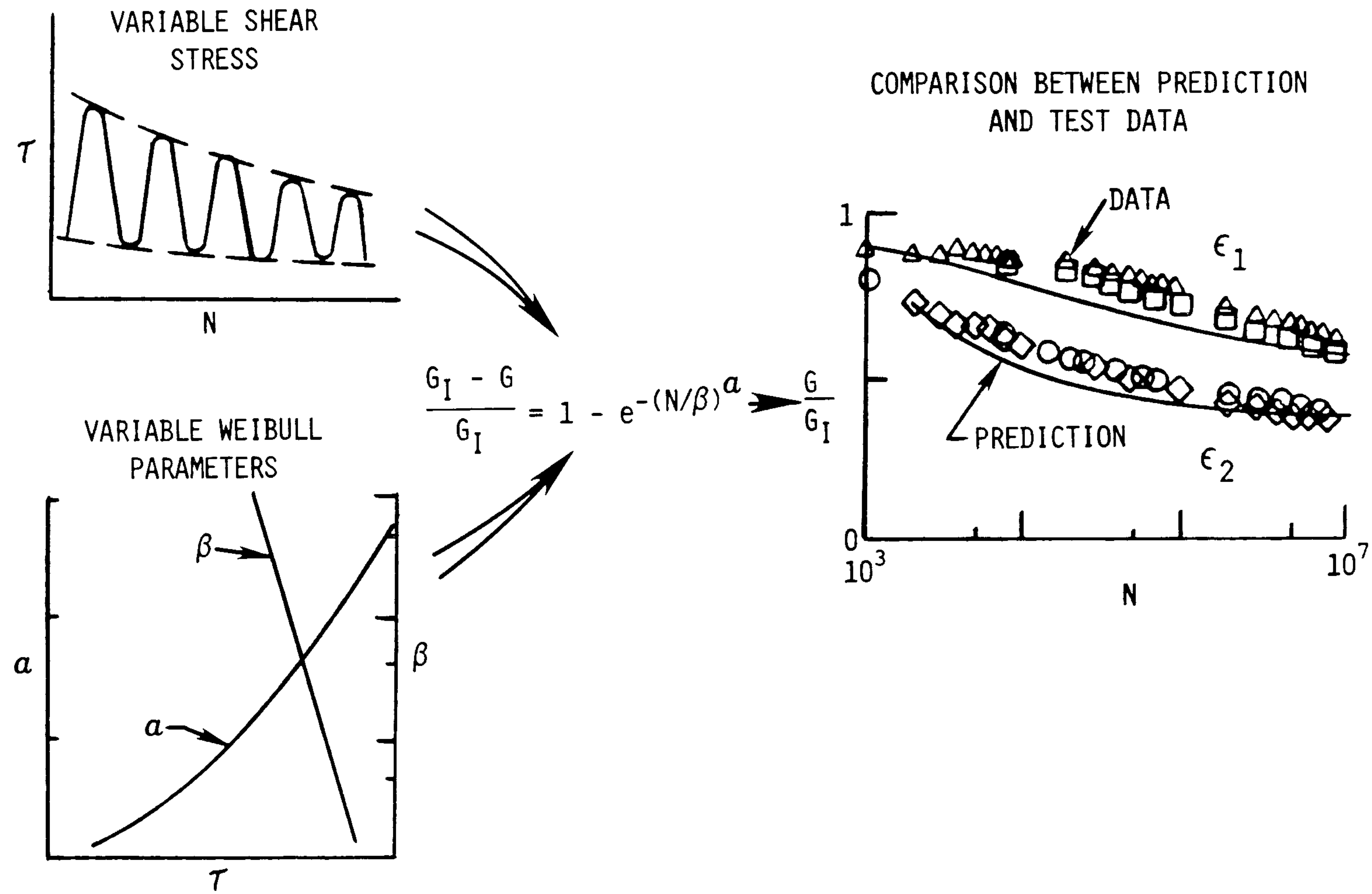

Figure 12.

SHEAR MODULUS PREDICTION FOR STRAIN-CONTROLLED FATIGUE TEST OF $[\pm 45_2]_s$ LAMINATES

(Figure 12)

The figure shows that shear modulus changes can be predicted for ±45 laminates that have been fatigued under strain-controlled loads. As indicated at the left of the figure, in a strain-controlled fatigue test of $[\pm 45_2]_s$ laminates, shear stresses change with applied load cycles. To predict this behavior with the Weibull equation shown in figure 11, the Weibull parameters α and β were expressed in terms of the maximum cyclic shear stress. These expressions were determined with simple curve fits. The fits are shown at the lower left of the figure. As shown in the center of the figure, the values were then used in the Weibull equations to predict change in modulus as a function of both the cyclic shear stress and the number of applied load cycles. The figure shows inplane shear modulus, normalized by the initial shear modulus, plotted against the number of applied load cycles. The symbols represent data from strain-controlled tests of $[\pm 45_2]_s$ boron/epoxy laminates. Two fatigue tests were run at each of two strain levels. The solid line indicates predictions from the Weibull equations. The agreement between the data and the prediction indicates that the Weibull equations may be used to predict modulus changes in plies of laminates subjected to variable-amplitude loads.

PREDICTION OF FATIGUE DEGRADATION

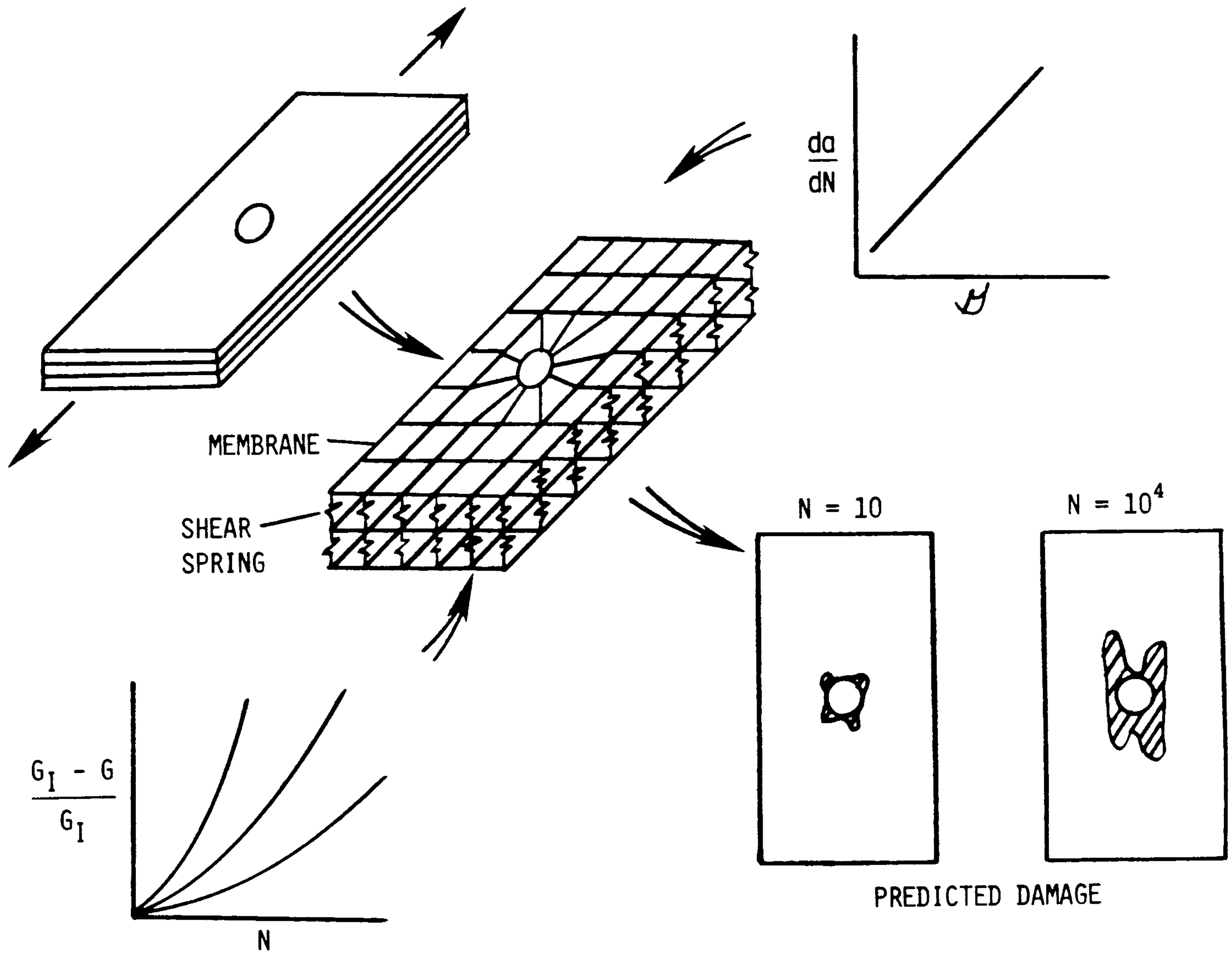

Figure 13.

PREDICTION OF FATIGUE DEGRADATION

(Figure 13)

A fatigue analysis was developed to predict both inplane and interlaminar damage growth in notched composite laminates. The fatigue analysis uses a finite-element stress analysis to calculate inplane and interlaminar stresses. Membrane elements represent each ply. As indicated in the figure, the membrane elements of adjacent plies are connected with shear springs. To simulate damage growth, the properties of the membrane elements and shear springs are altered. The criteria for change are based on relationships similar to those shown in figures 9 and 11. As indicated in the figure, the fatigue analysis has the potential to predict damage growth as a function of applied load cycles. In the future, the analysis will be refined and evaluated.

SUMMARY

A fatigue analysis is being developed to predict damage growth in notched laminates. As shown by experimental studies, fatigue damage is dominated by matrix failure. Criteria have been developed to relate matrix failure to cyclic stresses in and between plies. Delamination growth, which is matrix failure between plies, has been correlated with strain-energy-release rate. Inplane shear modulus change, which reflects matrix damage within plies, has been related to cyclic shear stresses. A simplified finite-element model has been developed to determine stresses in laminates that contain matrix damage. Failure criteria are being integrated with the finite-element model to form the fatigue analysis.

DAMAGE TOLERANCE RESEARCH ON COMPOSITE COMPRESSION PANELS

Marvin D. Rhodes

INTRODUCTION

If graphite-epoxy composite materials are to be used in high strength structures, the damage tolerance of these materials must be understood. A number of investigations have been conducted to evaluate the damage tolerance of composites and some typical results are reported in references 1 and 2. These results have shown that severe degradation in material strength may occur due to impact damage and that reduced strain allowables should be considered to compensate for possible impact damage. Since these studies were presented, additional research in this area has been conducted in the Structural Mechanics Branch of the NASA Langley Research Center. The focus of the research has been aimed at (1) understanding the mechanisms of failure involved in impact so that local damage will be reduced and (2) arrest of propagating fracture initiated at impact locations.

This paper presents typical compression strength reductions for damage due to impact by a 1.27 cm diameter spherical projectile in thick laminates representative of wing skin panels. Also discussed are the results of concepts recently evaluated to improve damage tolerance. These concepts range from improvements at the materials level to advanced structural configurations designed to arrest or limit the growth of propagating fractures. The results indicate that substantial improvements in the damage tolerance of graphite-epoxy composite structures can be achieved through the proper combination of materials and structural design.

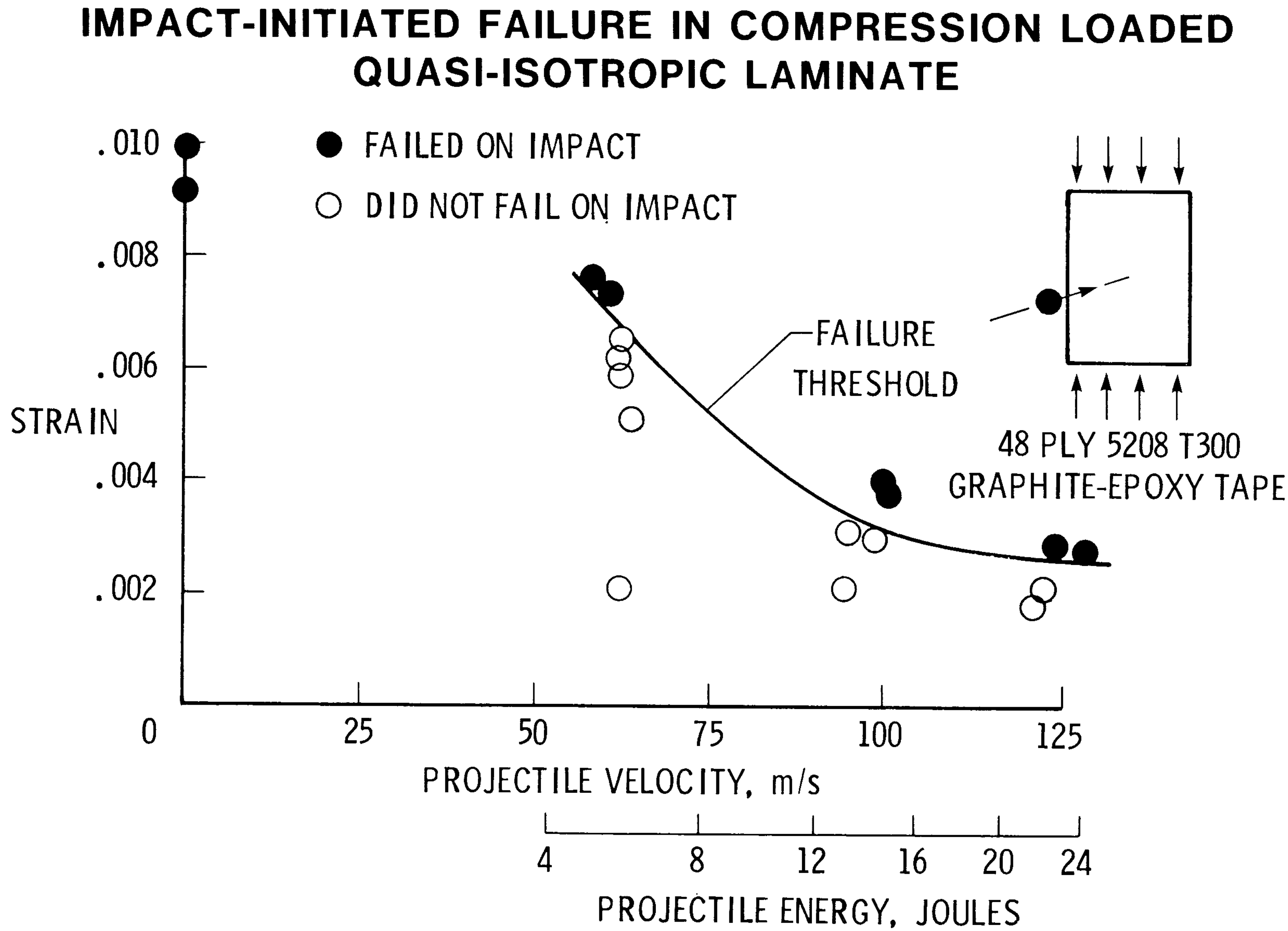

IMPACT-INITIATED FAILURE IN COMPRESSION LOADED
QUASI-ISOTROPIC LAMINATE
FAILED ON IMPACT
DID NOT FAIL ON IMPACT
STRAIN
.010
.008
.006
.004
.002
0
25
50
75
100
125
PROJECTILE VELOCITY, m/s
4
8
12
16
20
24
PROJECTILE ENERGY, JOULES
FAILURE
THRESHOLD
48 PLY 5208 T300
GRAPHITE-EPOXY TAPE

Figure 1.

IMPACT-INITIATED FAILURE IN COMPRESSION LOADED QUASI-ISOTROPIC LAMINATE

(Figure 1)

A typical example of the effect of low-velocity impact on the compression strength of a 48 ply quasi-isotropic laminate $(\pm 45/0/90/\mp 45/0/90)_{3s}$ is shown in the figure. The ordinate is the applied axial compression strain when impact occurred and the abscissa is the projectile impact velocity. The projectile kinetic energy is also shown on the abscissa for reference. The projectile was a 1.27 cm diameter aluminum sphere. The specimens were rectangular flat plates that were 12.5 cm wide by 25.4 cm long. The solid symbols represent specimens that failed on impact. The open symbols represent specimens that carried load after impact occurred even though they may have sustained local damage. The curve labeled "failure threshold" was faired between the open and closed symbols to represent a lower bound to the applied compression strain which will precipitate failure at the given impact condition.

The data shown on the ordinate represent undamaged control specimens that failed after buckling and, therefore, are not necessarily indicative of the ultimate compression strength of the test laminate. The failure strains, however, are well above traditional design strains of conventional aluminum aircraft materials. The specimens that failed due to impact, however, represent strength failures and the strains at the higher velocities are below the traditional design values for strength critical components such as heavily loaded upper surface wing panels.

A discussion of the mechanisms and the effect of damage on the residual compression strength can be found in reference 3.

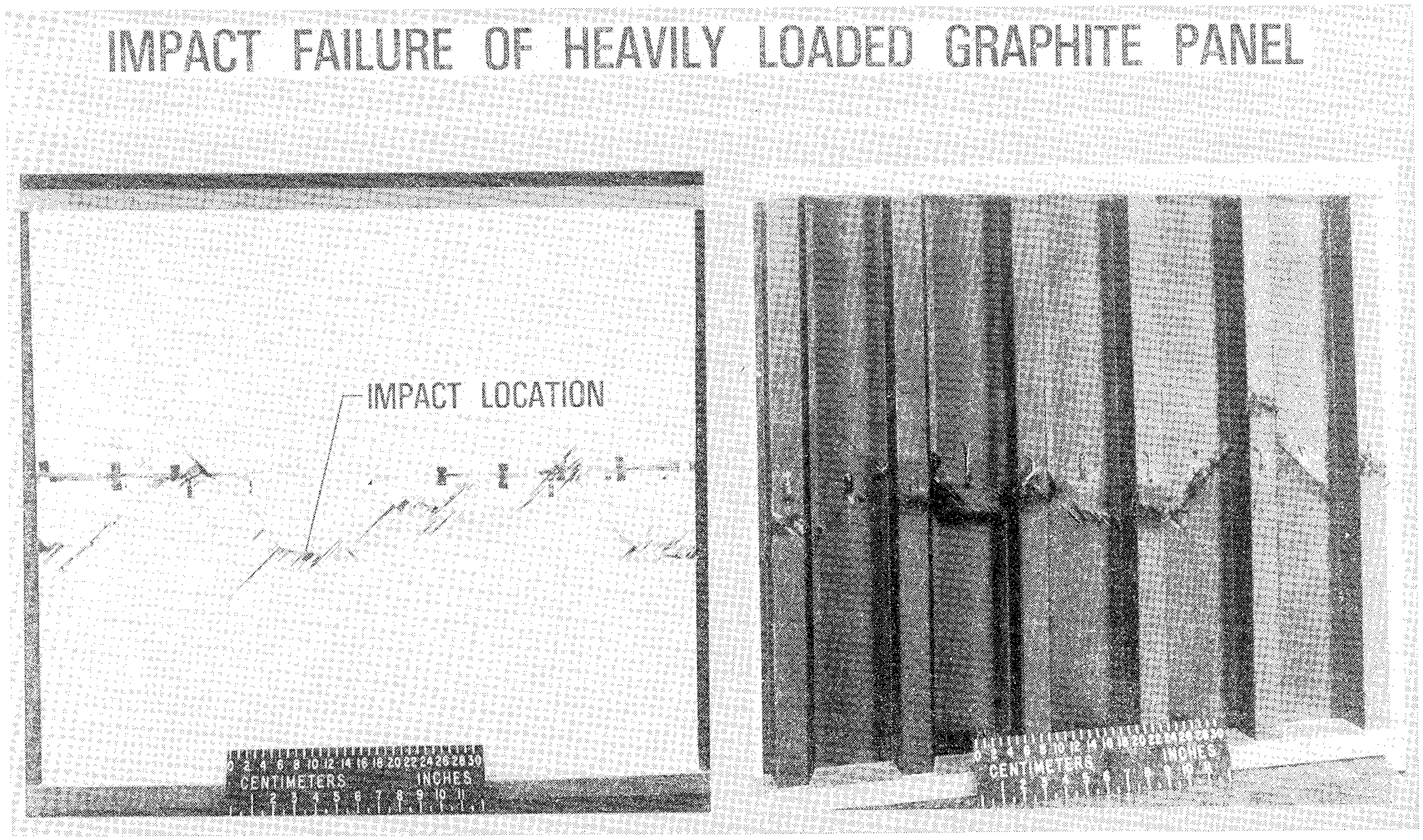
IMPACT FAILURE OF HEAVILY LOADED GRAPHITE PANEL
IMPACT LOCATION
CENTIMETERS
INCHES
CENTIMETERS
INCHES

Figure 2.

IMPACT FAILURE OF HEAVILY LOADED GRAPHITE PANEL

(Figure 2)

Failures similar to those due to impact in rectangular flat plates have also been observed in stiffened compression panels. A typical panel 5 stiffeners wide is shown in the figure after being damaged by impact while loaded at an applied strain of 0.0038. This panel was designed to have minimum-mass subject to buckling and strength constraints. The design load was 1.88 MN/m at a strain of 0.0080. Control panels were tested in compression and met the design conditions. The panels had regions of high axial stiffness in the skin below the hat and regions of low axial stiffness composed of $\pm 45^{\circ}$ material between hats. The panel shown in the figure was damaged by impact in the region of high axial stiffness below one of the two center hat sections as indicated in the figure. The failure propagated laterally to the panel edges at the instant of impact. A number of panels tested have exhibited similar failures including some which had boron-epoxy in the region of the stiffeners. The results of this investigation are reported in reference 4.

DAMAGE PROPAGATION-DELAMINATION

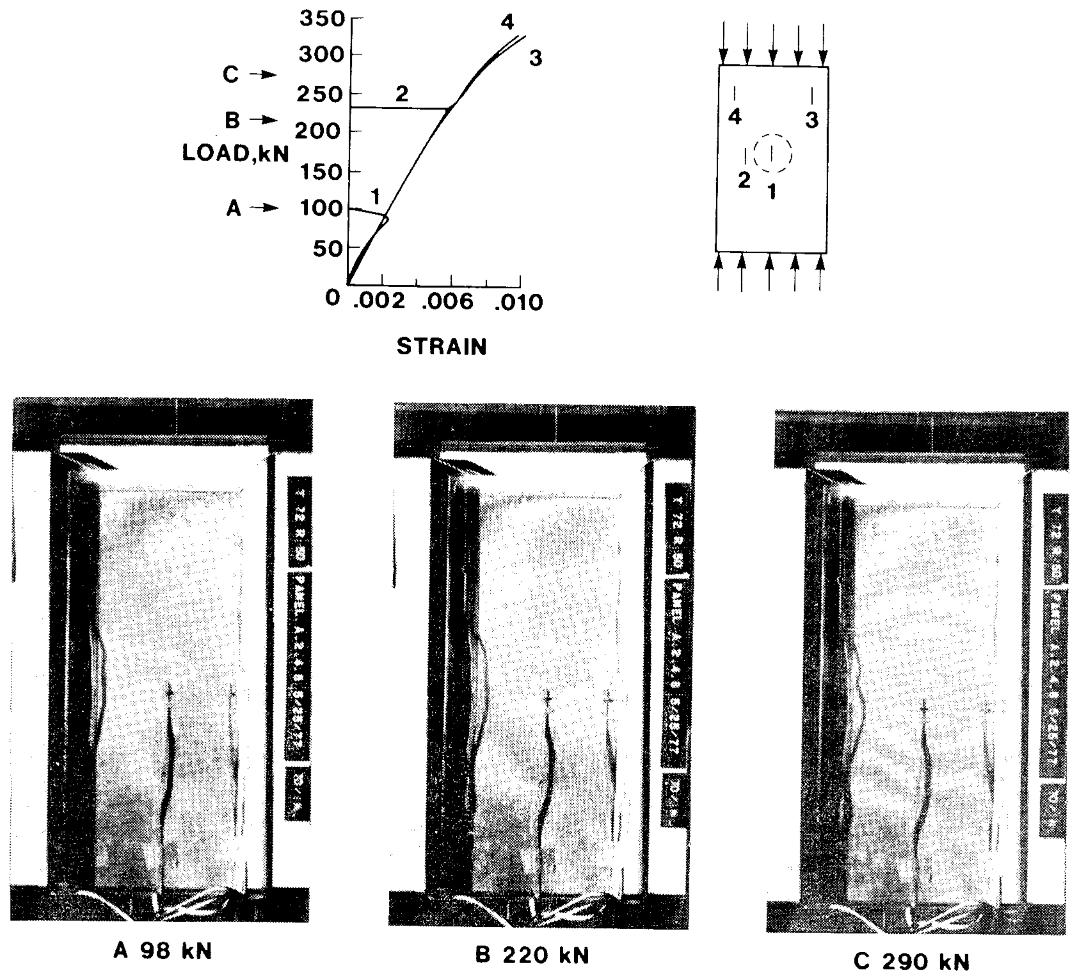

Figure 3.

FAILURE PROPAGATION - DELAMINATION

(Figure 3)

On examination, the cross sections of specimens damaged by impact have been observed to contain fractures at ply interfaces. These fractures are most pronounced at interfaces where there is a major change in the angle between plies, e.g. between 0° and 45° plies or 0° and 90° plies. When panels with interface fractures (delamination) are loaded, the plies near the surface can buckle locally. This local buckling creates high internal transverse tension or peel stresses causing the delamination to propagate.

Several panels were fabricated with plastic inserts between plies to study delamination propagation. The results of a typical test panel are shown in the figure. This specimen is a 48 ply quasi-isotropic test panel with 2.5 cm dia. plastic inserts located at 2 plies and at 6 plies beneath the surface (± 45 I/0/90/∓ 45 I/0...). Strain gages located on the panel were used to monitor the panel response and photographs of moire fringe patterns representing out-of-plane displacements were taken during the test. It is apparent that the plies near the surface buckled locally at a load near 80 kN. As the load increases, the local out-of-plane deformation propagates laterally across the specimen, significantly enlarging the initial delamination. This reduces the bending stiffness of the laminate near the panel center and results in general panel instability at a load of about 240 kN. Two general observations noted from this and similar test panels are: (1) In panels where the inserts were small or deep within the laminate and local buckling did not occur, the strength and panel stability were unaffected by the inserts. (2) Local buckling due to the inserts always propagated laterally across the specimen regardless of the insert location.

DAMAGE PROPAGATION-TRANSVERSE SHEAR

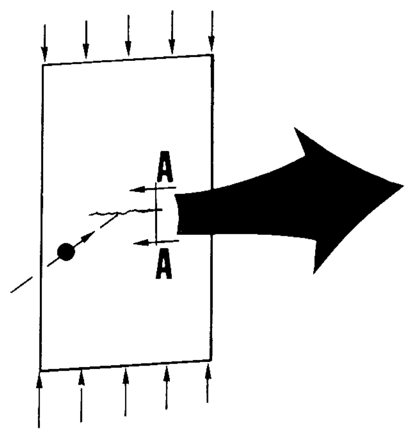

48 PLY LAMINATE
$(\pm 45/0_2/\pm 45/0_2/\pm 45/0/90)_{2S}$

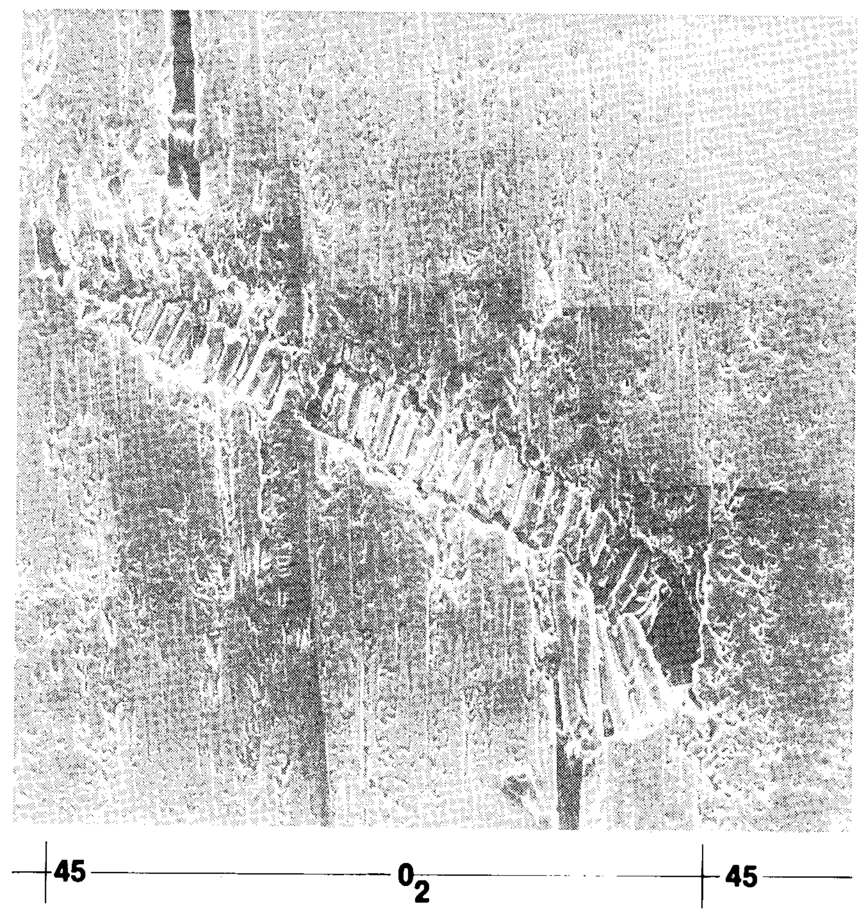

SECTION AA-TYPICAL 0_2 REGION

Figure 4.

DAMAGE PROPAGATION - TRANSVERSE SHEAR

(Figure 4)

Several specimens sectioned longitudinally through the failure zone were observed to have failed by transverse shearing of the high stiffness 0° fibers. A photograph of one such specimen is shown in the figure. The section was cut from a 48 ply orthotropic panel which was damaged by impact while subjected to an applied compression load. The panel failed locally near the impact site. The section shown in the photograph is from the region near the end of the failure. The shear failure in the 0° plies is typical of those through the thickness of the specimen. The length of most of the crippled fibers is approximately 4 fiber diameters. It is apparent from the photograph that the shear failure displaces the 0° fibers in such a manner that a delamination is initiated near the orientation interface.

EFFECT OF DESIGN STRAIN ON TYPICAL WING PANEL STRUCTURAL EFFICIENCY

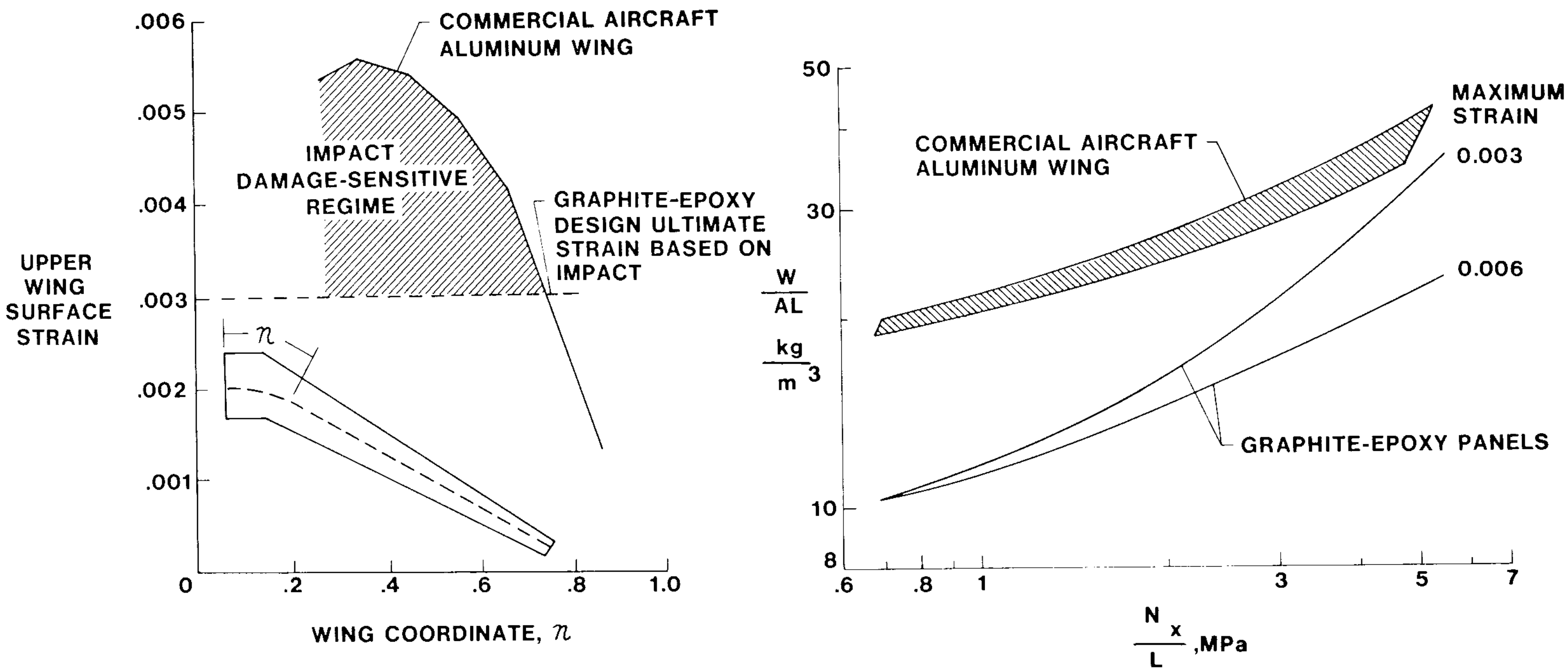

Figure 5.

EFFECT OF DESIGN STRAIN ON TYPICAL WING PANEL STRUCTURAL EFFICIENCY

(Figure 5)

Results such as those shown in figure 1 indicate that considerable reductions in strength occur in graphite-epoxy laminates due to defects introduced by low-velocity impact. Although composite structures have been introduced into commercial service in secondary structural components, these articles are designed by stiffness requirements and operate at low strains where impact damage does not degrade structural performance. However, heavily loaded primary structures such as wing panels are designed by material strength and current aluminum components typically have design ultimate strains well above the impact-sensitive strain levels observed for composites. For example, a typical distribution of the design ultimate compression strain in upper wing surface panels is shown in the figure as a function of the wing semi-span. If, based on impact test results, a design ultimate strain of .003 is considered, it is apparent that most of the wing upper surface lies in a design strain region that is sensitive to impact damage.

To assess the effect of design strain on panel structural efficiency, several strain levels have been evaluated and the results are presented in reference 5. Selected results are shown in the figure. The ordinate is the mass W of an optimized design compression panel divided by the cross-sectional area A and the panel length L. The abscissa is the design compression load per unit width N_x divided by the panel length L. Two curves shown on the figure indicate the mass variation of graphite-epoxy panels with maximum design strains of 0.0030 and 0.0060. The lower value corresponds to a value which might be inferred from the results of impact damage studies and the larger value is a maximum based on matching the bending and torsional stiffness of an existing aluminum wing. These results indicate that graphite-epoxy panels designed for a maximum strain of 0.0060 have a potential mass savings of 40 to 50 percent when compared to current aluminum designs represented by the cross-hatched region. The mass savings potential is considerably reduced for heavily loaded designs if the impact sensitivity is accounted for.

DAMAGE TOLERANCE CONCEPTS BEING INVESTIGATED

MATERIALS

- GRAPHITE FABRIC
- RESIN MODIFICATIONS
- TRANSVERSE REINFORCEMENT

STRUCTURAL CONFIGURATIONS

- DISCRETE STIFFNESS DESIGN
- MECHANICAL FASTENING

Figure 6.

DAMAGE TOLERANCE CONCEPTS BEING INVESTIGATED

(Figure 6)

The preceding results suggest that a substantial need exists for improvements in damage tolerance of heavily loaded composite compression structures. Research on this subject is being pursued in two major thrusts in the Structural Mechanics Division at the Langley Research Center. These thrusts are shown on the figure as (1) Materials and (2) Structural Configurations. The thrust in the materials area is aimed at understanding the damage mechanisms so that the local damage created by impact will be reduced and the failure threshold of the test laminates can be increased. Physical test variables such as peel strength, transverse tensile strength and resin ductility of commercially available resin systems are being evaluated to permit correlation of neat resin properties with composite damage tolerance. The thrust in the area of structural configurations is aimed toward arresting or limiting the growth of local impact induced damage. This involves examining techniques for arresting propagating fractures and redistributing inplane and imposed bending loads. The remainder of the presentation is devoted to discussing some preliminary results from these damage tolerance concepts.

MATERIALS-GRAPHITE FABRIC

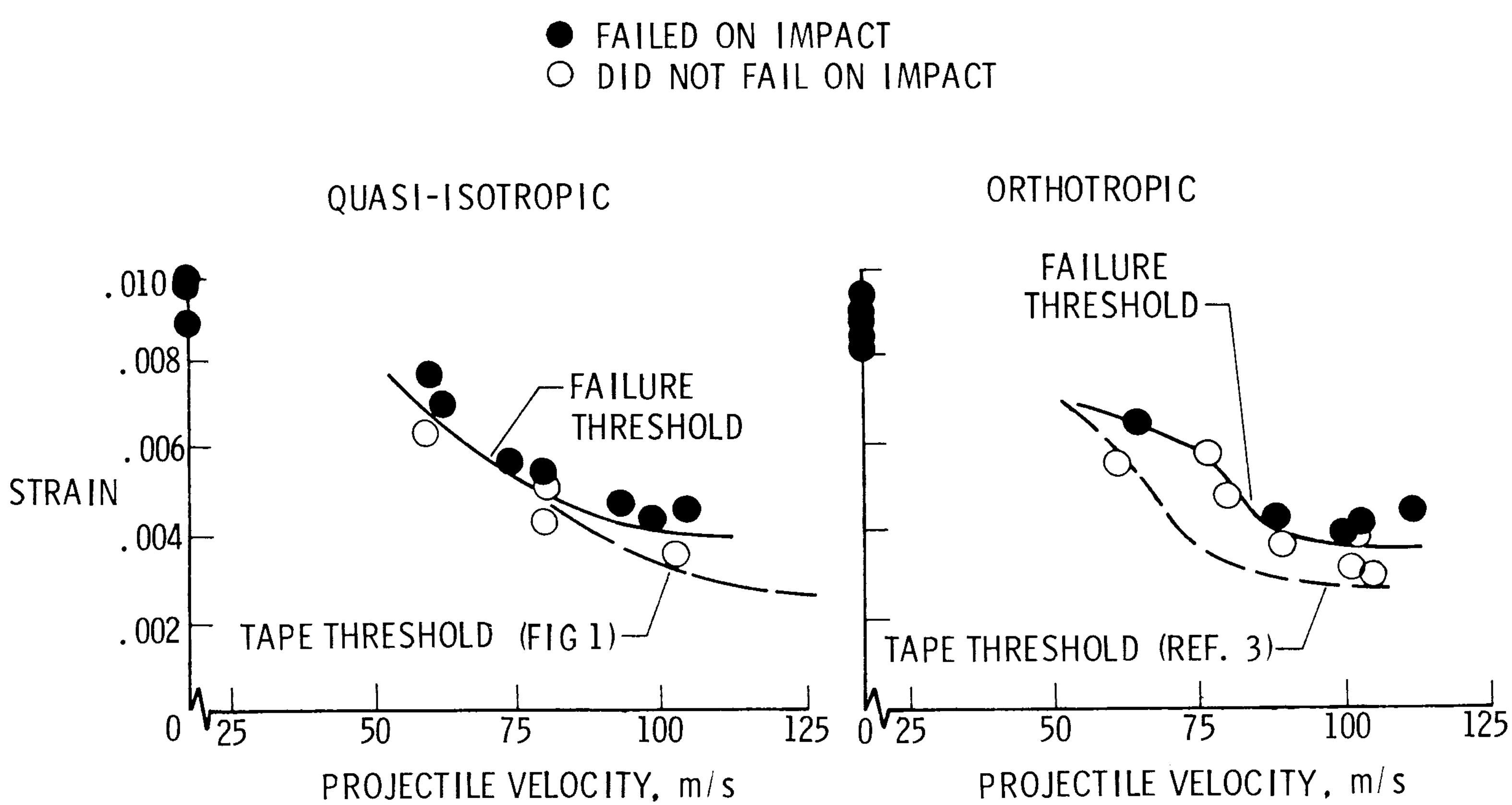

Figure 7.

MATERIALS - GRAPHITE FABRIC

(Figure 7)

Results of impact-initiated failure in two compression loaded test laminates fabricated from woven graphite fabric are shown in the figure. The ordinates are the applied axial strain in the specimen due to applied compression load when impact occurred and the abscissas are the projectile impact velocity. These data were obtained using a similar test specimen and impact projectile as that described in Figure 1. It is apparent from this data that improvements of 25-30 percent in the failure threshold at a projectile velocity of approximately 100 m/s can be obtained using graphite fabric material as opposed to unidirectional tape.

It was noted earlier that failures in the laminate interior due to impact were most pronounced when there is a major change in the angle between plies such as 0^o and 90^o laminas. The cross plies of woven graphite material are mechanically linked together thereby reducing the number of interfaces available to participate in delamination. Also, the plies of graphite fabric are generally thicker than the plies of tape, therefore, a higher load (strain) is required to cause the delamination to buckle locally.

MATERIALS-RESIN MODIFICATIONS

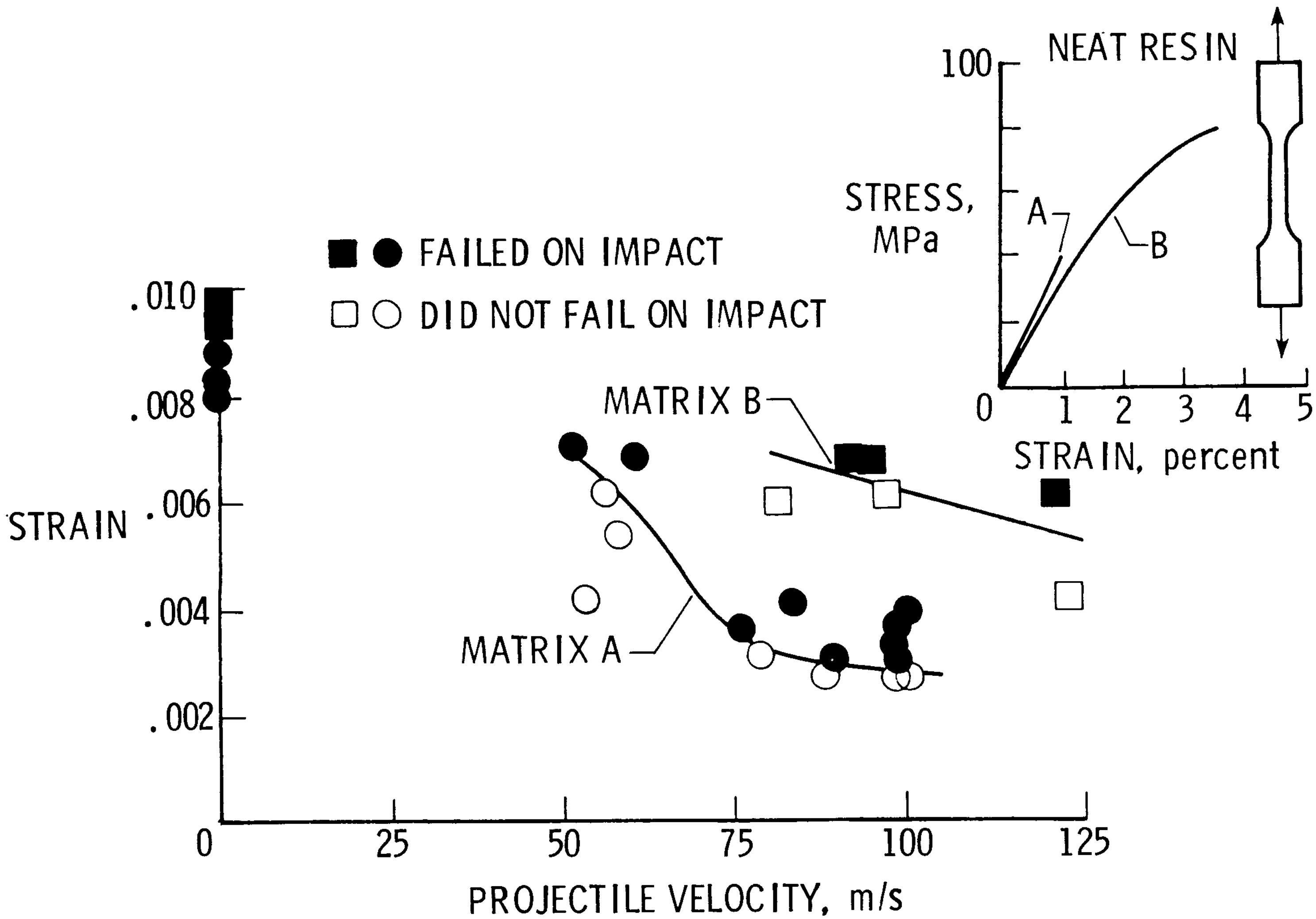

Figure 8.

MATERIALS - RESIN MODIFICATIONS

(Figure 8)

The propagation of failure through delamination discussed in an earlier figure suggests that the matrix material may play an important role in the damage tolerance of composites. Preliminary studies have been conducted to evaluate the potential of the matrix in improving the compression strength of panels damaged by impact and some results are shown in the figure. The ordinate and abscissa shown on the plot are similar to those of Figures 1 and 7. The data shown were obtained using test panels and impact conditions which were also similar to those of the earlier figures. A 48 ply orthotropic laminate with the following orientation, $(\pm 45/0_2/\pm 45/0_2/\pm 45/0/90)_{2s}$, was used to make the test specimens for both matrix systems A and B. The same high strength graphite fiber was used with both matrices so that a direct comparison could be made. The test results show that the failure threshold strain is substantially higher for the laminate with the matrix B material especially at the higher impact velocities. For example, the failure threshold strain for a 100 m/s impact speed is about 0.0028 for matrix A specimens compared to approximately 0.0062 for the matrix B specimens.

Although it is unclear as to what material property of the matrix accounts for this difference in impact behavior, an examination of the neat resin tensile properties (see insert on figure) shows clearly that the resins perform substantially differently. The ultimate strength of matrix B is approximately twice that of matrix A and the strain is approximately four times as large. Additional insight into the behavior of these matrices may be obtained from the next figure.

MATERIALS - RESIN MODIFICATIONS

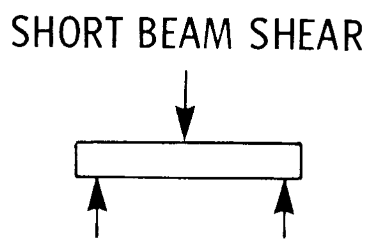

MATRIX	SHEAR STRENGTH kN/cm	FRACTURE ENERGY kJ/ m^2
A	11.2	0.21
B	9.1	0.94

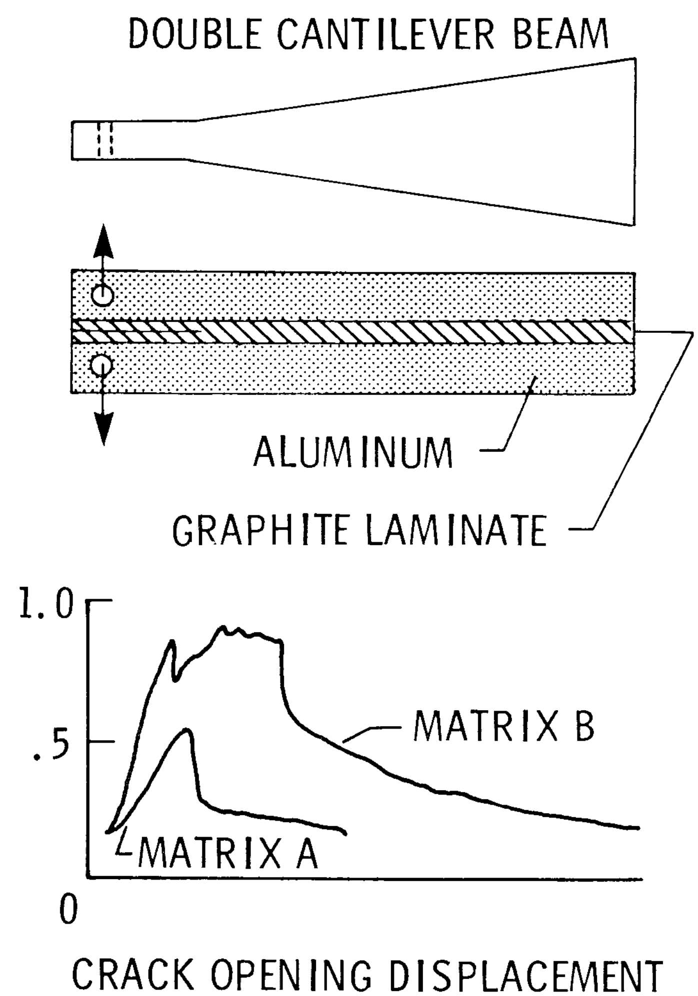

Figure 9.

MATERIALS - RESIN MODIFICATIONS

(Figure 9)

Tests on composite laminates with epoxy matrices A and B have been performed to examine material properties that may be associated with damage tolerance. The results of tests performed under NASA contract and reported in reference 6 are shown on the figure. These are the standard short beam shear test and a width tapered double cantilever beam test. The double cantilever beam tests are similar to those reported by Bascom, et al., in reference 7; however, the laminate was bonded to an aluminum bar instead of testing an all-composite beam. As can be seen in the figure, the maximum crack opening load of the matrix B material is nearly twice that of A and the fracture energy is over four times as great. The low short beam shear strength of the matrix B material was somewhat surprising. Impact creates some out-of-plane deformation (see ref. 3) and it was anticipated that a high interlaminar shear strength might correlate directly with damage tolerance.

MATERIALS-TRANSVERSE REINFORCEMENT

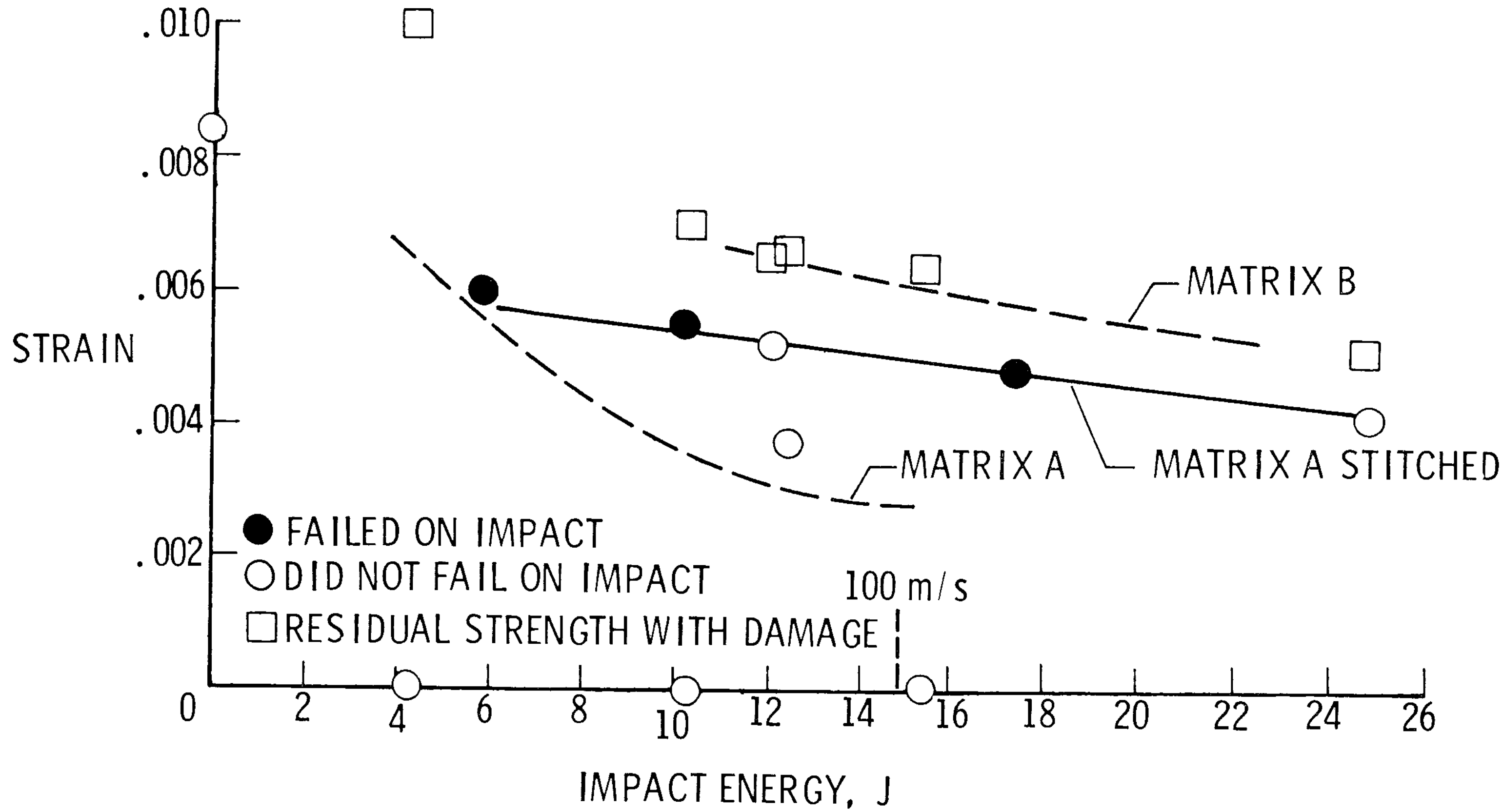

Figure 10.

MATERIALS - TRANSVERSE REINFORCEMENT

(Figure 10)

In addition to alternate matrices, other methods for improving damage tolerance of compression loaded composite panels are being examined. Recent tests have been conducted to evaluate the effect of stitching in suppressing interply delaminations created by impact. Results of these tests are shown in the accompanying graph. The test conditions and projectile are similar to those discussed on previous figures. The test specimens were 48 ply orthotropic panels fabricated from matrix A graphite-epoxy prepreg tape. The specimens were stitched in the impact region over a 0.64 cm square grid using a high breaking strength thread material. Also shown on the figure as dashed lines are the failure threshold curves from Figure 8 for panels without stitching fabricated from both matrices A and B. Stitching significantly increases the failure threshold of panels fabricated from the matrix A material. The residual strength of stitched panels which did not fail on impact, as indicated by the square symbol, is the same as the failure threshold of the matrix B panels.

Although it is difficult to determine the exact failure mode from post test examination of a failed specimen, the unstitched panels fabricated from matrix A probably fail primarily by delamination whereas those fabricated from matrix B fail by transverse shear. Matrix A is a brittle material with a low fracture energy, and delaminations initiated by impact are easily propagated. Stitching suppresses delamination by mechanically locking the laminate together, thereby restricting the failure to a higher energy transverse shear mode. The fracture energy of matrix B is apparently adequate to suppress delamination, and panels fabricated with this material fail by transverse shear, a mode related to the shear modulus of the matrix. Stitched panels similar to those shown in the figure fabricated from the matrix B material were tested and had the same threshold curve as panels without stitching. Therefore, without improvements in the matrix shear modulus, the matrix B curve probably represents the maximum compression strain capability that can be achieved with impact damage.

STRUCTURAL CONFIGURATIONS-DISCRETE STIFFNESS DESIGN

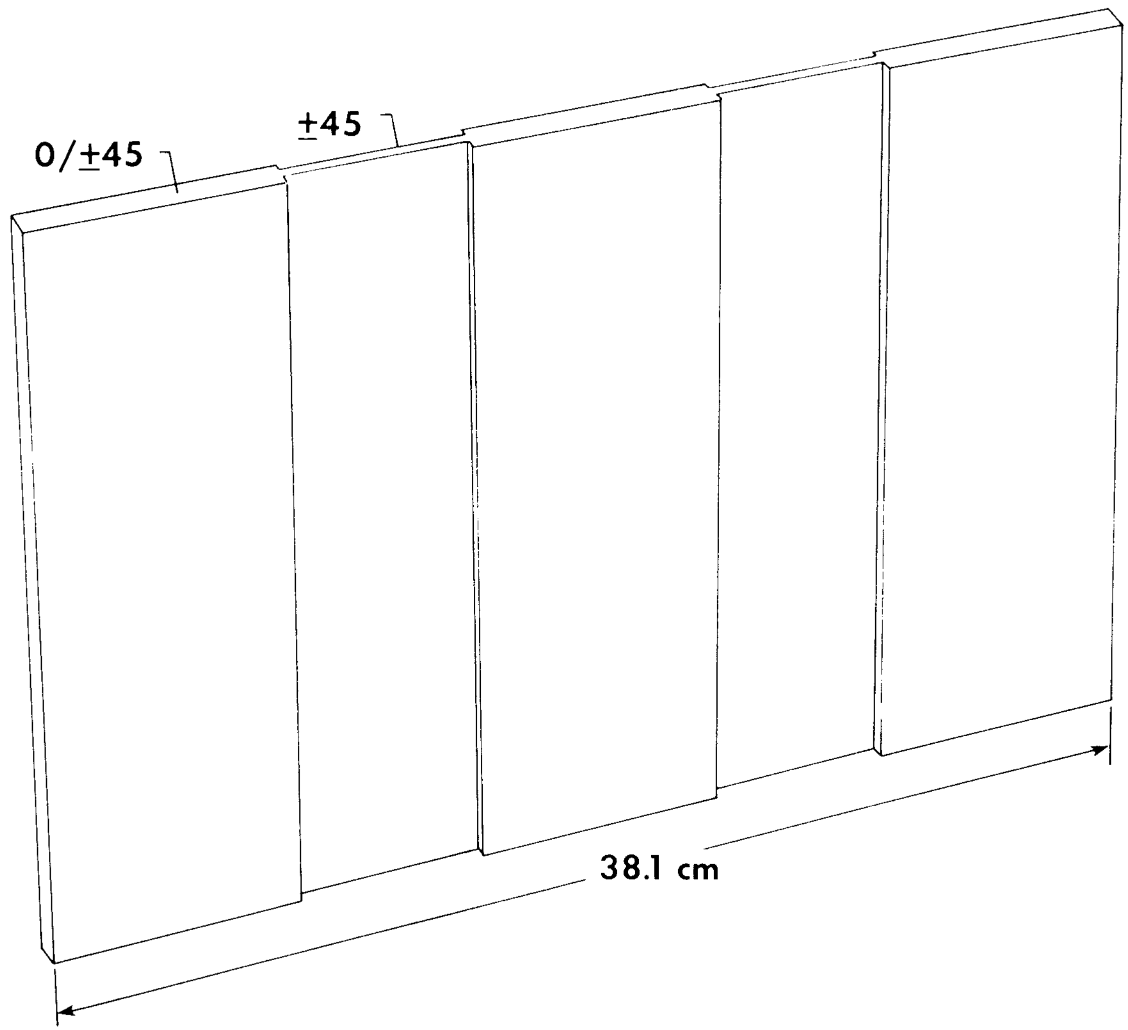

Figure 11.

STRUCTURAL CONFIGURATIONS - DISCRETE STIFFNESS DESIGN

(Figure 11)

One method to arrest damage propagation that is being investigated is to lump or isolate zones of a panel into regions of high and low axial stiffness. Regions of low axial stiffness (only $\pm 45^\circ$ plies) have been shown by tests to be tolerant to impacts (ref. 4). However, these tests were performed on hat-stiffened panels fabricated from the matrix A material and the low stiffness region would not arrest delamination damage that propagated into the region from an adjacent high axial stiffness region. Since matrix B has a higher fracture energy, several flat panels were fabricated using the matrix B material to determine if zones of discrete stiffness would be effective in arresting transverse shear in the high stiffness 0° plies. The panels are similar to the one shown by the sketch in the figure. They were designed to have the same amount of 0°, 45° and 90° material in the specimen as the orthotropic laminate for which data was shown in Figure 8. The test panels were 38 cm wide by 25.4 cm long. Some preliminary results from the panel tests are shown in Figure 12.

STRUCTURAL CONFIGURATIONS-DISCRETE STIFFNESS DESIGN

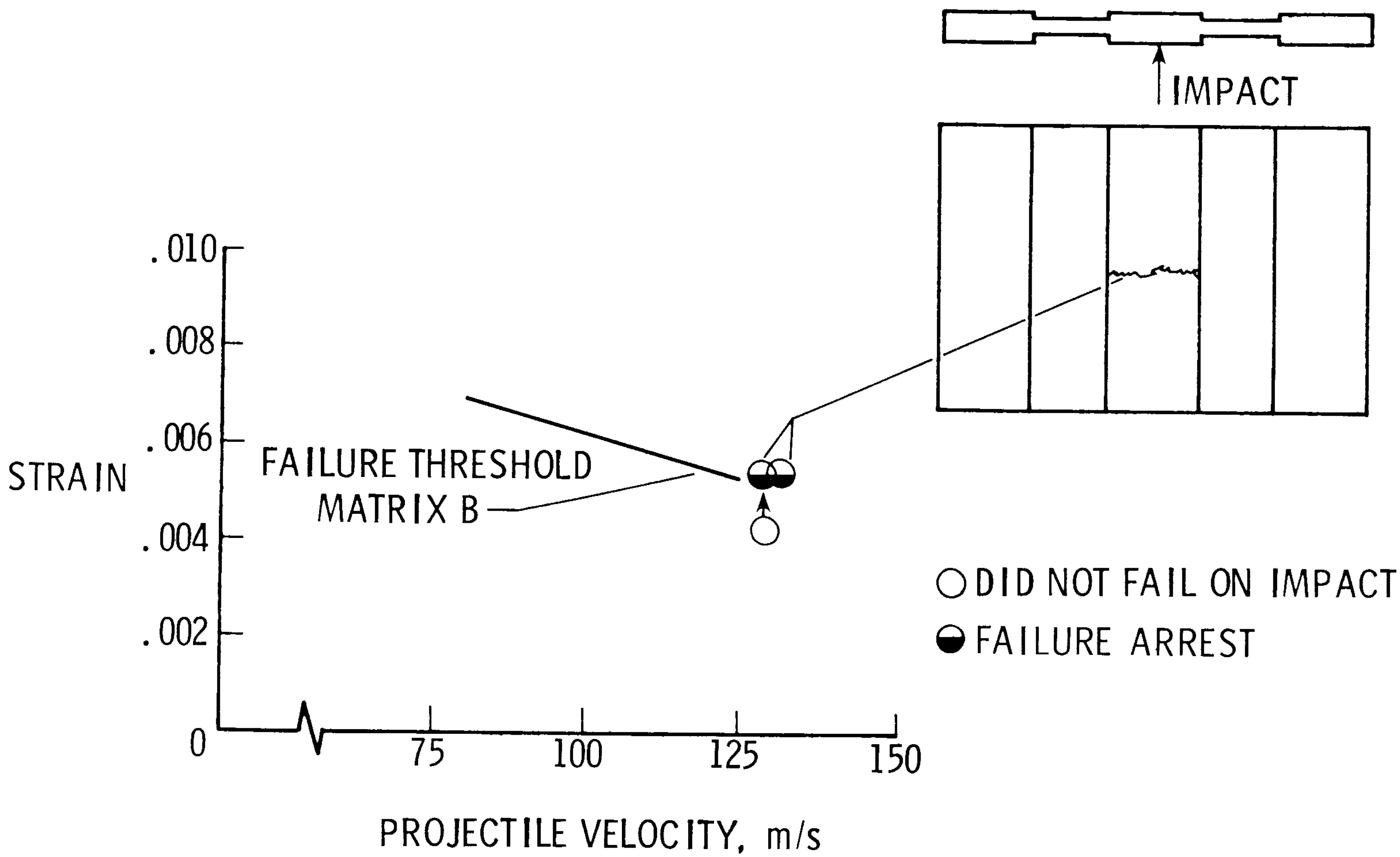

Figure 12.

STRUCTURAL CONFIGURATION - DISCRETE STIFFNESS DESIGN

(Preliminary Test Results)

(Figure 12)

Test results for two discrete stiffness panels are shown on the plot of Figure 12. Also shown on the plot is the failure threshold curve for the matrix B material from Figure 8. One test panel was damaged while loaded to an applied strain of 0.0044. No propagation occurred at that load and the panel was subsequently loaded to a strain of about 0.0055. At that strain the damage inflicted by the impact propagated in the high-axial-stiffness region in the center of the panel and arrested at the low-axial-stiffness region. The second test panel was damaged while loaded at an applied strain of about 0.0054. Upon impact, the high-axial-stiffness region failed and the damage arrested. The average strain recorded in each panel after damage arrest was about 0.0061. Although these tests were of a preliminary nature, they do indicate that with careful attention to configuration, damage can be arrested even at relatively high applied strains.

STRUCTURAL CONFIGURATIONS-MECHANICAL FASTENING

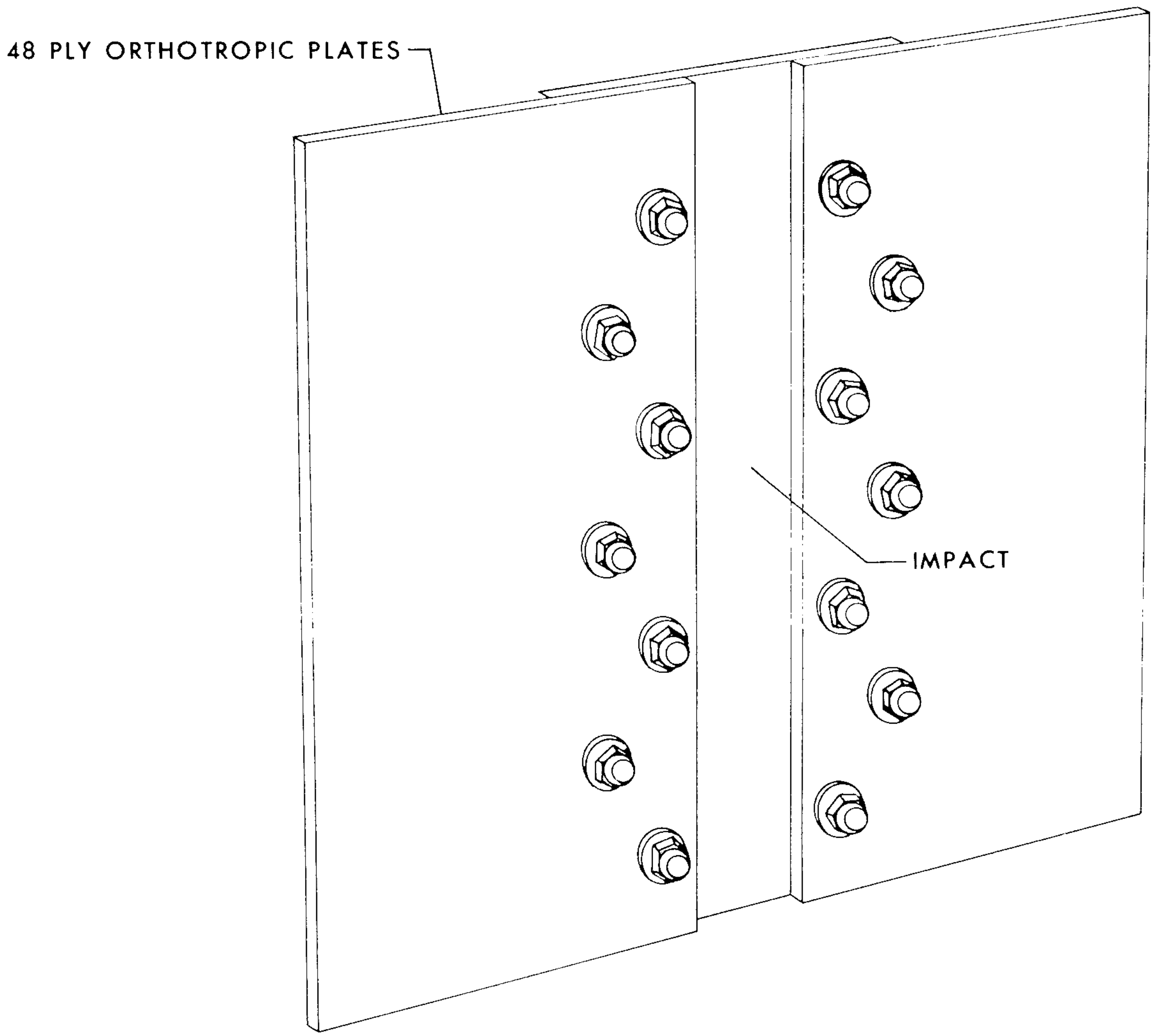

Figure 13.

STRUCTURAL CONFIGURATIONS - MECHANICAL FASTENING

(Figure 13)

A second structural configuration that has been investigated to arrest damage propagation is to mechanically fasten sections or panels together. Two 48 ply orthotropic panels such as those shown in the figure were fabricated from the matrix A material. The sections were fastened together with high strength aircraft bolts. The specimens were about 25 cm long by 29 cm wide. Each specimen was damaged by impact in the center panel while subjected to an applied load well above the laminate failure threshold. Some test results are shown in Figure 14.

STRUCTURAL CONFIGURATIONS-MECHANICAL FASTENING

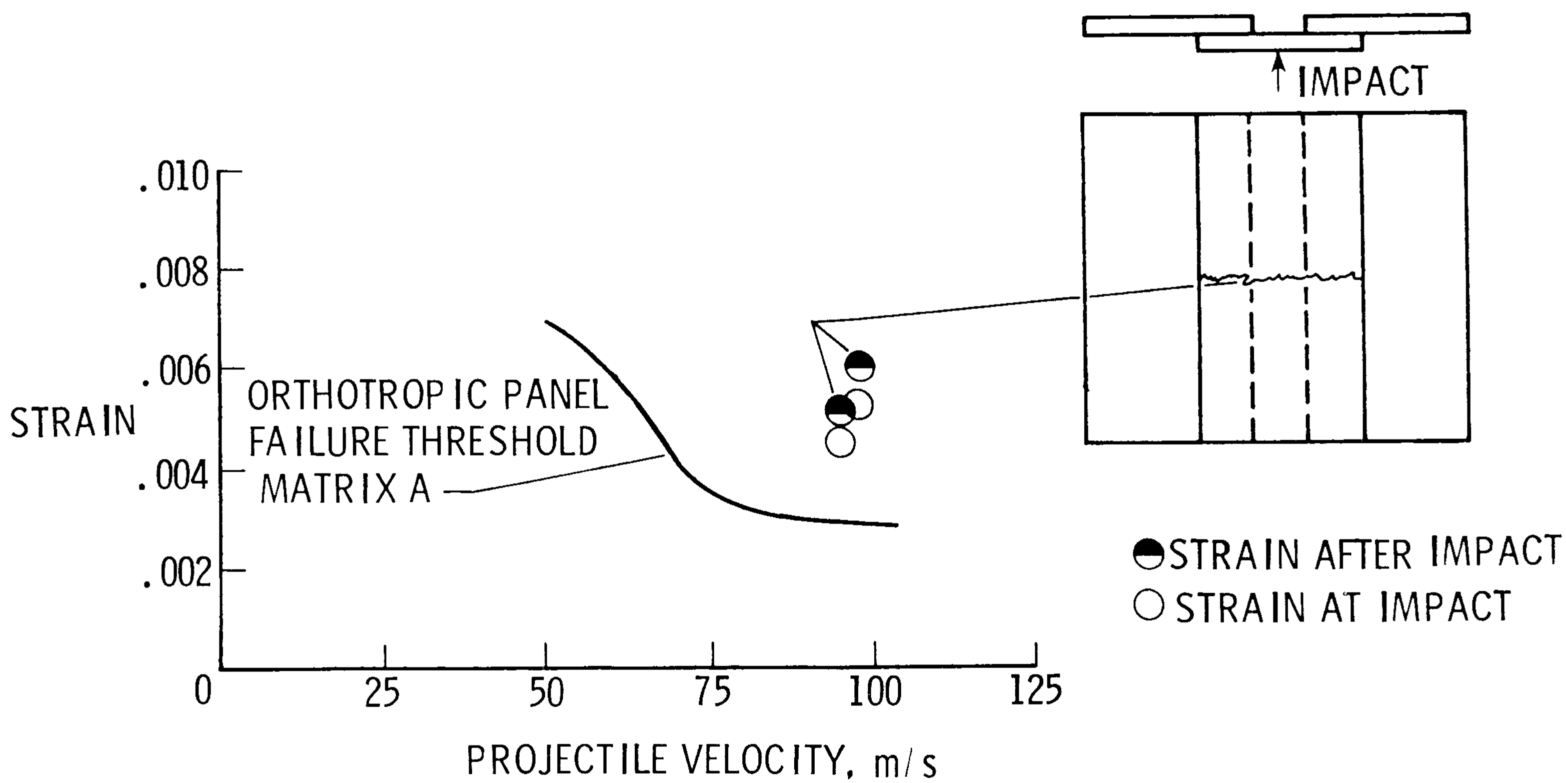

Figure 14.

STRUCTURAL CONFIGURATIONS - MECHANICAL FASTENING

(Preliminary Test Results)

(Figure 14)

Test results for the two mechanically fastened specimens are shown on the plot of the figure. Also shown for comparison is the failure threshold curve for the matrix A orthotropic laminate. The applied strain at impact is indicated by the open circle. Each specimen was damaged at an applied strain well above the failure threshold level to ensure that damage would propagate. The damage in each specimen was confined to the center region and the average strain after impact is indicated by the partially filled circle. These tests indicate an additional mechanism that may be used to arrest damage or keep it confined to a controlled region. Additional tests of longer specimens will be necessary to fully evaluate the concept and determine how load will be redistributed in specimens of this type.

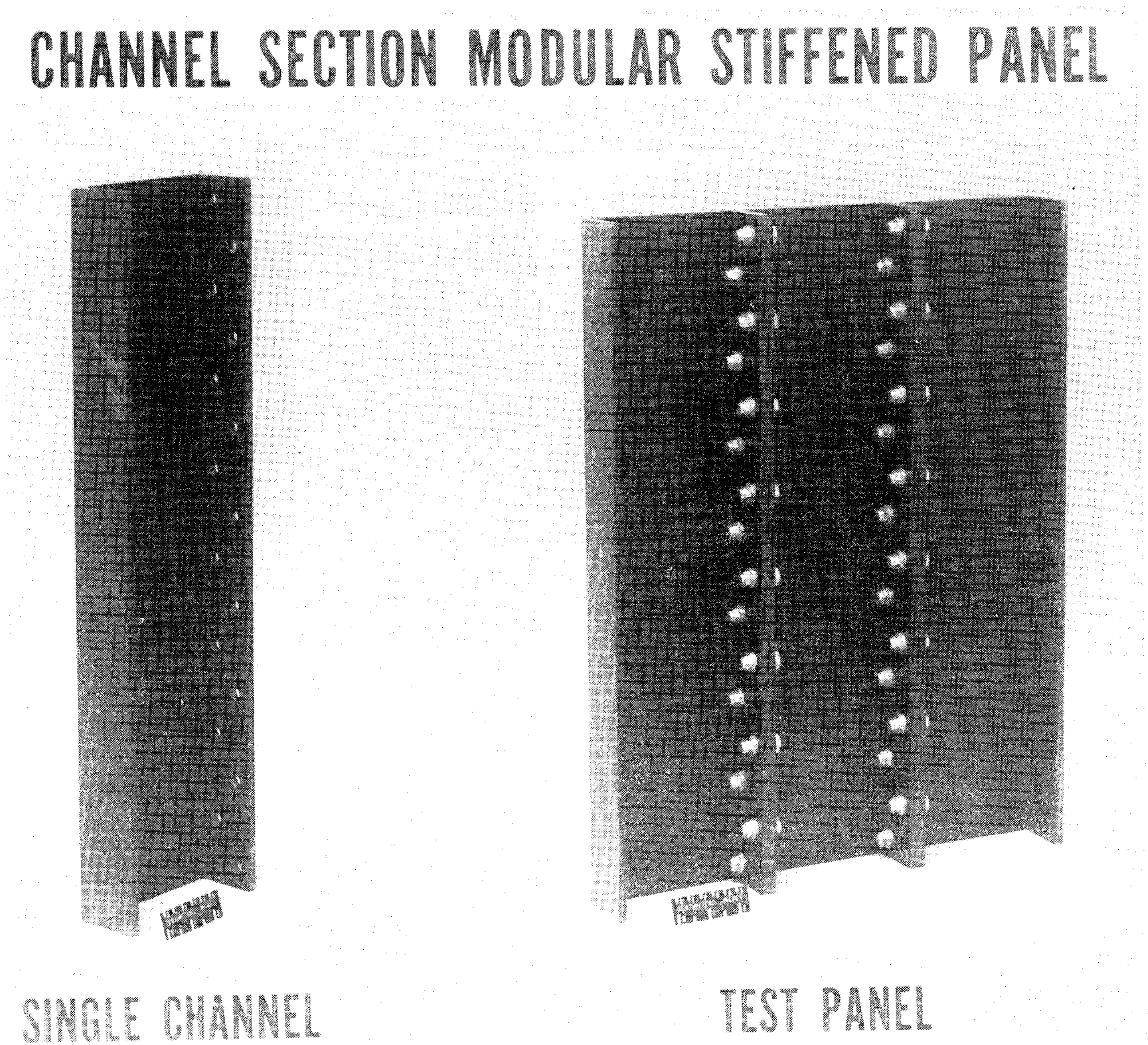
CHANNEL SECTION MODULAR STIFFENED PANEL
SINGLE CHANNEL
TEST PANEL

Figure 15.

CHANNEL SECTION MODULAR STIFFENED PANEL

(Figure 15)

One variation of the mechanically fastened concept for application to stiffened panels is shown in the figure. The single channel section shown on the left could be pultruded and several sections fastened together to form a blade stiffened panel. This concept, therefore, may have potential as a low cost fabrication technique. Preliminary results have been obtained on two test specimens such as the one shown at the right and the results were favorable; however, additional study will be necessary to fully evaluate the concept.

STRUCTURAL CONFIGURATIONS-BONDED JOINT

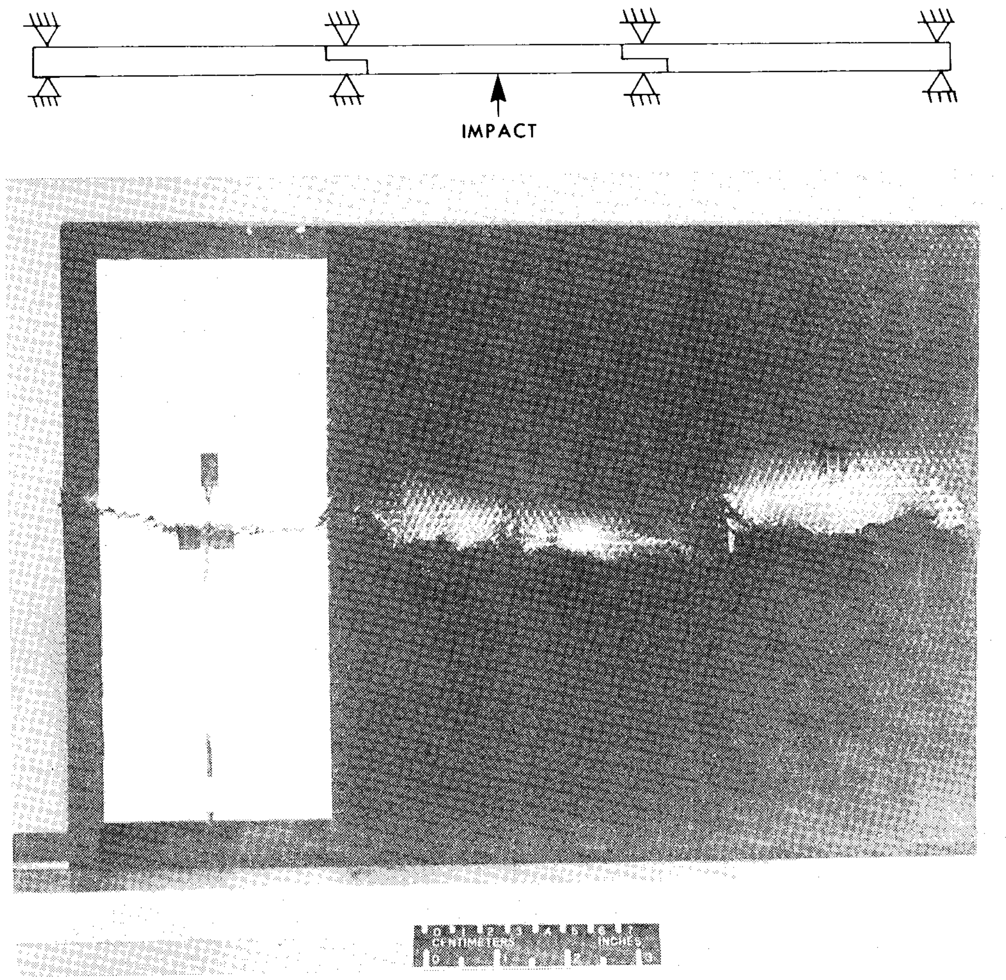

Figure 16.

STRUCTURAL CONFIGURATIONS - BONDED JOINT

(Figure 16)

A test program was conducted to study the effectiveness of bonded joints in arresting compression failure. The intent of these tests was to demonstrate that a discontinuity in the graphite plies would arrest delamination. An example of a test panel with bonded joints is shown in the figure. These panels were fabricated by machining three plates as indicated for the entire plate length and bonding them together with a flexible room temperature cure epoxy adhesive.

Two specimens were fabricated and tested. One was damaged by impact and tested to determine the residual strength and the second was damaged while loaded to an applied strain above the failure threshold. The bonded joints were not effective in containing damage and both panels failed across the specimen similar to the one shown in the figure. Examination of the failed panel indicated that there was some delamination; however, the principal failure propagation mode was by transverse shear which could not be arrested by the joint. This illustrates that damage tolerant structures must incorporate aspects that will be effective in suppressing both compression failure propagation modes.

DESIGN STRAIN LEVELS FOR COMPOSITE COMPRESSION STRUCTURES

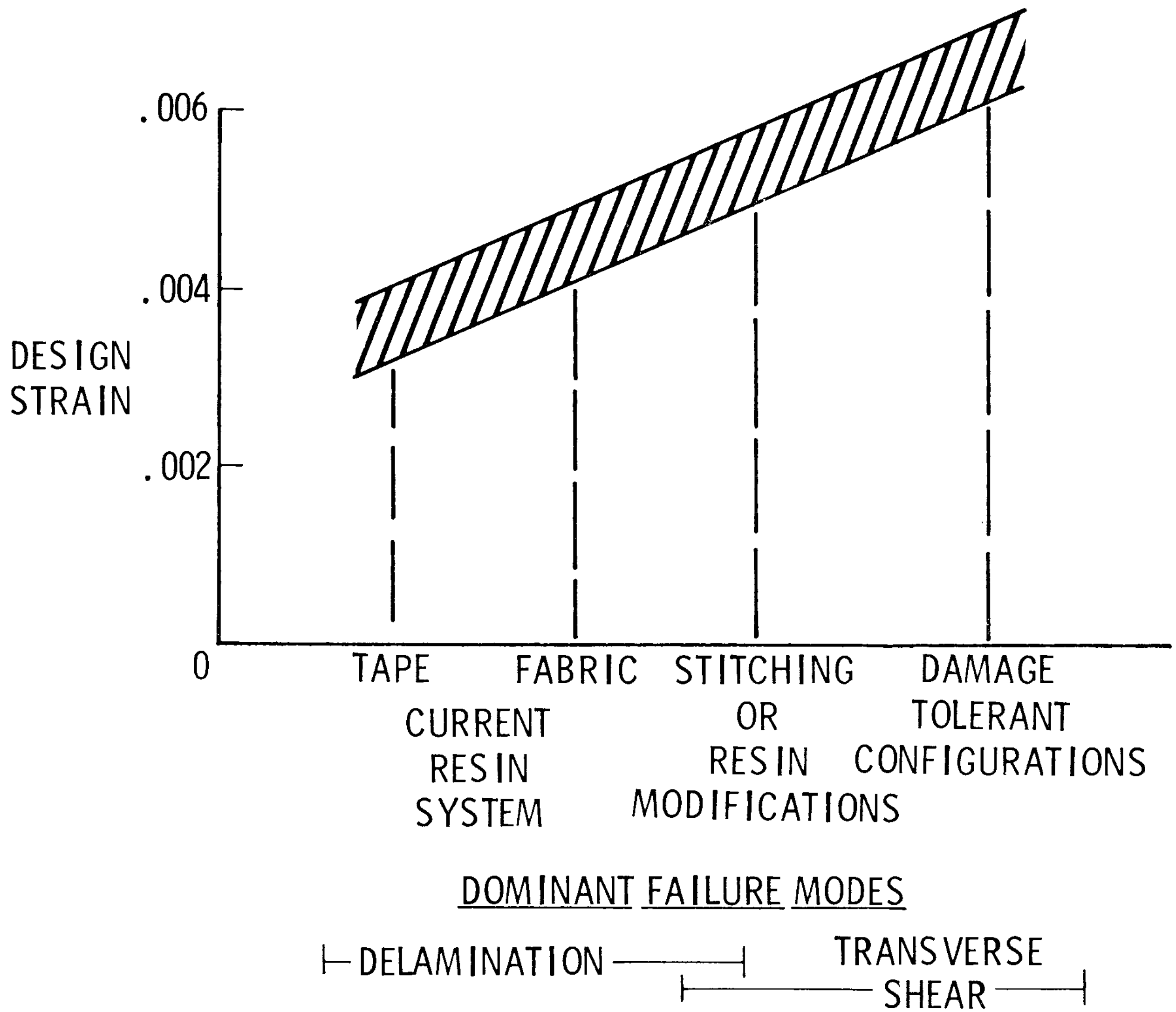

Figure 17.

DESIGN STRAIN LEVELS FOR COMPOSITE COMPRESSION STRUCTURES

(Figure 17)

The graph shown in the figure summarizes the current design strain capability for strength critical damage tolerant graphite-epoxy compression structures. Current brittle resin systems should be limited to strains between 0.0030 and 0.0040 for laminates fabricated from unidirectional tape. Test results indicate that modest increases in design strain can be achieved by using woven fabric in place of unidirectional tape. Suppression of delamination by either stitching or resin modifications to increase the fracture energy can produce significant improvements over current unstitched brittle epoxy systems. Since major increases in epoxy resin shear modulus will be required to suppress transverse shear failures, additional increases in design strain capability will probably result from structural design configurations. Through the proper combination of materials and structural design, strength critical composite structures that operate at high design ultimate strains can be achieved.

REFERENCES

1. Rhodes, M. D.: Impact Tests on Fibrous Composite Sandwich Structures. NASA TM-78719, 1978.

2. Gause, L. W., and Huang, S. L.: Compression Fatigue of Impact Damaged Graphite Epoxy Sandwich Beams. NADC-77305-60, April 1978.

3. Rhodes, M. D., Williams, J. G., and Starnes, J. H., Jr.: Low-Velocity Impact in Graphite-Fiber Reinforced Epoxy Laminates. Paper presented at the 34th Annual Conference Reinforced Plastics/Composite Institute, The Society of the Plastics Industry, Inc. (New Orleans, Louisiana), January 29 - February 2, 1979.

4. Rhodes, M. D., Williams, J. G., and Starnes, J. H., Jr.: Effect of Impact Damage on the Compression Strength of Filamentary-Composite Hat-Stiffened Panels. Paper presented at the 23rd SAMPE National Symposium and Exhibition (Anaheim, California), May 2-4, 1978.

5. Williams, J. G., Anderson, M. S., Rhodes, M. D., Starnes, J. H., Jr., and Stroud, W. J.: Recent Developments in the Design, Testing and Impact-Damage Tolerance of Stiffened Composite Panels. NASA TM-80077, 1979.

6. Byers, B. A.: Behavior of Damaged Graphite/Epoxy Laminates Under Compression Loading. NASA CR-159293, 1980.

7. Bascom, W. D., Bitner, J. L., Moulton, R. J., and Siebert, A. R.: The Interlaminar Fracture of Organic-Matrix, Woven Reinforcement Composites. Composites, pp. 9-18, January 1980.

HIGH TEMPERATURE RESIN MATRIX COMPOSITES FOR AEROSPACE STRUCTURES

John G. Davis, Jr.

ABSTRACT

Graphite/polyimide composite materials (Gr/PI) have been developed to the stage that application to a number of aerospace structures offers the potential for significant mass reduction and improved performance. NASA Langley Research Center has sponsored extensive effort in development of Gr/PI directed toward materials and structural concepts applicable to advanced space transportation systems and supersonic cruise aircraft. Research tasks include screening composites and adhesives, developing fabrication procedures and specifications, developing design allowables test methods and data, and design and test of structural elements and components.

Fabrication studies indicate that two polyimide resin matrix materials, LARC-160 and PMR-15, have the potential for near term applications. Processing and quality assurance specifications for Celion®/LARC-160 and Celion/PMR-15 prepreg are approaching maturity. High pressure liquid chromatography is an essential part of the quality assurance specifications. The capability to fabricate and nondestructively inspect laminates, skin-stiffened panels, honeycomb sandwich panels and chopped fiber moldings has been demonstrated. A hot forming method, which eliminates the need for autoclave processing, has been used to fabricate hat-shaped stiffeners. Initial studies indicate that the capability of Celion/LARC-160 to withstand long term exposure at elevated temperature can be significantly enhanced by coating the exterior surface with NR-150 polyimide resin.

Data on effects of moisture, temperature, thermal cycling and shuttle fluids on mechanical properties indicate that both LARC-160 and PMR-15 are suitable for application to shuttle orbiter components such as elevons or an aft body flap. Tests are underway to establish the maximum operating temperature for Celion/LARC-160 in supersonic cruise aircraft structures.

Design and analysis of Gr/PI compression and shear panels representative of shuttle orbiter and supersonic cruise aircraft structures indicate that mass savings in excess of thirty percent compared to metallic panels can be obtained. Both skin-stiffened and honeycomb sandwich configurations are being fabricated and are scheduled to be tested at room temperature and 589K (600°F) to validate the prediction. A five foot sector of the shuttle orbiter body flap is also under construction, and mechanical, thermal, and acoustic tests are planned to demonstrate the capability to design and build Gr/PI composite structures.

® Celion is a registered trademark of Celanese Corporation.

APPLICATION OPPORTUNITIES FOR GRAPHITE/POLYIMIDE COMPOSITES

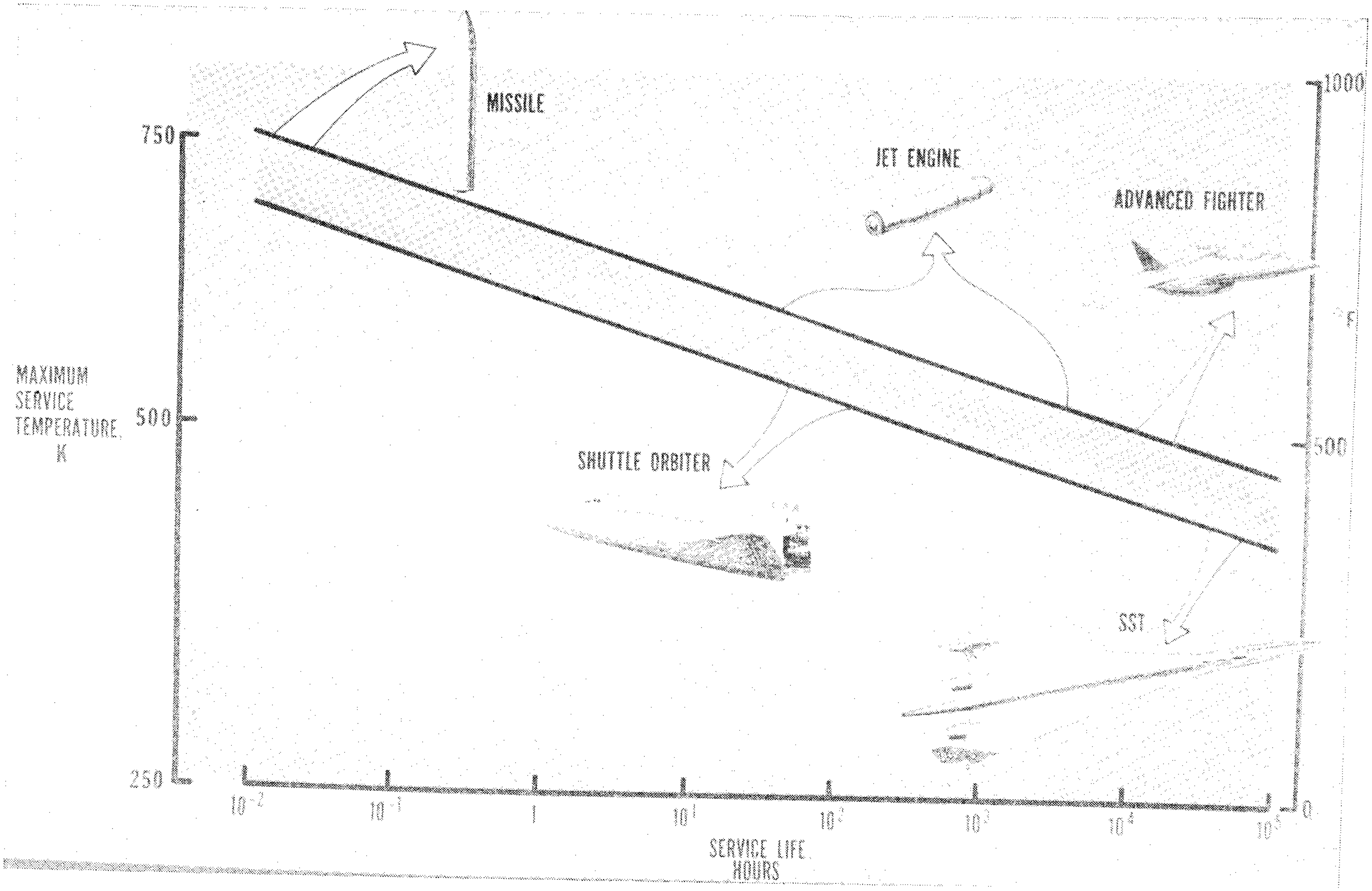

Figure 1.

APPLICATION OPPORTUNITIES FOR GRAPHITE/POLYIMIDE COMPOSITES

(Figure 1)

Graphite/polyimides have been developed to a stage that application to a number of structures which operate at elevated temperatures offers the potential for achieving significant mass savings compared to metallic or graphite/epoxy composite structures. Figure 1 shows the known or anticipated time-temperature capabilities of graphite/polyimides in general terms. For example, satisfactory structural performance may be obtained at 700 to 756K (800° to 900°F) for about one minute and satisfactory performance at 450 to 506K (350° to 450°F) is predicted for 70 000 hours. Also indicated in the figure is the expected service life required in several applications that would benefit from graphite/polyimide structures such as (1) missiles for a single flight, (2) space shuttle orbiter for a design life of 125 flights, (3) jet engine components for exposures to several thousand hours, (4) structures for advanced fighters for 10 000 hours service, and (5) structures for supersonic transport for 70 000 hours service.

NASA LANGLEY R&D
IN HIGH TEMPERATURE RESIN MATRIX COMPOSITES

PROGRAMS

- CASTS - COMPOSITES FOR ADVANCED SPACE TRANSPORTATION SYSTEMS
- SCR - SUPERSONIC CRUISE RESEARCH
- BASE RESEARCH & TECHNOLOGY

MATERIALS

- FIBER - HTS1, MODMOR-II, HTS2, CELION, AS4, T300
- MATRIX - LARC-160, PMR-15, NR150B2, THERMID 600, PMR-15-II, HR-600, F178, K601, NR150A/B, P13N, S703, S710, PPQ, X5230
- ADHESIVE - FM-34, LARC 13, NR150B2G, PPQ, A380, RTV560-SQX

TECHNICAL AREAS

- MATERIALS EVALUATION
- FABRICATION DEVELOPMENT
- MATERIALS TESTING
- STRUCTURAL ANALYSIS
- STRUCTURAL TESTING

Figure 2.

NASA LANGLEY R&D IN HIGH TEMPERATURE RESIN MATRIX COMPOSITES

(Figure 2)

Applications to both space and aircraft structures have been emphasized in research and development on high temperature resin matrix composites. Most of the effort has focused on application of graphite/polyimide composites to the space shuttle orbiter (CASTS) and supersonic cruise aircraft (SCR). In addition a limited amount of generic base research and technology effort has been conducted. Six types of graphite fibers, fourteen matrix materials and six adhesives have been evaluated. Celion, LARC-160, PMR-15, FM 34, LARC-13 and RTV560-SQX have been used predominately during the last three years. RTV560-SQX adhesive was evaluated for bonding RSI to 589K (600°F) graphite/polyimide composite substructure in space vehicles and the results indicate adequate performance. References 1 and 2 report results of screening tests on the materials listed in figure 2. Technical disciplinary areas included in the research and development are (1) evaluation of materials to determine suitability to withstand environmental exposure and potential to fabricate structures, (2) development of fabrication procedures, nondestructive evaluation methods and specifications, (3) determination of mechanical properties between 117K and 589K (-250° and 600°F), (4) design and analysis of compression and shear panels and bolted and bonded joints, and (5) mechanical, thermal and acoustic testing of structural elements and components.

STATE OF THE ART
FOR GRAPHITE/LARC-160 AND GRAPHITE/PMR-15

ITEM	LARC-160	PMR-15
o RESIN SYSTEM FORMULATED	1977	1974
o PREPREG COMMERCIALLY AVAILABLE	YES	YES
o PREPREG CHARACTERISTICS	SIMILAR TO EPOXIES	DRIER THAN EPOXIES
o SPECIFICATIONS	MATURING	MATURING
o STRUCTURAL ELEMENTS FABRICATED	YES	YES
o FABRICATION OF LARGE THICK PARTS	DIFFICULT	DIFFICULT
o MINIMUM REQUIRED AUTOCLAVE TEMPERATURE	547K (525°F)	589K (600°F)
o 125 HOURS SERVICE LIFE AT 589K (600°F)	YES	YES

Figure 3.

STATE OF THE ART FOR GRAPHITE/LARC-160 AND GRAPHITE/PMR-15

(Figure 3)

Based on NASA Langley in-house and contract research and development effort, LARC-160 and PMR-15 are the most promising polyimide matrix materials for near term application to aerospace structures. Both resins are relatively new; LARC-160 was formulated in 1977 and PMR-15 was formulated in 1974. Graphite fiber prepreg tape is available from several commercial sources. Graphite/LARC-160 prepreg tape exhibits tack and drape characteristics similar to graphite/epoxy prepregs used in the aerospace industry. Graphite/PMR-15 prepreg usually exhibits less tack and drape than graphite/epoxy prepreg. Materials and processing specifications for both composites are maturing and further refinements are anticipated. High Pressure Liquid Chromatography has contributed significantly to the development of specifications and minimized variability for both resins. References 3, 4, and 5 contain current specifications. Laminates, honeycomb sandwich and skin-stiffened structural elements have been successfully fabricated with each type of composite. However, fabrication of large area components more than 30 mm (0.12 in.) thick is difficult and additional effort is needed to achieve an acceptable level of success. Graphite/LARC-160 can be autoclave cured at 547K (525°F) whereas graphite/PMR-15 requires a maximum temperature of 589K (600°F). Both composites are suitable for 125 hours service at 589K.

SCR GRAPHITE/POLYIMIDE PANEL RESEARCH

NASA YF-12 AIRPLANE

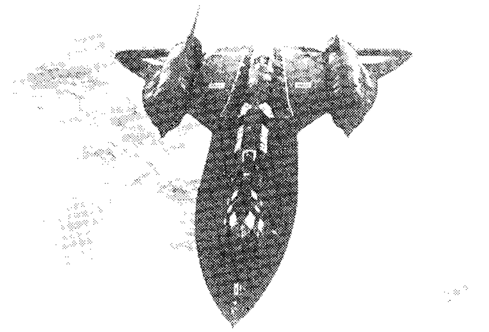

HTS/PMR-15 HONEYCOMB SANDWICH PANEL

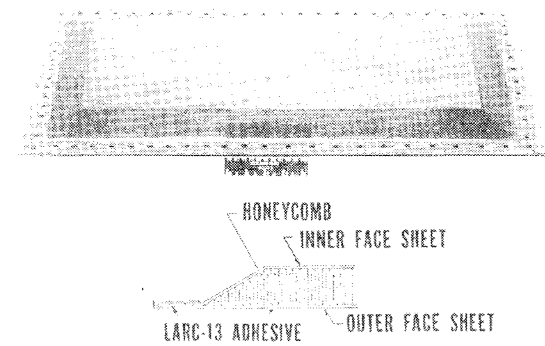

CELION/LARC-160 SKIN STIFFENED PANEL

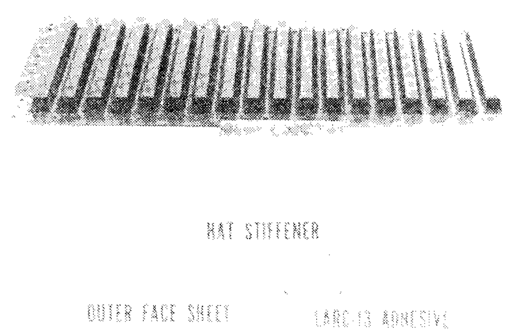

ACCOMPLISHMENTS

- ESTABLISHED AUTOCLAVE PROCESSES FOR FLIGHT QUALITY GR/PI PANELS
- DEVELOPED ADVANCED TOOLING AND VACUUM BAGGING TECHNIQUES
- DEVELOPED LARC-13 BONDING PROCESSES
- DEMONSTRATED LASER HOLOGRAPHY AND C-SCAN NDE FOR QUALITY ASSURANCE

PANEL	MASS KG	MASS (LB)	%
ORIGINAL TITANIUM	3.8	8.5	100
GR/PI H/C SANDWICH	2.0	4.5	53
GR/PI SKIN STIFFENED	1.7	3.7	44

Figure 4.

SCR GRAPHITE/POLYIMIDE PANEL RESEARCH

(Figure 4)

The NASA YF-12 is a high performance airplane capable of sustained flight at Mach 3 or above. The panel chosen as a Gr/PI fabrication feasibility component for this airplane is an upper surface wing panel located between the engine and fuselage. In this area the wing surface is aerodynamically heated to temperatures up to 524K (485°F) during flight at speeds near Mach 3. The current production panel for this location is a blade-stiffened titanium panel which is loaded primarily in shear. HTS1/PMR-15 and Celion 6000/LARC-160 are two of the primary materials that have been investigated for manufacture of composite wing panels. The configurations for the NASA LaRC honeycomb-stiffened and hat-stiffened Gr/PI YF-12 wing panels are shown. The outer face sheets and inner face sheets of the honeycomb panels are composed of 9 plies and 6 plies, respectively, of HTS1/PMR-15. The fiberglass/polyimide honeycomb material is 25.40 mm (1.00 in.) thick and has a density of $93 kg/m^3$ ($5.8 lbm/ft^3$). Spacer shims made from HTS1/PMR-15 are bonded to the panel flanges for correct fit to the airplane wing substructure. The outer and inner face sheets, honeycomb, and spacer shims are bonded together with LARC-13. The hat-stiffened panel was fabricated with Celion 6000/LARC-160. The face sheet for this panel is 10 plies thick. The corrugated hat-stiffeners are 4 plies thick with an additional 5 plies of unidirectional Celion 6000/LARC-160 reinforcement in the caps. The hat-stiffeners are bonded to the face sheet with LARC-13 polyimide adhesive. Some of the key accomplishments in this study are the establishment of advanced tooling and vacuum techniques which permitted the fabrication of numerous flight quality wing panels in succession, the refinement of cure profiles for defect-free sub-component and finished component fabrication, and the demonstrations of laser holography and C-scan techniques for accurate interrogation of finished articles. Based on the results and other NASA Langley sponsored research Celion/LARC-160 is being subjected to simulated time-temperature-stress environments that are predicted for supersonic cruise aircraft.

FLATWISE TENSILE STRENGTH OF GR/PI HONEYCOMB SANDWICH PANELS

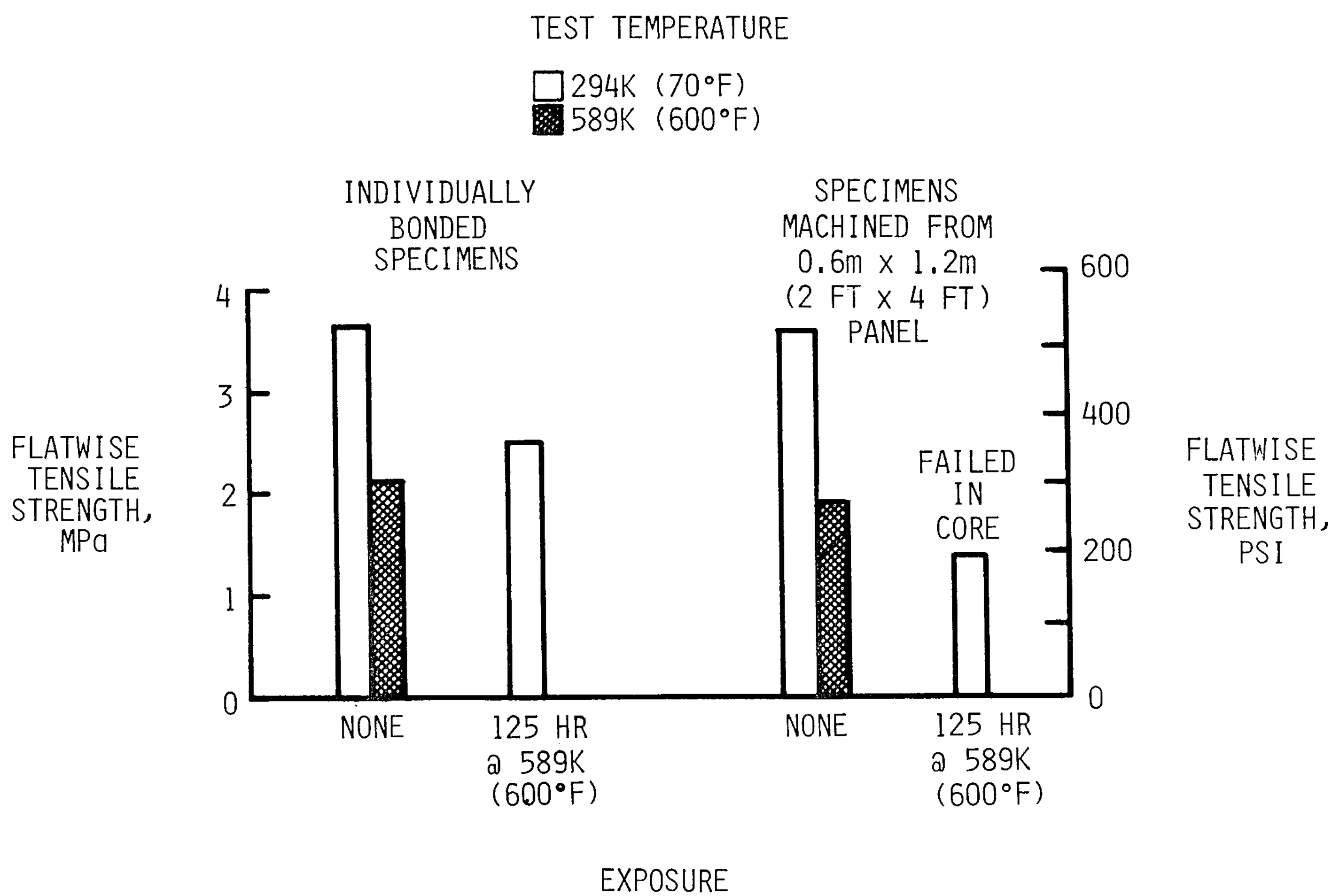

Figure 5.

FLATWISE TENSILE STRENGTH OF GR/PI HONEYCOMB SANDWICH PANELS

(Figure 5)

Feasibility of utilizing bonded honeycomb sandwich construction in graphite/polyimide structures for aerospace applications is dependent upon the capability to fabricate large area components. Previous investigators were generally unable to obtain uniform bond strength in large panels. The major problem is the amount of volatile gasses that evolve during cure and create voids and delaminations. A technique for venting the volatile gasses has been developed. Thin slits, 50 mm (0.2 in.) deep, 7.6 cm (3.0 in.) on center were cut in the top and bottom surfaces of the honeycomb using a razor blade. The top and bottom slits were made perpendicular to each other to provide vent paths from the interior of the panel to all four edges. FM-34 adhesive, 0.44 kg/m^2 (0.09 lbm/ft^2), and Celion/PMR-15 face sheets were used in the investigation. A 0.6 m x 1.2 m (2 ft x 4 ft) panel with HRH-327 glass/polyimide honeycomb was fabricated. Flatwise tensile specimens were machined from the center, edge, and quarter points of the panel and subsequently tested. Flatwise tensile strengths for as-fabricated specimens tested at room temperature and 589K (600°F) were 3.51 MPa (509 psi) and 1.90 MPa (275 psi), respectively. Specimens aged 125 hours at 589K (600°F) and tested at room temperature had a flatwise tensile strength of 1.40 MPa (200 psi). The strengths were uniform across the entire panel. Comparison of the strength of the as-fabricated specimens machined from the panel with the strength of 7.6 cm x 7.6 cm (3.0 in. x 3.0 in.) individually fabricated specimens indicates that the difference is less than 10 percent. Aged specimens from the panel failed in the honeycomb whereas the aged specimens that were individually fabricated failed along the bondline. Density of the honeycomb core used in the panel was 72.1 kg/m^3 (4.5 lbm/ft^3) whereas the individually fabricated specimens contained 96.1 kg/m^3 (6.0 lbm/ft^3) honeycomb core. The lighter core would be expected to degrade more rapidly and is probably the cause for the reduced strength and change in failure mode.

HOT FORMING GRAPHITE/POLYIMIDE

HAT-SHAPED STIFFENER

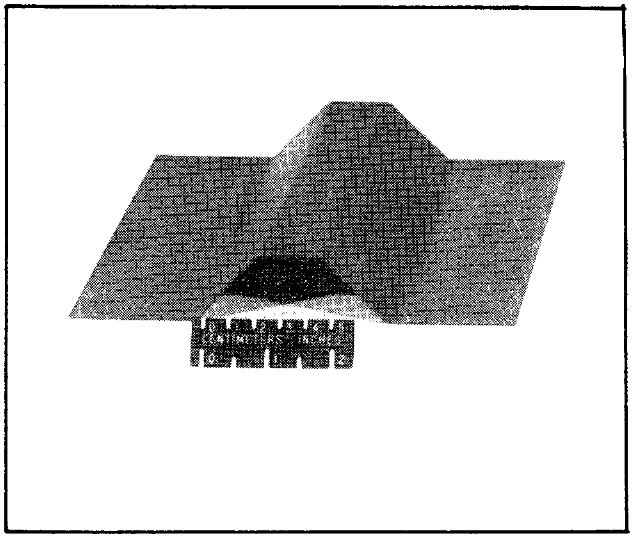

FORMING CYCLE

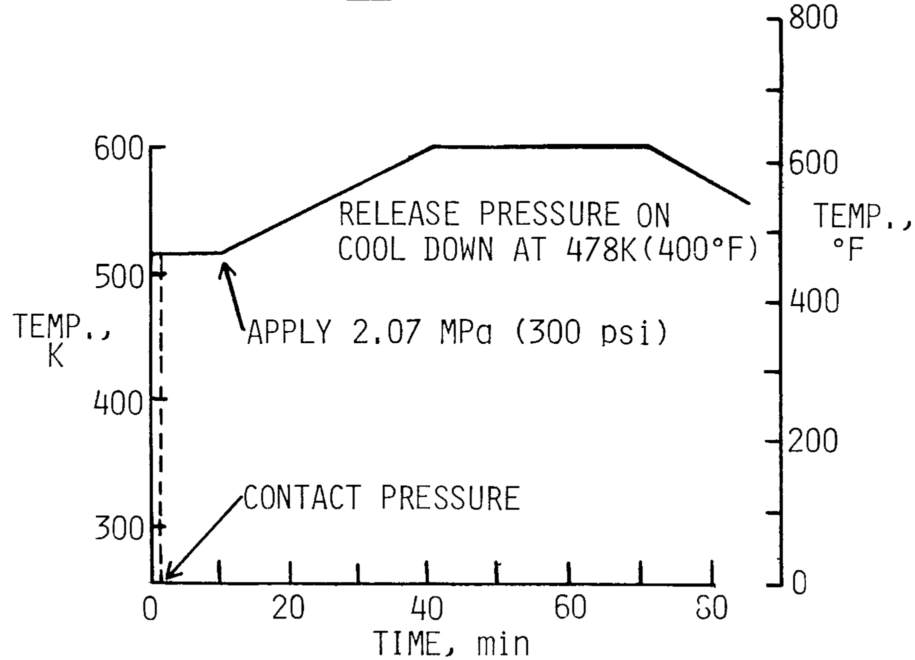

ADVANTAGES

- EXTENDED RT STORAGE CAPABILITY
- HIGH PROCESSING RELIABILITY
- APPLICABLE TO GR/PMR-15 AND GR/LARC-160
- ENERGY EFFICIENT

Figure 6.

HOT FORMING GRAPHITE/POLYIMIDE

(Figure 6)

A simple fabrication procedure which offers several advantages compared to conventional autoclave curing has been used to fabricate graphite/polyimide composite elements. Both Celion/LARC-160 and Celion/PMR-15 hat-shaped stiffeners, such as the one shown, have been built. Briefly, the procedure is: (1) the appropriate number of prepreg plies are assembled into the required orientation, (2) the resulting laminate is B-staged under vacuum, (3) the laminate is placed between 519K (475°F) preheated matched metal dies, (4) contact pressure is applied and maintained for 10 minutes, (5) 2.07 MPa (300 psi) pressure is applied and the temperature is increased at 3K/min (5°F/min) until 603K (625°F) is achieved, and (6) the part is maintained at 603K (625°F) for 30 minutes and then cooled at 3K/min (5°F/min) under pressure until the temperature is reduced to 478K (400°F). Free standing post cure in an air-circulating oven is used to increase the glass transition temperature of the composite element. Several advantages are apparent from results obtained to date. Once the B-staging operation has been completed, the composite can be stored at room temperature for at least six months without degrading. Ten replicas of three different batches of composite material have been successfully fabricated, which demonstrates the process reliability. Compared to autoclave curing, the hot forming process requires less energy.

EFFECT OF TEMPERATURE ON INTERLAMINAR SHEAR STRENGTH OF CELION/PMR-15

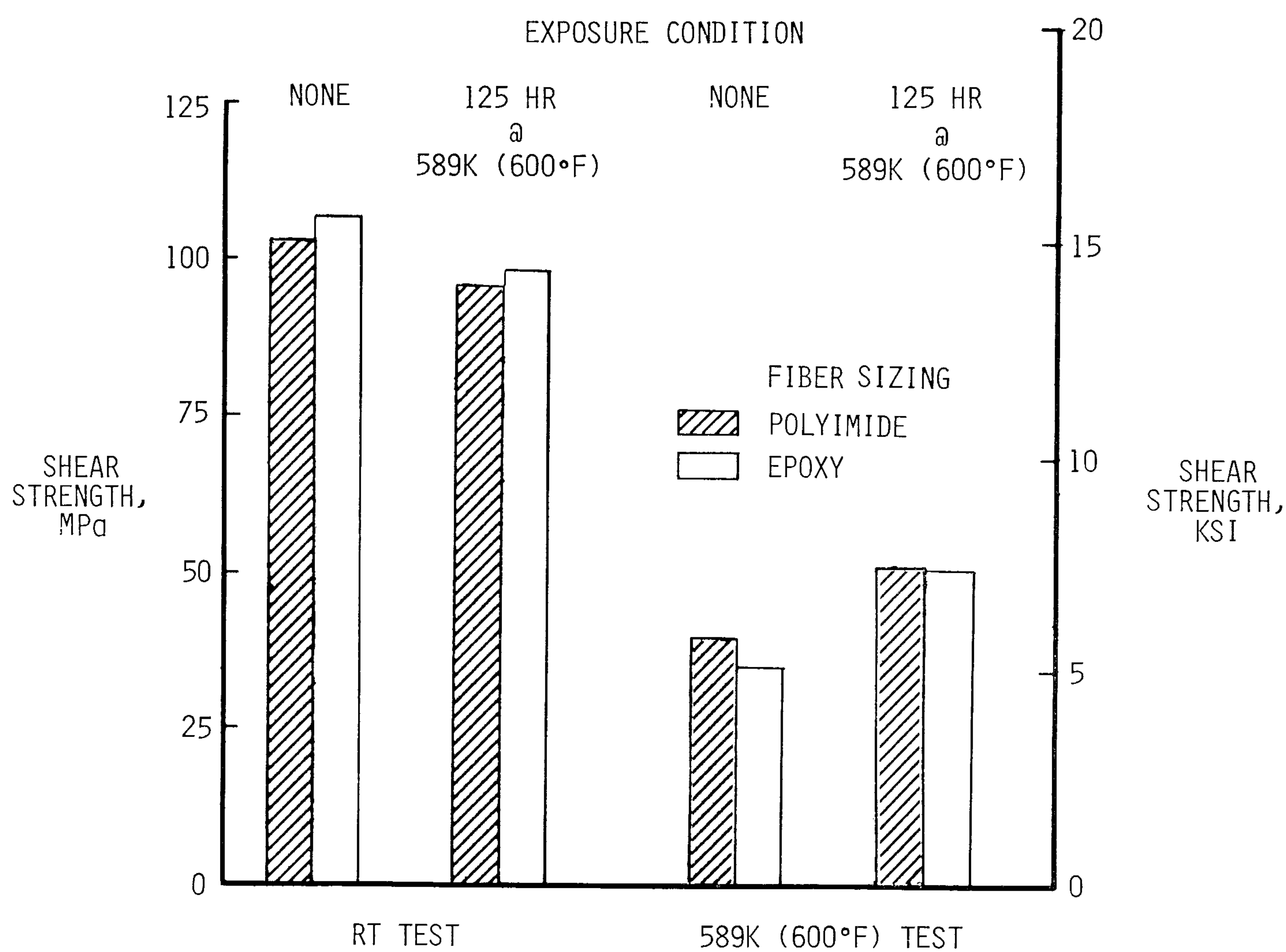

Figure 7.

EFFECT OF TEMPERATURE ON INTERLAMINAR SHEAR STRENGTH OF CELION/PMR-15

(Figure 7)

In the past three years, Celion graphite fibers with NR150B2 polyimide sizing were used predominately in graphite/polyimide composites R&D at NASA Langley because of availability and anticipation that epoxy sized fibers would degrade at elevated temperatures. Recently, NR150B2 was temporarily withdrawn from the market, and thus identification of an alternate sizing material became necessary. Preliminary data had indicated that epoxy sized Celion graphite fiber, which exhibits better handling characteristics and is less expensive than NR150B2 sized fiber, was a logical candidate for evaluation. Thus, Celion 6000/PMR-15 laminates were fabricated using epoxy sized and polyimide sized fibers. Flexure and interlaminar shear specimens were machined from the laminates and exposed to 589K (600°F) air for 125 hours. Tests were conducted at room temperature (RT) and 589K (600°F) on specimens in the as-fabricated condition and specimens which had been exposed. Results of the interlaminar shear tests are shown in the figure and indicate that the performance is essentially the same for epoxy and polyimide sized fiber.

EFFECT OF TEMPERATURE ON FLEXURE STRENGTH OF CELION/PMR-15

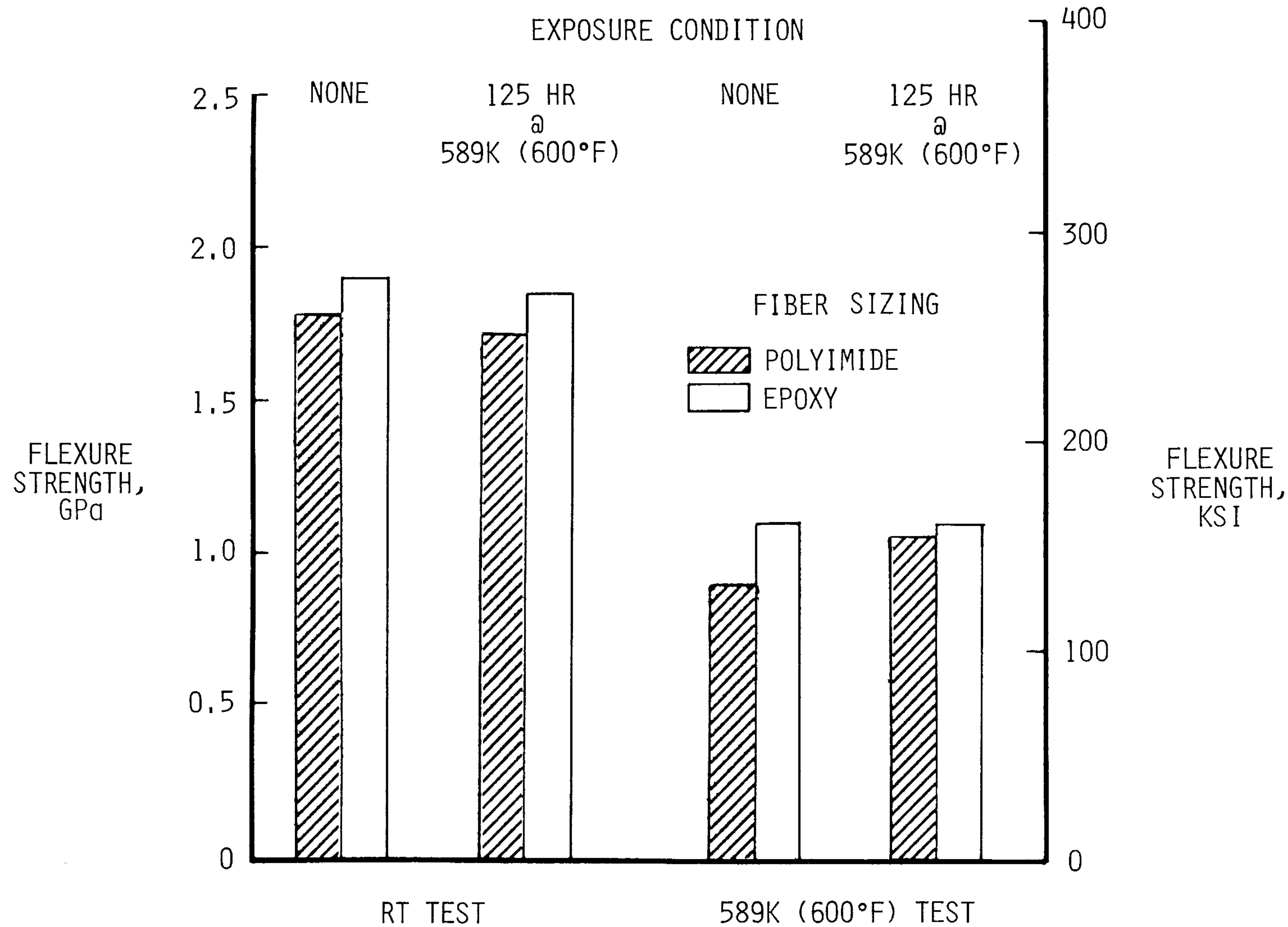

Figure 8.

EFFECT OF TEMPERATURE ON FLEXURE STRENGTH OF CELION/PMR-15

(Figure 8)

Results of flexure tests on Celion/PMR-15 specimens fabricated with epoxy sized fiber and polyimide sized fiber are shown. Tests were conducted at room temperature and 589K (600°F) on specimens in the as-fabricated condition and specimens which had been exposed to 589K air for 125 hours. The data indicate that performance is essentially the same for epoxy and polyimide sized fiber. Based on these results and the data in figure 7, epoxy sized fiber appears to be suitable for use in graphite/polyimide composites that must withstand 125 hours at 589K.

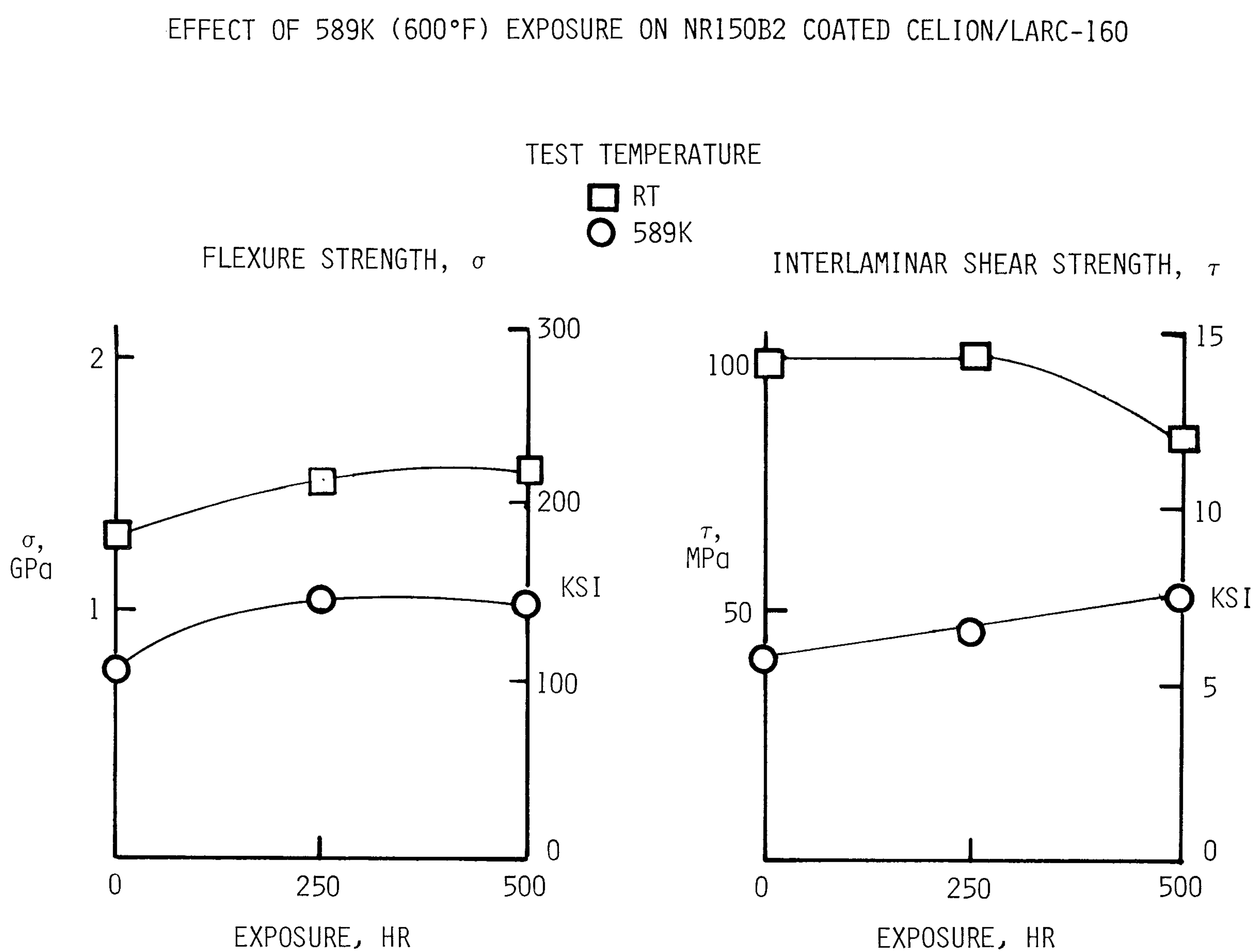
EFFECT OF 589K (600°F) EXPOSURE ON NR150B2 COATED CELION/LARC-160
TEST TEMPERATURE
RT
589K
FLEXURE STRENGTH, σ
σ, GPa
2
1
300
200
100
0
KSI
0
250
500
EXPOSURE, HR
INTERLAMINAR SHEAR STRENGTH, τ
τ, MPa
100
50
15
10
5
0
KSI
0
250
500
EXPOSURE, HR

Figure 9.

EFFECT OF 589K (600°F) EXPOSURE ON NR150B2 COATED CELION/LARC-160

(Figure 9)

Recent work demonstrated that the elevated temperature service life of Celion/LARC-160 composites can be significantly increased by applying a 50 μm (.002 in.) coating of NR150B2. Details of the investigation are reported in reference 6. A Celion/LARC-160 laminate was B-staged, then coated with NR150B2 and cured using the normal temperature and pressure cycles for Celion/LARC-160. Flexure and interlaminar shear specimens were machined from the as-fabricated laminate and portions of the laminate that had been exposed to 589K (600°F) air for 250 hours and 500 hours, respectively. Tests were conducted at room temperature and 589K and results are shown in the figure. Room temperature and 589K flexure strength and 589K interlaminar shear strength increased as a result of the 589K exposure. Room temperature interlaminar shear remained essentially constant through 250 hours exposure at 589K and decreased approximately 20 percent after 500 hours exposure. No obvious surface damage was observed on the NR150B2 coated laminate after 500 hours exposure at 589K whereas uncoated Celion/LARC-160 laminates exhibited very fuzzy and obviously severly degraded surfaces.

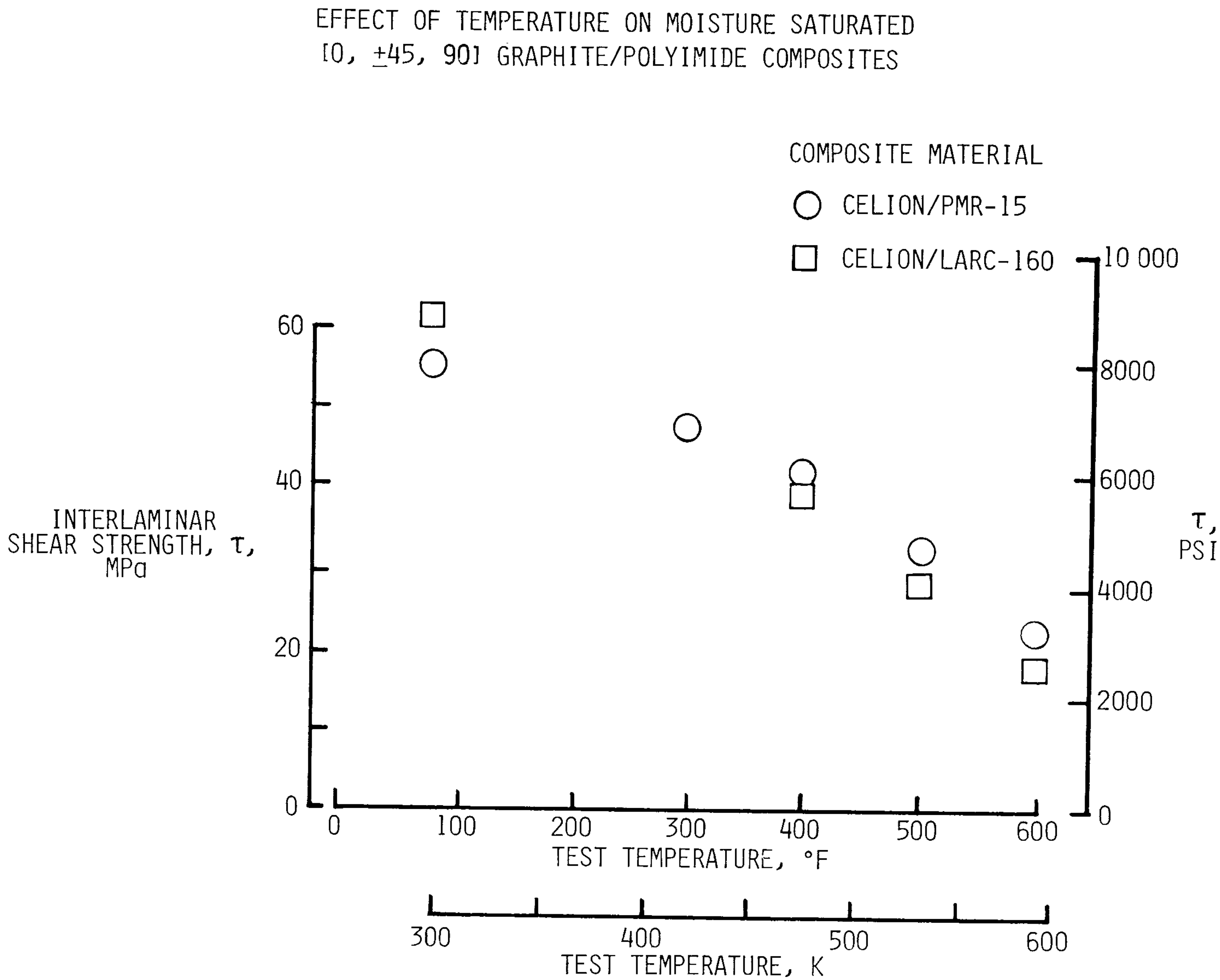
EFFECT OF TEMPERATURE ON MOISTURE SATURATED
[0, ±45, 90] GRAPHITE/POLYIMIDE COMPOSITES
COMPOSITE MATERIAL
CELION/PMR-15
CELION/LARC-160
INTERLAMINAR SHEAR STRENGTH, τ, MPa
0
20
40
60
τ, PSI
0
2000
4000
6000
8000
10 000
0
100
200
300
400
500
600
TEST TEMPERATURE, °F
300
400
500
600
TEST TEMPERATURE, K

Figure 10.

EFFECT OF TEMPERATURE ON MOISTURE SATURATED $[0,\pm45,90]$ GRAPHITE/POLYIMIDE COMPOSITES

(Figure 10)

Interlaminar shear strength tests were conducted on 16-ply $[0,\pm45,90]_s$ specimens of Celion/PMR-15 and Celion/LARC-160. All specimens were moisture saturated in a condensing humidity chamber that was maintained at 356K (180°F) and atmospheric pressure. Moisture saturation level equalled approximately 1.7 percent by mass. Tests were performed between RT and 589K (600°F). Strength monotonically decreases as the test temperature is increased. Both composite materials are affected approximately the same magnitude with the 589K (600°F) strength being reduced to about 35 percent of the room temperature value.

EFFECT OF TEMPERATURE AND MOISTURE
ON COMPRESSIVE STRENGTH OF CELION/PMR-15

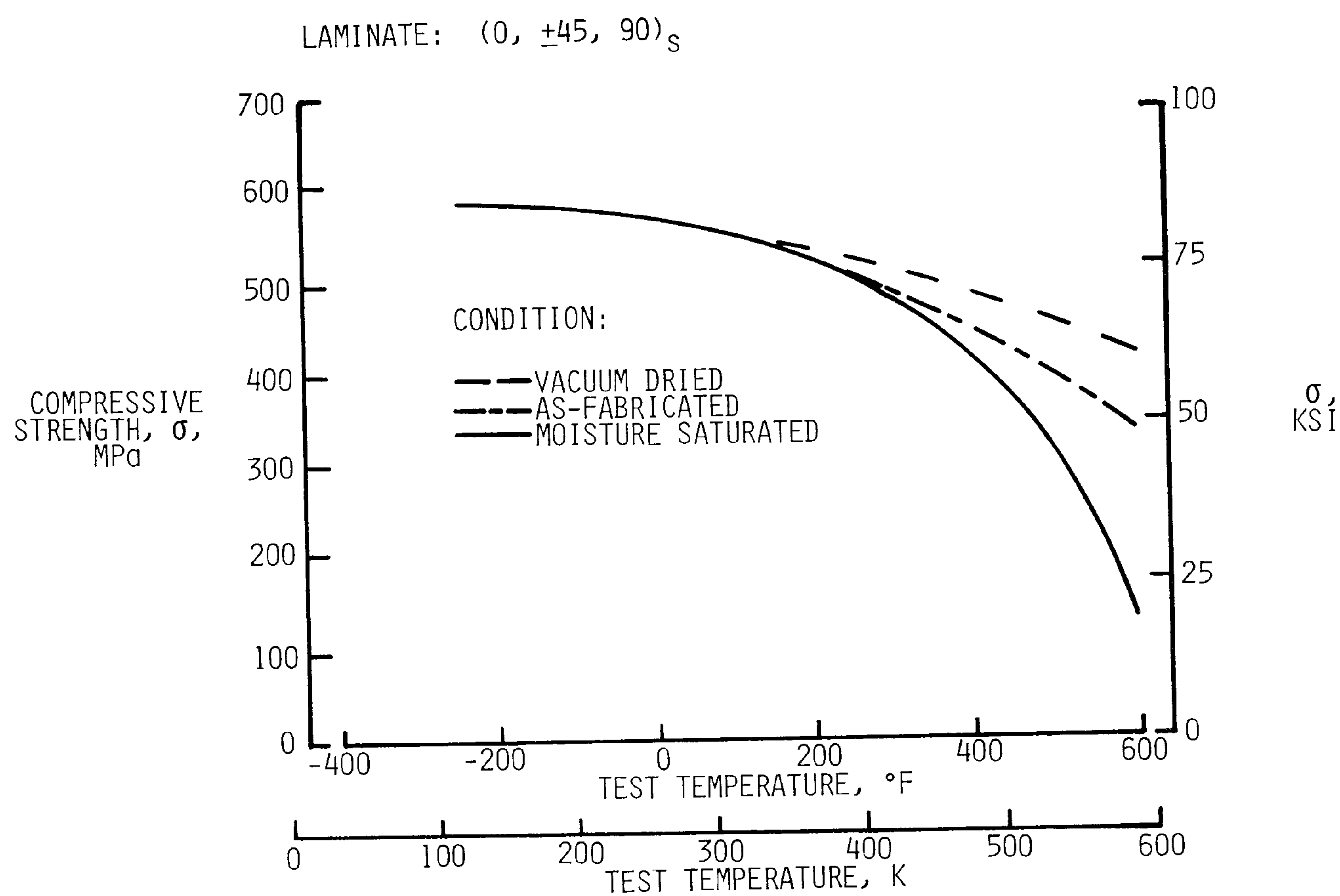

Figure 11.

EFFECT OF TEMPERATURE AND MOISTURE ON COMPRESSIVE STRENGTH OF CELION/PMR-15

(Figure 11)

Compressive strength tests were conducted on $[0,\pm 45,90]_s$ specimens over the temperature
range 117K to 589K (-250°F to 600°F). Specimen nominal dimensions were 2.54 cm x 30.48
cm (1.00 in. x 12.00 in.) and details of the apparatus and procedure are described in
reference 7. Tests were performed on specimens in vacuum dried, as-fabricated and mois-
ture saturated conditions. Vacuum drying was achieved in a chamber that was maintained
at 367K (200°F) and 10^{-5} to 10^{-6} torr. As-fabricated specimens contained approximately
0.5 percent moisture by mass. Moisture saturation equalled about 1.2 percent by
mass and was achieved by exposing specimens in a condensing humidity chamber maintained
at 356K (180°F) and atmospheric pressure. Between 117K and 367K (-250°F and 200°F) com-
pressive strength is independent of moisture content. As the test temperature is increased
beyond 367K, moisture content becomes a predominate influence on compressive strength.
Comparison of room temperature strengths and 589K (600°F) strengths indicates that the
589K strengths were 25 percent lower for vacuum dried specimens, 40 percent lower for as-
fabricated specimens and 75 percent lower for moisture saturated specimens. Reduction of
the elevated temperature strengths of the as-fabricated and moisture saturated specimens
is attributed to softening of the matrix material which is a result of the glass transi-
tion temperature being reduced by absorption of moisture.

MICROCRACKS PRODUCED BY THERMAL EXPOSURE OF CELION/PMR-15

THERMAL EXPOSURE	LAMINATE ORIENTATION $[45,-45,0,90]_s$	$[0,45,90,-45]_s$	$[0,60,0,-60]_s$	$[(0,90)_3]_s$
603K(625°F)→RT @ 3K(5°F)/MIN	0	0	0	0
RT→603K(625°F) @ 8K(15°F)/MIN & 603K(625°F)→78K(-320°F) @ 11K(20°F)/MIN	0	0	0	2/CM(5/IN.)IN OUTER 0° PLIES
RT→603K(625°F) @ 8K(15°F)/MIN & 603K(625°F)→78K(-320°F) BY LN_2 QUENCH	0	7/CM(19/IN.)IN 0 PLIES & 2/CM(4/IN.)IN 45° PLIES	8/CM(21/IN.)IN OUTER 0° PLIES & 4/CM(9/IN.)IN -60° PLIES	11/CM(28/IN.)IN OUTER 0° PLIES & 6/CM(16/IN.)IN MID-PLANE 90° PLIES

Figure 12.

MICROCRACKS PRODUCED BY THERMAL EXPOSURE OF CELION/PMR-15

(Figure 12)

An investigation was conducted to determine the effect of severe thermal exposures on Celion/PMR-15 composites. Details are reported in reference 8 and key results are summarized in the table. Upon cool down from the cure temperature of 603K (625°F) to room temperature each of the four types of laminates were free of microcracks. Reheating the specimens to 603K at 8K (15°F) per minute, cooling to 78K (-320°F) at 11K (20°F) per minute and then reheating to room temperature at 8K per minute produced cracks only in the $[(0,90)_3]_s$ laminate. Rapidly cooling the specimens from 603K to 78K by liquid nitrogen quenching produced significant cracking in all but the $[45,-45,0,90]_s$ laminate. Based on these results, the $[45,-45,0,90]_s$ laminate appears to be the most resistant to microcracking and three quasi-isotropic laminates can withstand 78K to 603K temperature exposure with heating and cooling rates less than 11K per minute without developing microcracks.

EFFECT OF THERMAL CYCLING BETWEEN 117K AND 589K
(-250°F to 600°F) ON CELION 6000/PMR-15 COMPOSITES

TESTED AT 589K (600°F)

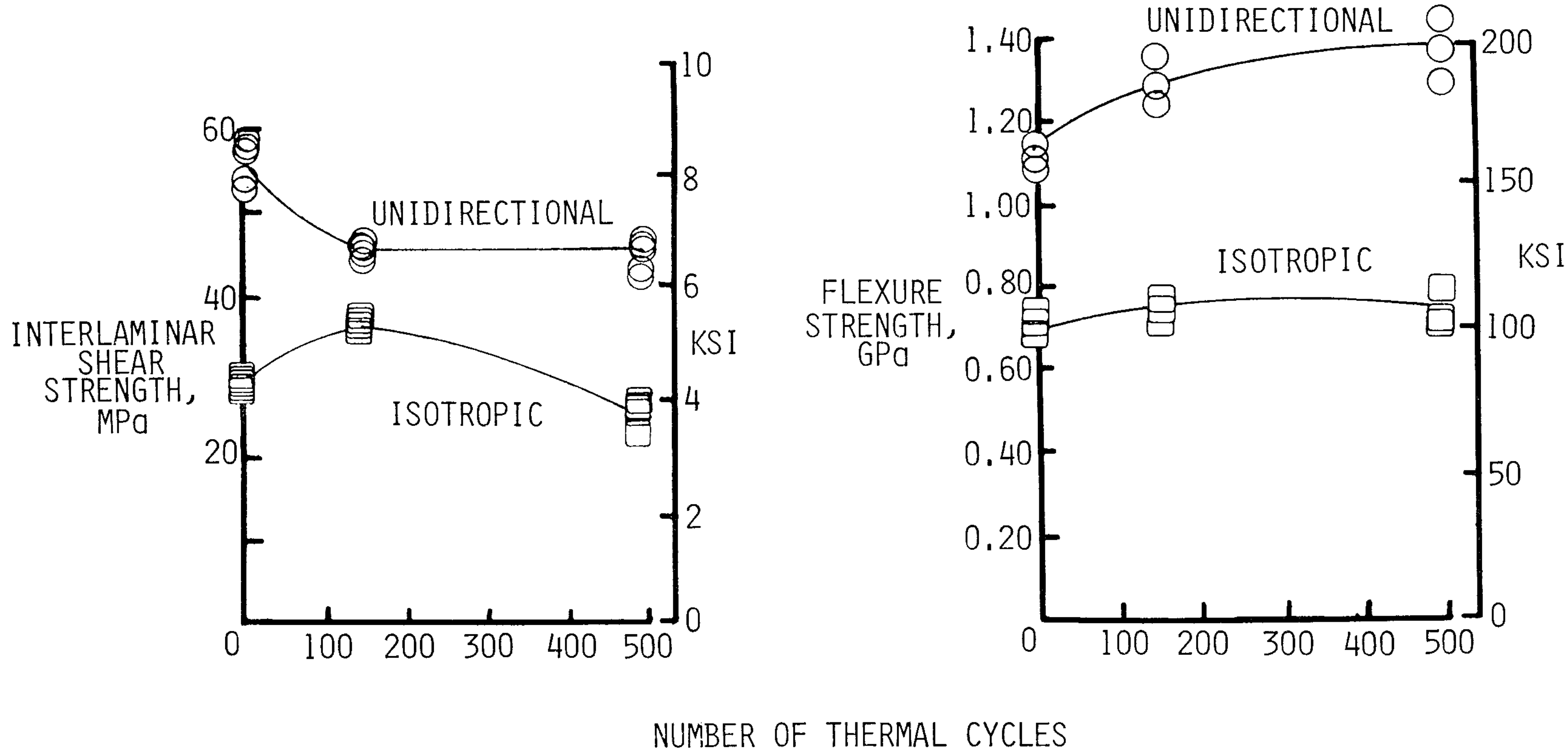

Figure 13.

EFFECT OF THERMAL CYCLING BETWEEN 117K AND 589K (-250°F TO 600°F) ON CELION 6000/PMR-15 COMPOSITES

(Figure 13)

An experimental study was conducted to determine the effect of thermal cycling on the residual mechanical properties of Celion/PMR-15 composite. Flexure and interlaminar shear specimens were cycled between 117K and 589K (-250°F to 600°F) over a period of approximately 23 minutes. Residual strengths for specimens tested at 589K (600°F) are shown in the figure. Interlaminar shear strength for unidirectional specimens decreased approximately 15 percent after 150 cycles and then remained essentially constant through 500 cycles of exposure. Interlaminar shear strength for isotropic specimens increased approximately 25 percent after 150 cycles and then decreased to 5 percent below the initial value after 500 cycles of exposure. Flexure strength for unidirectional specimens increased approximately 15 percent after 150 cycles and 20 percent after 500 cycles of exposure. Thermal cycling had no significant effect on the residual flexure strength of the isotropic specimens. Flexure strengths for unidirectional specimens tested at room temperature, not shown in figure, were not affected by thermal cycling; this indicates that perhaps the unidirectional flexure specimens tested at 589K were not fully cured. Microcracks were detected in the isotropic specimens after approximately 130 cycles. The number of cracks increased with the number of thermal cycle exposures. Tests are in progress to determine the effect of thermal cycling on the residual compression strength at 589K and the moisture sorption characteristics.

CELION/LARC-160 I-STIFFENED PANEL

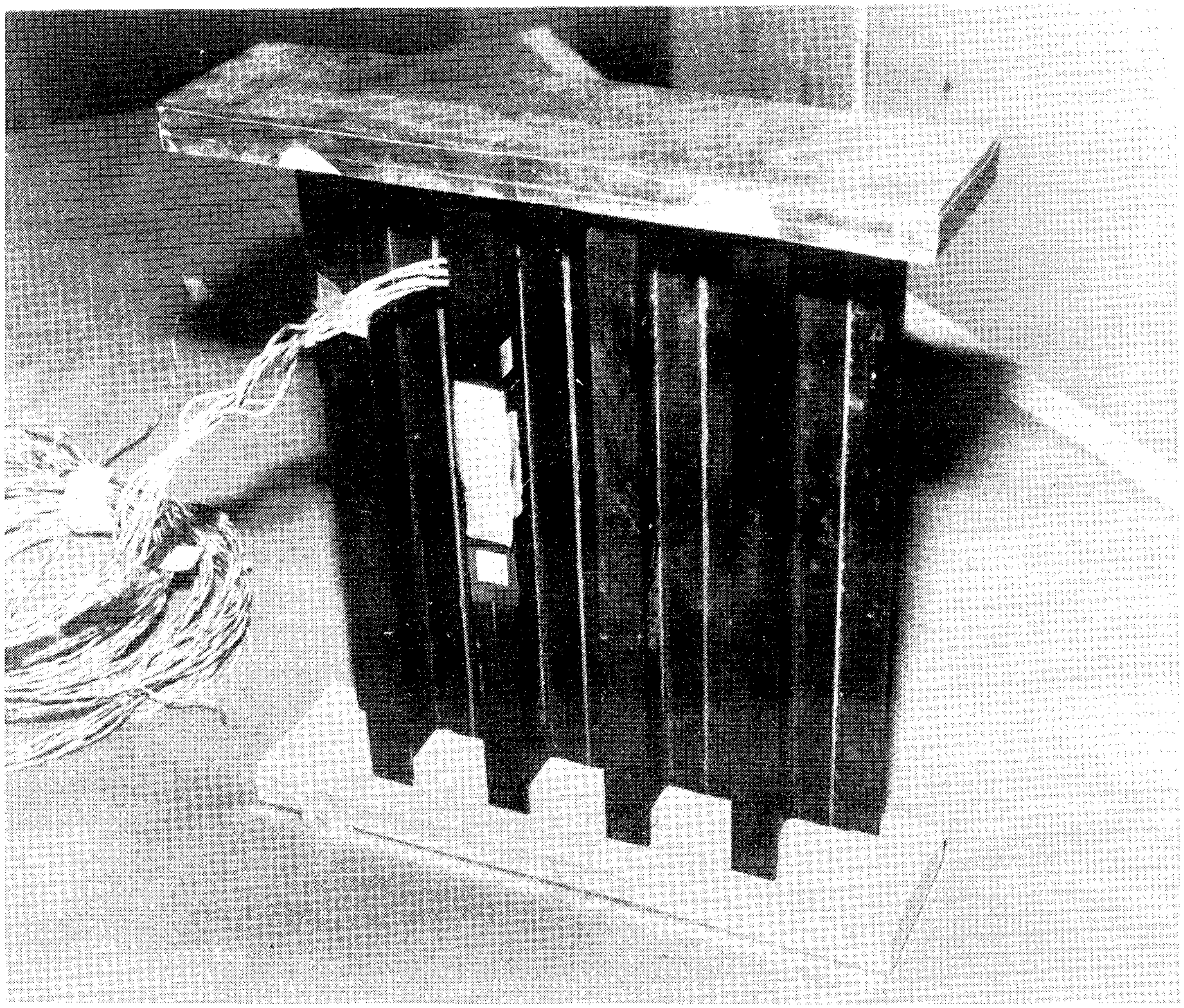

Figure 14.

CELION/LARC-160 I-STIFFENED PANEL

(Figure 14)

Efficient utilization of Gr/PI composite structures in aerospace vehicles is dependent upon the capability to design, fabricate and predict the response of compression loaded panels. A photograph of a Celion/LARC-160 I-stiffened panel is shown in the figure. The panel was designed to support an axial compression load of 525kN/m (3000 lbf/in.) over a span of 1.22 m (48 in.). An 8-ply $[0,\pm45,90]_s$ laminate configuration was selected for the skin. The webs of the I-stiffeners consists of a 4-ply $[\pm45]_s$ lay-up and the caps of the I-stiffeners were reinforced with $[0]_{14}$ plies. FM34B adhesive was used to bond the stiffeners to the skin. As shown in the photograph, the second stiffener from the left and the skin were instrumented with strain gages so that the panel response could be measured. The panel shown and five replicas were tested at 106K (-270°F), RT and 589K (600°F). Three of the panels were exposed in 589K (600°F) air for 125 hours prior to testing. All panels supported the design ultimate load without experiencing catastrophic failure. The as-fabricated panel tested at 589K developed compression failure of the skin in one corner of the panel. The thermally aged panel that was tested at 106K experienced a similar failure in the skin and damage in two stiffeners. Structural efficiency of the panel was compared with the structural efficiency of aluminum panels reported in reference 9 and the Celion/LARC-160 offers the potential for a 48 percent reduction in structural mass. Hat-stiffened panels have also been fabricated and tested and similar results have been obtained.

GRAPHITE/POLYIMIDE SKIN-STIFFENED SHEAR PANELS

TEST SET UP

DESIGN

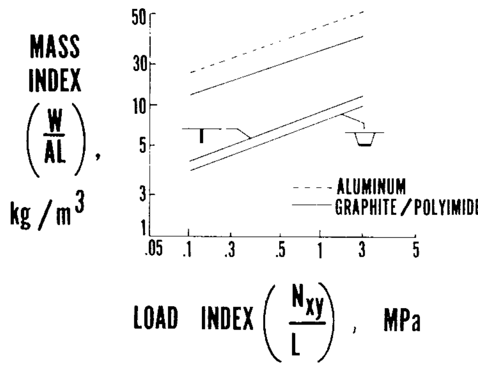

PANEL BEHAVIOR

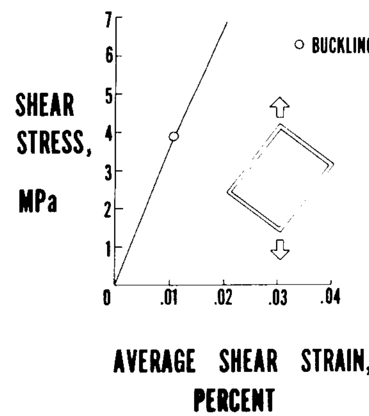

Figure 15.

GRAPHITE/POLYIMIDE SKIN-STIFFENED SHEAR PANELS

(Figure 15)

The objective of this study is to design, test, and analyze Gr/PI skin-stiffened shear panels. Initially, composite hat-stiffened and blade-stiffened shear panels were designed for comparison with unstiffened composite and unstiffened metal panels. As shown in the structural efficiency plot, the stiffened panels are 25-30 percent more efficient for a minimum mass design than the composite unstiffened panel. Unstiffened, hat-stiffened, and blade-stiffened Gr/PI panels are being tested at room temperature and 589K (600°F). Data are being obtained for buckling and post-buckling behavior and mode shapes are being monitored using the moire fringe technique. Shear stress and shear strain are plotted to experimentally determine buckling load. The data are compared to the theoretically predicted buckling load obtained from detailed finite element stress analysis. The finite element analysis models include the method of load introduction and test fixtures. Results obtained to date indicate excellent correlation between experimentally determined and predicted buckling loads.

DESIGN OF A GRAPHITE/POLYIMIDE HONEYCOMB SANDWICH PANEL

DESIGN LOADS

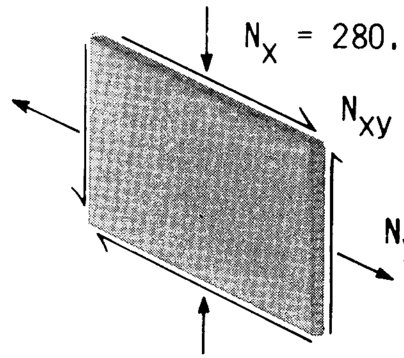

EFFECT OF PLY ORIENTATION ON MASS FOR t_c^* = 1.27 cm (0.5 in)

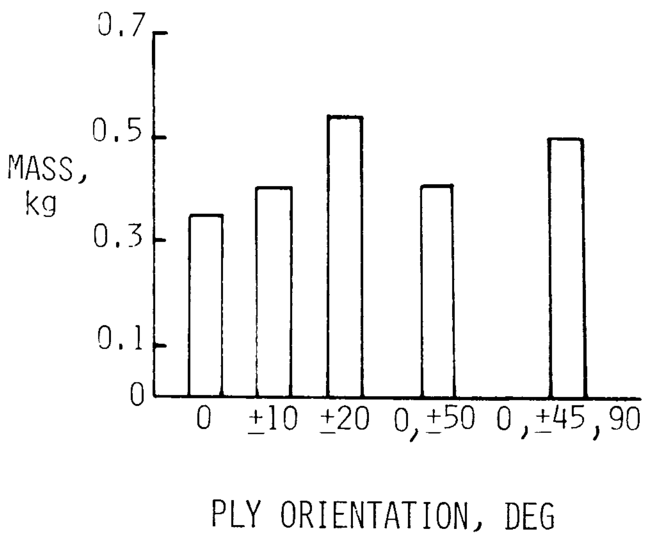

DESIGN SELECTED FOR FABRICATION AND TESTING

GRAPHITE/POLYIMIDE FACE SHEETS [0/±50]
HRH 327-3/16-4.5 GLASS POLYIMIDE CORE
t_c = 1.27 cm (0.5 in)

PANEL DIMENSIONS .51 m x .36 m (20 in x 14 in)
PANEL MASS = 0.40 kg (0.88 lb)

MASS SAVINGS COMPARED TO AN ALUMINUM SANDWICH PANEL = 32.3 PERCENT

* t_c = HONEYCOMB CORE THICKNESS

Figure 16.

DESIGN OF A GRAPHITE/POLYIMIDE HONEYCOMB SANDWICH PANEL

(Figure 16)

A study of the shear behavior of a graphite/polyimide panel representative of the front spar web in the space shuttle orbiter aft body flap is in progress. Using a computerized optimization code, the thickness and ply orientation of the panel were varied to determine a minimum mass design to withstand the load case indicated. A plot showing the panel mass as a function of face sheet ply orientation for a core thickness of 1.27 cm (.50 in.) indicates the minimum mass design is 2-ply, 0° face sheets. A design of this type is weak in the transverse direction and highly susceptible to transverse cracking. To eliminate this problem and increase the shear load carrying capability of the panel, a 3-ply [0/±50] layup design was selected. This design has a mass of 0.40 kg (0.88 lb) and shows a 30 percent mass savings when compared to a minimum mass aluminum sandwich panel. A computerized finite element analysis code is being used to determine the stresses and buckling loads on the panel. Since other studies on the compressive behavior of sandwich panels are underway, a series of picture frame shear tests will be conducted at RT and 589K (600°F) and the experimental results will be compared with analytical predictions.

CELION/LARC-160 FABRICATION DEMONSTRATION COMPONENT

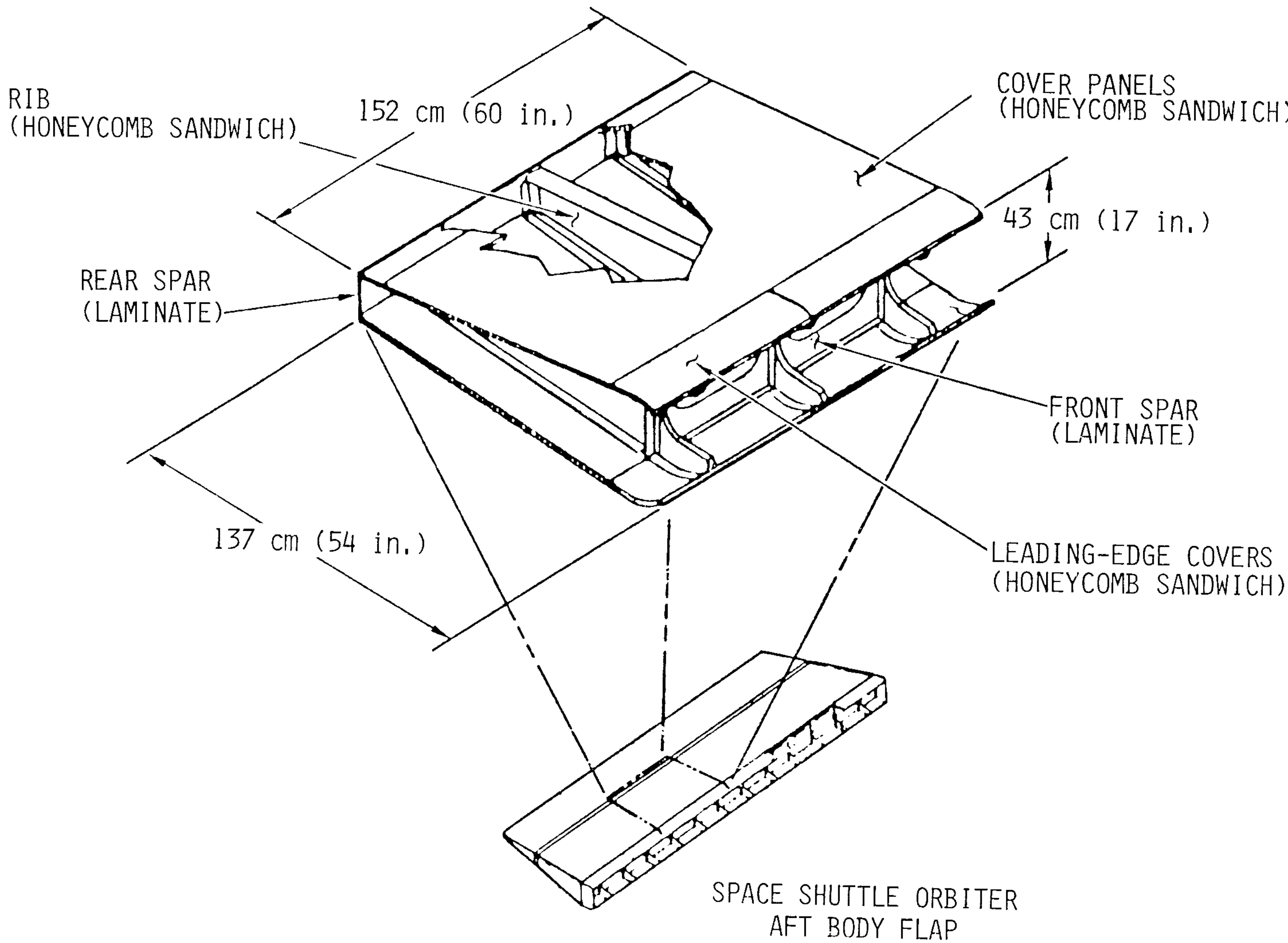

Figure 17.

CELION/LARC-160 FABRICATION DEMONSTRATION COMPONENT

(Figure 17)

A sketch of the component that is being constructed to demonstrate the capability to fabricate complex structures with Celion/LARC-160 is shown in the figure. The component represents a segment of a graphite/polyimide composite aft body flap for the space shuttle orbiter. Overall dimensions for the component are 152 cm x 137 cm (60 in. x 54 in.). Upper and lower cover panels, ribs, and leading edges will utilize honeycomb sandwich construction whereas the front and rear spars will be solid laminates. The leading-edge covers form curved surfaces. Dimensional tolerances that would normally be imposed on flight hardware are being used in fabrication of the component. Metallic attachments will be utilized to apply static and dynamic loads to the component to demonstrate structural integrity. Prior to testing, a thorough nondestructive inspection of the component will be performed.

PRELIMINARY TEST PLAN FOR BODY FLAP SECTOR

- o STATIC LIMIT LOAD
- o 125 THERMAL CYCLES FROM 117K (-250°F) TO 589K (600°F)
- o 4 LIFE TIMES OF SIMULATED FLIGHT LOADS
- o 4 LIFE TIMES OF ACOUSTIC LOADS
- o STATIC ULTIMATE LOAD
- o MACHINE COUPONS AND MECHANICALLY LOAD

Figure 18.

PRELIMINARY TEST PLAN FOR BODY FLAP SECTOR

(Figure 18)

An outline of the preliminary test plan for the Celion/LARC-160 aft body flap sector is shown in the figure. Strain, deflection, temperature and acceleration measurements will be made at key locations on the structure and the response will be compared to predicted behavior. Static limit loads for each design condition will be applied first. Next, the component will be thermally cycled 125 times from 117K to 589K (-250°F to 600°F). Four life times of simulated flight loads and four life times of acoustic loads will be applied next to demonstrate fatigue endurance. After the fatigue tests, the component will be subjected to static ultimate load for the most critical design condition. After each static load test and at periodic intervals during thermal cycling and fatigue testing, the component will be inspected for damage. Upon completion of the static ultimate load test, coupons will be machined from various locations in the component and mechanically loaded to failure to obtain additional information on the reliability of the component.

SUMMARY

- o STRUCTURAL COMPONENTS HAVE BEEN FABRICATED WITH TWO GR/PI COMPOSITES
- o EPOXY SIZED GRAPHITE FIBERS ARE SUITABLE FOR UTILIZATION IN GR/PI COMPOSITES FOR 125 HOURS AT 589K (600°F)
- o STRUCTURAL EFFICIENCY OF MODERATELY LOAD GR/PI PANELS HAS BEEN VERIFIED
- o NO TECHNICAL ROAD BLOCKS TO BUILDING A GR/PI COMPOSITE BODY FLAP HAVE BEEN IDENTIFIED

SUMMARY

(Figure 19)

Accomplishments and the outlook for graphite/polyimide composite structures are briefly outlined in the figure. Laminates, skin-stiffened and honeycomb sandwich panels, chopped fiber moldings, and structural components have been fabricated with Celion/LARC-160 and Celion/PMR-15 composite materials. Interlaminar shear and flexure strength data obtained on as-fabricated specimens and specimens that had been exposed for 125 hours at 589K (600°F) indicate that epoxy sized and polyimide sized Celion graphite fibers exhibit essentially the same behavior in a PMR-15 matrix composite. Analyses and tests of graphite/polyimide compression and shear panels indicate that utilization in moderately loaded applications offers the potential for achieving a 30 to 50 percent reduction in structural mass compared to conventional aluminum panels. Data on effects of moisture, temperature, thermal cycling and shuttle fluids on mechanical properties indicate that both LARC-160 and PMR-15 are suitable matrix materials for a graphite/polyimide aft body flap. No technical road blocks to building a graphite/polyimide composite aft body flap have been identified.

REFERENCES

1. Davis, John G., Jr.: Composites for Advanced Space Transportation Systems - (CASTS). Graphite/Polyimide Composites, NASA CP-2079, 1979, pp. 5-18.

2. Davis, John G., Jr., compiler: Composites For Advanced Space Transportation Systems - (CASTS). NASA TM-80038, 1979.

3. Sheppard, C. H.; Hoggatt, J. T.; and Symonds, W. A.: Manufacturing Processes For Fabricating Graphite/PMR-15 Polyimide Structural Elements. NASA CR-159129, 1979.

4. Sheppard, C. H.; Hoggatt, J. T.; and Symonds, W. A.: Manufacturing Processes For Fabricating Graphite/PMR-15 Polyimide Structural Elements - Task J Variability Program. NASA CR-159182, 1979.

5. Leahy, J. D.: Development and Demonstration of Manufacturing Processes For Fabricating Graphite/LARC-160 Polyimide Structural Elements. (7th Quarterly Progress Report for Contract NAS1-15371), July 1980. (Available as NASA CR-159303.)

6. Maximovich, M. G.; Bergren, O.; and Lockerby, S.: Development of LARC 160/NR150B2 Polyimide Graphite Hybrid Composites. NASA CR-159196, 1980.

7. Clark, Ronald K.; and Lisagor, W. Barry: Effects of Method of Loading and Specimen Configuration on Compressive Strength of Graphite/Epoxy Composite Materials. NASA TM-81796, 1980.

8. Mills, J. Steven; Herakovich, C. T.; and Davis, John G., Jr.: Transverse Microcracking in Celion 6000/PMR-15 Graphite-Polyimide. VPI-E-79-35, VPI&SU, 1979.

9. Williams, Jerry G.; and Mikulas, Martin M., Jr.: Analytical and Experimental Study of Structurally Efficient Composite Hat-Stiffened Panels Loaded in Axial Compression. AIAA Paper No. 75-754, May 1975.

AN INVESTIGATION OF POSSIBLE ELECTRICAL HAZARDS OF CARBON FIBER COMPOSITES

Robert J. Huston

INTRODUCTION

The use of high-performance composite structures in aerospace vehicles is anticipated to increase significantly in the next few years. Most of the technical obstacles to successful application have been overcome and several advantages of carbon composites (lightweight, high strength and high stiffness) are prompting increased consideration and application. However, the accidental release of long free fibers from a carbon fiber plant and laboratory tests developed a concern that a little-recognized consequence of the properties of carbon fibers could have significant adverse economic impact (ref. 1). Since carbon fibers are electrically conductive, lightweight, and have small diameters, they could create a hazard to electrical and electronic equipment if released in the atmosphere; for example, by an aircraft crash-fire. Fibers released in such fires may become airborne, be transported by the wind over a large area, and potentially damage equipment belonging to a large segment of the population.

As part of a federal study of the potential hazard associated with the use of carbon fibers, NASA has performed an assessment of the public risk associated with the release of carbon fibers from crash-fire accidents of civil aircraft having carbon composite structures. The overall national impact was shown to be extremely low in 1993, the year chosen as a focus for the study. Personal injury was found to be extremely unlikely.

Based on these findings, the risk of electrical failure from carbon fibers should not prevent the exploitation of composites in aircraft, and additional protection of aircraft avionics to guard against carbon fibers is unnecessary.

ORGANIZATION OF U. S. CARBON FIBER STUDY

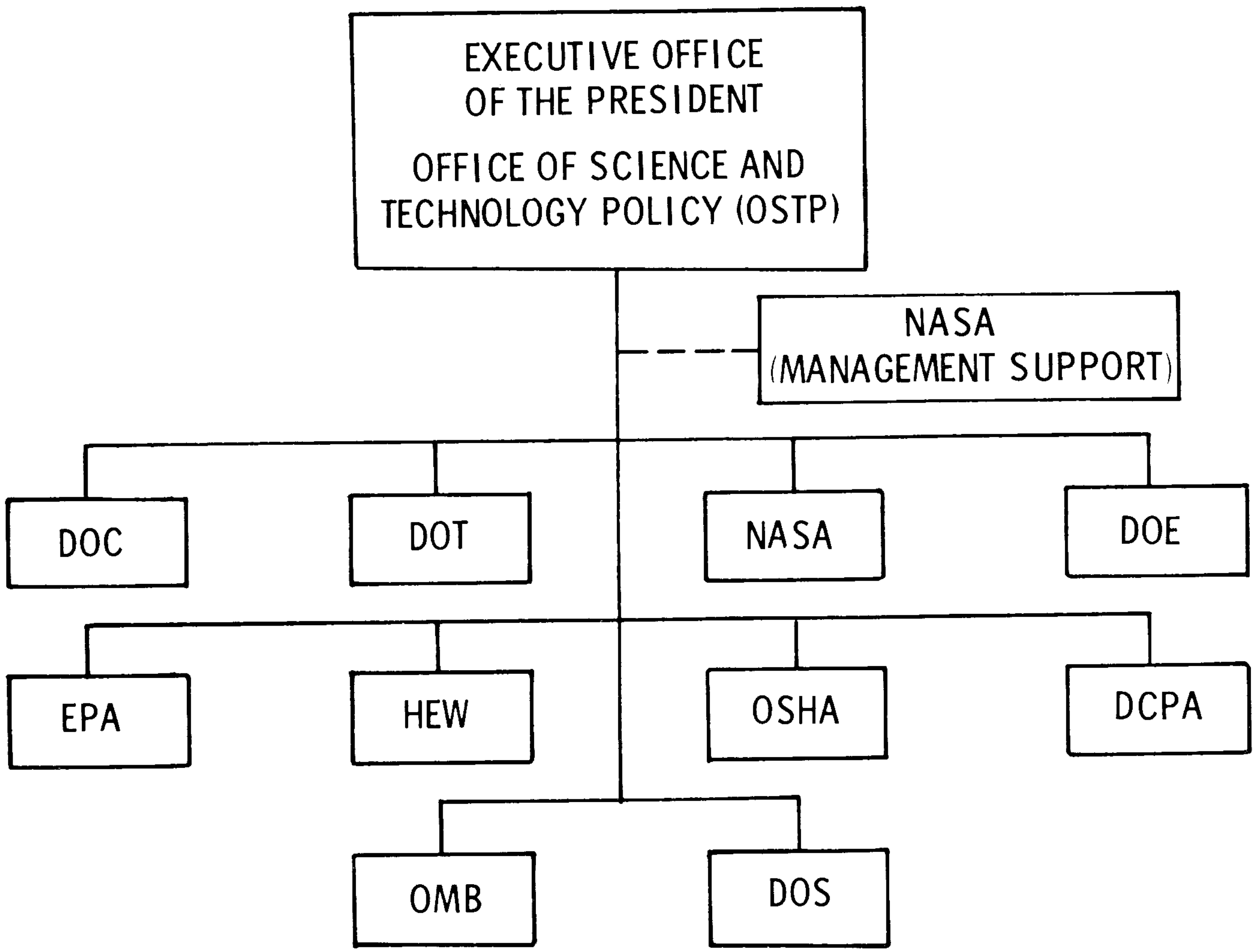

Figure 1.

ORGANIZATION OF U.S. CARBON FIBER STUDY

(Figure 1)

The possibility of damage to electrical equipment by carbon fibers was recognized by the government and in July 1977, the Director of the Office of Science and Technology Policy was directed by the President to conduct a study of the potential problems associated with the use of carbon fibers and to provide a plan for possible federal action. The study revealed that, in addition to major growth in the use of carbon fibers in military and civilian aircraft, a significant amount is used in consumer products (skis, fishing rods, golf clubs, etc.) and the amount used in automobile applications is likely to soar. Based on the study results, a national program on carbon fiber was established and announced in 1978 (reference 1). Responsibility for elements of the program was delegated to the agencies listed in the figure. The areas of carbon fiber investigation assigned to each agency were consistent with the normal responsibilities of the agency.

CARBON FIBER RISK ASSESSMENT

PROGRAM OBJECTIVES

- QUANTIFY RISK ASSOCIATED WITH ACCIDENTAL RELEASE OF CARBON FIBERS FROM CIVIL AIRCRAFT HAVING COMPOSITE STRUCTURES

- ASSESS THE NEED FOR PROTECTION OF CIVIL AIRCRAFT FROM ACCIDENTALLY RELEASED CARBON FIBER

Figure 2.

CARBON FIBER RISK ASSESSMENT PROGRAM OBJECTIVES

(Figure 2)

Since NASA has had heavy involvement in carbon fiber composite research and in the development of composites for use in civil aircraft, NASA was asked to quantify the risks associated with accidental release of carbon fibers from civil aircraft and to assess the need for protection of civil aircraft from accidentally released fibers.

Responsibility for the direction of the NASA study was assigned to the Graphite Fibers Risk Analysis Program Office, Materials Division, Structures Directorate of the Langley Research Center. The program office initiated studies, gathered the necessary data to perform a risk analysis, develop a risk computation method, and develop the conclusions and findings of this report.

RISK ANALYSIS SCENARIO

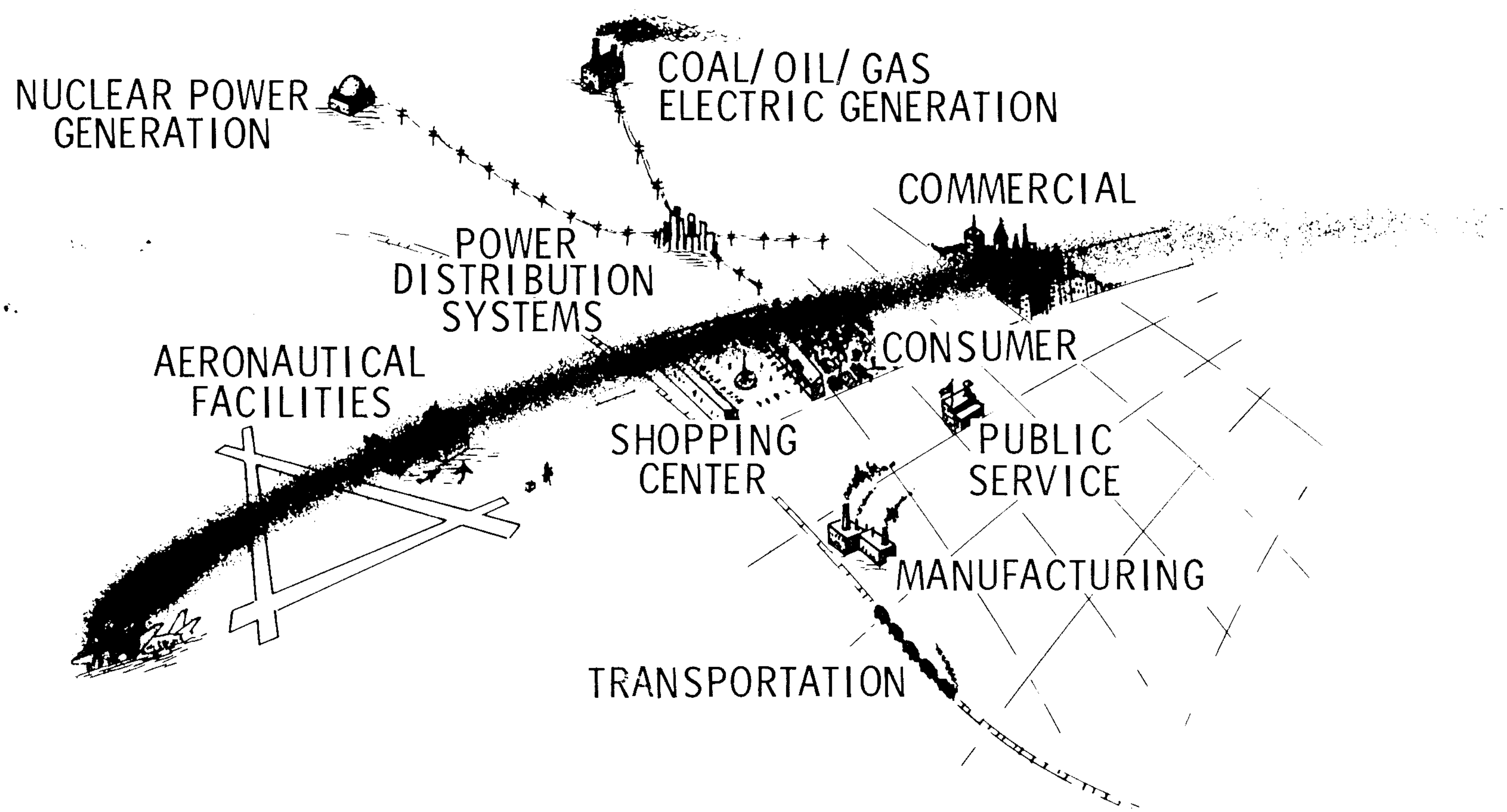

Figure 3.

RISK ANALYSIS SCENARIO

(Figure 3)

For the risk analysis, we have identified an accident scenario for evaluation that involves crashes of civil aircraft, which in the case of large air-transport aircraft, usually occur near large airports. In this scenario, a burning aircraft containing carbon composites releases smoke, soot and carbon fibers to be wafted downwind from the fire and, depending upon the wind direction, have the potential of adversely impacting on transportation, manufacturing, and public service facilities as well as the homeowner, commercial facilities and the power distribution systems.

RISK ANALYSIS ELEMENTS

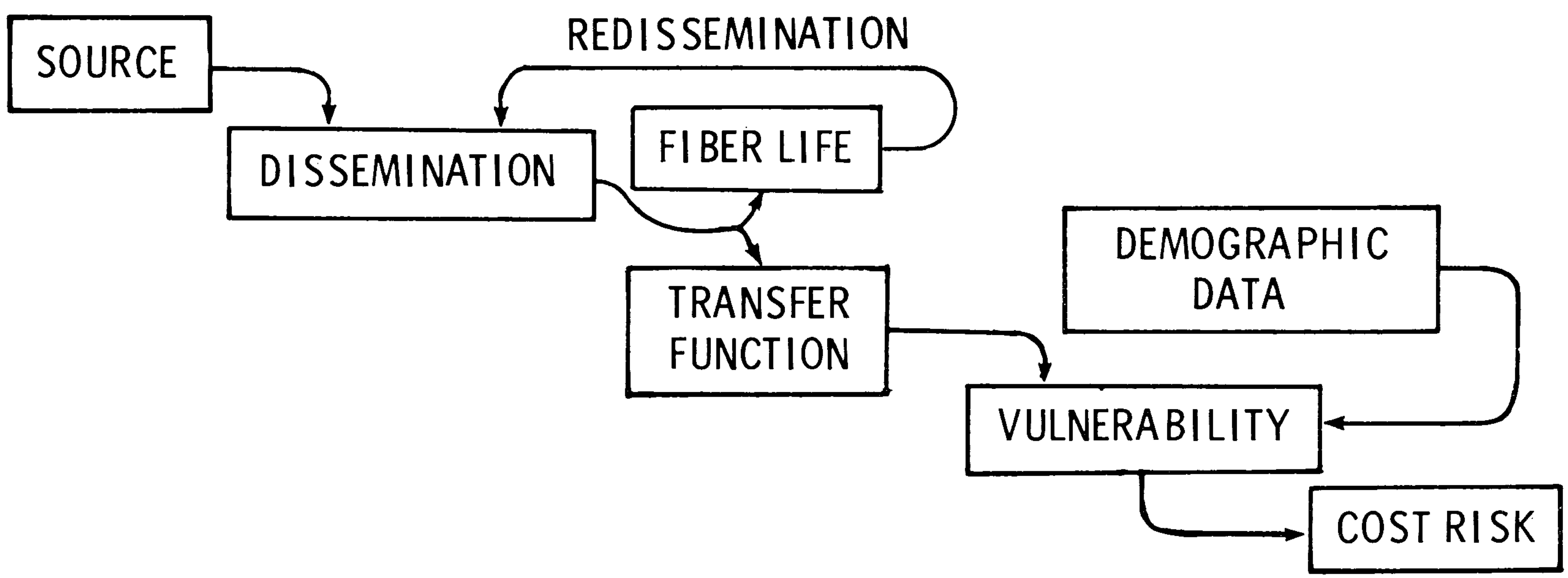

Figure 4.

RISK ANALYSIS ELEMENTS

(Figure 4)

Another dimension of the potential hazard is illustrated by the flow of analysis through the various elements that must be considered in the risk assessment. Data and methods of analysis had to be gathered or developed for each element.

Each element represents an independent area of study which was integrated into a larger system study. The element of source refers to all of the factors affecting the source of carbon fibers. These included carbon fiber usage projections, aircraft accident experience, fire damage to aircraft, fire dynamics, fire chemistry, and carbon composite fiber release characteristics. The element of dissemination refers to the atmospheric dissemination of the fibers released from a burning composite. Factors included were weather variables, amount of fuel burned and rate, and fiber fall rates. The element of fiber life and the associated redissemination of fibers refers to the potential long-term contamination of an area and to repeated exposures to the same fiber. This element included such factors as fiber dimensions and shape, wind velocity, surface condition and terrain type. The transfer function element includes filter efficiencies necessary to predict the penetration of building and equipment cases in order to evaluate the ratio of internal to external exposures to carbon fiber. The element of vulnerability included the evaluation of contaminated electrical equipment of all types with variables such as fiber length, diameter, exposure, bulk resistance, contact resistance, voltage, current, arcs, and failure modes. The element of demographics includes the population data required to enumerate electrical equipment in homes, businesses, industries, and public support facilities. The last element involved the determination of the economic impact of the unwanted consequence of a carbon fiber release. The element includes such factors as the domestic product of a plant, repair cost, lost time, overtime, and clean up costs. The economic impact in this study is stated in 1976 dollars.

CIVIL AIRCRAFT CF USAGE PROJECTION

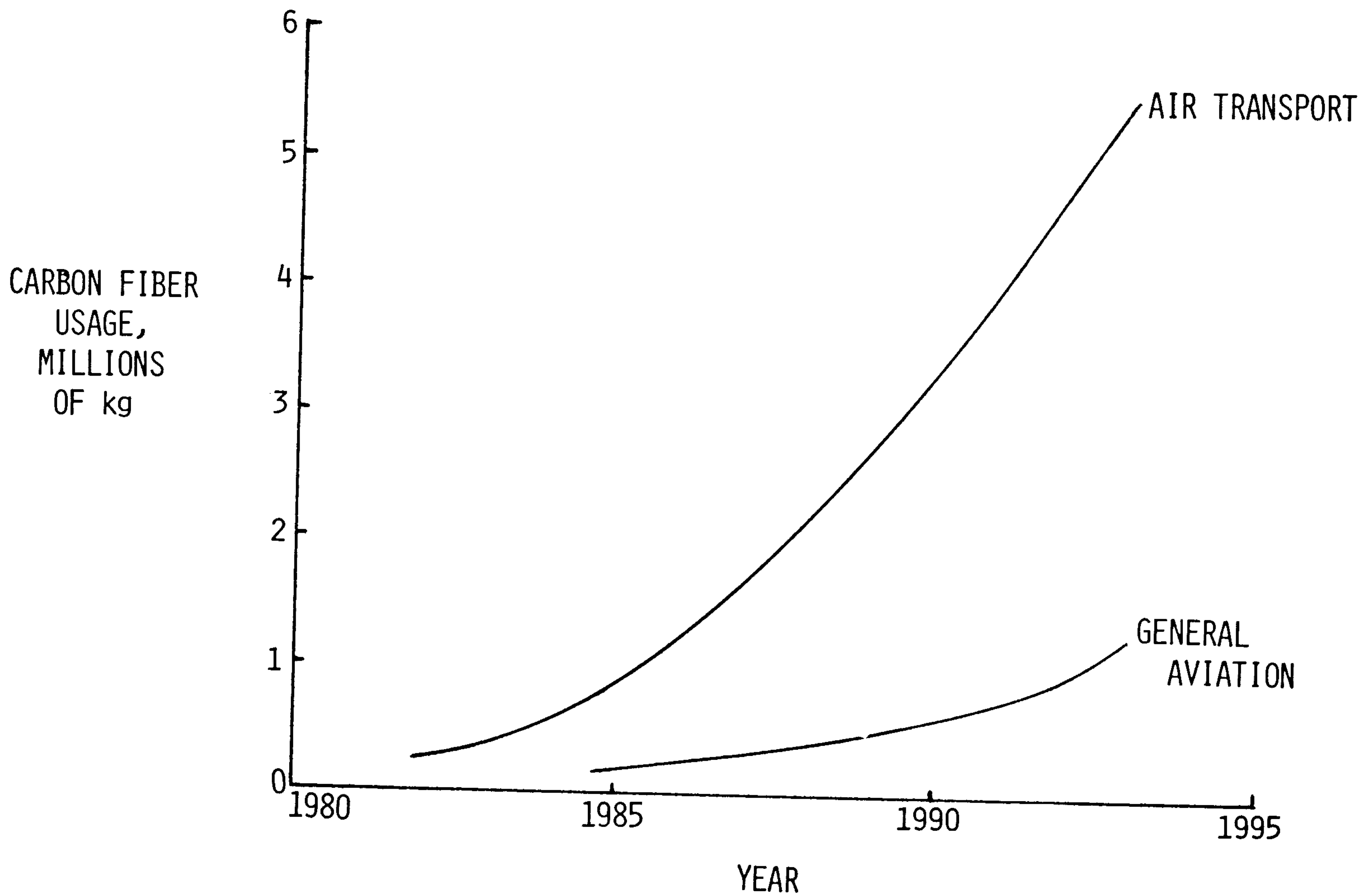

Figure 5.

CIVIL AIRCRAFT CARBON FIBER USAGE PROJECTION

(Figure 5)

At the time that the study was initiated, very few carbon composite parts of civil aircraft were scheduled for series production but extensive growth in air-transport usage was anticipated. Therefore, a two-part projection of the future use of carbon composite was developed. As part of the risk assessment, the manufacturers of commercial transport aircraft calculated the weight of carbon composite currently envisaged for each aircraft series to be built through 1993. This information was reviewed in light of the manufacturers' and FAA estimates of fleet size, fleet mix, and airplane retirements to predict the distribution of carbon composite on the fleet of air-transport aircraft. By 1993, about 73% of air-transport aircraft are expected to use at least some carbon composites and 0.5% of the fleet are expected to use as much as 10,954 kg of carbon fiber. This represents up to 10% of the airframe mass.

The figure shows the projection of the amount of carbon fiber in service for both air-transport and general aviation aircraft during the years 1980 through 1993. The projection for general aviation aircraft (which includes all other fixed- and rotary-wing aircraft) was based on projections from 1978 usage, increased at the same relative rate as shown for commercial air-transport aircraft.

CARBON FIBER RESIDUES RELEASED FROM FIRES

SINGLE FIBERS
SIZE: 3 TO 8 μm DIA., 0.1 TO 15 mm LONG
FALL RATE: 2 cm/sec
DISPERSION RANGE: 0 TO > 100 km

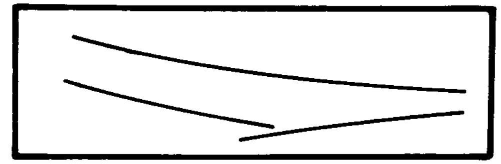

CLUSTERS OR LINT
HUNDREDS OF FIBERS
FALL RATE: 10 TO 20 cm/sec
DISPERSION RANGE: 0 TO 10 km

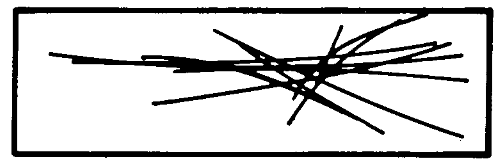

STRIPS
SINGLE LAMINA: 0.15 mm THICK, VARYING LENGTHS AND WIDTHS
FALL RATE: 1 TO 5 m/sec
DISPERSION RANGE: 0 TO 2 km

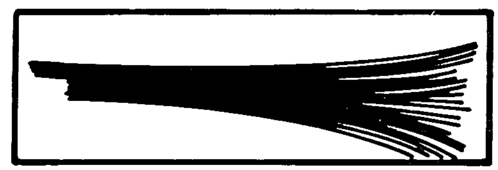

IMPACT FRAGMENTS
MULTIPLE LAMINATE PIECES
OCCUR ONLY IN IMMEDIATE VICINITY OF CRASH-FIRE

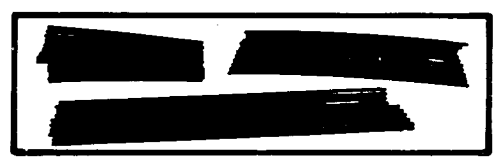

Figure 6.

CARBON FIBER RESIDUES RELEASED FROM FIRES

(Figure 6)

Many experiments in releasing fibers from burned composites were conducted at the Naval Surface Weapons Center, Dahlgren, Virginia. The tests, run in an enclosed room, allowed the complete containment of all fiber materials given off during the test. The test procedure involved the combustion of flat-plate carbon composite specimens up to 0.1 m^2 (1 ft^2) in area, of a variety of thicknesses, with a propane-air flame. Some of the tests involved the destruction, subsequent to the fire, of the composite panel with 57 grams (2 ounces) of explosive placed beneath the specimen. The figure shows the types of materials collected during a single test.

Single fibers had the potential for the greatest range of distribution due to their very slow settling rate, while lint or clusters of single fibers fell much faster than individual fibers. A third class of residue consisted of yet faster settling strips of fibers, generally resulting from a single ply of crossplied composite, with the fibers being bound together either by incompletely burned resin or the char formed by the burned resin. A fourth broad class of fibrous residue was fragments of the composite, widely varied in size and shape. These fragments, which were so heavy that in outdoor tests they were rarely found beyond the immediate vicinity of the fire, generally resulted only from a substantial impact to the burning or burned composite. Rarely were they formed as the result of a simple fire.

The emphasis of this study was placed on the quantification of single carbon fibers released from fire tests: First, because the spread of single fibers was considered to be the most extensive due to their buoyancy, and secondly, because they were most likely to penetrate the filters and cases of equipment to reach the vital interiors and cause electrical damage.

RESIDUAL MATERIAL

20 MINUTE BURN OF F-16 CARBON FIBER-EPOXY TAIL

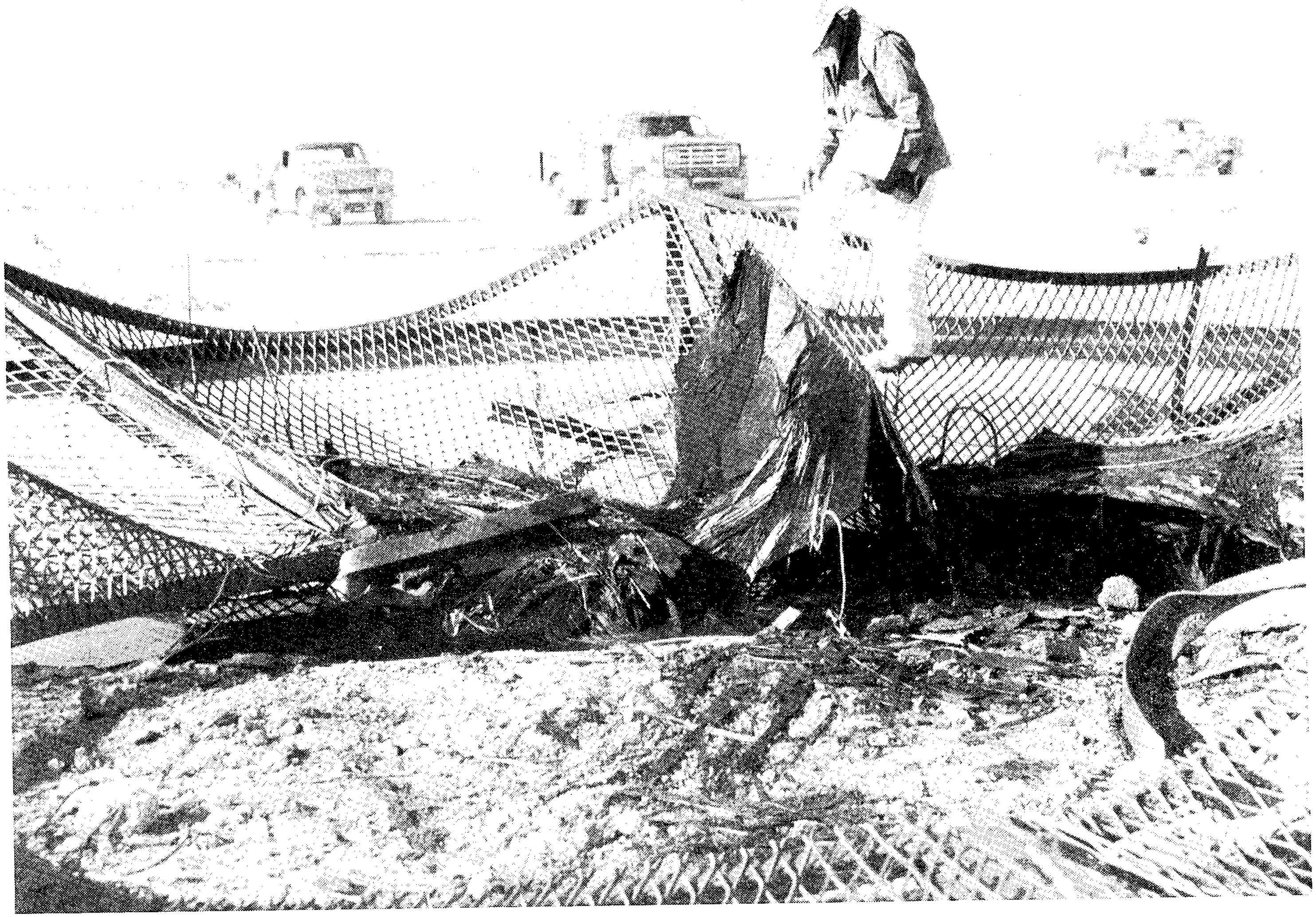

Figure 7.

RESIDUAL MATERIAL
(20-MINUTE BURN OF F-16 CARBON FIBER-EPOXY TAIL)

(Figure 7)

The figure shows typical residual material left from a composite burn. The debris in the photograph was left after a 20-minute outdoor burn of the vertical and horizontal stabilizer from a fighter aircraft. A significant portion of the structure remained in an identifiable shape in spite of major delaminations, oxidation of most matrix resin and the release of fibers. In the foreground are a large number of strips. (The expanded wire mesh on which the man is standing was the test stand that had supported the stabilizer about 2 m above the ground, but had sagged downward during the fire).

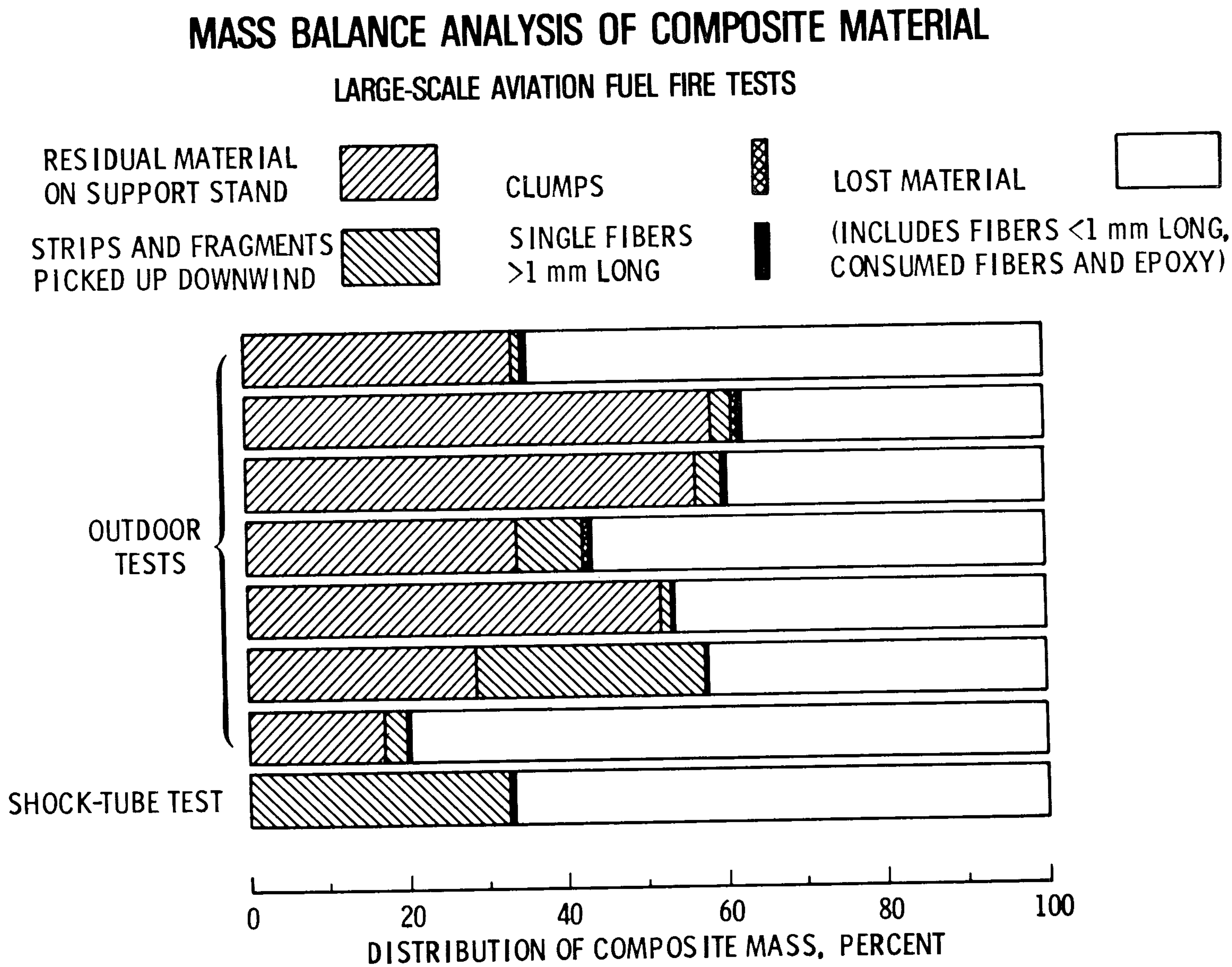
MASS BALANCE ANALYSIS OF COMPOSITE MATERIAL
LARGE-SCALE AVIATION FUEL FIRE TESTS
RESIDUAL MATERIAL ON SUPPORT STAND
STRIPS AND FRAGMENTS PICKED UP DOWNWIND
CLUMPS
SINGLE FIBERS >1 mm LONG
LOST MATERIAL
(INCLUDES FIBERS <1 mm LONG, CONSUMED FIBERS AND EPOXY)
OUTDOOR TESTS
SHOCK-TUBE TEST
0
20
40
60
80
100
DISTRIBUTION OF COMPOSITE MASS, PERCENT

Figure 8.

MASS BALANCE ANALYSIS OF COMPOSITE MATERIAL (LARGE-SCALE AVIATION FUEL FIRE TESTS)

(Figure 8)

A mass balance analysis of the composite materials placed in each of the large-scale aviation fuel fire tests is shown in the figure. Between 15 and 60% of the original mass remained as residual material after the fire, except for the test in the shock tube. In the shock-tube test, the composite was exposed for 2½ hours in a wire basket that rotated about a horizontal axis to tumble the parts until all residue had been dispersed. In the shock-tube tests, the total mass of single fibers released was 0.75% of the initial carbon fiber mass in the fire. In the outdoor tests, identifiable strips or fragments accounted for a significant portion of the original mass, while single fibers accounted for only 0.1% to 0.23% of the fiber originally available (0.07 to 0.16% of original composite mass). Clumps of fibers accounted for approximately 2.5 times the single-fiber mass. This left between 40 and 80 percent of the original mass not specifically accounted for. Up to 30 percent of the original mass was epoxy matrix and most of this material was consumed in the fire. Thus, at least 10 percent and perhaps as much as 50% of the original mass was "lost" carbon fiber. A substantial portion of the lost carbon was undoubtedly consumed by oxidation in the fire.

The amount of residual material or debris remaining was found to be many times that lofted into the air by the fire. This debris represents a potential delayed source of airborne carbon fiber and therefore should be removed. Care should be taken to prevent agitation of this debris before and during the clean-up. Fiber "hold-down" chemicals, such as polyacrylic acid (PAA), are being developed to prevent the spread of free fibers from crash sites. When sprayed on carbon composite debris, the chemical coats the carbon fibers and prevents them from being released upon handling of the fire debris.

BALLOON-SUPPORTED "JACOB'S LADDER" FIRE PLUME SAMPLING NET

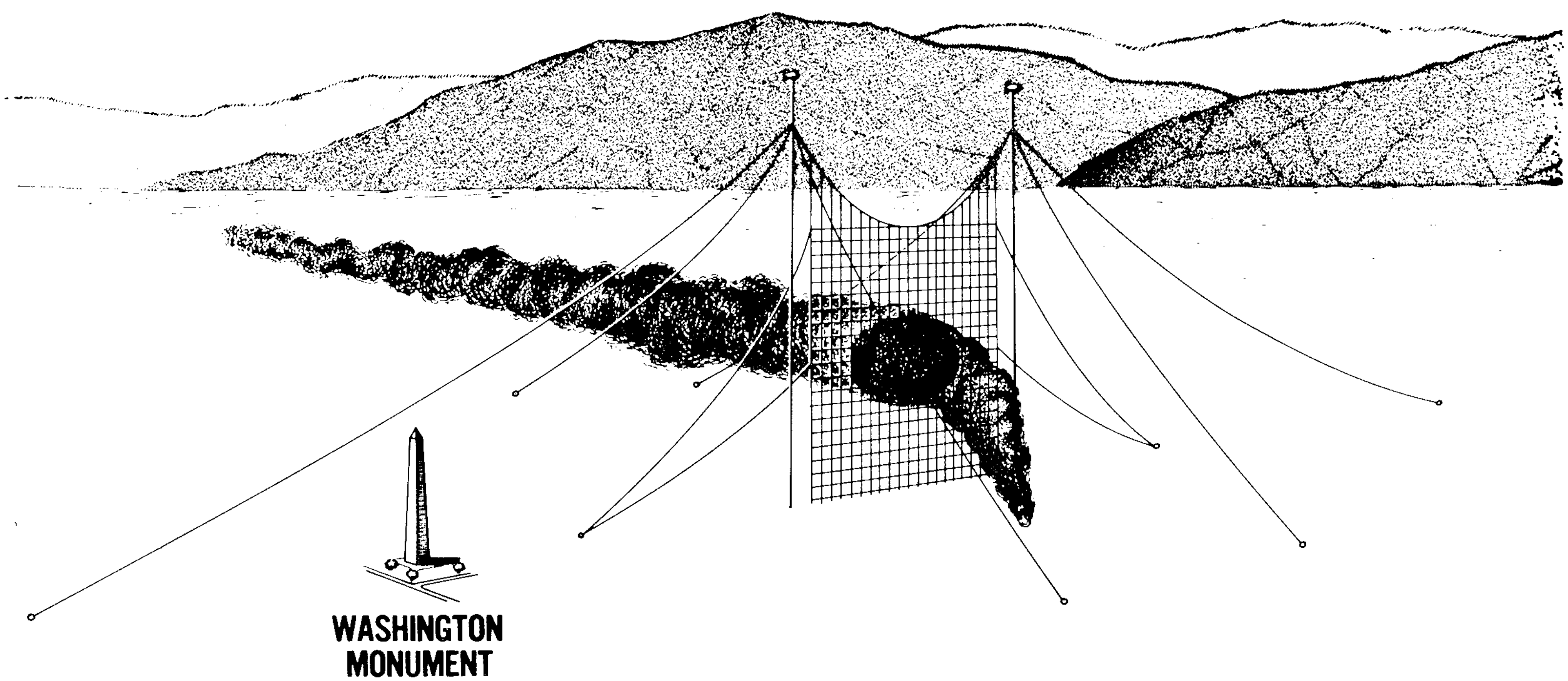

Figure 9.

BALLOON-SUPPORTED "JACOB'S LADDER" FIRE PLUME SAMPLING NET

(Figure 9)

In addition to hundreds of small composite specimen burn tests using propane fuel, a small number of large scale fire tests were conducted using aviation fuel. Outdoor pool-fire tests were conducted in which composite structural parts having aggregate masses of 45 kg or more per test were burned. Pool diameter (10.7 m) and length of burn (20 min.) were chosen to simulate a representative aircraft fire. Tests were conducted when weather conditions and wind directions assured maximum likelihood of accumulating the desired data. The efflux of carbon fibers was monitored in several ways. Fibers were collected just above the flames by an overhead array of samplers and about 60 m downwind by a vertical array. A huge "Jacob's Ladder" (305 m high by 305 m wide) was supported by two barrage balloons about 140 m downwind of the fire. It supported 565 samplers to monitor quantities and sizes of fibers. Over 1300 passive samplers were mounted about 0.5 m above ground in a fan-shaped array extending 19 km downwind of the fire to measure fiber dissemination. In addition, strips and larger fragments released from the fire and deposited as far as 1 km from the fire were collected by search teams and weighed for mass-balance accounting.

SHOCK TUBE FIRE FACILITY

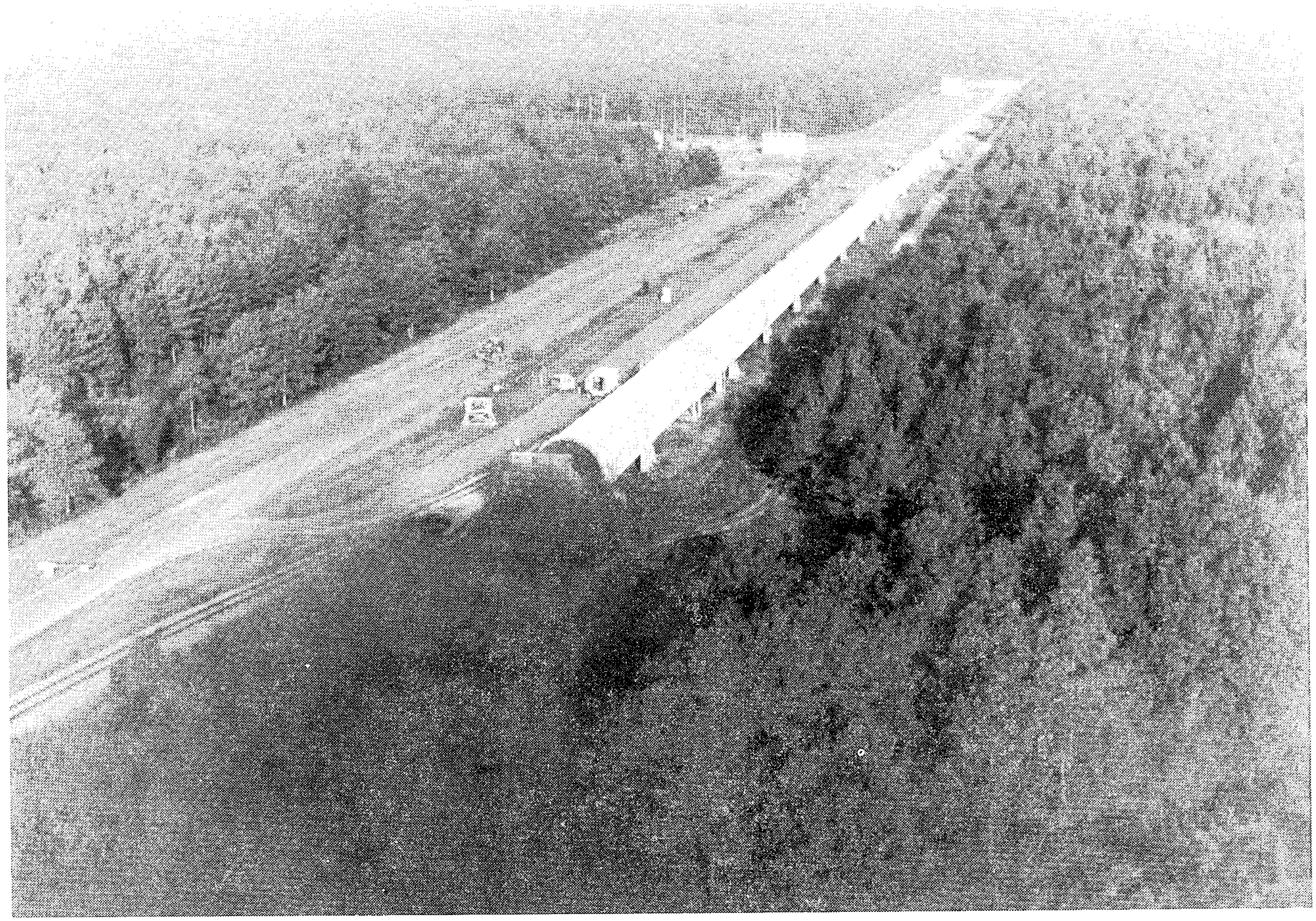

Figure 10.

SHOCK-TUBE FIRE FACILITY

(Figure 10)

One series of indoor large-scale fire tests was conducted. A part of a large steel shock-tube structure was modified to burn carbon fiber composites in an aviation jet-fuel fire. The fire was ignited inside the tube near its mid-length. The fire-released fibers, combustion products and heated air were transported approximately 270 m through the tube by exhaust fans installed in the large end. Samplers monitored quantities and sizes of carbon fibers released by the fire. In addition, electronic equipment was exposed in the tube near the exhaust end to obtain data on the effect of fire-released fibers on equipment vulnerability.

SUMMARY OF EFFECTS OF DISTURBANCE ON SINGLE FIBER RELEASE FROM COMPOSITES

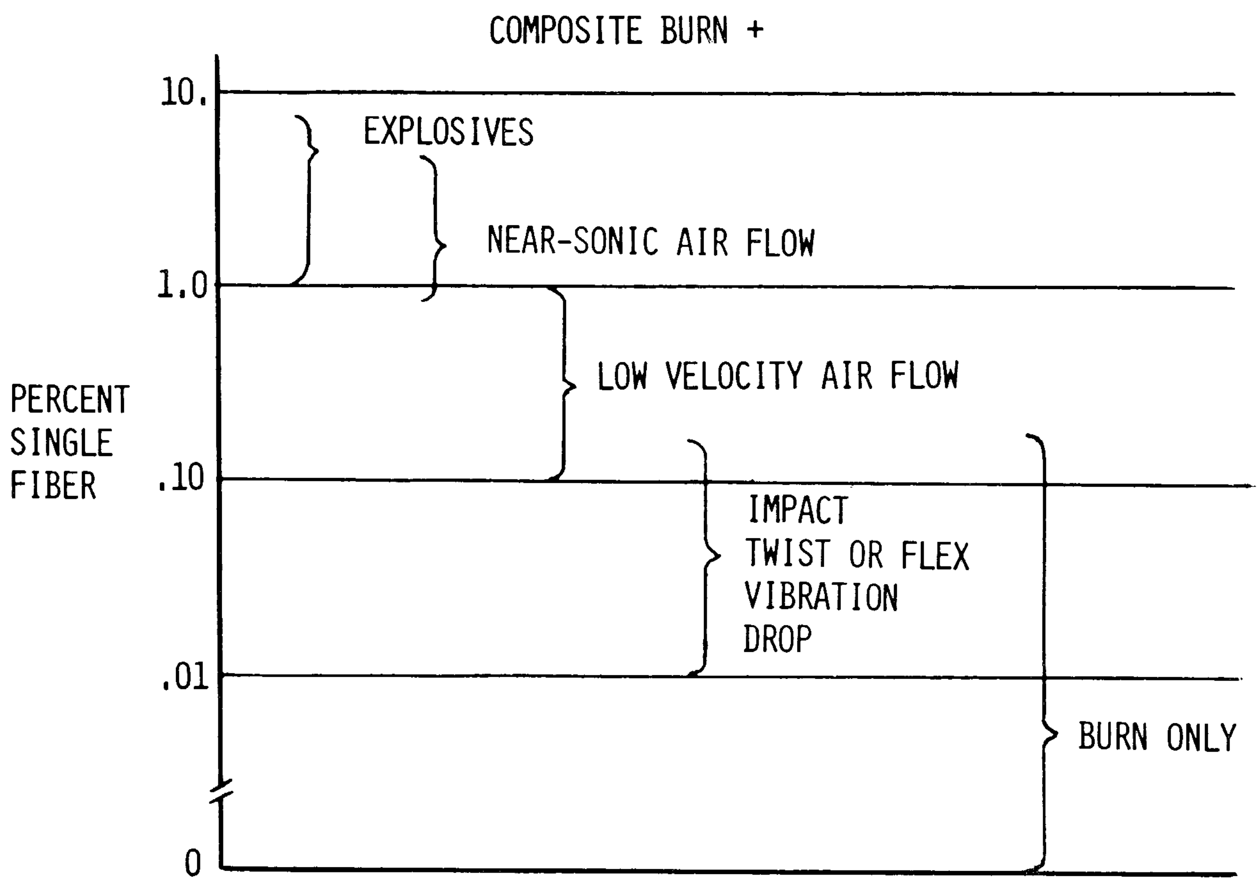

Figure 11.

SUMMARY OF EFFECTS OF DISTURBANCES ON SINGLE FIBER RELEASE FROM COMPOSITES

(Figure 11)

The outdoor tests confirmed earlier laboratory tests in which composites were burned until severely damaged and were subjected to mechanical agitation, airstreams and explosives. A summary of results from a large number of tests are plotted in the figure. Single fibers accounted for less than 0.2% of the original fiber mass available when the composite was burned without disturbance. When tests included agitation of the debris by falling masses or low velocity airflow (30 knots), single fibers accounted for 0.001% to 1% of the original fiber mass available. Only when near-sonic air blasts or explosives agitated the debris did single fibers account for more than 1% of the original fiber mass.

Based on the data shown in the figure, fiber-release values were chosen to represent the upper bounds of these data in risk assessment. For those aircraft crash-fires that had no explosion, 1% of the originally available fiber in the burn composite was assumed to be released as single fibers longer than 1 mm. In the remaining crash-fires, explosions were involved and 3.5% of the available fiber was assumed to be released.

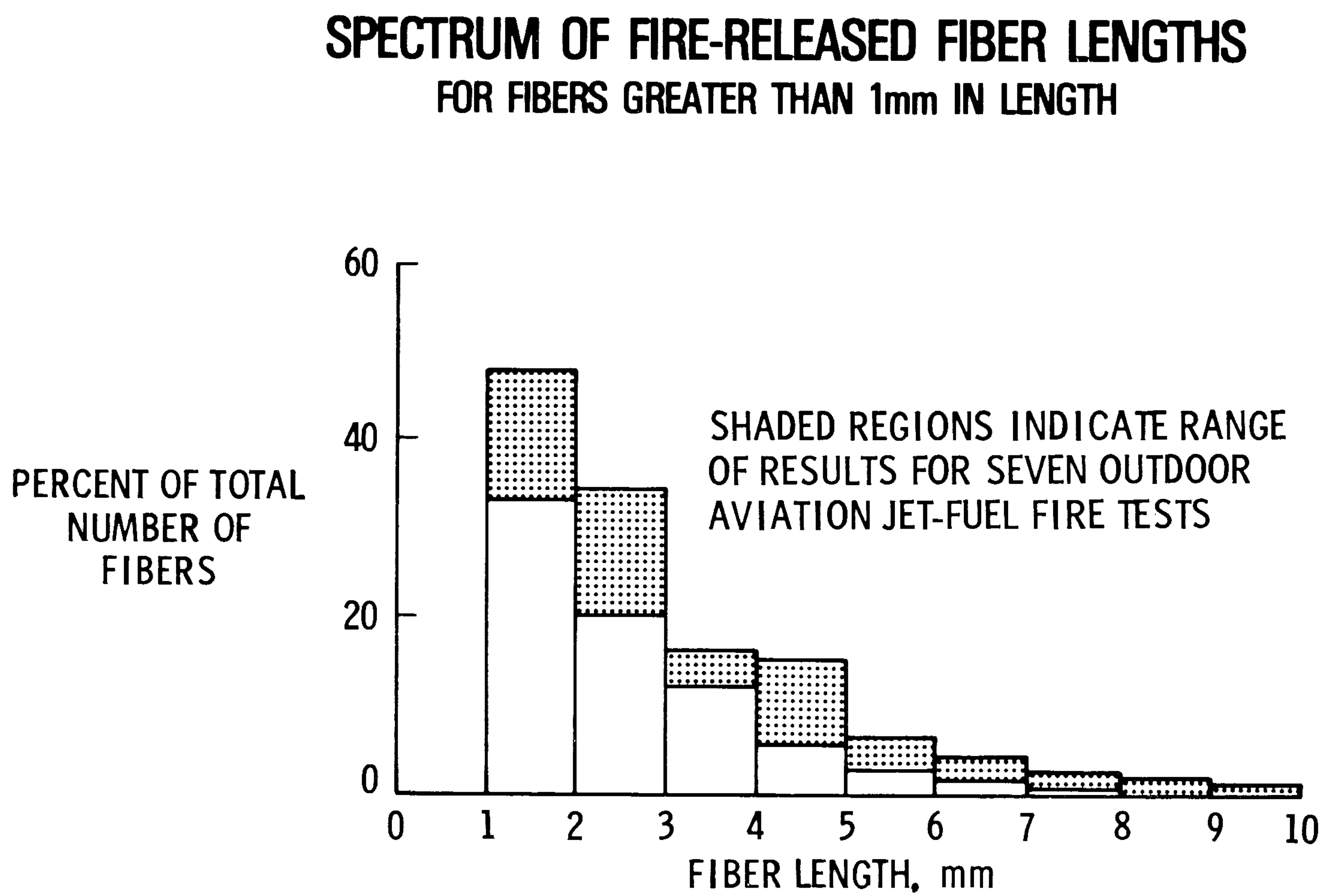
SPECTRUM OF FIRE-RELEASED FIBER LENGTHS
FOR FIBERS GREATER THAN 1mm IN LENGTH
PERCENT OF TOTAL NUMBER OF FIBERS
60
40
20
0
SHADED REGIONS INDICATE RANGE OF RESULTS FOR SEVEN OUTDOOR AVIATION JET-FUEL FIRE TESTS
0
1
2
3
4
5
6
7
8
9
10
FIBER LENGTH, mm

Figure 12.

SPECTRUM OF FIRE-RELEASED FIBER LENGTHS (FOR FIBERS GREATER THAN 1 mm IN LENGTH)

(Figure 12)

Single fibers observed in these studies were much shorter than originally expected. To assess electrical risk, only those fibers longer than 1 mm were of interest. Their lengths were distributed as indicated in the figure for 7 outdoor tests. The shaded portions of the figure represent the range of data. A closely similar distribution of lengths was observed in nearly 300 laboratory tests which included significant variations, such as in the degree of agitation of the debris. Considering the many variables in the tests, this agreement is considered excellent. In each set of data, the preponderance of fibers were between 1 and 3 mm long, and very few fibers were longer than 4 mm. The mean length of fibers longer than 1 mm was between 2 and 3 mm. A 2 mm mean length is equivalent to 5×10^9 fibers per kilogram. This number was used in the risk assessment computations.

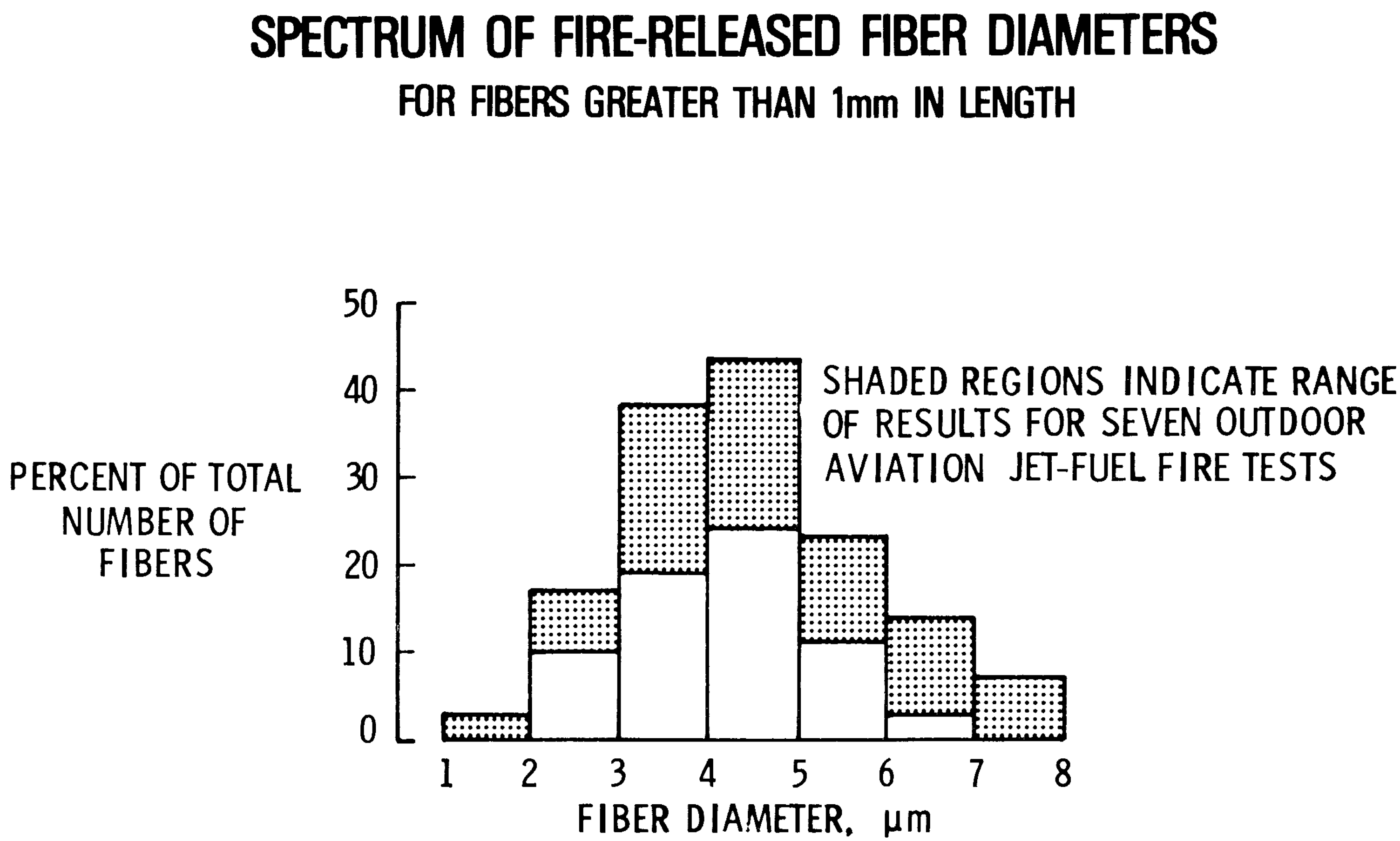
SPECTRUM OF FIRE-RELEASED FIBER DIAMETERS
FOR FIBERS GREATER THAN 1mm IN LENGTH
PERCENT OF TOTAL NUMBER OF FIBERS
50
40
30
20
10
0
1
2
3
4
5
6
7
8
FIBER DIAMETER, µm
SHADED REGIONS INDICATE RANGE OF RESULTS FOR SEVEN OUTDOOR AVIATION JET-FUEL FIRE TESTS

Figure 13.

SPECTRUM OF FIRE-RELEASED FIBER DIAMETERS
(FIBERS GREATER THAN 1 mm IN LENGTH)

(Figure 13)

The phenomenon that led to short fibers almost always also led to small fiber diameters. Sample fibers were analyzed to determine their diameters. Clearly, most diameters were reduced significantly. The means of these samples were 4.0 to 4.7μm. The shaded portion of the figure represents the ranges of values observed.

The possible health consideration of fibers which were smaller than those of electrical concern led to a study to assess the prevalence of those fibers which fell in a domain conservatively selected to define fibers of potentially respirable size (less than 80μm long, less than 3μm in diameter, and with length-to-diameter ratios from 3:1 to 10:1.) The results of that study disclosed that no more than 23% of the fibers released from aviation jet-fuel fire tests fell in that size domain. In the absence of any evidence that carbon fibers of any size could have adverse health effects on humans (except for the cutaneous allergic reactions typically caused by many fibrous substances), comparisons were made to the quantities of concern in the case of asbestos fibers. Using the conditions and some of the results of one of the large-scale, outdoor composite burn tests as the scenario for an extreme-case aircraft crash-fire, a maximum concentration of respirable-sized carbon fibers which was carried downwind in the densest part of the smoke plume was computed (reference 2). The total exposure to carbon fibers from the extreme-case accidental crash-fire was predicted to be less than one percent of the OSHA-allowable 8-hour exposure to asbestos fibers.

Field tests conducted during the outdoor tests showed lower values than had been calculated for the extreme case in reference 2. The actual maximum concentration of potentially respirable fibers 140 meters from the fire was only 14% of the OSHA ceiling concentration for asbestos fibers in the work environment, while the actual total exposure for the entire test was less than 0.3% of the OSHA-allowable 8-hour exposure to asbestos fibers.

This combination of computed and experimental data for potentially respirable fire-released fibers indicated that low quantities are released from burning aircraft composite structural parts, and these fibers are not known to have adverse physiological effects on humans.

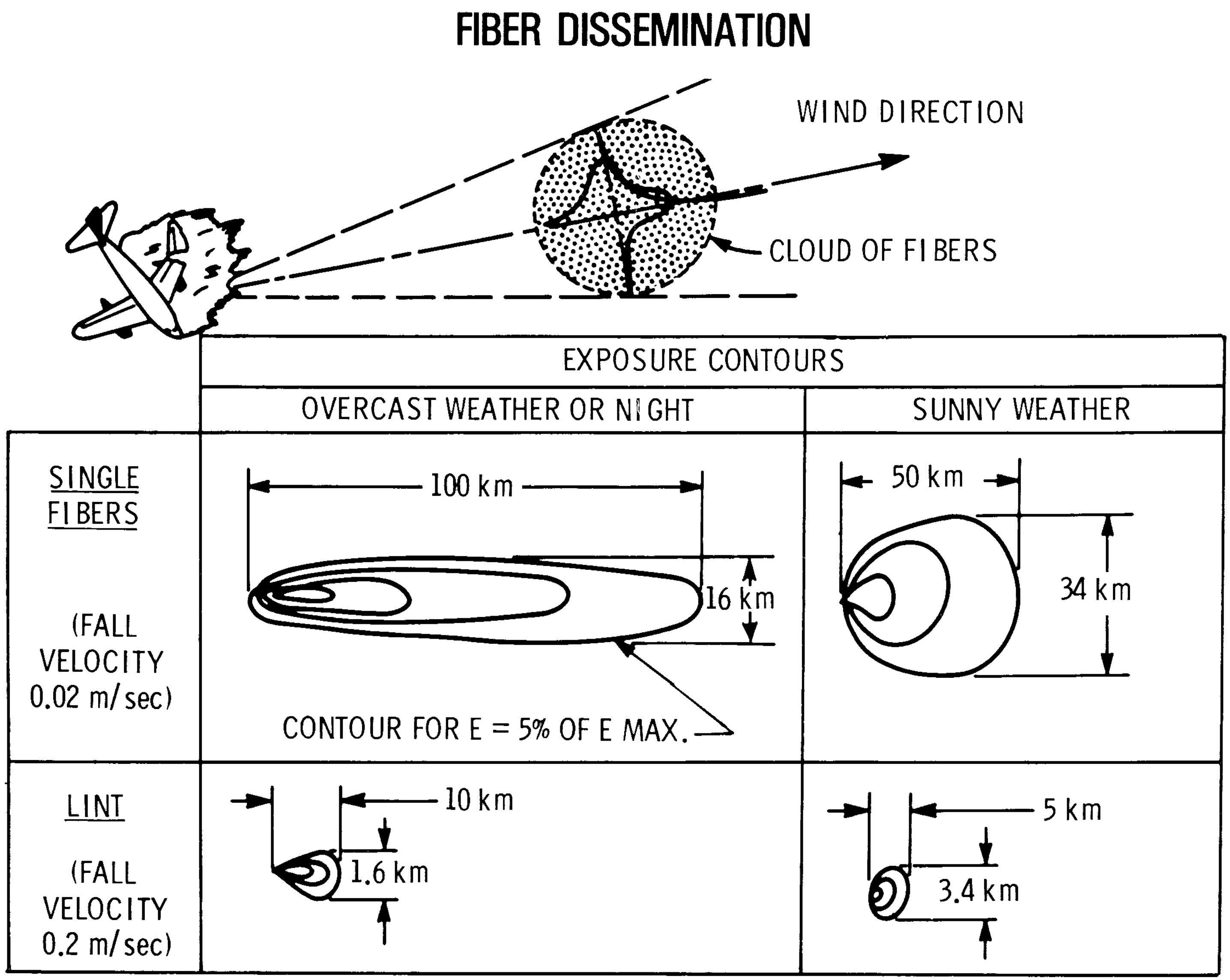
FIBER DISSEMINATION
WIND DIRECTION
CLOUD OF FIBERS
EXPOSURE CONTOURS
OVERCAST WEATHER OR NIGHT
SUNNY WEATHER
SINGLE FIBERS
(FALL VELOCITY 0.02 m/sec)
100 km
16 km
CONTOUR FOR E = 5% OF E MAX.
50 km
34 km
LINT
(FALL VELOCITY 0.2 m/sec)
10 km
1.6 km
5 km
3.4 km

Figure 14.

FIBER DISSEMINATION

(Figure 14)

The fiber materials released from a fire form a cloud which moves with the velocity of the wind and in the same direction as the wind. At a short distance from the fire, the fibers are diffused along the direction of travel and across the spread of the cloud roughly in a Gaussian distribution. The rate of spreading and also the maximum altitude of the fibers within the cloud are determined by the weather conditions. The ground level exposure can be described by a series of contours or "footprints" which link points of equal exposures. Overcast or nighttime conditions generally produce longer, narrower contours, with fall-out distances of up to 100 kilometers. Fall velocity has a direct effect on distance, with the heavier lint falling out in proportionately shorter distances. Conditions tyical of sunny weather tend to give shorter but broader contours. Existing Gaussian models for the dissemination of fire effluents were found to be acceptable for the carbon fiber risk analysis.

Several related pollution factors are usually used to measure the fiber dissemination. These are:

- Concentration, $C = \frac{\text{Number of particles}}{\text{Volume}}$
- Exposure (or dosage), $E = \text{Concentration} \times \text{Time}$
  $= \int C \, dt$
- Deposition, $D = \frac{\text{Number of particles}}{\text{Area}}$
  $= E \times \text{Particle velocity}$
- Flux, $F = \text{Deposition per unit time}$

The measure of fiber pollution usually used in elements of the risk analysis is exposure.

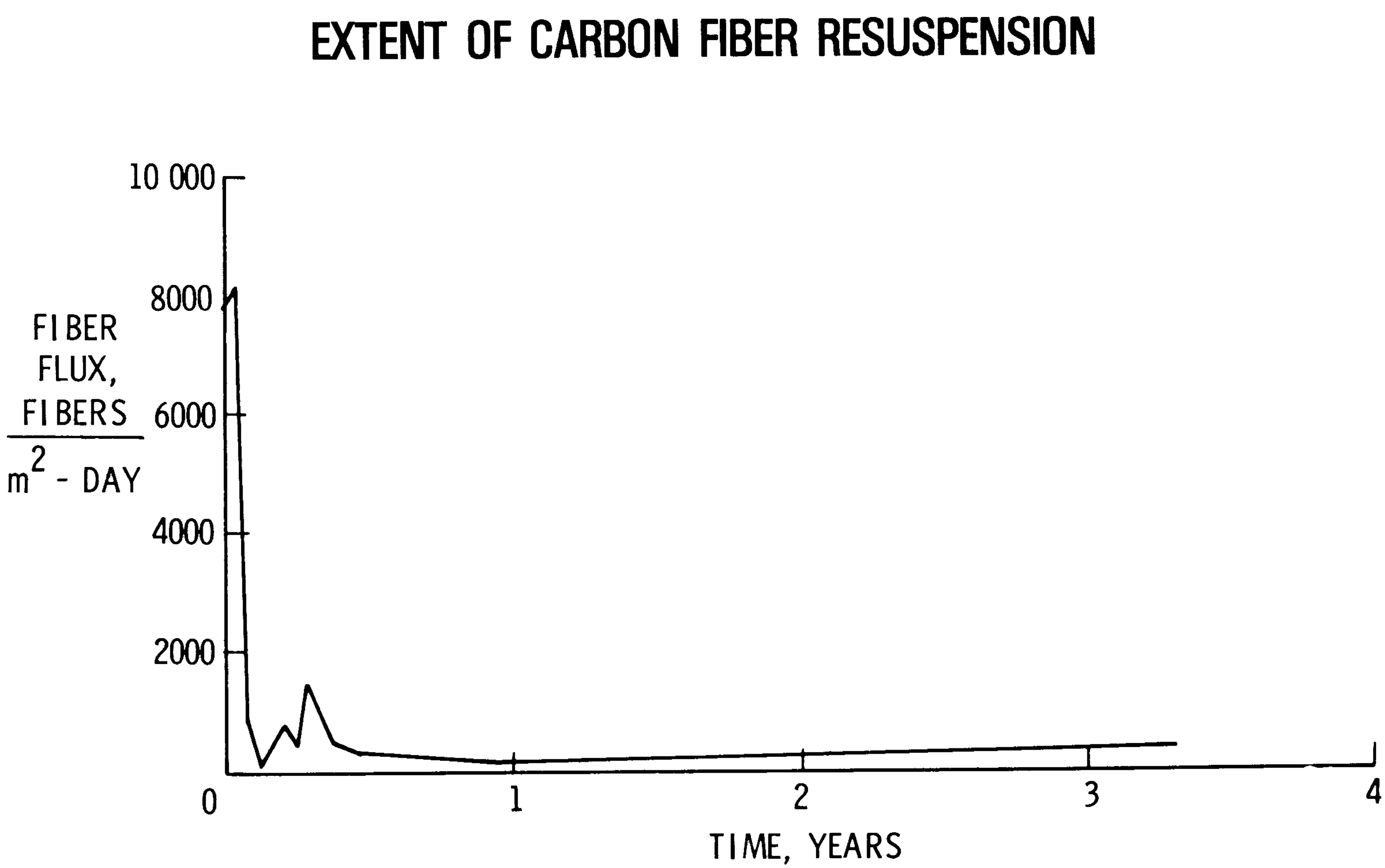
EXTENT OF CARBON FIBER RESUSPENSION
10 000
8000
6000
4000
2000
0
FIBER FLUX, FIBERS / m2 - DAY
1
2
3
4
TIME, YEARS

Figure 15.

EXTENT OF CARBON FIBER RESUSPENSION

(Figure 15)

The resuspension of deposited particles is the phenomenon which occurs in dust and sand storms and has been studied to understand many pollution problems. But the models which appeared applicable to sand and dust were considered unsuitable for carbon fibers because the aerodynamic characteristics of cylindrical fibers are quite different from those of more nearly spherical dust and sand. Therefore, a study was conducted to monitor the resuspension of graphite fibers from a desert area where about 50 kg of cut fibers had been deposited (ref. 3). The fiber flux from that area was monitored and analyzed at regular intervals for more than three years. As shown in the figure, the initial rate of resuspension was highest and a few fibers were still being released from the area after three years. However, the total quantity calculated as having been resuspended is less than 1 percent of the original quantity deposited. An analysis of the length of the airborne fibers shows that, after three years, only small 1-mm fragments were being resuspended. Therefore, resuspended fibers contribute only a small part to the total exposure and they are of a length that has only a marginal influence on the failure rate of equipment. Based on these observations, the risk assessment was made without any contribution from resuspended particles.

FILTRATION OF CARBON FIBERS

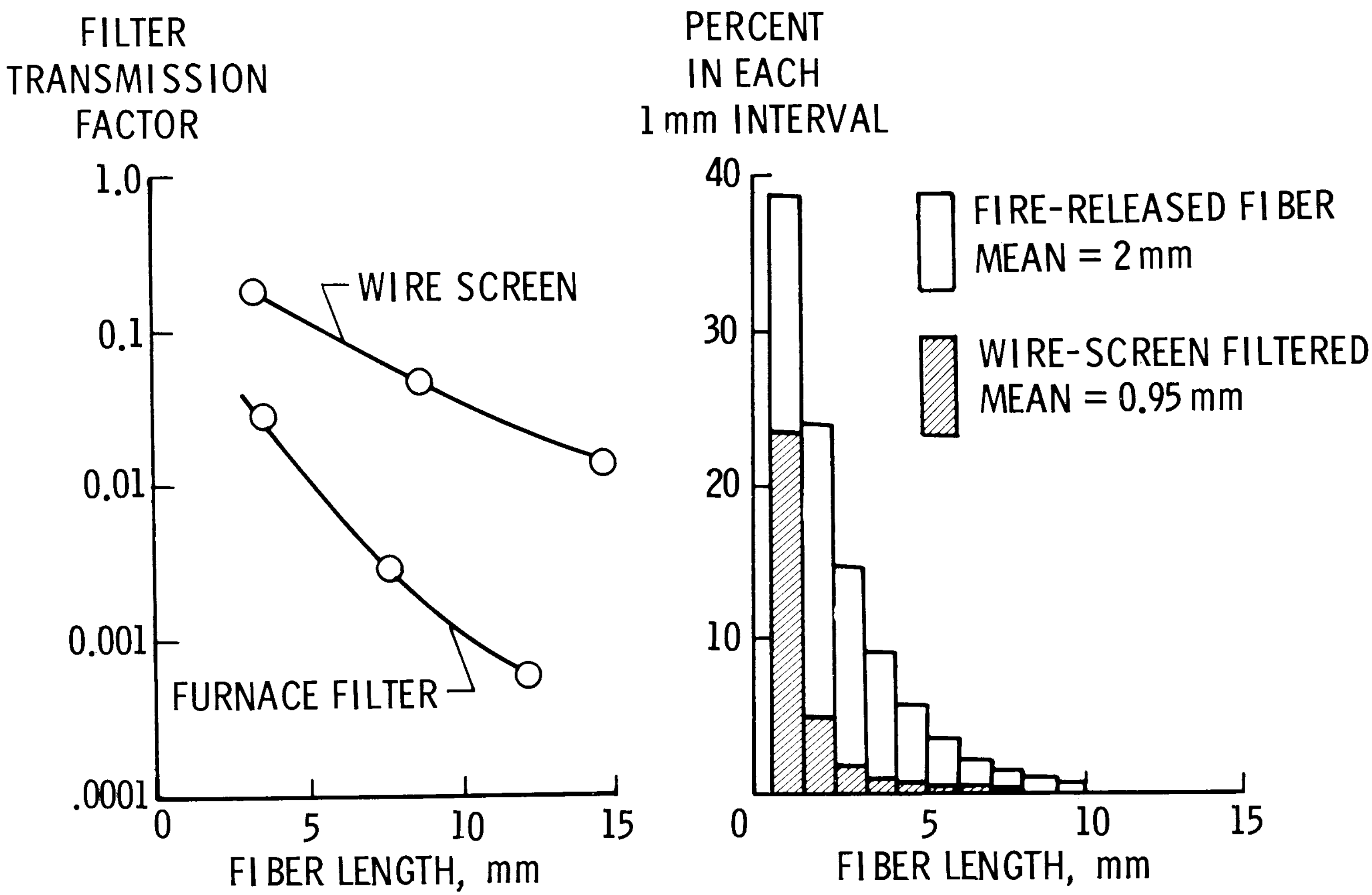

Figure 16.

FILTRATION OF CARBON FIBERS

(Figure 16)

Most of the electrical and electronic equipment which is vulnerable to carbon fibers is seldom exposed outside of buildings. Instead, buildings, filters and cabinets protect such equipment. Airflow models were developed to determine the possible flow of fibers into buildings and to establish the transfer functions. These models indicated that airflow rates, filter factors, fiber fall velocity, building height, and floor area all influenced the transfer functions. While airflow data for ventilation and leakage were available from building standards, new data had to be developed for filtration through filters and screens. Ordinary window screens were found to transfer only 10% of the 3-mm fibers striking them and furnace filters were found an order of magnitude more effective. Naturally, the effectiveness was higher than for spherical particles of the same diameter, the normal rating basis for filters. Also, the filters were more effective at stopping long fibers than short fibers. As a result, the fiber length distribution after filtration contained relatively more short fibers than before filtration. The risk calculations ignored this effect and conservatively used the fiber length distribution measured at the fiber source.

NASA CARBON FIBER TEST CHAMBER

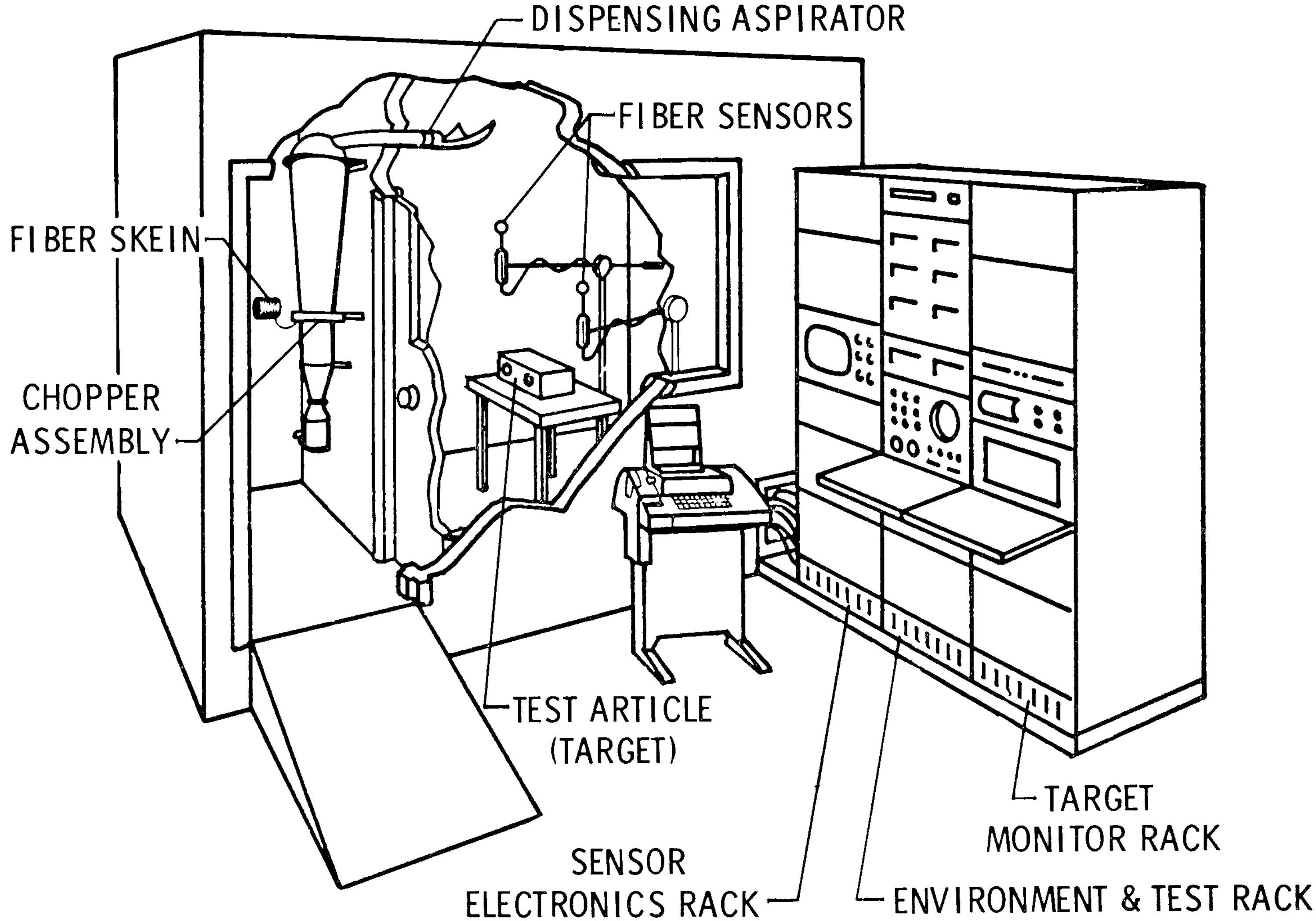

Figure 17.

NASA CARBON FIBER TEST CHAMBER

(Figure 17)

The vulnerability of electrical and electronic equipment to malfunction or damage when exposed to carbon fibers and the potential shock hazard was assessed in a systematic series of experiments. These experiments included:

Probing the circuitry with shunts of known resistance.

Exposing equipment to chopped virgin fibers in a closed chamber.

Exposing equipment to fire-released fibers.

Over 150 pieces of equipment were tested, including household appliances, moderately complex electronics and avionics. For most of the tests with chopped fibers, T-300 fibers were utilized because this type of fiber is representative of fibers used in aircraft structural composites. Fiber concentrations were approximately 10^3 fibers/meter^3, a value that is higher than experienced in the fire-release tests. Equipment was exposed until failure or until 10^8 fiber-sec/meter^3 was achieved. This exposure deposited essentially a continuous mat of fibers on the floor of the test chamber. The fibers were chopped to uniform lengths for each test, but the length was varied to study effects of length over the range from 1 to 20 mm. This range of lengths covered the range of fiber lengths expected to be significant contributors to electrical risk. One of the test chambers used is illustrated in the figure. Generally, the tests were performed with fibers falling freely in still air.

AVERAGE EXPOSURE TO FAILURE FOR VULNERABLE EQUIPMENT

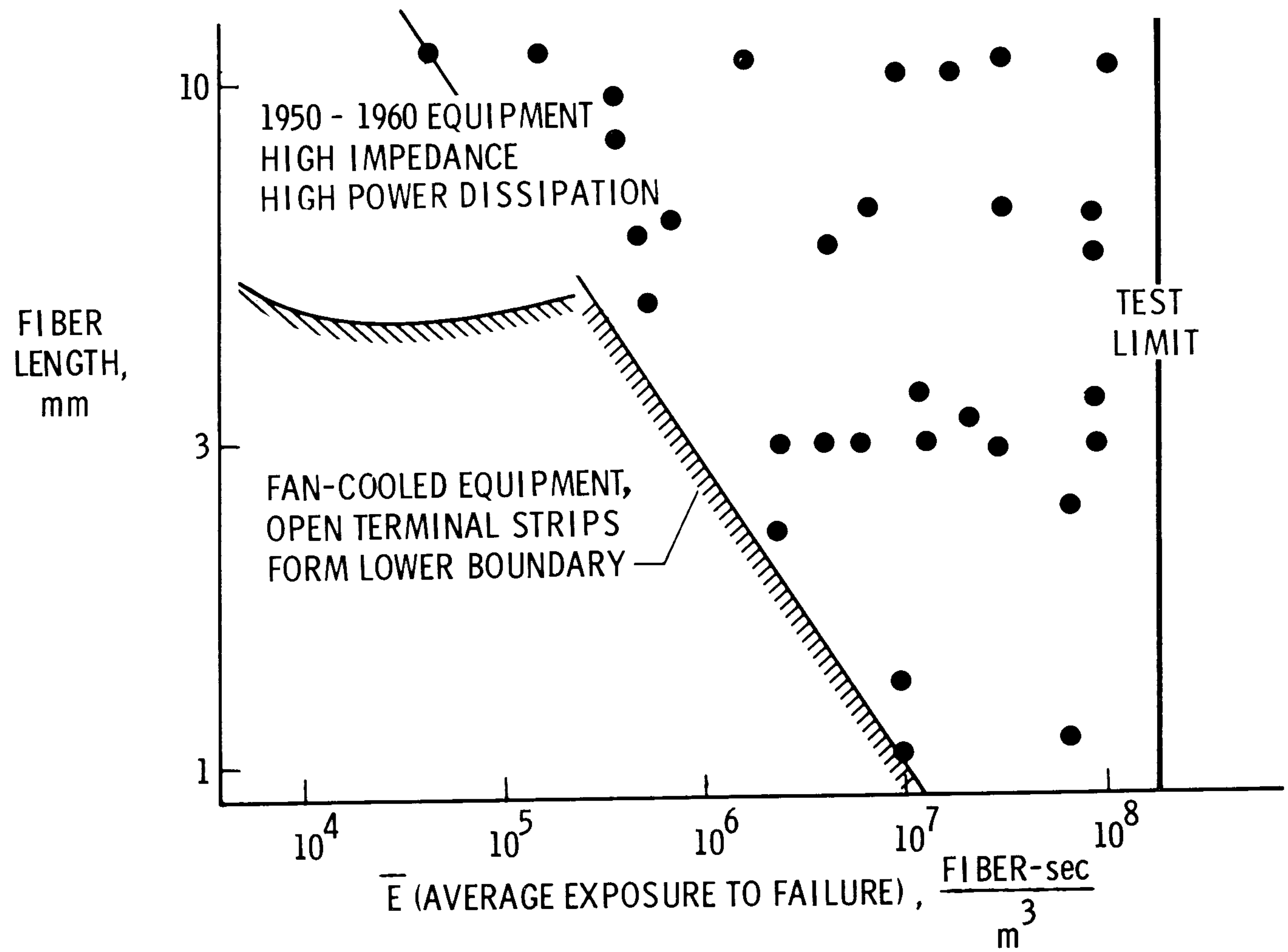

Figure 18.

AVERAGE EXPOSURE TO FAILURE FOR VULNERABLE EQUIPMENT

(Figure 18)

In general, the equipment was less vulnerable than had been expected. In almost all cases, the equipment was restored by vacuum cleaning the affected circuitry. Low-voltage equipment (0 to 15 volts) was susceptible to failures if fibers could reach critical circuitry. However, many devices had few vulnerable contacts and others were well protected against intrusion by fibers. Permanent malfunctions sometimes occurred because insufficient voltage was available to burn away ingested fibers. In some low-power circuits, such as in computers, these malfunctions were errors in logic or displays. The majority of the equipment found susceptible was low-voltage, low-power.

Medium-voltage equipment (15 to 220 volts) usually survived exposures to fibers because the voltage was high enough to burn out the fiber in a short time without damage to the equipment. Such short-duration phenomena may cause malfunctions, but this is statistically unlikely. The inherent invulnerability of 110-volt devices was demonstrated by tests on home appliances, motors and thermostats.

High-voltage equipment (440 volts, 60 Hz) is used in many industrial applications. Tests of various terminal configurations indicated no sustained arcs for this voltage level on single-phase power drawn from a commercial line. Three-phase systems sometimes sustained fiber-initiated arcs that damaged connectors. This damage was limited by the circuit-protection devices employed.

High-voltage (>440 volts) power system insulators were found to survive exposures in excess of 10^7 fiber-sec/meter^3 (for fibers 2 or 4.3 mm long) without flashover (ref. 4).

The figure shows the average exposure to failure for a variety of different types of equipment. High vulnerability was exhibited by older equipment types using vacuum tubes and other high-impedance components. Modern electronic designs are based on highly integrated circuits, with few discrete parts and, in general, operate with no ventilation and low power. Thus, they are correspondingly less vulnerable.

Experiments on vulnerability of electrical and electronic equipment were generally performed with 5 or more exposures to failure to determine the mean exposure to cause failure, $\bar{E}$. This was accomplished at each of a number of fiber lengths. In realistic situations, E is likely to be one or more orders of magnitude smaller than $\bar{E}$. To apply the observations to these practical exposures, analysis shows that the probability of failure, P_f, due to exposure to single fiber is $P_f = 1 - e^{-E/\bar{E}}$, where $\bar{E}$ was obtained from tests at a fiber length of 2.8 mm.

EFFECT OF FIBER LENGTH ON EQUIPMENT VULNERABILITY

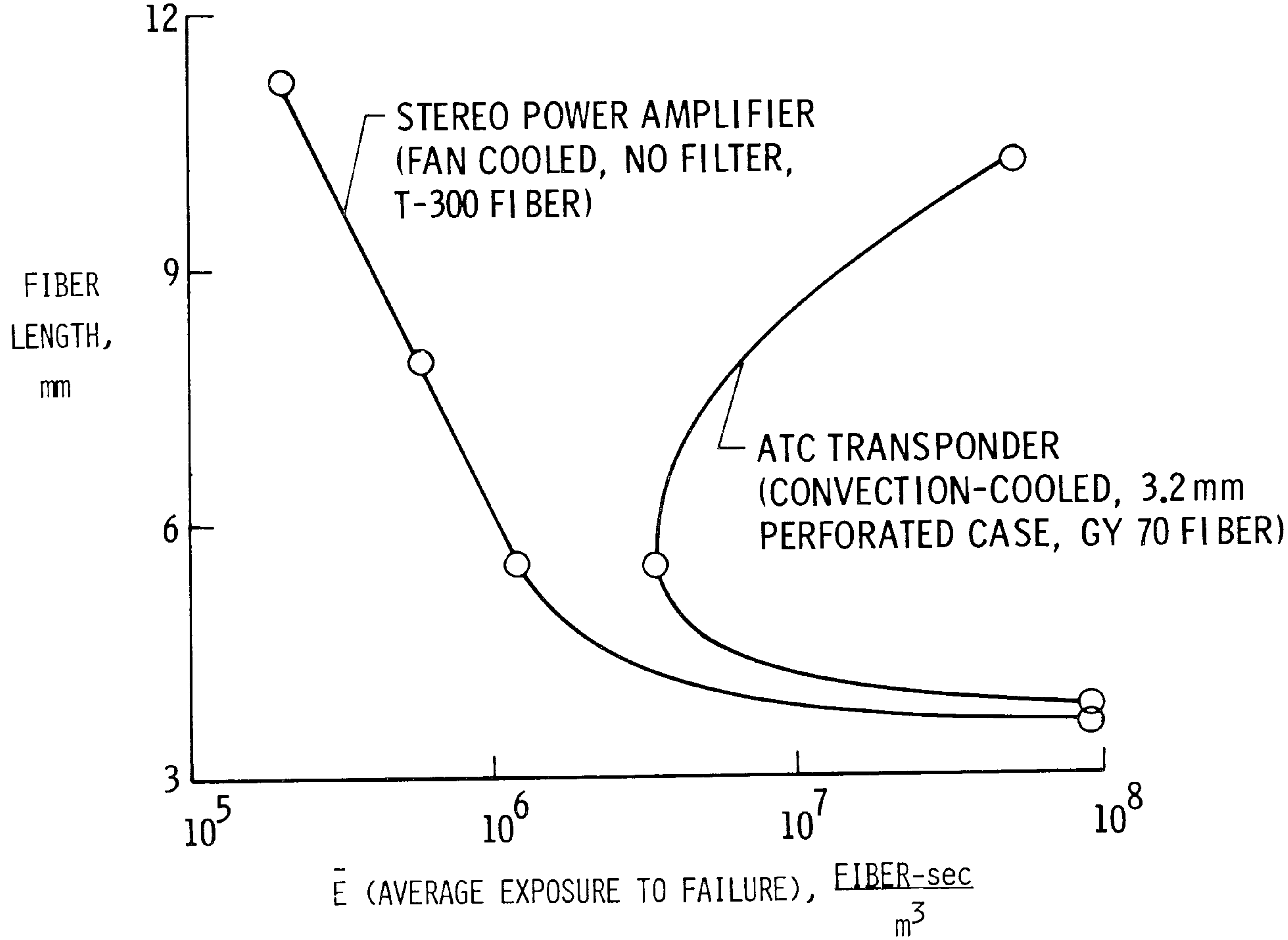

Figure 19.

EFFECT OF FIBER LENGTH ON EQUIPMENT VULNERABILITY

(Figure 19)

The figure illustrates specific test results for two types of equipment. The stereo power amplifier was fan cooled and had no filtration. This case configuration offered no effective impediment to any length of fibers. The number of fibers which may deposit on open electrical equipment is proportional to the concentration, time of exposure and the free-fall rate of the fibers. For this reason, vulnerability is best correlated with exposure (the integral of concentration over time) for a given system. Case-enclosed electronics generating low convection velocities, such as the ATC transponder, are relatively invulnerable. When the dissipated power is sufficient to generate convective air velocities larger than fiber-fall velocity, the induced circulation may entrain fibers and, thus, increase deposition density and system susceptibility. The most susceptible systems have been shown to be those that are cooled by unfiltered forced air.

The stereo power amplifier follows the generally observed experimental rule that the average exposure to failure is inversely proportional to the fiber length squared. The ATC transponder, at the shortest fiber lengths, follows the general rule but at longer fiber lengths the small case holes effectively prevent fibers from entering the component, thereby increasing the average exposure required to cause a failure. This transponder test data set was obtained with a highly graphitic fiber, GY70, which was found to produce approximately an order of magnitude lower average exposures to failure than the use of T-300 fibers.

Because of the specific responsibility of the NASA study regarding the potential need for protection to aircraft, special attention was given to determine the vulnerability of avionics equipment used in scheduled commercial or general aviation aircraft. No equipment had mean exposures to failure, $\bar{E}$, less than 10^7 fiber-sec/meter^3 even when the test included noise and vibration to simulate the environment of the avionics bays in aircraft. These data, combined with airflow and filtration data pertinent to specific aircraft, were used to evaluate the risk to air-transport aircraft safety and the need for protection.

FACILITY SURVEYS

PUBLIC SUPPORT	NO.	COMMERCIAL INSTALLATION	NO.
HOSPITALS	7	DEPARTMENT STORES	2
AIR TRAFFIC CONTROLS	6	FINANCIAL INSTITUTIONS	2
AIRPORTS-AIRLINES	3	RADIO AND TV STATIONS	6
POLICE HEADQUARTERS	2	ANALYTICAL LABORATORIES	1
FIRE DISPATCH	2	**MANUFACTURING OPERATIONS**	
POST OFFICES	1	MEAT PACKING	1
TRAFFIC CONTROL	1	TEXTILE MILL	1
UTILITIES		GARMENTS	1
TELEPHONE EXCHANGES	3	PULP AND PAPER	1
POWER GENERATION AND DISTRIBUTION	3	PUBLISHING	2
REFUSE INCINERATORS	2	TEXTILE FIBERS	1
AMTRAK RAILWAY SYSTEM	1	TOILETRIES	1
		STEEL MILLS	2
		WIRE, CABLE	1
		ELECTRICAL EQUIPMENT	6
		AUTOMOTIVE FAB./ASSY.	4

Figure 20.

FACILITY SURVEYS

(Figure 20)

Surveys were conducted to gather the data required to assess the economic impact of electrical incidents attributable to fire-released fibers. Over 60 public, utility, commercial, and industrial installations were visited to gather data on:

(a) the sensitivity of life-critical or emergency services to airborne carbon fibers,

(b) the sensitivity of commercial and industrial equipment to airborne carbon fibers, and

(c) the associated economic impact of fiber-induced failures.

The surveys indicated that life-critical services, such as hospitals, were already protected against contamination. Their air-conditioning systems also provided isolation from airborne carbon fibers. Critical systems in more than half of the 21 industrial installations visited were equipped with high-efficiency filters or coated circuit boards that would provide effective protection against airborne carbon fibers. Continuous-process operations and assembly lines, where equipment failures could halt operations, had similar features adequate to protect against airborne carbon fibers. Most industrial installations were able to shift operations or to work around electrical failures in equipment without major cost impact. Where a high incidence of equipment failures occur, interchangeable spares were generally maintained. The results of these surveys were combined in the analysis models with census data to calculate the economic impact of carbon fiber accidents.

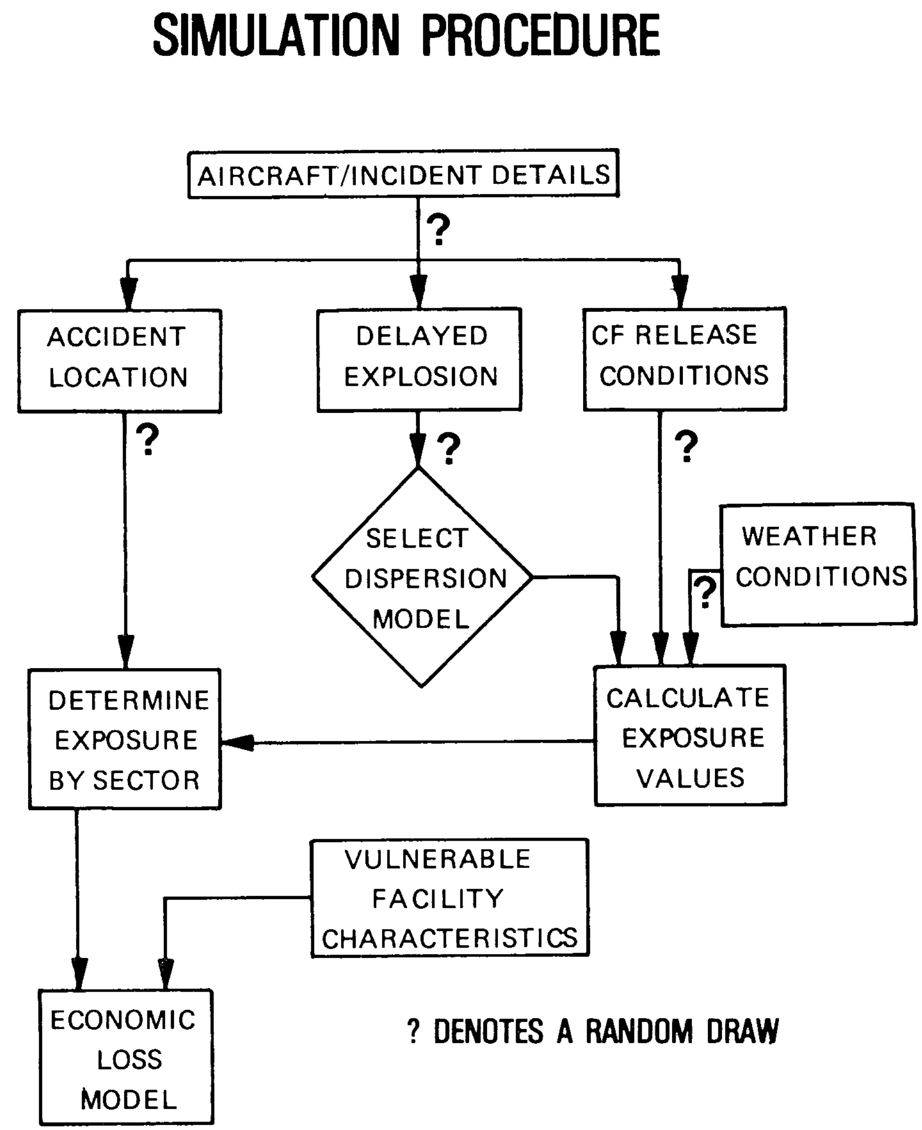
SIMULATION PROCEDURE
AIRCRAFT/INCIDENT DETAILS
?
ACCIDENT LOCATION
DELAYED EXPLOSION
CF RELEASE CONDITIONS
?
?
?
SELECT DISPERSION MODEL
WEATHER CONDITIONS
?
DETERMINE EXPOSURE BY SECTOR
CALCULATE EXPOSURE VALUES
VULNERABLE FACILITY CHARACTERISTICS
ECONOMIC LOSS MODEL
? DENOTES A RANDOM DRAW

Figure 21.

SIMULATION PROCEDURE

(Figure 21)

In computing the risk associated with the use of carbon fibers in air-transport aircraft, many thousands of aircraft accidents were simulated, each differing by numerous variables. The individual accidents were simulated by random selections of the variables associated with the accident location, the operational mode, the type of aircraft, the extent to which carbon fibers were involved and whether or not explosion occurred. The behavior of the fire plume that carries the released fibers aloft and the downwind transport and diffusion processes were modelled using established methods. The necessary meteorological inputs for these calculations were drawn at random from local weather statistics for each of the airports for which the calculations were made. The transport and diffusion calculations provided the fiber exposures or dosages downwind of the simulated accident. The downwind areas were subdivided into sectors. The distributions of businesses, industries, public facilities and private residences within these sectors were then determined from county-based economic and census data. Equipment complements were assigned based on data gathered during the facility surveys. Critical exposure levels, $\bar{E}$, for equipment and equipment combinations were established based on the test data acquired. On the basis of the calculated interior exposures, the probability of equipment failure and the cost of the failure was computed for households as well as each type of business, industry and public facility. The vulnerability of avionics equipment aboard aircraft parked at an airport and airport ground control equipment was included in the above computation.

From the foregoing costs of failures in industries, businesses, public facilities, households, and parked aircraft, the models generated an estimate of the total economic impact of one accident. This process was repeated until sufficient accidents had been simulated to establish a stable distribution of the individual accident costs for an airport. From this distribution, similar distributions generated for other airports, the local aircraft operational rate, and the annual frequency of air-transport aircraft crash-fire accidents, a national annual distribution and risk profile were developed.

CARBON FIBER RISK PROFILES

AIR-TRANSPORT ACCIDENTS

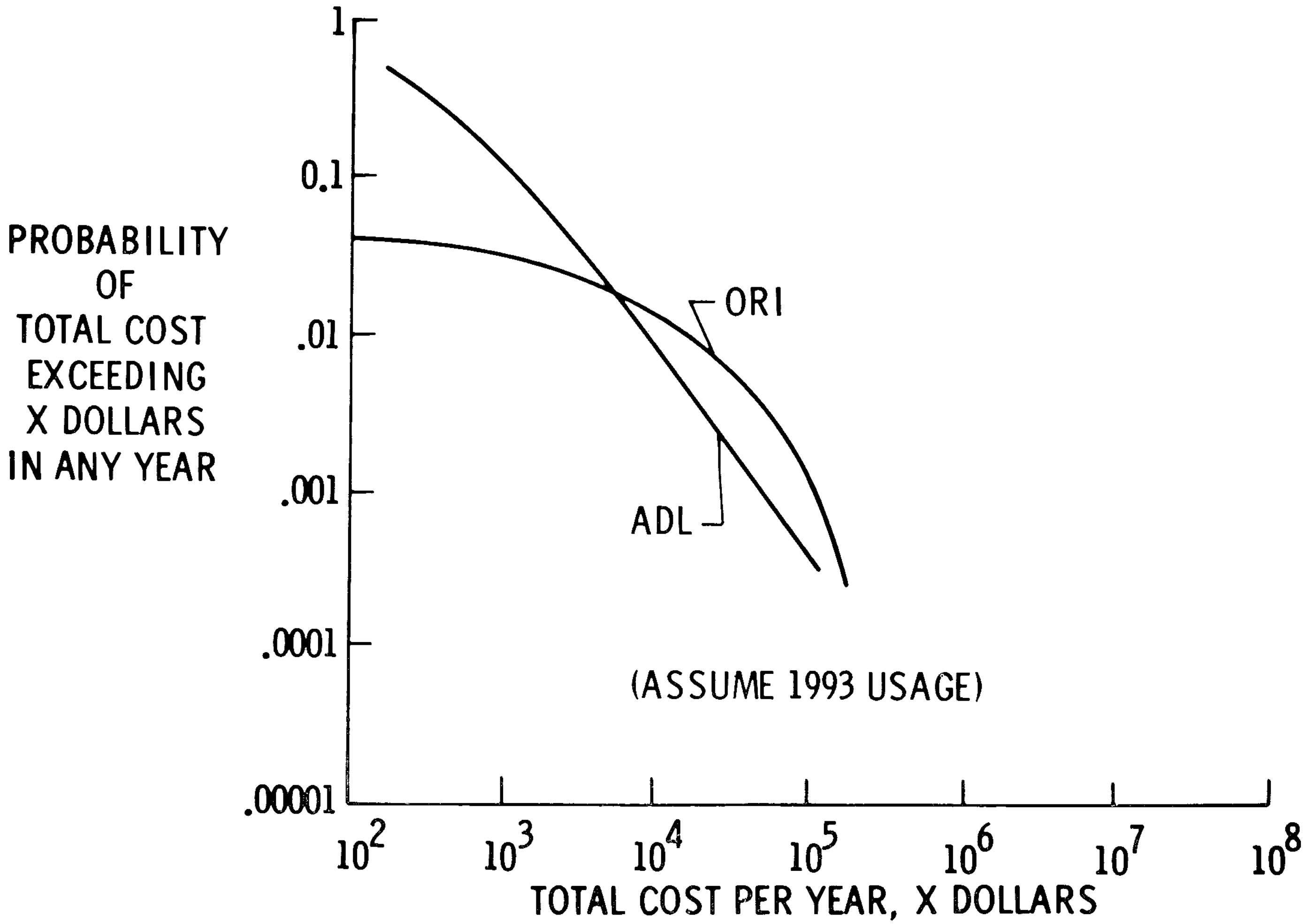

Figure 22.

CARBON FIBER RISK PROFILES
(AIR-TRANSPORT FIRE ACCIDENTS)

(Figure 22)

The results of the Monte Carlo simulations of air transport accidents, portrayed in the form of risk profiles, are presented in Figure 22. The two profiles were independently calculated by ORI and Arthur D. Little (references 5 and 6 . The mean annual damage is almost identical at $450, but the ORI results show a somewhat higher standard deviation. Both studies found that the damage was principally sustained by business and industry, with one-third or less of the damage occurring in households. The largest simulated damage found in the Monte Carlo simulation was $178,000 in the ORI analysis and $74,000 in the Arthur D. Little analysis.

The potential damage to the avionics of commercial aircraft was included in the national risk profile and was separately and independently analyzed by the aircraft manufacturers (references 7 , 8 , 9). The expected number of equipment failures, due to carbon composite crash fires, was found to be of the order of 0.0003% of the current normal operational failure rate and no situations could be identified in which the safety of the aircraft was affected.

By comparison, a study of the costs of the 155 non-minor aircraft accidents between 1966 and 1975 showed that the mean cost of these air-transport aircraft accidents was about 6 million dollars, with the worst-case accident costing about 50 million dollars. Such a comparison indicates that even the worst-case carbon fiber incident simulated ($178,000 cost, which was expected only once in 34,000 years) is a relatively low-cost event (reference 5).

RISK PROFILE SENSITIVITY TO INPUT PARAMETERS

AIR-TRANSPORT ACCIDENTS

CHANGE TO INPUT	CHANGE TO MEAN	CHANGE TO STANDARD DEVIATION
DOUBLE CF RELEASED	2X	2X
DOUBLE ACCIDENT RATE	2X	1.7X
ALL AIRCRAFT HAVE 10,954 kg OF CF (7 TIMES AVERAGE CF PER AIRCRAFT)	7X	4.5X
EXPLOSIONS WITH ALL FIRES (3.5 TIMES "FIRE-ONLY" FIBER RELEASE)	3X	2X
ALL WEATHER CLASS E	1.5X	1.2X

Figure 23.

RISK PROFILE SENSITIVITY TO INPUT PARAMETERS
(AIR-TRANSPORT ACCIDENTS)

(Figure 23)

The sensitivity of the risk from air-transport accidents to variations in input parameters was analyzed. The figure shows the effect of five changes on mean damage and standard deviations. The effects on the risk profile, in the first three instances, are roughly equal to the change in the input parameters. In addition, only a small effect is observed from significant variations in the details of the fiber dissemination mechanism (explosions vs fire plume, all one class of weather vs historical distribution of weather).

CARBON FIBER RISK ANALYSIS

GENERAL AVIATION FIRE ACCIDENTS

BASIS

- SIMPLIFIED ANALYSIS
- DEMOGRAPHICS, EQUIPMENT VULNERABILITY, FILTRATION FACTORS SAME AS AIR-TRANSPORT ANALYSIS
- ALL CIVILIAN AIRCRAFT OTHER THAN AIR CARRIERS CONSIDERED AS GENERAL AVIATION
- 354 FIRE ACCIDENTS PER YEAR
- 25% OF AIRCRAFT HAVE FROM 7 TO 50 kg OF CF
- 0.7% TO 2.9% OF CF RELEASED

RESULT

- ECONOMIC IMPACT OF CARBON-FIBER-INDUCED EQUIPMENT FAILURES

	EXPECTED VALUE	STANDARD DEVIATION
PER INCIDENT	$2.88	$ 114
ANNUAL	$253	$1067

Figure 24.

CARBON FIBER RISK ANALYSIS
(GENERAL AVIATION FIRE ACCIDENTS)

(Figure 24)

The use of the air carrier procedures to analyze risk from general aviation accidents would have required a prohibitive effort because these accidents occur with much greater frequency and at much more widely scattered points. On the other hand, much smaller quantities of carbon fiber are likely to be released and, therefore, a much smaller risk is involved in a given accident. Accordingly, a simplified analytic approach was developed that utilized expected values for many of the input data (reference 10). The quantities thus defined were combined in all relevant combinations and with appropriate weighting factors to establish a mean number of electrical failures per accident. Because very small masses of fibers were expected to be released in any accident, the mean number of electrical failures per accident was only 0.022. About 98% of all accidents were not expected to cause any failures. Because the number of accidents per year and the number of failures per accident are appropriately assumed to be random variables with Poisson distributions, their means also determine their variance. From this, standard deviation of annual national risk was computed to be $1067. From probability analysis, it was determined that the chance of exceeding $100,000 annual loss was one in ten thousand.

CONCLUSIONS

- LIFE IS NOT ENDANGERED
  - POSSIBILITY OF A SHOCK HAZARD IS REMOTE
  - SAFETY OF EXPOSED AIRCRAFT IS NOT AFFECTED
- ECONOMIC IMPACT IS INSIGNIFICANT
  - EXPECTED VALUE OF ANNUAL DAMAGE $<$ \$1000
  - LOW-PROBABILITY WORST-CASE SIMULATED INCIDENT $\ll$ COST OF AIRCRAFT

Figure 25.

CONCLUSIONS

(Figure 25)

A comprehensive assessment of the possible damage to electrical equipment caused by accidental release of carbon fibers from burning civil aircraft with composite parts has been completed. The study concluded that the amount of fiber likely to be released is much lower than initially predicted. Footprints of carbon fiber determined from dispersion models were found to be much larger in area than originally estimated, but were correspondingly much lower in fiber concentrations. Long-term redissemination of fiber was shown to be insignificant assuming reasonable care is exercised in accident clean-up. The susceptibility of electrical equipment to current structural fibers was low. Consumer appliances, industrial electronics, and avionics were essentially invulnerable to carbon fibers.

Shock hazards (and thus potential injury or death) were found to be extremely unlikely. The expected number of avionic equipment failures, due to carbon composite crash-fires, was found to be of the order of 0.0003% of the current normal operational failure rate. No situations were identified in which the safety of the aircraft was affected.

The overall costs were shown to be extremely low in 1993, the year chosen as a focus of the study. The expected annual cost was shown to be less than $1000 with only one chance in two thousand of exceeding $150,000 loss annually. For comparison, a study of 1966-1975 aircraft accident costs showed that the costs of air-transport aircraft accidents range from less than a million dollars to nearly fifty million dollars per accident (non-fire accidents are included). The mean cost of those accidents, where the aircraft sustained at least substantial damage, was about 6 million dollars. Thus, even the worst-case carbon-fiber incident simulated is relatively low cost.

REFERENCES

1. Carbon Fiber Study. Compiled by Intergovernmental Committee. NASA TM-78718, 1978.

2. Sussholz, B.: Evaluation of Micron-Size Carbon Fibers Released from Burning Graphite Composites. (TRW Defense and Space Systems Group, NASA Contract NAS1-15465). NASA CR-159217, 1980.

3. Trethewey, John D.; and Whiting, John H.: Surveillance Sampling of Carbon Fiber Material, June 1975-August 1978. DPG-FR-79-304, U. S. Army Dugway Proving Ground, 1978.

4. Assessment of Carbon Fiber Electrical Effects. NASA CP-2119, 1980.

5. Pocinki, Leon; Cornell, Merrill; and Kaplan, Lawrence: Advanced Risk Assessment of the Effects of Graphite Fibers on Electronic and Electric Equipment. (ORI, Inc., NASA Contract NAS1-15379). NASA CR-159210, 1980.

6. Kalelkar, Ashok; Fiksel, Joseph; Rosenfield, Donald; Richardson, David L. and Hogopian, John.: An Assessment of the Risk Arising from Electrical Effects Associated with Carbon Fibers Released from Commercial Aircraft Fires (Arthur D. Little, Inc., NASA Contract NAS1-15380). NASA CR-159205, 1980.

7. Clarke, C. A.; and Brown, E. L.: Assessment of Risk to Boeing Commercial Transport Aircraft From Carbon Fibers. (Boeing Commercial Airplane Company, NASA Contract NAS1-15510). NASA CR-159211, 1980.

8. Daniledes, James; and Koch, John R.: Carbon/Graphite Fiber Risk Analysis and Assessment Study. Assessment of the Risk to the Lockheed Model L-1011 Commercial Transport Aircraft. (Lockheed-California Company, NASA Contract NAS1-15509). NASA CR-159201, 1980.

9. Schjelderup, H. C.: Carbon/Graphite Fiber Risk Analysis and Assessment Study. An Assessment of the Risk to Douglas Commercial Transport Aircraft. (McDonnell Douglas Corporation, Douglas Aircraft Company, NASA Contract NAS1-15508). NASA CR-159212, 1980.

10. Rosenfield, Donald; and Fiksel, Joseph: An Assessment of the Risk Arising from Electrical Effects Associated with the Release of Carbon Fibers from General Aviation Aircraft Fires. (Arthur D. Little, Inc., NASA Contract NAS1-15380). NASA CR-159206, 1980.